Performance Analysis of Doubly-Fed Induction Generator (DFIG)- Based Wind Turbine with Sensored and Sensorless Vector Control

Amer Obaid Kareem

B.Sc., M.Sc

Student Number: 089112111

A thesis submitted for the degree of

Doctor of Philosophy

November 2016

School of Electrical and Electronic Engineering

Newcastle University

United Kingdom

ABSTRACT

Conventional energy sources are limited and pollute the environment. Therefore more attention has been paid to utilizing renewable energy resources. Wind energy is the fastest growing and most promising renewable energy source due to its economically viability. Wind turbine generator systems (WTGSs) are being widely manufactured and their number is rising dramatically day by day. There are different generator technologies adopted in wind turbine generator systems, but the most promising type of wind turbine for the future market is investigated in the present study, namely the doubly-fed induction generator wind turbine (DFIG). This has distinct advantages, such as cost effectiveness, efficiency, less acoustic noise, and reliability and in addition this machine can operate either in grid-connected or standalone mode. This investigation considers the analysis, modeling, control, rotor position estimation and impact of grid disturbances in DFIG systems in order to optimally extract power from wind and to accurately predict performance. In this study, the dynamic performance evaluation of the DFIG system is depicted the power quantities (active and reactive power) are succeed to track its command signals. This means that the decouple controllers able to regulating the impact of coupling effect in the tracking of command signals that verify the robust of the PI rotor active power even in disturbance condition.

One of the main objectives of this study is to investigate the comparative estimation analysis of DFIG-based wind turbines with two types of PI vector control using PWM. The first is indirect sensor vector control and the other type includes two schemes using model reference adaptive system (MRAS) estimators to validate the ability to detect rotor position when the generator is connected to the grid. The results for the DFIG-based on reactive power MRAS (QRMRAS) are compared with those of the rotor current-based MRAS (RCMRAS) and the former scheme proved to be better and less sensitive to parameter deviations, its required few mathematical computations and was more accurate. During the set of tests using MATLAB®/SMULINK® in adjusting the error between the reference and adaptive models, the estimated rotor position can be obtained with the objective of achieving accurate rotor position information, which is usually measured by rotary encoders or resolvers. The use of these encoders will conventionally lead to increased cost, size, weight, and wiring

complexity and reduced the mechanical robustness and reliability of the overall DFIG drive systems. However the use of rotor position estimation represents a backup function in sensor vector control systems when sensor failure occurs.

The behavioral response of the DFIG-based wind turbine system to grid disturbances is analyzed and simulated with the proposed control strategies and protection scheme in order to maintain the connection to the network during grid faults. Moreover, the use of the null active and reactive reference set scheme control strategy, which modifies the vector control in the rotor side converter (RSC) contributes to limiting the over-current in the rotor windings and over-voltage in the DC bus during voltage dips, which can improve the Low Voltage Ride-through (LVRT) ability of the DFIG-based wind turbine system.

ACKNOWLEDGMENTS

In the Name of God, the most Gracious, the most Merciful, say Glory to Allah, who has given me the strength, patience, ability, and knowledge to finish my PhD study.

From the depths of my heart, I would like to express my sincere gratitude to my supervisor, Dr. Shady Gadoue, for his guidance and support, intellectual advice and patience thoughtout the study process. I give him heartfelt thanks for his time and assistance throughout my PhD journey. I wish you the best and further success and achievement in your life. I also wish to thank my co-supervisor, Dr. Mohamed Elgendy, for his support and helpful suggestions.

Of course, no acknowledgments would be complete without giving thanks to my parents, my wife Nadeen, my brothers (Mr. Kareem and Dr. Nagham) and my uncle (Mr. Bassil) to whom I would like to express my sincere gratitude. They provided me with love, guidance, prayers, support and wisdom. Thank you very much for being the motivational element in my life, enhancing me in every moment and giving me the ability to complete this work successfully. My wife's insights and words of encouragement have often inspired me and renewed my hopes for completing my PhD research.

Special appreciation goes to the School of Electrical and Electronic Engineering, Newcastle University, for providing me with this opportunity to complete my study and research.

I would also like to express special thanks to my home country of Iraq and its Ministry of Planning for providing a scholarship for my study.

TABLE OF CONTENTS

LIST OF SYMBOLS

$\rho = {}^{d}/_{dt}$	First derivative with respect to time.
C_{bus}	Capacitance of the DC link.
f	Fundamental frequency.
f_{cr}	Carrier frequency.
f_g	Grid frequency.
f_m	Modulation frequency.
f_r	Rotor frequency.
f_s	Stator frequency.
$i_a, i_b i_c$	Three-phase, *abc*, currents.
i_{dr}, i_{qr}	Two-phase DC rotor currents, rotating *dq*-axis.
i_{ds}, i_{qs}	Two-phase DC stator currents, rotating *dq*-axis.
$i_{ar}^s, i_{br}^s, i_{cr}^s$	Three-phase, *abc*, rotor currents in the stationary reference frame.
$i_{as}^s, i_{bs}^s, i_{cs}^s$	Three-phase, *abc*, stator currents in the stationary reference frame.
$i_{\alpha r}^s, i_{\beta r}^s$	Two-phase AC rotor currents, alpha/beta, in the stationary frame.
$i_{\alpha s}^s, i_{\beta s}^s$	Two-phase AC stator currents, alpha/beta, in the stationary frame.
i_{dr}^e, i_{qr}^e	Two-phase DC rotor currents, rotating dq-axis synchronous frame.
i_{ds}^e, i_{qs}^e	Two-phase DC stator currents, rotating dq-axis synchronous frame.
i_{dg}^e, i_{qg}^e	Two-phase DC grid currents, rotating dq-axis synchronous frame.
ji_{qr}, ji_{qs}	Polar currents relating to the imaginary axis of rotor and stator q-axis.
$i_{error\_dr}^e$	*d*-axis rotor error current in synchronous reference frame.
$i_{error_{qr}}^e$	*q*-axis rotor error current in synchronous reference frame.
$i_{dr}^{ref^e}$	*d*-axis rotor reference current in synchronous reference frame.
$i_{qr}^{ref^e}$	*q*-axis rotor reference current in synchronous reference frame.
ki, kp	Proportional and integral gain of PI controller.
L	Inductance.
$L_{lr,} L_{ls}$	Rotor and stator leakage inductance.
L_r, L_s	Rotor and stator self-inductance.
L_m	Magnetizing inductance.
L_{dc}	DC link inductance.
m_f	Frequency modulation index.

n_r	Rotor speed of induction generator, RPM.
n_s	Rotor speed of induction generator, RPM.
p	Pole pairs of induction machine.
P	Active Power.
P_r	Rotor active power.
P_s	Stator active power.
P_m	Mechanical active power.
P_{error}	Active power error.
P_s^{ref}	Reference stator active power.
Q	Reactive power.
Q_r	Rotor reactive power.
Q_s	Stator reactive power.
Q_{error}	Reactive power error.
Q_s^{ref}	Reference stator reactive power.
r_r,r_s	Rotor and stator resistance.
s	Induction machine slip.
T_e, T_m	Electrical and mechanical torque of the DFIG.
V_a, V_b, V_c	Three-phase, *abc*, voltages.
V_{bus}	DC link bus voltage.
V_m	Modulated voltage.
V_α, V_β	Two-phase alpha/beta voltages.
V_{dr}, V_{qr}	Two-phase DC rotor voltages, rotating *dq*-axis.
V_{ds}, V_{qs}	Two-phase DC stator voltages, rotating dq-axis.
V_{ra}^s,V_{rb}^s, V_{rc}^s	Three-phase, *abc*, rotor voltages in the stationary reference frame.
$V_{as}^s, V_{bs}^s, V_{cs}^s$	Three-phase, *abc*, stator voltages in the stationary reference frame.
V_{ma}, V_{mb}, V_{mc}	Three-phase, abc, sinusoidal modulation waveform, PWM.
$V_{\alpha r}^s, V_{\beta r}^s$	Two-phase AC rotor voltages, alpha/beta, in the stationary frame.
$V_{\alpha s}^s, V_{\beta s}^s$	Two-phase AC stator voltages, alpha/beta, in the stationary frame.
V_{dr}^e, V_{qr}^e	Two-phase DC rotor voltages, rotating dq-axis synchronous frame.
V_{ds}^e, V_{qs}^e	Two-phase DC stator voltages, rotating dq-axis synchronous frame.
jV_{qs}, jV_{qr}	Polar voltages relating to the imaginary axis of rotor and stator q axis.
λ_r, λ_s	Rotor and stator flux.

$\lambda_{dr}, \lambda_{qr}$	Rotor dq-axis flux.
$\lambda_{ds}, \lambda_{qs}$	Stator dq-axis flux.
$j\lambda_{qs}$,$j\lambda_{qr}$	Polar flux relating to the imaginary axis of rotor and stator q-axis flux.
$\frac{d\lambda}{dt} = \rho\lambda$	Flux differential with respect to time.
$\rho\lambda_{dr}$, $\rho\lambda_{qr}$	Rotor flux differential with respect to time.
$\rho\lambda_{ds}$, $\rho\lambda_{qs}$	Stator flux differential with respect to time.
ω_r	Angular rotor speed (rev/s).
ω_s	Angular synchronous peed (rev/s).
ω_{sl}	Angular slip speed (rev/s).
θ_r	Rotor angular displacement position.
θ_s	Stator angular displacement position.
θ_{sl}	Angular slip displacement position.
σ	Leakage factor of induction machine. $\sigma = 1 - \frac{L_m^2}{L_s L_r}$
$\int \mathrm{dt}$	Integral with respect to time.

ACRONYMS AND ABBREVIATIONS

AC	Alternate current
DFIG	Doubly-fed induction generator
DC	Direct current
Dy	Delta star connection
FRT	Fault ride-through
GSC	Grid-side converter
LVRT	Low voltage ride-through
MPPT	Maximum power-point tracking
MRAS	Model reference adaptive system
IG	Induction generator
PF	Power factor
PMSG	Permanent magnet synchronous generator
PWM	Pulse with modulation
RSC	Rotor-side converter
SCIG	Squirrel cage induction generator
SG	Synchronous generator
WECS	Wind energy conversion system
THD	Total harmonic distortion
WRIG	Wound-rotor induction generator
WRSG	Wound-rotor synchronous generator
WT	Wind turbine

SUPERSCRIPTS

Avg	Average
max	Maximum
min	Minimum
s	Stator-oriented reference frame
ref	Reference

UNITS OF MEASURE

A	Amps
V	Volts
MW	Megawatts
Ω	Ohms
rad/s	Radian per second
RPM	Revolution per minute
$MVAr$	Mega volt ampere reactive

LIST OF FIGURES

LIST OF TABELS

CHAPTER ONE

CHAPTER ONE

INTRODUCTION

1-1 Overview of Wind Energy Conversion System Technology

Renewable energy conversion systems have become increasingly popular over recent years; and there has been a strong penetration of renewable energy into power generation systems due to the prioritizing of secure energy supplies, environmental concerns and the recognition of climate change, peak oil and the finite supplies of other fuel. All these factors have contributed to strengthening demand for wind power and other renewable energy solutions. Wind power is one of the most important renewable energy sources and it has contributed in historical developments since the ancient times of Babylon and Egypt where the wind was used to irrigate crops (1700 B.C). Some other civilizations, like the Persians (500–900 A.D.), used wind power to grind grain, while others have used the wind to propel ships and other early industrial applications [1]. The rapid growth of the use of wind energy has not only been stimulated by financial enhancement mechanisms of different types, but also by the maturing of the technology. Wind is free energy and does not pollute unlike the traditional fossil energy sources. The emissions reduction involved depends on the technology that wind replaces. For example, coal creates about 1 kg of CO_2 for each kWh, oil creates 0.75 kg for each kWh and gas creates 0.5 kg for each kWh [2]. Wind energy depends on weather patterns caused by the sun's uneven heating of the earth's atmosphere. Variations in atmospheric pressure produced by differential heating propel air from high-pressure to low-pressure regions, generating winds that are mainly affected by the earth's rotation and surface geography as illustrated in figure 1.1 showing the major wind belts encircling the planet [3].

The kinetic energy of the wind represents a clean source of electrical power when the force of the wind is employed to drive a turbine which rotates the generator to produce electricity.

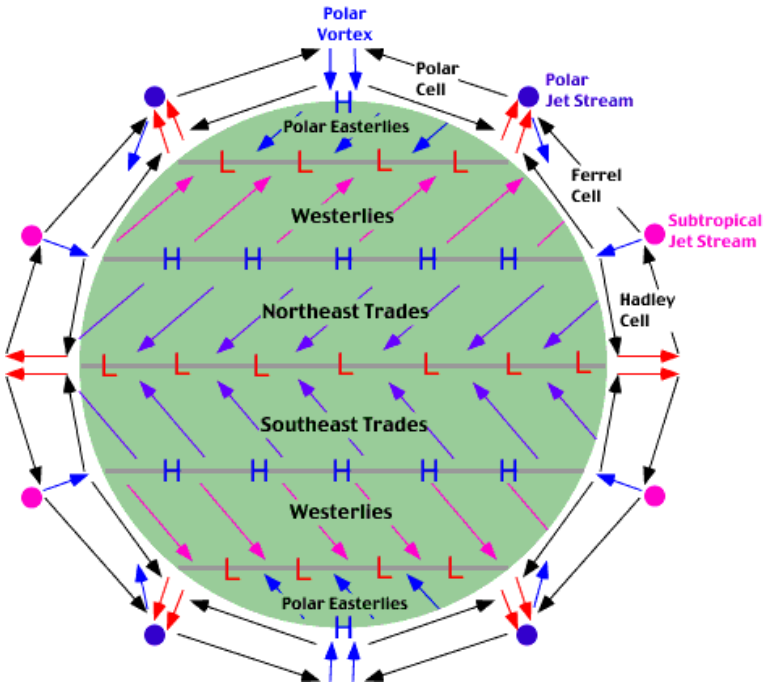

Figure 1.1: Atmospheric cells and latitudinal wind belts [3].

The cost of electrical power produced by a wind power conversion system is decreasing dramatically due to developments in the manufacturing technology of power electronics the increases in the average level of power produced. Figure 1.2 shows the growth in wind power systems installed around the world. In the sector statistics of cumulative wind capacity categorized by country shown in figure 1.2. (c), China and the USA hold the leading positions in installed wind capacity of (152) GW which has broken all previous records. As illustrated in figure 1.3, the total installed wind power capacity at the end of 2011 had grown to around 240 GW, making it the second largest contributor to renewable generation capacity after hydropower. On the other hand, even through wind energy represents environment-friendly source of electrical power, it has limitations due to its discontinuous nature as compared to other renewable power sources.

The doubly-fed induction generator (DFIG) represents one of the most attractive technologies to be adopted in wind farms and it has contributed to the wind turbine market. A DFIG-based wind turbine may suffer from various situations in both normal condition, and during grid disturbances as with other conventional generators that reduce system efficiency and/ or reliability. This thesis presents a comprehensive performance evaluation of a DFIG-based wind turbine model with different scenarios of operation after the confirmation of a DFIG model system built mathematically using the

MATLAB/ SIMULINK® platform. The mathematical models for DFIG sub-systems are then derived. These mechanical, electrical, and control sub-systems are employed to determine the system performance. The generator control sub-systems with different reference frame orientations are presented to design the cascade control loops of the rotor-side converter (RSC) and grid-side converter (GSC). Two schemes are employed in this research to estimate the generator's rotor angle position are investigated the accuracy and sensitivity of these estimators in different operation conditions. A control modification for the RSC power loop is introduced to enhance the fault ride-through (FRT) ability of the DFIG during short voltage dip conditions and illustrated it capability is demonstrated to reduce stator/rotor over-current oscillation, thus satisfying the desired system's grid code specifications.

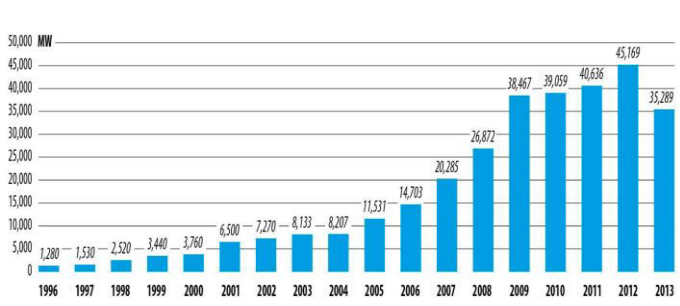

(a)

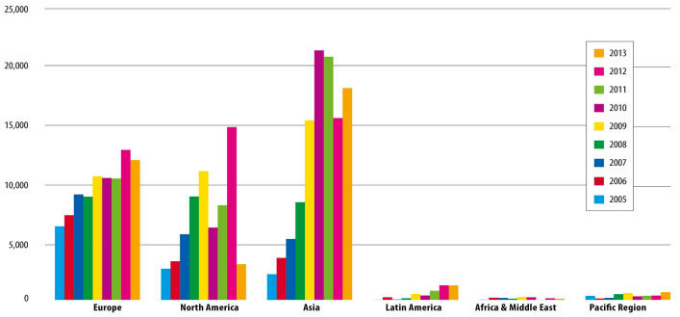

(b)

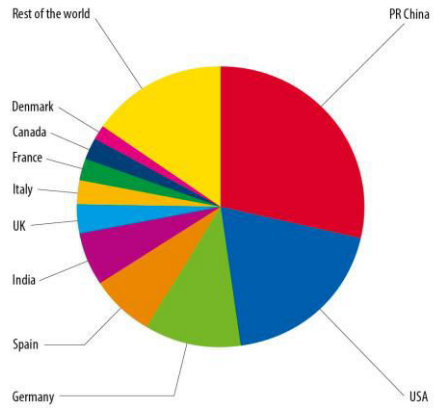

Country	MW	% SHARE
PR China	91,412	28.7
USA	61,091	19.2
Germany	34,250	10.8
Spain	22,959	7.2
India	20,150	6.3
UK	10,531	3.3
Italy	8,552	2.7
France	8,254	2.6
Canada	7,803	2.5
Denmark	4,772	1.5
Rest of the world	48,332	15.2
Total TOP 10	**269,773**	**84.8**

(c)

Figure1.2: (a) Annual wind installed global capacity 1996-2013; (b) annual wind installed capacity by region 2005-2013; (c) top countries cumulative installed capacity in 2013 [4].

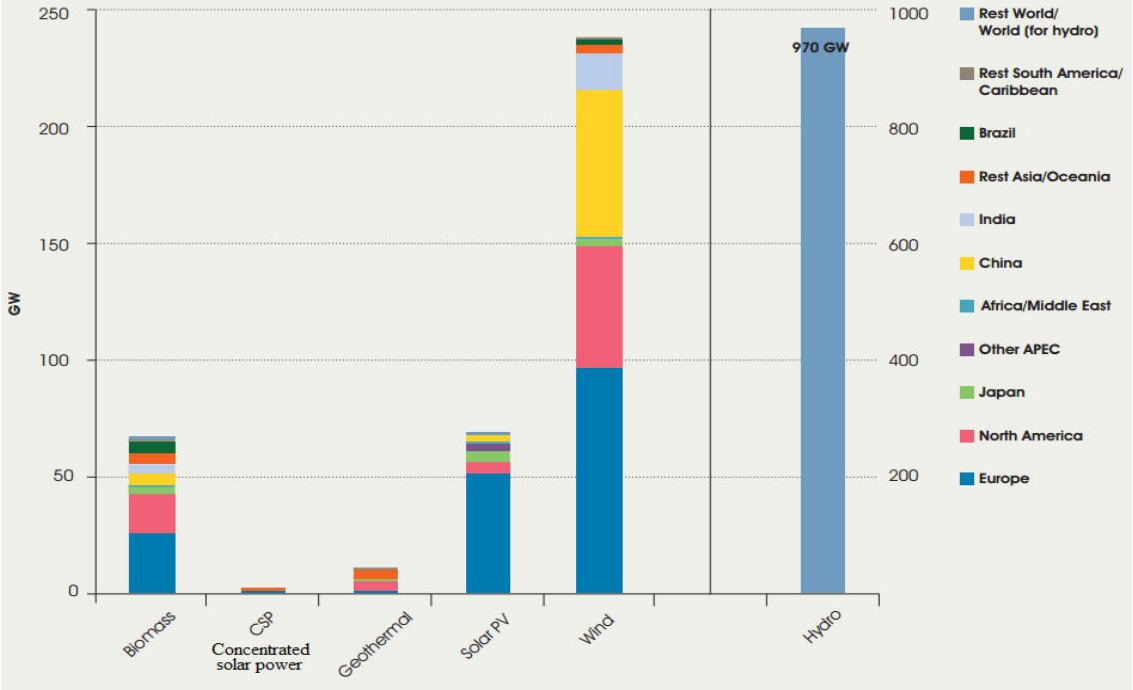

Figure 1.3: Installed renewable power generation capacity by type, end 2011[5].

1-2 Wind Power Generators

As shown in figure 1.4, the typical wind energy conversion system (WECS) consists of a wind turbine (WT) and nacelle [2]. The electrical generator, bearing, gearbox, rotor shaft, yaw, break system and control system are included inside the nacelle, while the anemometer is usually located upon the cover of the nacelle to measure the wind speed [6, 7]. Today, the most common criteria adopted to design wind turbines focus on the available options for blade number, the orientation of rotor rotation (downwind or upwind of the tower), fixed or variable rotor speed, gearbox or a direct drive generator, synchronous or induction generator, hub design (rigid, teetering or hinged), power control via aerodynamic stall control or variable pitch blade control, turbine tower type (Lattice tower, monopole tower, or tube tower: as shown in figure 1.5), axis of rotation as horizontal or vertical, orientation by self-align action (free yaw), or direct control (active yaw) [6, 8]. The rotor is used to collect the energy from the wind and it is composed of blades which are attached to a hub and is regulated by pitch control system to achieve either the maximum use of the wind or to brake the rotation of the rotor. The rotor shaft transfers the motion from the low speed side via the gearbox which raises the speed of the rotational shaft connected to the generator, and then it converts the mechanical, rotational movement into electricity. Then the induced current, power

converters are used to create electrical power to match the criteria of the grid in terms of voltage, current, frequency, power factor, active and reactive power of system [9-11].

Wind turbines are designed to operate either at fixed speed (equipped with induction generators directly connected to the grid) or variable speed with induction or synchronous generators, directly or indirectly connected to the grid. As the name suggests, fixed speed wind turbines rotate at almost a constant speed, which is determined by the gear ratio, the grid frequency, and the number of poles of the generator in addition to its maximum conversion efficiency which can be achieved only at a given wind speed. On the other hand, variable speed wind turbines can achieve maximum energy conversion over a wide range of wind speeds [6, 12]. The converter in a variable speed wind turbine gives the possibility to decouple control over the power output of the wind turbine, which is important for the integration of wind turbines into the grid [11].

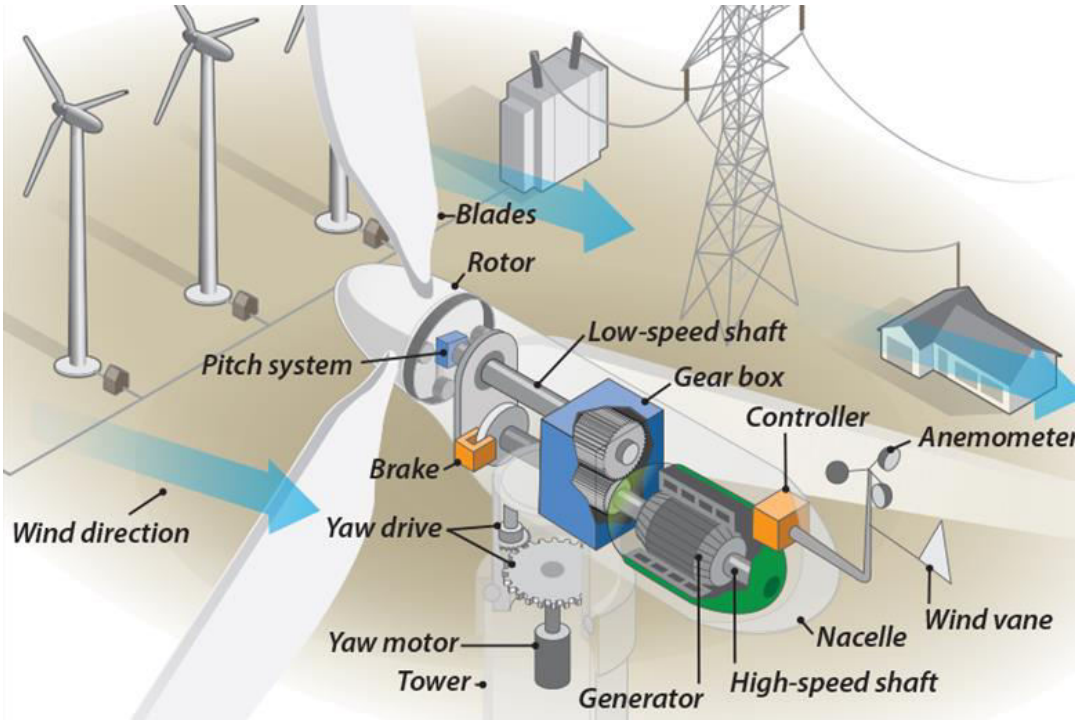

Figure 1.4: Typical components of horizontal axis, three-bladed wind turbine [13].

(a) (b) (c)

Figure 1.5: Types of tower used in wind conversion system: (a) monopole tower; (b) lattice tower; (c) tube tower [7].

According to their method of excitation, induction generators are classified into two basic categories which are constant voltage constant freuncy and variable voltage variable frequency generators. Constant-voltage, constant-frequency generators is illustrated in figure 1.6. This generator uses the grid to excite its drive. This type of system called the grid connected induction generators (GCIG). The power generated is fed to the supply when the rotor is driven above the synchronous speed. In the cage rotor type, the power will flow through the stator at low negative slip, and when the rotor is the wound type the machine can feed power through the stator and rotor windings across a wide range of operating speeds [14].

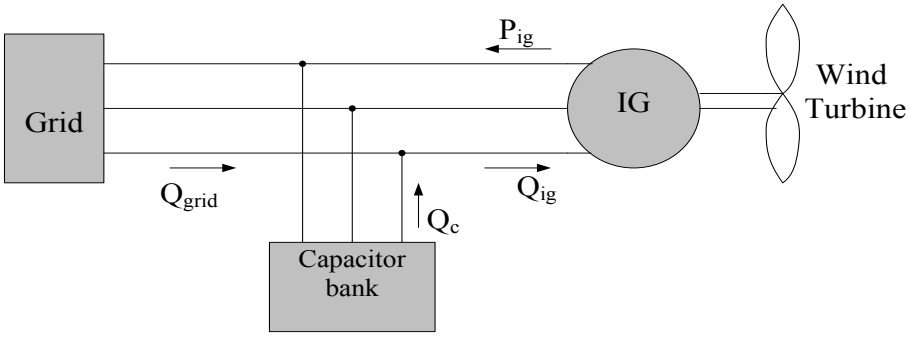

Figure (1.6): Induction generator feeding to a utility grid with excitation capacitor [14].

Grid-connected induction generators can be divided into two types: single-output and double-output systems. The single output system generally utilizes the squirrel cage induction generator (SCIG), and the power feeds to the grid only through the stator winding which is run in either fixed-speed or semi-variable-speed. In the semi-variable speed system, a winding type induction generator is used in which the rotor resistance can change by using power electronics [15- 17]. With changes in rotor resistance, the torque/speed characteristics of the generator are changed, giving a decrease in rotor speed of about 10% from the nominal rotor speed. In this generating system, a limited variable speed capability is achieved at relatively low cost [18]. The optimal value of the power coefficient must be achieved in harvesting power by choosing the ratio to perform this condition for the most frequent wind speed, while the wind turbines must limit the power by using either blade pitch regulation or stall regulation [19]. The generator always draws reactive power from the network and capacitors are conventionally used to compensate this lagging VAR.

The basic configuration of the Double-Output System is illustrated in figure 1.7. In this type, the power can be tapped both from the stator and from the rotor windings over a wide range of speed by suitable control of the exchanging rotor power. This can be achieved by the use of a slip-ring induction motor with a bidirectional AC-DC-AC converter connected between the slip-ring terminals and the grid [20]. Double-output systems can be categorized into two types according to the technology of the bidirectional converter: current converters and voltage converters [14, 21-23]. The solid-state system is used in the double-output system with current converter to control the slip power at variable speed through current converters as shown in Figure 1.8. The main function of using the smoothing reactor is to regulate the current's continuity and to reduce ripples in the link circuit. Rotor and supply-side converters are operated to exchange electrical power from the rotor circuit to the supply in the rectification and inversion modes respectively. However, for power flows in the reverse direction, the supply side converter acts as a rectifier and the rotor side converter as an inverter. The step-down transformer between converter and supply extends the control range of the firing delay angle of the supply side converter [24].

Double-output system with voltage converter is utilize the dual PWM voltage-fed, current-regulated converters, connected back to back, in the rotor circuit of wound rotor

induction generator gives the ability to overcome the problems of naturally commutated, line-commutated converters and low-frequency forced-commutated converters. As depicted in figure 1.9 the PWM converters with DC link offer the ability to decoupled control of the generator's active and reactive power, with low stator, rotor, and supply current distortion in, owing to the shift of the harmonic spectra from lower to higher order, requiring a small-sized filter for attenuation of higher harmonics. This system will improve the overall system power factor through the control of the displacement factor between the voltage and current of the grid side converter (GSC) [7].

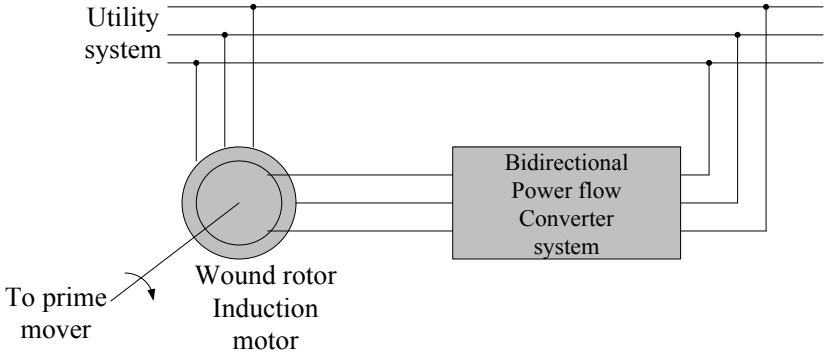

Figure 1.7: Double-output induction generator system [20].

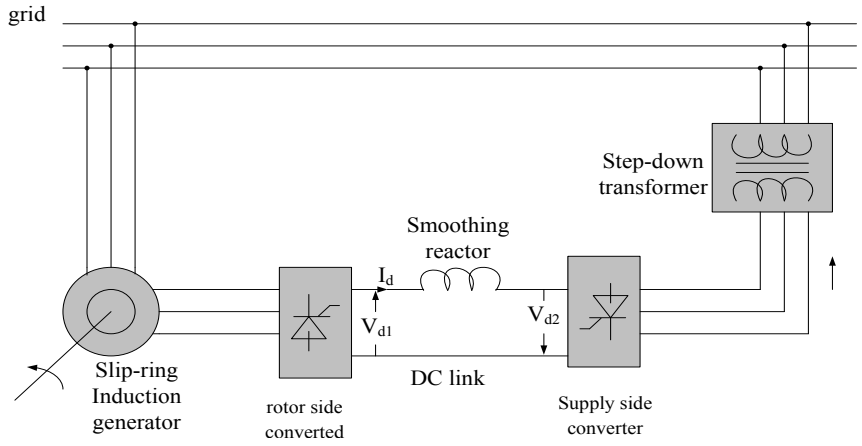

Figure 1.8: Double-output system with direct current link [24].

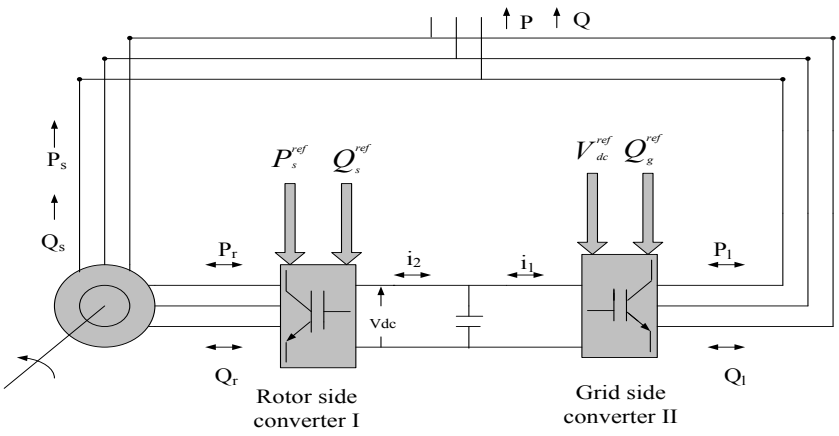

Figure 1.9: Power flow in slip power control scheme with DC-link voltage.

The squirrel cage machine is usually used in variable-voltage, variable-frequency generators with the capacitor connected across the terminal as shown in figure 1.10 to enhance the voltage built up. This is because when the load current increases, the current pass through the capacitance also increases, and more magnetizing reactive power is furnished to the machine. Hence the voltage drop with load will be less severe and achieved safety voltage regulation. Such induction generators are called self-excited induction generators (SEIG). The possibility to use the SEIG where the three-phase capacitor bank are connected to feed the reactive power requirement of the load and generator was discovered by Basset and Potter in the 1930s [25]. If an appropriate capacitor bank is connected across the terminals of an externally driven induction machine, and if the rotor has sufficient residual magnetism, an electromotive force (EMF) is induced in the machine windings due to the excitation provided by the capacitor and if the EMF if sufficient to circulate leading currents in the capacitors [26-27], the flux produced due to these currents would boost the residual magnetism. This will increase the machine flux and a larger EMF will be induced. This in turn increases the currents and the flux. The induced voltage and current will continue to rise until the reactive power supplied by the capacitor is balanced by the reactive power demanded by the machine and this condition is essentially decided by the saturation of the magnetic circuit. The induced voltage keeps on rising until saturation is reached [28].

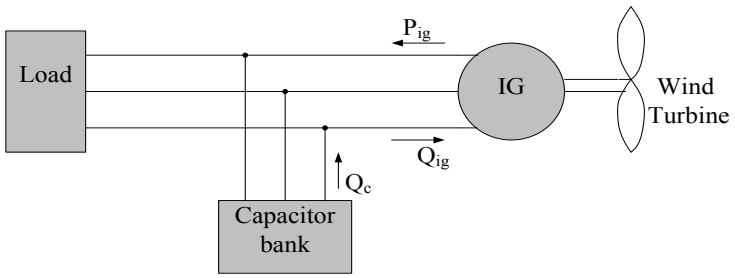

Figure 1.10: Self-excited induction generator feeding a load.

Table 1.1 summaries the technical comparison of different wind turbine system configuration in terms of fixed and variable speed conversion systems and presents their benefits and drawbacks with the comments on grid control, cost, maintenance, internal turbine systems and some other important issues for wind turbines. According to the table and based on industrial reports, the wind power industry is seriously considering the use of the fully-rated power converter-based generator due to the fault ride-through (FRT) limitations of the DFIG.

Table 1.1: Comparison between different wind turbine systems. ++ Very positive (low cost); + positive; 0, not competitive in cost [11].

	Wind Turbine Type					
	Fixed Speed	**Variable Speed**				
Generator type	SCIG	WRIG + variable rotor resistance	DFIG	SCIG	SG	PMSG
Power converters	No	Partial	Partial	Full	Full	Full
Converter capacity	N/A	Small	Reduced	Full	Full	Full
Speed range	<1% of rated	<10% of rated	±30% of rated	Full, 100% of rated	Full, 100% of rated	Full, 100% of rated
Soft starter	Yes	Yes	No	No	No	No
Flicker (sensitive)	Yes	Yes	No	No	No	No
Gearbox	Yes	Yes	Yes	Yes	Optional	Optional
Aerodynamic power control	I – Pitch II – Stall III – Active Stall	Pitch	Pitch	Pitch	Pitch	Pitch
Grid side reactive power compensator	Yes	Yes	No	No	No	No
Active power control and MPPT	N/A	Limited	Yes	Yes	Yes	Yes
Short circuit (fault active)	No	No	No/Yes	Yes	Yes	Yes
Short circuit power	Contribute	Contribute	Contribute	Limit	Limit	Limit
Standby function	No	No	Yes +	Yes ++	Yes ++	Yes ++
Investment cost	++	++	+	0	0	0
Maintenance	++	++	o	+	+	+
Efficiency rating	Low	Low / reduced	Good	Good	Good	Good

1-3 Research Methodology and Challenges

This study presents a research methodology to investigate the dynamic comparative behaviour of the grid connected doubly-fed induction generator (DFIG) with different scenarios of operation. At the beginning, the study focuses on modelling the mechanical, electrical and control systems and examines the system results with another software demo station model to double checked the system built in MATLAB/SIMULINK®. Then after this step, a comparative estimation analysis of the DFIG-based wind turbine is conducted with two types of PI vector control using a pulse width modulation (PWM) modulator, the first is indirect sensore vector control and the other type uses two schemes of estimators which are utilized to validate the ability to detect the rotor position angle when the generator is connected the to the grid. The behavioral response of the DFIG system to grid disturbances is analyzed and simulated using the control strategies and the protection scheme in order to maintain the connection to the network during grid faults. Moreover the null active and reactive reference set scheme control strategy modifies the vector control in the rotor-side converter contributing to limiting the over-current in the rotor windings during short voltage dips, which can improve the low voltage ride-through ability of the DFIG system. Furthermore, a reconfiguration scheme of control strategies for the system is proposed to meet the latest grid code requirements. With this specific methodology, the system can stay connected to the grid in the case of grid faults. In addition, the fault ride-through capability of the DFIG system can be greatly supported by providing ancillary reactive power under voltage dips of different durations, which can increase the voltage at PCC during the fault and thus provide support to the grid. The system can resume normal operation immediately after the clearance of the fault. Thus the system can meet the requirements of the grid code.

SIMULINK has become a fundamental element of most studies and applications in this field. Utilizing simulink can save money and time. Simulink also offer flexibility, and enable repeatability, control and the pushing of boundaries. This method proves to be very efficient for testing and running the proposed model, and for testing and observing its dynamic behaviour in different scenarios. The software used in this study is MATLAB/SIMULINK®. These tools are used for modelling, simulating and examining the proposed DFIG wind turbine system with its controller, sensorless schemes, grid system, aerodynamic system and protection models. This includes MATLAB/SIMULINK®

software with all its modules and library models, and in addition the PLECS®/DFIG demo model platform is adopted for the confirmation of the system.

As the popularity of the DFIG wind turbine continues to increase, the effect of changes in wind speed, grid voltage disturbances, and variation in generator parameters represent severe challenges in assessing the behaviour of the model reference adaptive system (MRAS) observer. In addition the, grid codes have been revised challenges to demand from the DFIG based wind turbine to operate as conventional power plants, with focus on fault ride-through behavior. In this study, a control strategy is designed to extract power from wind as well as to satisfy reactive power constraints and to decouple control of active and reactive power. However, in the presence of grid faults, wind turbines should be controlled so that they can remain connected to the grid and supply adequate reactive power to help the grid voltage recover. In addition, the estimation of rotor position should remain accurate and be less sensitive during DFIG operation. Therefore, reconfiguration of the control strategies for the wind turbine system must be performed in accordance to the operation condition.

1-4 Objectives and Contributions of the Study

In summary, the main objectives of this research are as follows:-

- To model in detail the doubly-fed induction generator (DFIG)-based wind turbine using MATLAB/SIMULINK® software. The model should be as real as possible, and simulating the power converter in detail.

- To investigate the dynamic behaviour of the grid connected DFIG-based wind turbine in addition confirm the system built in MATLAB/SIMULINK® using PLECS® platform.

- To demonstrate the ability of the phase lock loop (PLL) used in the DFIG-based wind turbine system to track changes in grid frequency in different operating conditions (frequency responses, input harmonics responses, and grid voltage disturbances).

- To estimate rotor angle position with two model reference adaptive system (MRAS) schemes and to compare the robustness of these schemes in different scenarios. In this study, rotor current-based MRAS (RCMRAS) and rotor reactive power-based MRAS (QRMRAS) are used in the estimating of the rotor position angle because the currents and voltage are available as measured quantities in $\alpha\beta$ coordination, and therefore the implementation of RCMRAS and QRMRAS observers is simple.

- To provide a better understanding of the dynamic comparative performance of the DFIG-based wind turbine with sensored and sensorless vector control during different operating conditions in order to contribute to the development of a better controlled, viable DFIG system.

- To analyze the voltage disturbance response of the DFIG-based wind turbine with and without the modified vector control scheme to show its influence on the dynamic behaviour of the wind turbine system.

- To utilize the active and reactive power null technique which enhance the fault ride-through (FRT) ability of the DFIG with voltage dips. In addition this strategy will keep the back-to-back converter connected to the DFIG even the grid suffer from the short time voltage drop also it can be equipped with the conventional crowbar against severe grid faults to order to reduce the activated time of the crowbar as much as possible.

The main contributions of this thesis are summarized as following:-

- A complete dynamic comprehensive performance assessment is conducted for grid-connected variable-speed wind turbines based on a DFIG which is built mathematically in the MATLAB/SIMULINK® platform and the system is verified with PLECS®. Although the wind turbine model and its control system are designed based on conventional machine theories, the modelling has prove to be able to support the study the sensorless vector control and FRT issues of such grid-connected wind turbines and their interactions with the grid.

- Rotor angle estimation using rotor reactive-based MRAS (QRMRAS) is identified to be superior in terms of accuracy and robustness, as compared with the rotor current-based MRAS (RCMRAS) and it is found to be promising for rotor position estimation for DFIG-based wind turbines.

- This study improves the methodology for utilizing the available electrical measurements to detect rotor angle position and to enhance the fault ride-through ability of grid connected DFIG-based wind turbines. Therefore, such a system will be more reliable in remote areas and stable against disturbances when the control modification is adopted. This structure more satisfies all of the standards of connection to electrical networks imposed by the most demanding operators.

1-5 Thesis Layout

The objective of the thesis is to investigate the dynamic behaviour integrated control, rotor angle estimation and protection system of the doubly-fed induction generator-based wind turbine to fulfill the revised grid requirements. The following parts of the dissertation are organized as follows:

In chapter 2, the literature review describes doubly-fed induction generator (DFIG)-based wind turbine systems and more specifically addresses the modeling, control, sensorless control, and interaction of DFIG systems with grid disturbances.

In chapter 3, a whole model is built of the grid connected doubly-fed induction generator (DFIG)-based wind turbine and the back-to-back PWM voltage source converters in the rotor circuit. The model includes the wind speed model, the aerodynamic model of the wind turbine, the mechanical model of the transmission system and models of the electrical components, namely the DFIG.

Chapter 4 includes complete analyses of two schemes based on the model reference adaptive system (MRAS) which have been employed in this study to estimate the rotor position of doubly-fed induction generator (DFIG) system and utilized in which are the control of the stator flux orientation of the rotor side converter (RSC).

Chapter 5 analyzes in detail the dynamic responses of the control schemes and the DFIG-based wind turbine during a voltage dip across the point common coupling of the grid. In this disturbance condition, a control strategy is employed without the use of the crowbar to assist in the recover of the DFIG-based wind turbine's terminal voltage, which is verified by the simulation results.

Finally, chapter 6 summarizes the most important results obtained in this work and presents the conclusions of the study and makes recommendations for future work.

CHAPTER TWO

CHAPTER TWO

LITERATURE SURVEY

2-1 Introduction

Recently, due to the continuous and rapid increase in the cumulative installed power of grid-connected wind turbines, the control strategies used methods for estimation of the rotor position, and system response with its FRT ability during issues of grid connected wind turbines disturbances have attracted considerable interest. This has led to the publication of numerous papers, investigations and reports dealing with these aspects.

In this chapter, a literature review is presented describing doubly-fed induction generator (DFIG)-based wind turbine systems.

2-2 Modeling and Control System of the DFIG

Only the standard doubly-fed induction machine and brushless type of systems have been employed in the manufacture of wind turbine generator systems, although another type of DFIG system is the cascaded doubly-fed induction machine as shown in figure 2.1[29-32]. Conventionally, the synchronous reference frame orientation is adopted in DFIG modelling to simplify the design of the control system, since the currents and voltages will be expressed as DC vectors. On the other hand some studies have utilized the stationary stator reference frame and rotor reference frame [7, 33-37].

Some papers have presented models of the DFIG system of different order so as to reduced the required for computational time for the evaluation of system behaviour during different operating conditions. The mean of reduce order model is summarized by neglect the differential terms and some parameters in the voltage equation of the machine as illustrated in table 2.1 [38]. Many studies have performed comparisons between the full order model and reduced order models with various scenarios [39-43]. A comparative study has been introduced of three different order models of DFIG (1^{st}, 3^{rd} and 5^{th}) using mathematical modeling with considering and ignoring saturation effects [39]. The third order model of DFIG is characterized by neglecting the derivative terms of the stator flux and is widely used in power system transient

stability analysis, while the first order model is presented by neglecting both the derivative terms of the stator flux and rotor flux and where the only differential equation left is the swing equation which is suitable for long-term studies of power system dynamics [44].

Table 2.1: Brief description of different order models [38].

	5th order	3rd order	1st order
Assumption	$\frac{d\lambda_{ds}}{dt} \neq 0$	$\frac{d\lambda_{ds}}{dt} = 0$	$\frac{d\lambda_{ds}}{dt} = 0$
	$\frac{d\lambda_{qs}}{dt} \neq 0$	$\frac{d\lambda_{qs}}{dt} = 0$	$\frac{d\lambda_{qs}}{dt} = 0$
	$\frac{d\lambda_{dr}}{dt} \neq 0$	$\frac{d\lambda_{dr}}{dt} \neq 0$	$\frac{d\lambda_{dr}}{dt} = 0$
	$\frac{d\lambda_{qr}}{dt} \neq 0$	$\frac{d\lambda_{qr}}{dt} \neq 0$	$\frac{d\lambda_{qr}}{dt} = 0$
	$\frac{d\omega_m}{dt} \neq 0$	$\frac{d\omega_m}{dt} \neq 0$	$\frac{d\omega_m}{dt} \neq 0$

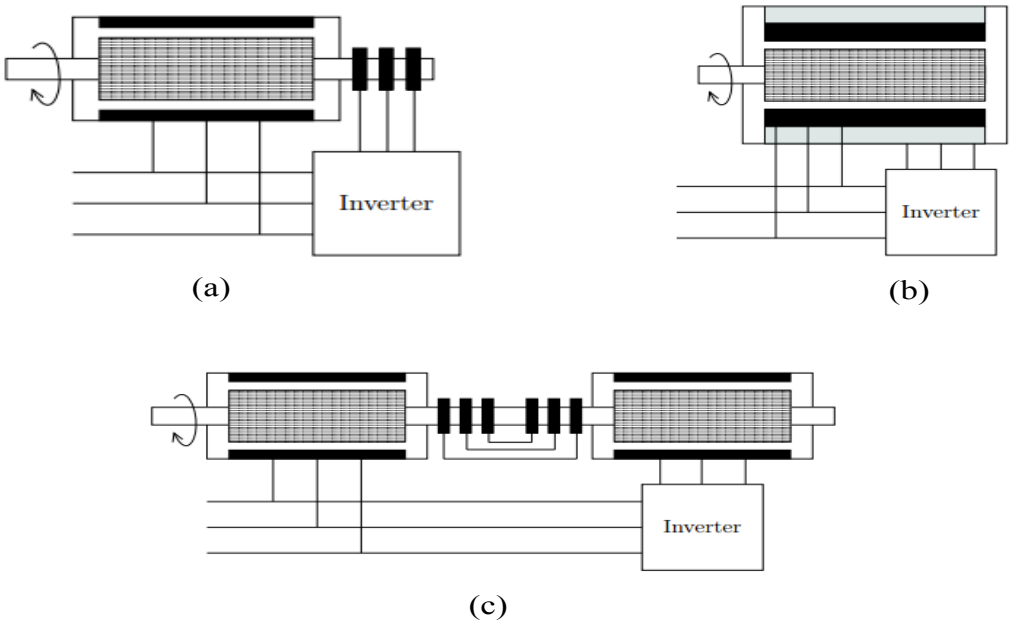

Figure 2.1: Types of DFIG: (a) standard doubly-fed induction machine; (b) brushless doubly-fed induction machine; (c) cascaded doubly-fed induction machine [29-32].

Based on the dynamic mathematical model of the DFIG, many publications have presented different control strategies, such as vector control, direct power control, direct torque control, predictive control, sensorless control and non-linear control. Conventional designs of DFIG control systems are based on rotor current vector

control techniques. The control system is usually defined in the synchronous *dq* frame oriented to the stator flux [22, 45-47], the stator voltage (or grid flux) [48-51] or the gap flux [52]. On the other hand a detailed DFIG-based wind turbine model in MATLAB/SIMULINK® using field-oriented control-based on a rotor flux-oriented reference frame has been proposed and compared with the conventional stator flux vector control in [53]. The stator-flux oriented control is basically adopted in DFIG control designs in which the *q*-axis current component is used for active power control and the *d*-axis component is used for reactive power control. On the other hand, in stator voltage-oriented control, the opposite is the case and the *d*-axis component is used for active power control and the *q*-axis current component is used for reactive power control. The steady state and dynamic analysis associated with controllers are based on the small signal stability criteria in the detailed modeling of the DFIG-based wind turbine to evaluate system stability. The system has a very extensive stability region and intrinsic stability of electromagnetic torque has investigated [54, 55]. The dynamic variations in DFIG flux, wind turbine, power converter and phase-locked loop (PLL) have been studied [56] and a non-linear mathematical model of DFIG system connected to a series-compensated transmission line was developed. Direct power control (DPC) and closed loop stator flux orientation have been proposed by Yongchang and Kostyantyn [57, 58] respectively to control the brushless doubly-fed induction generator. Basic direct torque control has also been applied to a doubly-fed induction generator [59-61]. Direct torque control (DTC) was achieved without a current regulator and without coordinate transformations. Knowledge of grid voltages, rotor currents, and rotor position is needed in this type of controller [62]. Rotor flux linkage magnitude and generator torque can be controlled by specifically selecting the inverter switching states [63]. Starting from the basic rules of DTC, direct power control (DPC) has been introduced [64] and applied to DFIG systems [65-68]. Etinne and Ambrish [69] have introduced a comparative performance assessment using vector control, DTC and DPC strategies to control DFIG-based wind turbine system. The authors concluded that vector control (VC) has lower THD while the direct schemes are faster than the vector control in their transitory response. Because this is in the direct control strategy shown in table 2.2, the only vectors required are electromagnetic torque stator active power and stator reactive power which are used during the control computations without pulse width modulation (PWM) and in

cascaded loop control (i.e. inner and outer loops as in vector control). Thus the converter switching states in the direct schemes are selected by the switching table based on the instantaneous errors between the commanded and estimated values of stator flux and active and reactive power, while the rotor control voltage in vector control scheme is generated after a cascade of PI controllers [69].

Table 2.2: Transitory time response of vector control, DTC, and DPC [69].

Reference value	**Transitory time response (*ms*)**		
	VC	**DTC**	**DPC**
-ve step: i_{qr}^{ref} /T_e^{ref}/P_s^{ref}	10	2.5	2.5
+ve step: i_{qr}^{ref} /T_e^{ref}/P_s^{ref}	10	1.5	1.5
-ve step: i_{dr}^{ref} /λ_r^{ref}/Q_s^{ref}	10	2.5	2.5
+ve step: i_{dr}^{ref} /λ_r^{ref}/Q_s^{ref}	5	2.5	2.5

Since the phase locked loop (PLL) is a central component in a control structure for converters in the DFIG, it is discussed here in the context of grid component models. The PLL is used to estimate the grid angle and therefore to generate the control signals for the grid-side converter. A generalized PLL structure is shown in figure 2.2.

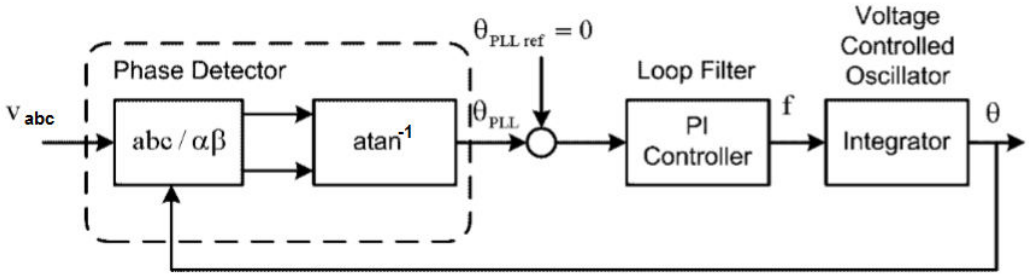

Figure 2.2: General structure of a phase locked loop [70].

The phase-locked loop (PLL) as implemented on study [7] is typically employed to measure the stator voltage angle as illustrated in figure 2.3 where this signal is important in vector control. The PLL consists of a voltage-controlled oscillator (VCO) which is initially tuned to a frequency close to the desired frequency. A circuit called a phase comparator causes the VCO to seek and lock onto the desired frequency.

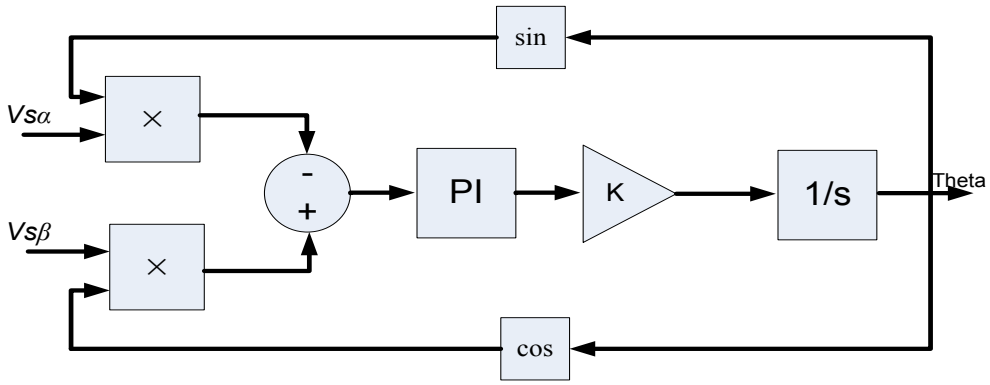

Figure 2.3: Block diagram of stator voltage angle calculation [7].

The three-phase voltage inputs are transformed into $\alpha\beta$ components referring to the grid voltage phasor. Using these components, sufficient information about the phase angle is obtained. A phase detector range of $(-\pi/2; \pi/2)$ is obtained using a simple inverse tangent function, while if a four quadrant inverse tangent function is used in this range can be expanded to $(-\pi, \pi)$. The loop filter contains a low-pass filter to suppress noise and high frequency terms in the signal from the phase detector; for example, asymmetry in the three-phase voltages. To avoid stationary error in phase after a step in the input signal frequency, a PI controller is added. The performance of the PLL depends on the phased detector and the selected bandwidth of the loop filter. With slow dynamic of the PLL loop, higher rejection of the disturbances can be achieved, although with a poor tracking of the grid angle. In power system applications, the voltage-controlled oscillator is usually implemented as an integrator. The loop is closed by feeding the estimated angle into the $\alpha\beta$-transformation. As long as the phase angle is correct, the output of the phase detector is zero, and thus the frequency input to the integrator is constant and this means that the PLL is in lock. If the estimated angle is not correct, the frequency is adjusted and the phase angle of the grid phasor voltage is changed.

2-3 Sensorless Control of the DFIG-Based Wind Turbine

Several sensorless control strategies have been proposed in DFIG-based wind turbine systems with the main challenges being designing rotor position scheme estimation at stable and well detection and in any speed of operating range. The vector control strategy in the back-to-back power converter of DFIG-based wind turbine generators essentially requires rotor position information which is conventionally provided by

mechanical sensor coupled to the rotor shaft [71]. The position of the rotor is employed to transfer rotor variables from their natural reference frame coordination to the stator flux-oriented reference frame or the stator voltage-oriented reference frame and vice versa. In addition, the rotor's angular speed could be detected using the position sensor signal by calculating the position difference over a small sampling period. Recently, researchers have attempted to remove the position sensor from the DFIG system in an effort to improve the reliability of the system without affecting the dynamic behaviour of the controller [72]. The elimination of the mechanical sensor will benefit the DFIG system in several ways: reduced hardware complexity, reduced size of the drive machine, elimination of the sensor cable, better noise immunity, increased reliability, and less maintenance requirements. Operation in hostile environments mostly requires motors without position sensors [73].

Open-loop estimator approaches have been implemented in [74-79], where the rotor position is directly computed from measured voltages and currents by reference frame transformation, and the rotor speed is obtained via differentiation. A position sensorless scheme based only on rotor variables as has been introduced [80], but this gives poor position detection around synchronous speed because during the rotor slip frequency, the accuracy of detection is very low during this condition of operation which effected by the integration of the rotor back electromotive force (back-EMF). Open loop methods have been used [75-78] which compare the estimated and measured currents so as to compute the rotor position using open-loop algebraic calculation. However, these methods have no error correction mechanism, low accuracy, instable to modify speed convergences in addition its sensitive to parameters variations. The rotor angular speed is calculated via differentiation the position signal which may produce noisy speed estimation [76]. Alternatively it has been based on the comparison of stator current values calculated in different ways to estimate rotor position with good speed transient characteristics [78] but the results are influenced by the operational state of the machine. The phase comparison of an estimated air-gap power vector and the measured rotor current in a common reference frame has been implemented with a closed loop PI adjuster controller [79]. This has the advantage of performing the estimation in the rotor or in field reference frame; however this has sensitive to stator no load power. The rotor current in the stator flux-

oriented reference has also been estimated from the stator current in the stationary reference frame [76].

The model reference adaptive system (MRAS) method is used to estimate speed and position using the outputs of two different machine models, as illustrated in figure 2.4. One of these is position dependant, which is the adaptive model (AM), while the other types dose not involve the estimated position in computation and is named the reference model (RM) [78, 80-82]. Based on Popov's hyperstability criterion, the difference between the RM and the AM outputs is used to derive a suitable adaptive mechanism to generate the estimated speed used to minimize the error between the reference and estimated values [83]. This scheme for estimation can be used for position or speed detection, which are investigated using a proportional-integral (PI) or hysterias controller in DFIG systems implemented in different stator or rotor reference frames [79, 84-86].

Different techniques have been adopted to form error vectors employed to detect rotor position. The proposed sensorless methods [78, 81, 82, 86, 87] are based on stator flux MRAS, rotor flux MRAS, rotor current MRAS , stator current MRAS, rotor active power and rotor reactive power, and a comparison of these methods briefly summarized in table 2.3 with different operating conditions including grid connected and stand-alone DFIG system. The closed-loop MRAS observers has an adaptive models based on static flux-current relations, therefore this makes the estimation process very sensitive to machine inductances according to sensitivity analysis. In addition the stationary reference frame is adopted in the transformation of input variables and this may become inaccurate or even unstable in digital implementations. A non-linear control approach which uses non-linear static and dynamic state feedback controllers with a wind speed estimator in a wind turbine-generator system has been proposed [88] while predictive control in DFIG system has also been discussed [89-91].

Table 2.3: Basic comparison between different MRAS schemes.

	MRAS based on					
	Stator flux	Rotor flux	Rotor current	Stator current	Active power	Reactive power
Advantages	Best choice in stand alone	Good estimation with different operation condition with $i_{dr\neq0}$	Best choice in grid tide and have good stability and simple reference model	Stable only at Grid tide condition and have simple reference model	Simple to implemented	Independent on rotor resistance variation
Disadvantages	Instable at grid tide with $i_{dr} = 0$	PI gain is complex and sensitive to incorrect machine parameters	Sensitive to incorrect estimation of $\frac{L_m}{L_s}$	Complex PI gain implementation and instable at stand alone.	Sensitive to rotor resistance variation and low accuracy	Reasonable accurate

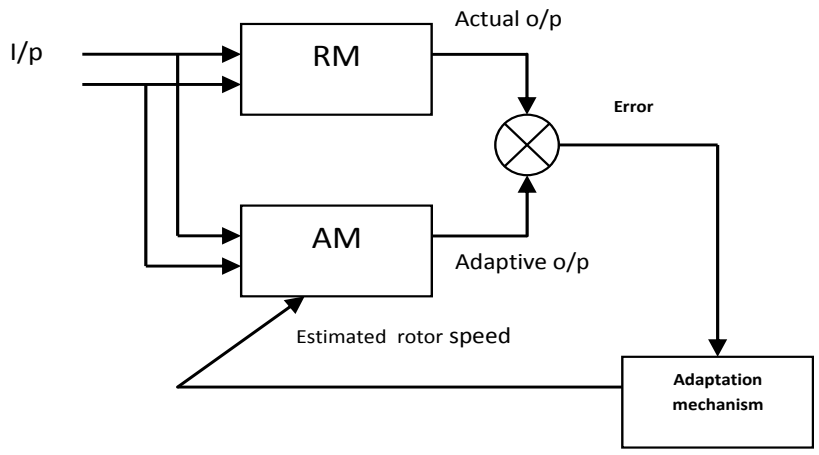

Figure 2.4: Typical model of reference adaptive system (MRAS) block diagram [83].

2-4 Maximize Power Point Tracking (MPPT) in DFIG-Based Wind Turbines

Variable-speed wind turbines are designed with a strategy to achieve maximum aerodynamic efficiency over a range of wind speeds. However, this technique requires a power control scheme to track the existing maximum power and to limit the power captured when the wind speed exceeds a certain level. For variable-speed wind turbines, there are two types of power control: aerodynamic and generator control. Aerodynamic control aims to limit the power in very high winds in order to avoid

damage to the wind turbine. The most commonly used type of aerodynamic power control is to adjust the attack angle of the turbine blades (i.e. pitch blade angle) according to the wind speed. On the other hand, generator control is realized by adjusting rotor speed in order to capture the energy from the wind in an optimal manner. Any change the rotor speed induces a change in the turbine's power capture [7, 92, 93]. Figure 2.5 illustrates the typical maximum power curve of a wind turbine with maximum power point tracking (MPPT) as a function of wind speed (V_w). MPPT is a method of assessment adopted to recover the maximum of the turbine's power in adjusting a new set point torque with slip at the optimum level [94, 95]. The operation of the wind turbine is considered in four speed regions. In region I, from zero to the minimum speed of generation (CUT-IN), the wind speed is usually below 3 m/s. Up to this limit, the power generation just supplies the friction losses. Therefore, the turbine is shut down. In region II, the turbine operates with fixed-pitch and variable-speed, and the generator speed is controlled in order to obtain the maximum power available from the wind [92, 96]. In this operating region, the objective of speed control is to follow the path of maximum power extraction [7]. In the literature, different methods have been proposed to regulate the wind turbine to follow the maximum power extraction trajectory, as explained later.

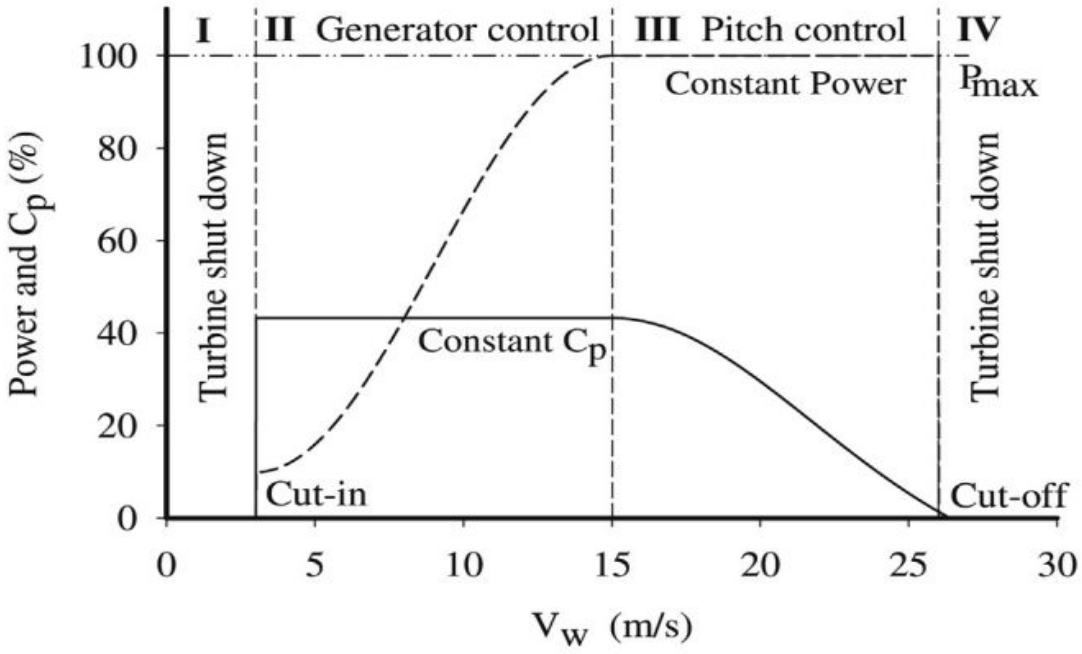

Figure 2.5: Ideal power curve for wind turbines [41].

Ideally, aerodynamic control only starts to operate when the power generated achieves its rated value, which characterizes the beginning of region III. In cases where the wind speed is above the rated value, turbine speed and power must be limited to its rated value in order to prevent mechanical damage. Therefore, operation with MPPT is no longer applied. The pitch blade angle mechanism is activated in order to reduce power capture with increasing of the wind speed, and this allows the turbine to work even with wind speeds above the rated level up to certain limit. In the fourth region IV, the wind speed is considered too high and the turbine is shut down. The combination of generator and pitch control comprises the MPPT, limited to rating values of turbine and generator. Figure 2.6 illustrates the combination of generator and aerodynamic control used to form the MPPT through several wind speeds [6]. The values of the wind speed and turbine power are represented in per unit for simplicity.

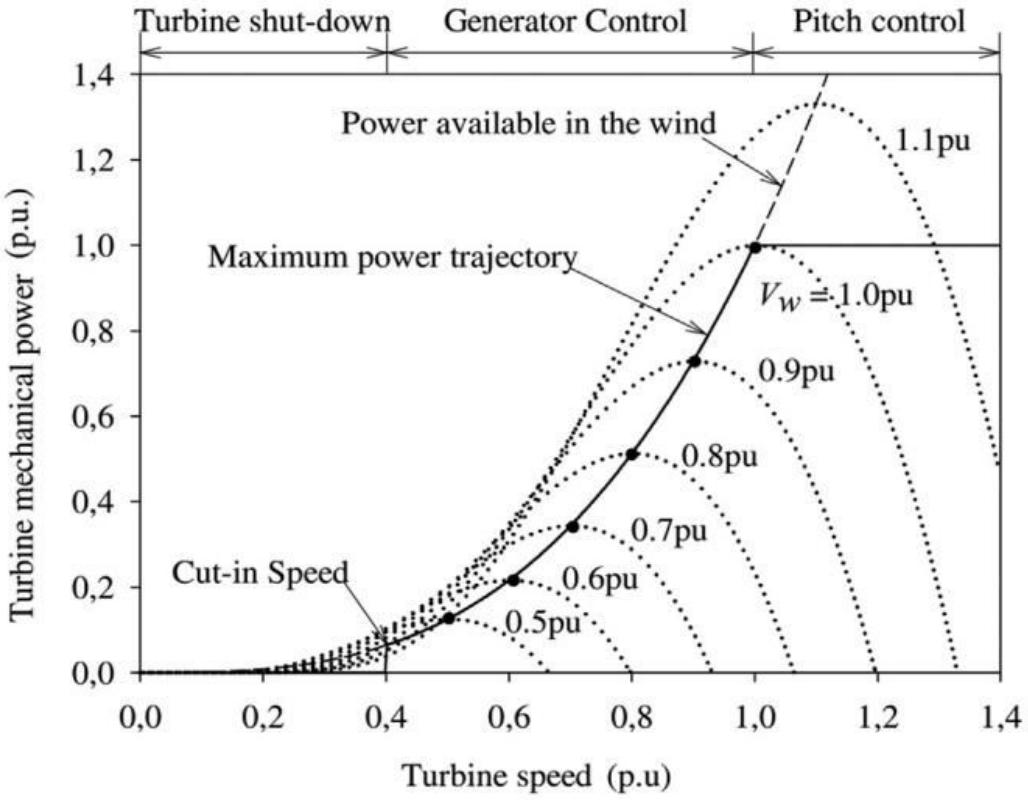

Figure 2.6: Maximum power point tracking (MPPT) of the DFIG system [92].

For each wind speed, there is an optimal turbine rotational speed which takes the maximum power from the wind. The combination of turbine speed and mechanical

power form, therefore, the operating point of the turbine. In other words, MPPT consists of maintaining the operating point along the maximum power trajectory presented in figure 2.6 by means of variable-speed control. To achieve variable-speed operation, a back-to-back converter is placed between the generator and the grid. The power converter will apply voltages of variable frequency and amplitude to the generator in order to control the rotor currents, which in turn allows control of the generator torque and speed [7]. The wind turbine used with the technique of maximum power tracking is a very appropriate power source for the grid [93]. Basically, there are three traditional methods of achieving MPPT: tip speed ratio (TSR) control, power signal feedback (PSF) control and hill-climb searching (HSC) control. In TSR, wind velocities are difficult to obtain accurately, while the PSF control method requires knowledge of the maximum power curve of the wind turbine. This method can effectively avoid fluctuations in output power and is easy to execute [97]. Wind speed measurement and estimation is required in most types of variable speed vector control to track the desired wind power with changes the rotational speed of the turbine generator based on the variation in wind velocities [98]. Conventionally, a number of anemometers surrounding the wind turbine were used to measure wind velocities, but this method is usually costly and unreliable [99].

Ahmed and Kalil [100] have used an algorithm of support vector regression (SVR) to estimate an unknown system's wind speed depending on the power of the turbine and its speed based on training data of the optimal tip speed ratio. However, this study is not purely sensorless because the turbine speed is measured with an encoder. A power coefficient polynomial method has been proposed [101] to compute the wind velocity iteratively by deducing the polynomial roots numerically. This has the advantage of being applicable to all doubly-fed machines. However, this method would increase the complexity computation, consume more time, and adversely affect system performance. The rotor position phase and PLL have been applied track the maximum power point of a DFIG [98] and this method has the advantage of parameter independent and insensitive to measurement noise. Based on the two dimensional look-up table of the power coefficient with power mapping, which is used to track the MPPT with or without wind speed measurement to estimate the optimal torque from the estimating on rotating speed. This has the drawback of requiring greater memory size which influences on the accuracy of estimation [102, 103].

Another method of sensorless vector control has employed an artificial neural network (ANN) with a three-layer radial basis function network (RBFN) used for estimating a shaft speed [104]. In addition, an extended Luenberger and another neuronal observer were used to estimate the wind velocity so as to impose MPPT.

2-5 Fault Ride-Through (FRT) of the DFIG Based Wind Turbine

Fault ride-through (FRT) represents the ability of the DFIG wind turbine to remain connected to the grid even when the voltage level across the point common coupling (PCC) is drops to 20% [2, 105]. This requirement is essential in the new grid code of power systems in different countries since the isolation of the wind turbine (WT) from the grid system in conditions of sever voltage dip will lead to the loss of stability in the power system [7]. The utilities adopted to enhance FRT capability in wind turbines deals with issues of over-current in the stator and rotor circuit windings of generators in addition to over-voltage across the DC-link capacitor in the back-to-back power converter of the DFIG system [2, 38]. The low power rating of the converter in the DFIG system configuration means priority is given to protecting the converter from the risk of damage due to short-circuit fault effects producing a fluctuating high currents in the stator and rotor windings of the generator. Therefore it is essential to protect the converter so as to keep the DFIG operating and connected to the grid in order to fulfil the requirements of the grid code. Figure 2.7 illustrates a summary of the voltage profile for ride-through capabilities in the grid codes, and its condition that only when the grid voltage goes below the curves are turbines permitted to be isolated from the grid. Moreover, when the voltage is in the special area, the turbines should supply reactive power [36, 105, 106]. Different countries have issued grid codes for wind turbines with a special focus on their ride-through capability, including fault ride-through (FRT) at the point of common coupling (PCC) for wind farms and low voltage ride-through (LVRT) for wind turbine generators.

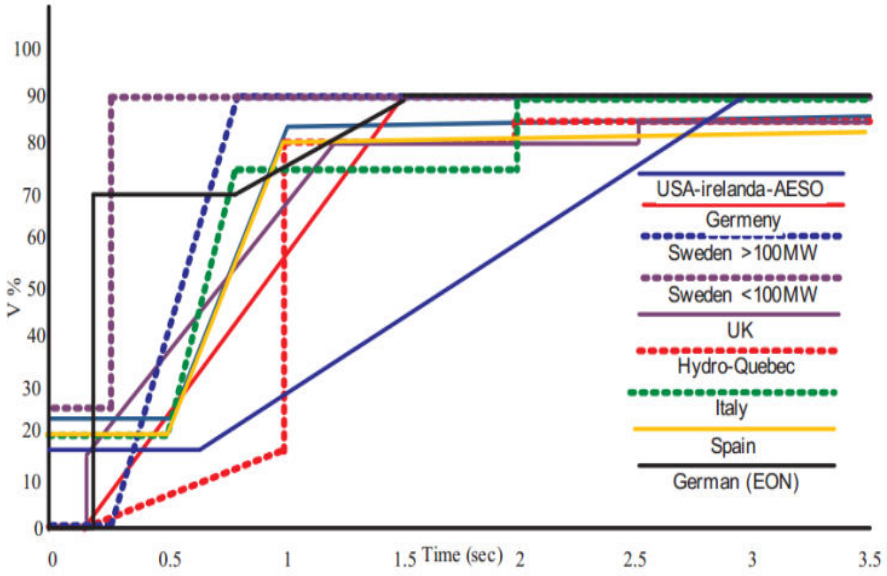

Figure 2.7: FRT requirements for various grid codes [106].

The basic definition of a voltage dip is a sudden reduction in grid *rms* voltage in the range of 0.1-0.9 pu for a short period of time between 0.5-30 cycles. The duration of a voltage dip is generally evaluated based on the clearing time of the protection devices. Voltage dips represent one of the most harmful power quality problems and the major concern for the industry. The main causes of this problem as follows [37]:-

- Short-circuit in the grid
- Switching operation associated with a temporary disconnection of the supply
- Flow of peak current caused by starting a large motor
- Peak current caused by arc furans
- Peak current caused by transformer in saturated

Based on the space vector transformations, seven types of voltage dips in the DFIG-based wind turbine have been listed [107], and this classification enables the evaluation of the severity and characteristics of each type of voltage dip. Choudhury [108] has observed the main effects of a sudden change in grid voltage on the behaviour of DFIG wind turbine systems under steady state conditions. The configuration of the DFIG has a stator circuit directly connected to the grid while the rotor winding is connected to the grid via the back-to-back converter, and this is the reason for all of the efforts to develop the fault ride-through (FRT) capability. Where a power grid system is with a voltage drop at the PCC; the stator voltage of the DFIG

will immediately change, and if it not suddenly varies the rotor voltage will be compensate the dropping in stator voltage and this will drive to oscillate the stator and rotor currents with high incremental in its values [36, 106]. This disturbance in the stator and rotor currents will cause damage to the rotor converter and increase the mechanical stress on the wind turbine as a result of the transient in the electromagnetic torque of the generator [2]. An algorithm for support and safety operation requirements for the DFIG system to ride this condition is presented in figure 2.8, which describes the main aims of FRT ability enhancement in DFIG system.

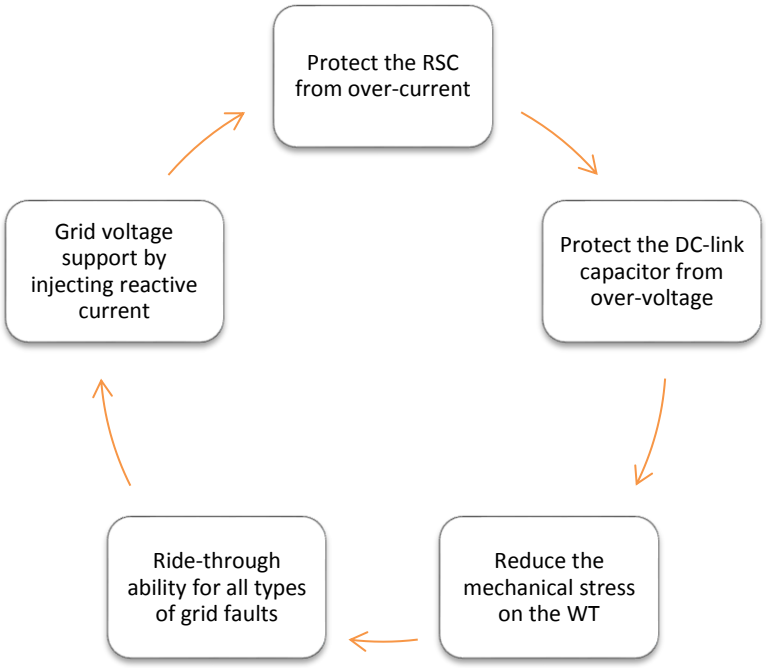

Figure 2.8: Algorithm to support FRT in DFIG wind turbines.

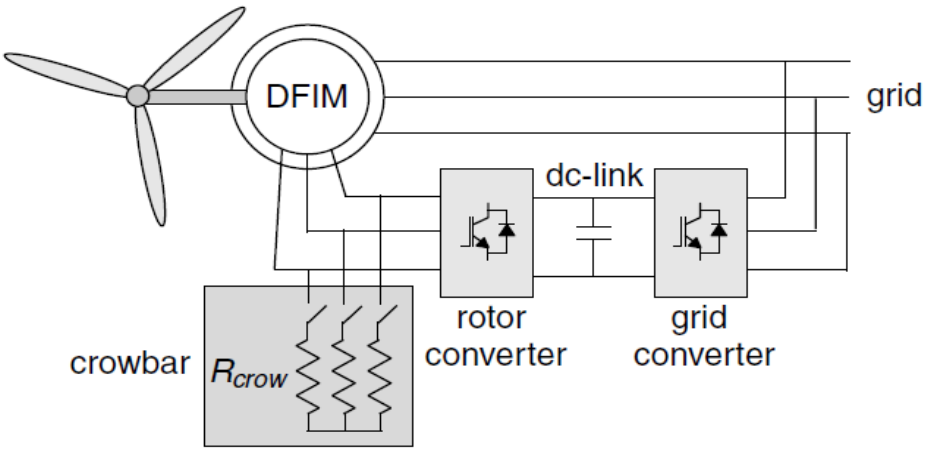

Figure 2.9: DFIG system equipped with a crowbar [31].

Traditionally, the protective systems utilized to enhance the behaviour of DFIG-based wind turbines in severe voltage dips can be summarized as crowbar circuits, energy storage systems, stator switches, and auxiliary parallel grid side rectifier (stator reactive power converter) [109-112]. The auxiliary parallel grid side rectifier is represent another method to enhance the FRT capability of the DFIG system which is characterized by connect the GSC in series with the stator voltage rather than in parallel as in the conventional DFIG. This configuration can be accomplished alone or with adding extra rectifier. It can be used to control two different variables which are the stator voltage and stator flux control. In stator flux control it has been used to remove the oscillations in the stator flux and so regulating the stator current and the rotor current. The disadvantage of this method is regulating the stator flux at a low value during the fault consequently; the stator power will be regulated at a lower value during the fault which differs from the operating value, leading to lose the maximum power tracking during faults. Another problem with this technique is using a flux estimator, which adds a time delay, inaccuracy and system complexity. When it used to control the stator voltage, this technology has the same targets of containing the stator current, rotor current and the DC voltage within their safe limits has been achieved. Moreover, the stator power is regulated at its operating value which keeps maximum power tracking even during faults [112].

. The crowbar system is the most common technique used in protects the RSC during voltage dip, and it's concept of operation is based on the rotor current flowing through an external resistor during faults to dissipate the unbalanced power which results from the rotor over-current as shown in figure 2.9. [2, 7, 31] it is used to avoid the voltage bus exceeding the maximum value once the RSC loses current control, providing a path for the rotor currents [111]. The crowbar short-circuits the rotor and the machine operates as a squirrel cage machine. There are two types of crowbar which are passive (use a Thyristor to connecting the crowbar resistor to the rotor winding with no gate turn-off feature and it will not be able to resume operation as soon as the transient current and voltage have decayed) and active (a three phase rectifier and power semiconductor device with gate turn off- capability and external resistor and this configuration is fast response and is able to resume to the normal operation condition state) [7]. The crowbar and DC chopper protection schemes have been used to enhance

the FRT ability in DFIG-based wind turbine systems [113, 114]. The main demerits of utilizing the crowbar in a DFIG wind turbine system is that when activated, the DFIG runs as a squirrel cage machine where the rotor windings are short circuited [115-117] .The DFIG start to absorb reactive power from the grid and the decoupled control of active and reactive power is no longer available [118]. This means that the situations deteriorate during a grid fault and the fault recovery process will slow down or it may even result in voltage collapse [119]. Thus, it is better to reduce the connection time of the crowbar and enable the wind turbine to return to normal operation as soon as the transients have decayed [116].

Some of the most important studies relating to DFIG modeling, simulation and analysis are reviewed in this section. Lihui [36] proposed a mathematical modification to the control system for both the rotor side converter (RSC) and the grid side converter (GSC) to improve the low voltage ride-through (LVRT) capability of the DFIG wind turbine during voltage dip based on an increase in the generator's rotor speed and adding a compensation term temporally when faults occur to absorb the excessive energy and damp the oscillation of DC-link voltage. The simulation results were verified by comparison of the modification with crowbar protection. It was shown that the speed, electromagnetic torque, DC-link voltage, current variation and pitch control with longer duration of voltage dip in crowbar has better LVRT behaviour upon the proposed method even the later have better enhancement to ride through grid faults at the short period conditions. In addition, theoretical analysis has utilized the stator feedback and power (PQ) null method to enhance the DFIG's ability to ride-through the voltage dip [120, 121]. [122] have considered the theoretical transient responses of DFIG wind turbines subjected to symmetrical and unsymmetrical voltage sags. An 80% voltage sag was used when employing the full-order and reduced order models to measure the power quality impact on the DFIG system, and it was found that the flicker emission is very low, the reactive power is close to zero and the current total harmonic distortion (THD) is always less than 5%. Another study [123] simplified dynamic model for DFIG-based wind turbines was presented, which was tested theoretically with different conditions during both the steady state and the transient of the grid voltage by means of PDCAD/EMTDC simulations.

2-6 Wind Turbine Topologies

Many choices are available to the academics and industry for a wind turbine with no assent among them for the best wind turbine generator technology. In conventional, wind turbine generators (WTGs) categorized in three main types, which are the direct current (DC), alternating current (AC) synchronous and AC asynchronous generators. Figure 2.10a shows the DC wind generator system which consist of a wind turbine, a generator, inverter, system control, and transformer. The power is injected through brushes connecting the commentator which is utilized to rectify the generated AC power into DC output [162]. This type of technology is costly as a result of using the commutators and brushes. Furthermore, this wind turbine generator is preferred to use where the load is closed to the generator. Secondly, switched reluctance-based WTs illustrated in figure 2.10b which includes stator and salient rotors and it is characterized by laminated steel sheets. Stator current induced as a result of magnetic circuit linking the stator and rotor changes through shaft rotation. The primary advantages of this WT are the ability to operate even in harsh environment, high reliability, and simplicity. However, switched reluctance-based WTs suffer from the high weight of generator. Permanent magnet excitation is greatly adopted in newer smaller scale wind turbine designs, because of its higher efficiency and reduced the diameter of blade. Furthermore, this generator does not need external excitation current. The permanent magnets (PMs) are the source of DC excitation in this generator where these rugged PMs are installed on the rotor to generate a constant magnetic field and the generated electrical power will transfer to grid from the stator [162, 163]. The permanent magnet synchronous generator (PMSG) shown in figure 2.10c which unable to produced electrical power with fixed frequency to the grid. Therefore, the stator required to connect to the power grid through full rated AC-DC-AC power converters because the converter is connected to the stator. Squirrel-cage induction generator (SCIG) depicted in figure 2.10d where the schematics of the system including the wind turbine, pitch control, and reactive power compensator. This type of WT generally exchanges energy with the interconnected grid via only the stator winding. The rotor winding in this category almost is short-circuited. A rotating magnetic field is established across the air-gap [162]. If the rotor rotates at a speed different to synchronous speed, a slip is created and the rotor circuit is energized. This type of WT is simple, reliable, and cost effective. However, induction machines draw

reactive power from the grid and thus some form of reactive power compensation is needed such as the use of capacitors or power converters. Table 2.4 is summarized different wind turbine topologies.

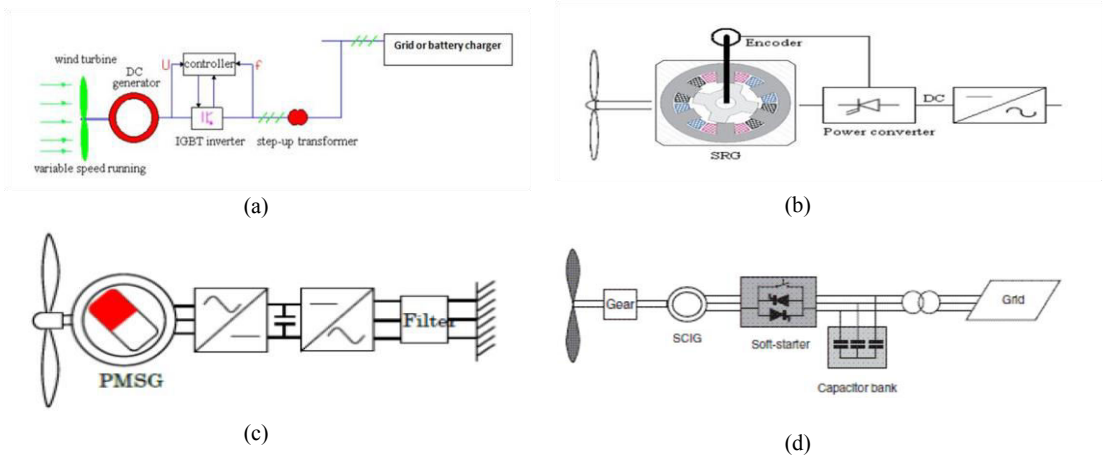

Figure 2.10: Configuration of wind turbine topology using: (a) DC generator; (b) switch reluctance generator; (c) PMSG; (d) Squirrel cage induction generator [162].

Table 2.4: Overall comparison of WT generator topologies [162]

	DC	Asynchronous		Synchronous	
	DC generators	SCIG	DFIG	PM	Reluctance
Speed	variable	fixed	variable	variable	variable
Power supply	directly to the grid	directly to the grid	partially stator-converter	totally via converters	totally via converters
Controllability	poor	poor	good	good	good
Active-reactive power control	no	dependent	separate	separate	separate
Grid-support capability	low	low	high	very high	medium
Reliability	poor	medium	high	high	very high
Fault response	slow	slow	high	high	high
Cost	low	low	medium	high	medium
Mass saving	low	low	high	very high	low
Suitability	low power, residential application	small wind turbines	medium-large wind turbines	direct drive; small-medium wind turbines	early stage

2-7 Conclusions

In this chapter, an overview has been given of different approaches to modelling the doubly-fed induction generator (DFIG)-based wind turbine system in addition to different control strategies with their various advantages and disadvantages.

In the second part of a chapter, different methods developed in the literature for the detection of the rotor position of DFIG systems have been described. Although there are methods estimate the rotor position of the DFIG with different phases of configurations and electric quantities measured to provide position information for the rotor, it appears that the most attractive techniques are categorized based detecting position with acceptable error in addition to the insensitivity to variation in the system's parameters.

A brief overview of maximum power point tracking (MPPT) methods for DFIG systems in the literature has also been presented.

Based on the literature survey, several types of improvements designed to enhance the fault ride-through (FRT) capability of the DFIG-based wind turbine have been introduced in the fourth part of this chapter.

CHAPTER THREE

CHAPTER THREE

MATHEMATICAL MODEL OF DOUBLY- FED INDUCTION GENERATOR SYSTEM

3-1 Introduction

In this chapter a dynamic model of different parts of the DFIG based wind turbine including both the mechanical and electrical components are presented in order to fully understand the dynamic performance of the system in any specific operating conditions and to design the control system. Firstly, the main mathematical equations, that characterize the relationship between voltage and fluxes in the machine. These are the basic equations used for deriving the dynamic model. Models of the aerodynamic and mechanical parts are also presented. The decoupling control active and reactive power in this model is also explained. The vector control strategy for the grid-side converter is studied based on the dynamic models of the grid-side system formed by the grid, the grid-side filter, and the grid-side converter itself. This control strategy highlights the two main objectives of the grid-side converter: control of both the bus voltage of the DC-link and the active and reactive powers exchanged bi-directionally between the rotor of the machine and the grid. Based on the final modeling of the machine and control system equations, a detailed evaluation of the behaviour of the system is carried out, resulting in performance curves that can reveal the current, voltage, or different magnitude requirements, depending on the specific operating conditions of the machine.

In Chapters Four and Five respectively, the simulation results obtained from the Simulink model developed in this chapter will be employed with the corresponding rotor position estimation and in the performance comparison results of the system under unbalance dynamic behavior condition.

3-2 Dynamic Model of Doubly-Fed Induction Generator

The equivalent circuit of a DFIG shown in figure 3.1 can be characterized by different reference frames such as the stationary frame, rotor frame, or the synchronous frame oriented to either stator flux [22] or stator voltage [47]. The simplified DFIG model can be described as three windings in the stator and three windings in the rotor,

as shown in figure 3.2. The instantaneous stator and rotor voltages, current, and flux of the machine are given as follow:

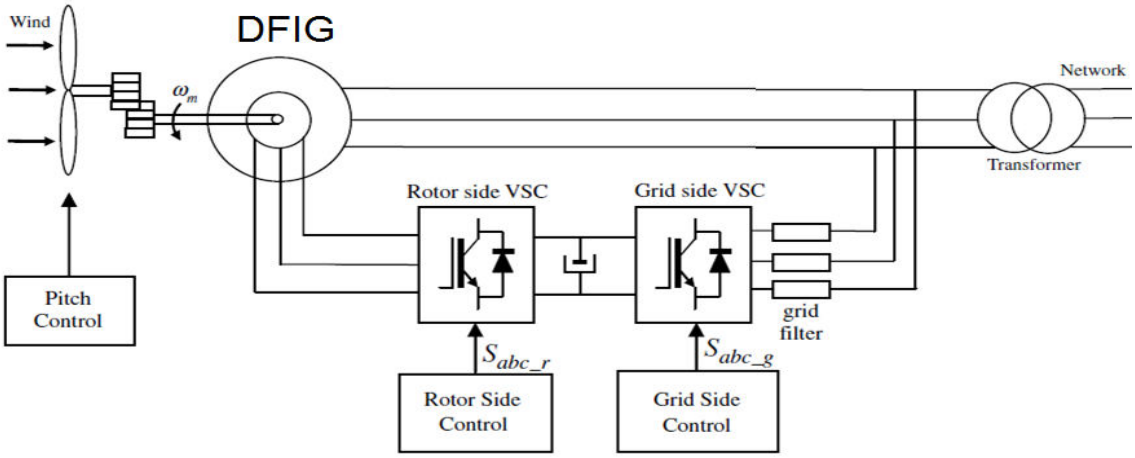

Figure 3.1: System configuration of the DFIG-based wind turbine [7].

$$v_{as}(t) = r_s i_{as}(t) + \rho\lambda_{as}(t) \quad (3.1)$$

$$v_{bs}(t) = r_s i_{bs}(t) + \rho\lambda_{bs}(t) \quad (3.2)$$

$$v_{cs}(t) = r_s i_{cs}(t) + \rho\lambda_{cs}(t) \quad (3.3)$$

$$v_{ar}(t) = r_r i_{ar}(t) + \rho\lambda_{ar}(t) \quad (3.4)$$

$$v_{br}(t) = r_r i_{br}(t) + \rho\lambda_{br}(t) \quad (3.5)$$

$$v_{cr}(t) = r_r i_{cr}(t) + \rho\lambda_{cr}(t) \quad (3.6)$$

where:-

r_s: is the stator resistance.

r_r : is the rotor resistance referred to the stator.

$v_{as}(t)$,$v_{bs}(t)$, and $v_{cs}(t)$: are the applied stator voltages.

$i_{as}(t)$,$i_{bs}(t)$, and $i_{cs}(t)$: are the stator currents of phases.

$v_{ar}(t)$,$v_{br}(t)$, and $v_{cr}(t)$: are the stator referred rotor voltages.

$i_{ar}(t)$,$i_{br}(t)$, and $i_{cr}(t)$: are the stator referred rotor currents of phases.

$\lambda_{as}(t)$,$\lambda_{bs}(t)$, and $\lambda_{cs}(t)$: are the stator fluxes.

$\lambda_{ar}(t)$,$\lambda_{br}(t)$, and $\lambda_{cr}(t)$: are the rotor fluxes.

At steady state condition the following hold:-

- The stator side electric magnitudes have a constant sinusoidal angular frequency (ω_e).

- The rotor side electric magnitudes have a constant angular frequency (ω_r).

The relationship between the stator angular frequency and the rotor angular frequency can be expressed as:

$$\omega_r + \omega_m = \omega_e \tag{3.7}$$

where (ω_m) is the electrical angular frequency of the machine.

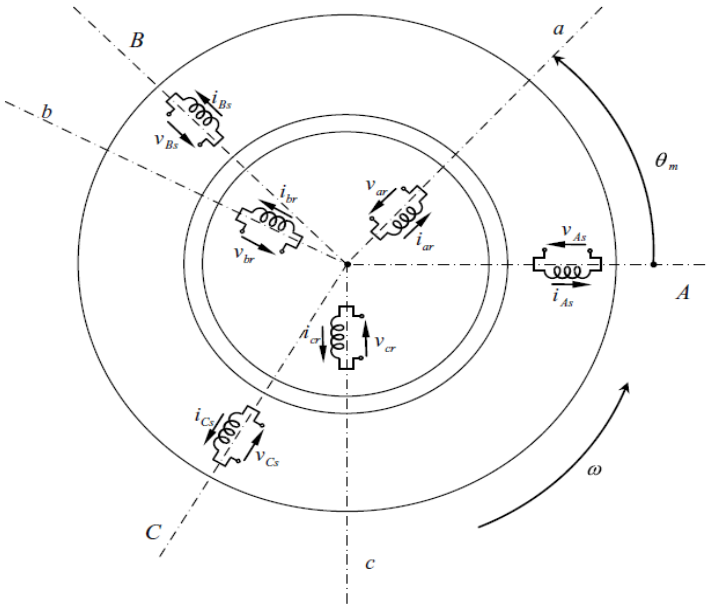

Figure 3.2: Ideal three-phase windings (stator and rotor) of the DFIG [7].

In generalized electrical machine theory, the inclusion of space vector analysis is based on the following hypotheses shown in:

1. The distributions of flux and magneto-motive force (MMF) are represented by their fundamental harmonic component alone.
2. The effect of slotting winding distribution can be neglected.
3. Commutation effects and brush-connections are considered to be ideal.
4. The influences of eddy currents and hysteresis can be neglected.
5. Magnetic saturation is not present.

Magnetic linearity is assumed in order to produce linear superimposition magnetic fields, which simplifies model development considerably. In practical, if magnetic saturation has an effect on the machine, it will limit the transient over-shoot current and power in the step response of the vector control, and restrict the instant excesses of fault response. The linear magnetic analysis will therefore derive a worst-case response in terms of transient response to both control and faults. Therefore, the stator and rotor

voltage and magnetic flux equations of the DFIG in the stationary reference ($\alpha\beta$) frame are as follows [7, 31, 34]:

$$v_{\alpha s} = r_s i_{\alpha s} + \rho\lambda_{\alpha s} \tag{3.8}$$

$$v_{\beta s} = r_s i_{\beta s} + \rho\lambda_{\beta s} \tag{3.9}$$

$$v_{\alpha r} = r_r i_{\alpha r} + \omega_r \lambda_{\beta r} + \rho\lambda_{\alpha r} \tag{3.10}$$

$$v_{\beta r} = r_r i_{\beta r} - \omega_r \lambda_{\alpha r} + \rho\lambda_{\beta r} \tag{3.11}$$

In the (dq) frame, the voltages can describe as:

$$v_{qs} = r_s i_{qs} + \omega_e \lambda_{ds} + \rho\lambda_{qs} \tag{3.12}$$

$$v_{ds} = r_s i_{ds} - \omega_e \lambda_{qs} + \rho\lambda_{ds} \tag{3.13}$$

$$v_{qr} = r_r i_{qr} + (\omega_e - \omega_r)\lambda_{dr} + \rho\lambda_{qr} \tag{3.14}$$

$$v_{dr} = r_r i_{dr} - (\omega_e - \omega_r)\lambda_{qr} + \rho\lambda_{dr} \tag{3.15}$$

where: $\rho = d/dt$, and the stator and rotor flux linkage equations in the ($\alpha\beta$) frame are:

$$\lambda_{\alpha s} = L_s i_{\alpha s} + L_m i_{\alpha r} e^{j\theta_r} \tag{3.16}$$

$$\lambda_{\beta s} = L_s i_{\beta s} + L_m i_{\beta r} e^{j\theta_r} \tag{3.17}$$

$$\lambda_{\alpha r} = L_m i_{\alpha s} + L_r i_{\alpha r} e^{j\theta_r} \tag{3.18}$$

$$\lambda_{\beta r} = L_m i_{\beta s} + L_r i_{\beta r} e^{j\theta_r} \tag{3.19}$$

The stator and rotor flux linkage equations in the (dq) frame are:-

$$\lambda_{qs} = L_s i_{qs} + L_m i_{qr} \tag{3.20}$$

$$\lambda_{ds} = L_s i_{ds} + L_m i_{dr} \tag{3.21}$$

$$\lambda_{qr} = L_m i_{qs} + L_r i_{qr} \tag{3.22}$$

$$\lambda_{dr} = L_m i_{ds} + L_r i_{dr} \tag{3.23}$$

where, $v_{dqs}, v_{dqr}, i_{dqs}, i_{dqr}, \lambda_{qds}, \lambda_{dqr}$ are respectively the stator and rotor voltages, currents, and flux vector in the synchronous reference frame r_s, r_r represent the stator and rotor resistance; L_s, L_r the stator and rotor self-inductance; L_m the mutual inductance; and ω_e, ω_r the synchronous and rotor angular speed.

The stator and rotor active and reactive power in the ($\alpha\beta$) frame are calculated as follows:

$$P_s = \frac{3}{2} Re\{\overline{v_s}.\overline{i_s^*}\} = \frac{3}{2}(v_{\alpha s} i_{\alpha s} + v_{\beta s} i_{\beta s}) \quad (3.24)$$

$$P_r = \frac{3}{2} Re\{\overline{v_r}.\overline{i_r^*}\} = \frac{3}{2}(v_{\alpha r} i_{\alpha r} + v_{\beta r} i_{\beta r}) \quad (3.25)$$

$$Q_s = \frac{3}{2} Im\{\overline{v_s}.\overline{i_s^*}\} = \frac{3}{2}(v_{\beta s} i_{\alpha s} - v_{\alpha s} i_{\beta s}) \quad (3.26)$$

$$Q_r = \frac{3}{2} Im\{\overline{v_r}.\overline{i_r^*}\} = \frac{3}{2}(v_{\beta r} i_{\alpha r} - v_{\alpha r} i_{\beta r}) \quad (3.27)$$

The stator/rotor active and reactive power and electromagnetic torque expressions in (dq) frame:-

$$P_s = \frac{3}{2} Re\{\overline{v_s}.\overline{i_s^*}\} = \frac{3}{2}(v_{ds} i_{ds} + v_{qs} i_{qs}) \quad (3.28)$$

$$Q_s = \frac{3}{2} Im\{\overline{v_s}.\overline{i_s^*}\} = \frac{3}{2}(v_{qs} i_{ds} - v_{ds} i_{qs}) \quad (3.29)$$

$$P_r = \frac{3}{2} Re\{\overline{v_r}.\overline{i_r^*}\} = \frac{3}{2}(v_{dr} i_{dr} + v_{qr} i_{qr}) \quad (3.30)$$

$$Q_r = \frac{3}{2} Im\{\overline{v_r}.\overline{i_r^*}\} = (v_{qr} i_{dr} - v_{dr} i_{qr}) \quad (3.31)$$

where the superscript * represents the complex conjugate of a space vector, as used in phasors. Finally, the electromagnetic torque can be found from:

$$T_e = \frac{3}{2} Im\{\overline{\lambda_s}.\overline{i_r^*}\} = \frac{3}{2} p \frac{L_m}{L_s}(\lambda_{qs} i_{dr} - \lambda_{ds} i_{qr}) \quad (3.32)$$

3-3 Vector Control System

The control strategy utilized to control the RSC and GSC in this study is vector-oriented control in the synchronous reference frame since it has the several merits of a good dynamic response in regular and fault operating conditions, it is robust to parameter variation and measurement noise, and has fixed switching frequency. Furthermore, a wide range of reference material is available. On the other hand, this method has drawbacks when compared with DTC, DPC, and vector-oriented control in the rotor/stationary reference frame, including slower response time compared to direct methods and the need to estimate the flux angle [97].

3-3-1 Vector Control of the Rotor Side Converter (RSC)

The main objective of the use RSC is to decouple control of the active and reactive power in normal and fault operating conditions, in addition to controlling and synchronizing the stator voltages fed to the grid in the start-up phase. To give better differentiation between the RSC and the GSC controllers, the control variables utilized to conduct the vector orientation in this study are based on the stator active and reactive power. Table 3.1 demonstrates the different scenarios which may be adopted in the vector control of the RSC [22, 98, 124].

Table 3.1: Possibilities of vector control in RSC controller.

	Synchronous Frame	Rotor Frame
Vector of Control	Stator/grid flux Stator voltage Air-gap flux Rotor flux	Stator/grid flux Stator voltage Air-gap flux Rotor flux
Appearance of Control Variables	DC	AC
Controller	Classical PI	Adaptive Proportional-Resonant controller

The generic expressions for the DFIG can be simplified by using a reference frame aligned with the stator flux (i.e.$\lambda_{ds} = \lambda_s,\ \lambda_{qs} = 0$) as shown in figure 3.3 to decouple the control of the rotor quantities. In these reference frames, the control variables appear as DC values, and classical PI control can be employed.

Under the hypothesis of stator flux orientation and neglecting the stator phase resistance, the equations of the currents, fluxes and the voltages, may be written as follows [7]:

$$i_{ds} = \frac{1}{L_s}(\lambda_{ds} - L_m i_{dr}) \tag{3.33}$$

$$i_{qs} = -\frac{L_m}{L_s} i_{qr} \tag{3.34}$$

$$\lambda_{dr} = \frac{L_m}{L_s}\lambda_{ds} + \sigma L_r i_{dr} \tag{3.35}$$

$$\lambda_{qr} = \sigma L_r i_{qr} \tag{3.36}$$

After simplifications of equations 3.12 - 3.15 by assuming that stator resistance is small, and because the direct stator flux component is constant in the case of stator flux orientation (i.e. $\rho\lambda_{ds} = 0$), therefore:

$$v_{ds} = 0 \tag{3.37}$$

$$v_{qs} = \omega_e \lambda_{ds} \tag{3.38}$$

$$v_{dr} = r_r i_{dr} + \sigma L_r \rho i_{dr} - (\omega_e - \omega_r) L_r \sigma i_{qr} \tag{3.39}$$

$$v_{qr} = r_r i_{qr} + \sigma L_r \rho i_{qr} + (\omega_e - \omega_r)(L_r \sigma i_{dr} + \frac{L_m}{L_s}\lambda_{ds}) \tag{3.40}$$

In addition, active and reactive stator power and electromagnetic torque can be formulated after simplification as:

$$P_s = -\frac{3L_m}{2L_s}(v_{qs} i_{qr}) \tag{3.41}$$

$$Q_s = \frac{3v_{qs}}{2L_s}(\lambda_{ds} - L_m i_{dr}) \tag{3.42}$$

$$T_e = -\frac{3}{2} p \frac{L_m}{L_s}(\lambda_{ds} i_{qr}) \tag{3.43}$$

where $\sigma = 1 - L_m^2 / L_s L_r$

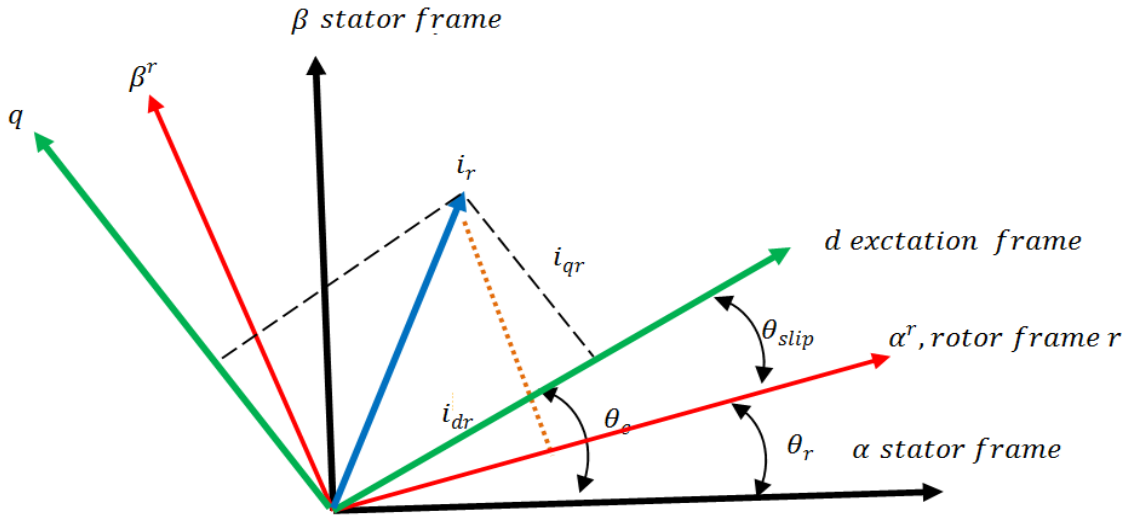

Figure 3.3: Reference frames and angles [76].

The q-axis current component is used to control the active power using a maximum power point tracking (MPPT) strategy to calculate the active power reference [125].

The measured active power is compared with the reference active power and the error result is fed to the PI controller to estimate the reference value for the *q*-axis rotor current. This signal is then compared to its actual value and the error is passed through a second PI controller determining the reference voltage for the q-axis component.

The d-axis is used to control the reactive power exchanged with the grid, which in normal operation is set to zero in order to operate with unity power factor. Similar to the control strategy for the *q*-component, when the sensed reactive power is compared with the reference reactive power, an error is produced on processing through the PI controller, computes the reference d-axis component of the rotor current. This signal is compared to the d-axis current value and the error is sent to a second PI controller which determines the reference voltage for the d-axis component. Finally, the *dq*-reference voltages are passed through the PWM module and the modulation indices for the control of the RSC are determined, as shown in figure 3.4.

The inner and outer control loops shown in figure 3.4 have been judge by four PI controllers in determining the reference *dq* rotor currents in the outer loop and the reference *dq* voltages in the inner loop. The transfer functions of the stator active and reactive power (outer loop) control are given as follows:

From equations 3.39 and 3.40, if it is assumed that:

$$e_1 = -(\omega_e - \omega_r)L_r\sigma i_{qr} \tag{3.44}$$

$$e_2 = (\omega_e - \omega_r)(L_r\sigma i_{dr} + \frac{L_m}{L_s}\lambda_{ds}) \tag{3.45}$$

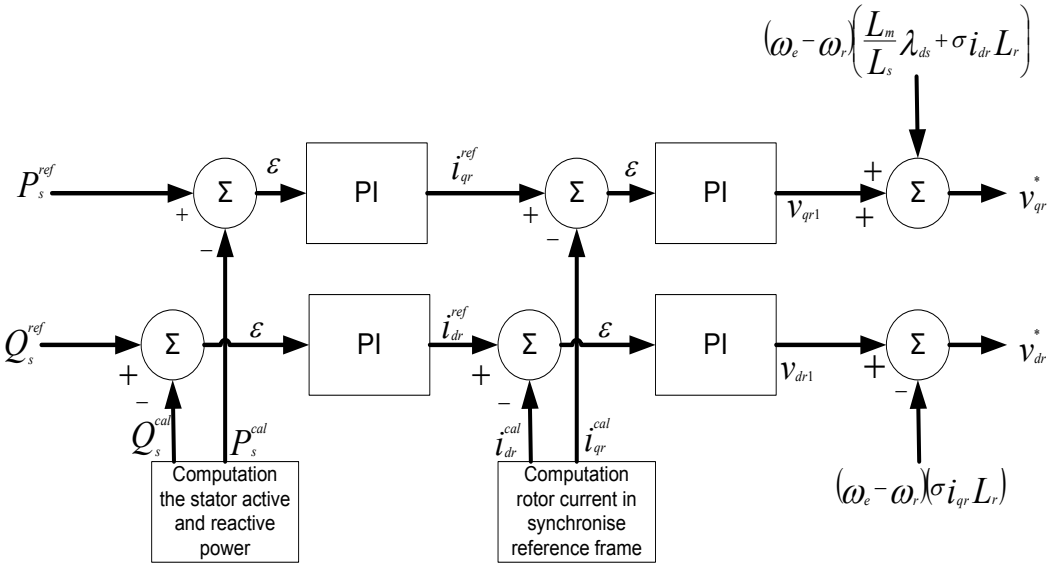

Figure 3.4: Block diagram of RSC controller.

Substituting equations 3.44 and 3.45 in equations 3.39 and 3.40 respectively gives:

$$v_{dr} = r_r i_{dr} + \sigma L_r \rho i_{dr} + e_1 \tag{3.46}$$

$$v_{qr} = r_r i_{qr} + \sigma L_r \rho i_{qr} + e_2 \tag{3.47}$$

From equations 3.46 and 3.47, the plant model includes the voltage drop in the transitory inductance σL_r, cross-coupling from the orthogonal loop and the *emf* induced by the stator flux. These couplings are nulled at the controller output by the compensating terms. This results in the same closed-loop transfer function for the two current control loops. Furthermore simplifications of equations 3.46 and 3.47, gives:

$$i_{dr} = \frac{(v_{dr} - e_1)}{r_r + s\sigma L_r} \tag{3.48}$$

$$i_{qr} = \frac{(v_{qr} - e_2)}{r_r + s\sigma L_r} \tag{3.49}$$

Figure 3.5 shows the closed loop system using the rotor current control by a PI controller. The inner control loop has a significant advantage for the protection of the DFIG. It can naturally protect the system from over-current, since current limiters can easily be inserted in the control system shown below. Because general PI controllers are widely used and have proven to be effective, they are also applied in the following analysis [7, 126]:

Hence, the plant for the current control loops is given by:

$$N(s) = \frac{i_{dr}}{v_{dr}} = \frac{i_{qr}}{v_{qr}} = \frac{1}{r_r + L_r \sigma s} \tag{3.50}$$

The (i_{dr}) and (i_{qr}) current control loop forms are then:

$$\left.\begin{aligned} v_{qr}^1 &= (r_r + \sigma s L_r) i_{qr} = \left(k_{p1} + \frac{k_{i1}}{s}\right)\left(i_{qr}^{ref} - i_{qr}\right) \\ v_{dr}^1 &= (r_r + \sigma s L_r) i_{dr} = \left(k_{p1} + \frac{k_{i1}}{s}\right)\left(i_{dr}^{ref} - i_{dr}\right) \end{aligned}\right\} \tag{3.51}$$

Then the transfer functions between the reference and actual currents are changed to the following:-

$$\left.\frac{i_{qr}}{i_{qr}^{ref}} = \frac{\frac{1}{\sigma L_r}\left(s k_{p1} + k_{i1}\right)}{s^2 + \frac{s\left(r_r + k_{p1}\right)}{\sigma L_r} + \frac{k_{i1}}{\sigma L_r}}\right\} \tag{3.52}$$

$$\frac{i_{dr}}{i_{dr}^{ref}} = \frac{\frac{1}{\sigma L_r}(sk_{p1} + k_{i1})}{s^2 + \frac{s(r_r + k_{p1})}{\sigma L_r} + \frac{k_{i1}}{\sigma L_r}}$$

The design of the current controllers follows directly from equation 3.50, which can be written in the z-domain as:

$$N(z) = \frac{(1-A)r_r}{(z-A)} \tag{3.53}$$

where: $A = e^{-\left(r_r/L_r\sigma\right)T_s}$

(T_s), is the sample time 0.5ms. The control of the current in RSC in z-domain is shown in figure 3.6.

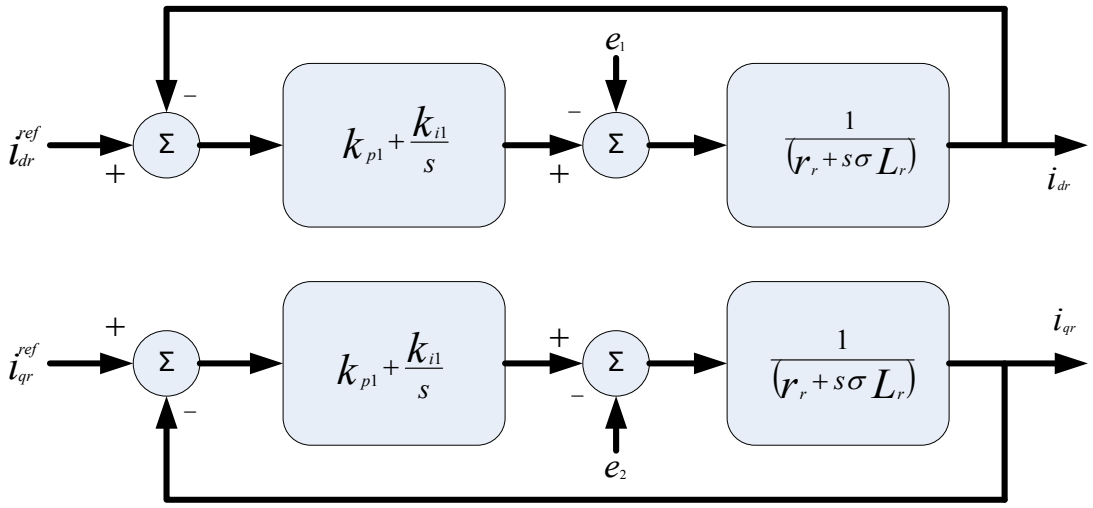

Figure 3.5: Closed loop current control of RSC in S-domain.

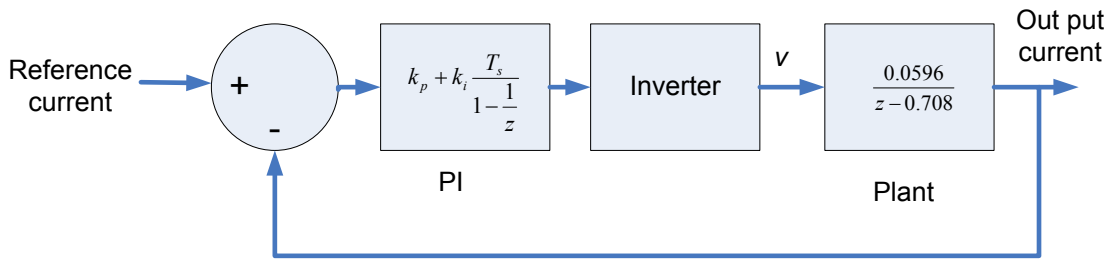

Figure 3.6: Closed loop GSC current-control in z-domain.

Choosing a compromise control for the parameters is necessary to gain good performance even through the whole system might be able to run with a wide range of parameters. Most previous studies have selected the gains of control using experience or trial and error, but this method is not good, particularly when the control system is implemented for different system. Furthermore the most important objective is to keep the system in a stable condition by choosing appropriate parameters for the control to use to tune up according to the specific behavioural requirements. The transfer function of the outer control loop of the rotor-side converter control is given by the following procedure:

From equations 3.20 - 3.23, the following expression can be deduced for the stator and rotor currents:

$$i_{ds} = \frac{\lambda_{ds}}{\sigma L_s} - \frac{L_m \lambda_{dr}}{\sigma L_s L_r} \tag{3.54}$$

$$i_{qs} = \frac{\lambda_{qs}}{\sigma L_s} - \frac{L_m \lambda_{qr}}{\sigma L_s L_r} \tag{3.55}$$

$$i_{dr} = \frac{-\lambda_{ds} L_m}{\sigma L_s L_r} + \frac{\lambda_{dr}}{\sigma L_r} \tag{3.56}$$

$$i_{qr} = \frac{-\lambda_{qs} L_m}{\sigma L_s L_r} + \frac{\lambda_{qr}}{\sigma L_r} \tag{3.57}$$

Substituting equations 3.38 and 3.56 in equation 3.42 gives, the stator reactive power formula as equation:

$$Q_s = \frac{3\omega_e}{2\sigma L_s}\left(\lambda_{ds}^2 - \frac{L_m}{L_r}\lambda_{ds}\lambda_{dr}\right) \tag{3.58}$$

Differentiating equation 3.58 with respect to time gives:

$$\rho Q_s = \frac{-3L_m \omega_e \lambda_{ds} \rho\lambda_{dr}}{2\sigma L_s L_r} \tag{3.59}$$

Solving equation 3.59 in term of $\rho\lambda_{dr}$ then gives:

$$\rho Q_s = \frac{-3\omega_e L_m \lambda_{ds}}{2\sigma L_s L_r}\left(v_{dr} - r_r i_{dr} - \sigma L_r(\omega_e - \omega_r)\left(i_{qr}\right)\right) \tag{3.60}$$

In addition, the PI controller formula will be:

$$B\rho Q_s = \left(k_{pq} - \frac{k_{iq}}{s}\right)\left(Q_s^{ref} - Q_s\right) \tag{3.61}$$

where:-

$$B = \frac{2\sigma L_s L_r}{3\omega_e L_m} \tag{3.62}$$

The transfer function of stator active power control is derived as the same procedure in equations 3.58-3.61, equations 3.38 and 3.57 are substituted in equation 3.41 and differentiation is applied to both sides of the equation with respect to time, giving:

$$\rho P_s = \frac{-3\omega_e L_m \lambda_{ds} \rho \lambda_{qr}}{2\sigma L_s L_r} \tag{3.63}$$

Solving equation 3.63 in terms of $(\rho\lambda_{qr})$ gives:

$$\rho P_s = \frac{-3\omega_e L_m \lambda_{ds}}{2\sigma L_s L_r}\left(v_{qr} - r_r i_{qr} - \sigma L_r(\omega_e - \omega_r)\left(i_{dr} + \frac{L_m \lambda_{ds}}{\sigma L_s L_r}\right)\right) \tag{3.64}$$

The PI controller formula for the stator power loop is formulated as follows:

$$z\rho P_s = \left(k_{pq} - \frac{k_{iq}}{s}\right)\left(P_s^{ref} - P_s\right) \tag{3.65}$$

And it is know:

$$z = \frac{2L_s L_r}{3\omega_e L_m} \tag{3.66}$$

The rotor side controller will give the DFIG model feedback control, with the system outputs constantly inputted back into the system, giving a more efficient and stable system. The tuning of the discrete PI synchronization controller defined in equation 3.50 has been implemented by the MATLAB/SISO Tool, by assuming acceptable bandwidth, phase and gain margins as can be observed in the controller design plots in figure 3.7. The root locus of the RSC current control loop gives a stable loop as illustrated in figure 3.7. The open loop test of the current control loop is stable because the poles on the left hand plane (LHP). In addition, this is confirmed by simulation results of RSC control loop in section (DFIG system model verification) with very good tracking of the reference values to the measured values and with minor oscillation.

The frequency response of a system can be represented by a Bode diagram, where one graph shows magnitude versus frequency and the other shows phase versus frequency. The root-locus provides information on the closed-loop system's transient response, while the frequency response shows the steady-state or low-frequency performance and stability margins. Several parameters need to be considered in the design using frequency response analysis. In this investigation, the phase margin (PM) and gain margin (GM) have been used. The observation of the open loop frequency response

results of the system control are illustrated in figure 3.7. There is no frequency oscillation with phase margin of 60 *deg* and frequency at 79.6 rad/sec, and in addition the step response is characterized by an overshoot of 11.6% at 0.038 sec with a peak amplitude of 1.12, rise time of 0.0184 sec and settling time of 0.0612 sec. The significant overshoot in this step response analysis is present due to the derivative term in the numerator. This is not desirable as it may cause damage to the converter.

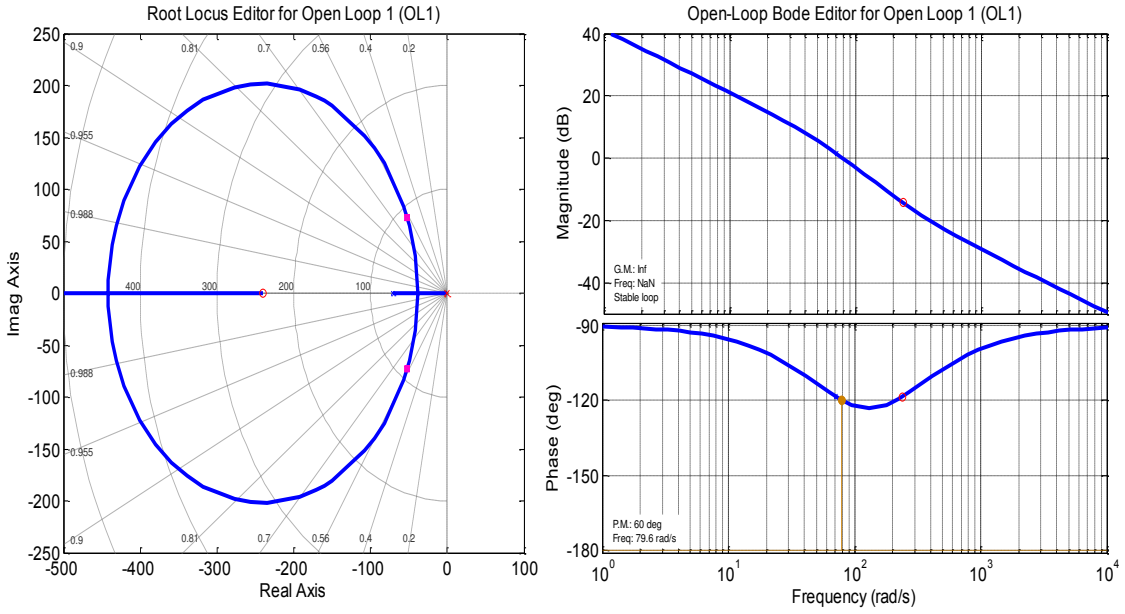

(a)

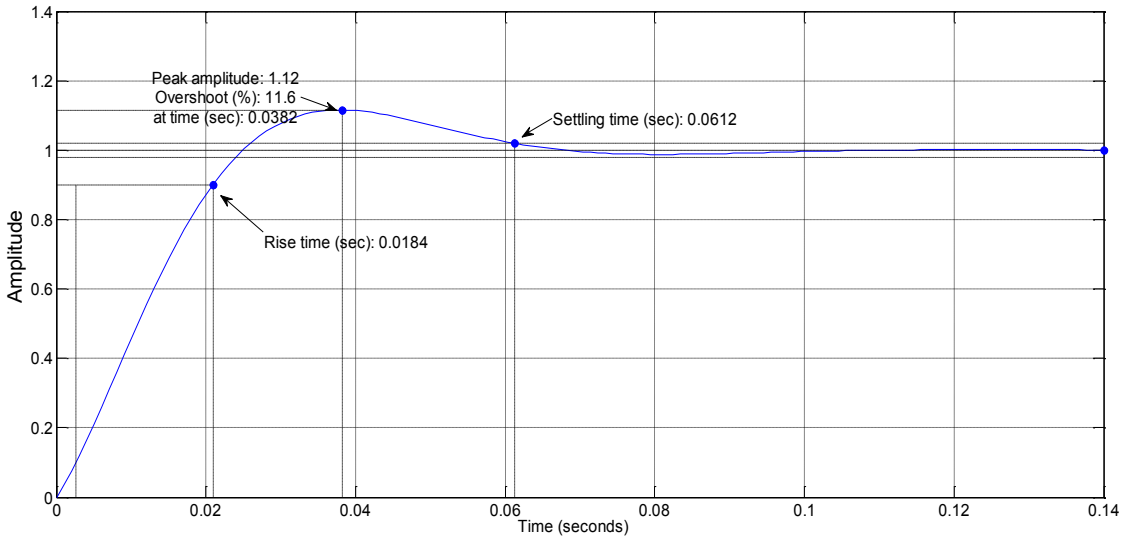

(b)

Figure 3.7: RSC controller tuning of the PI parameters: (a) root locus, open-loop Bode plot; (b) step response.

3-3-2 Vector Control of the Grid Side Converter (GSC)

The grid-side converter, grid side filter, and grid voltage terminal represent the grid-side system as shown in figure 3.8. The grid side converter is characterized as ideal bidirectional switches that convert voltage and currents from DC to AC given that the exchange of power can be conducted in both directions from AC to DC (rectifier mode) and from DC to AC (inverter mode) [7]. The main objective of the grid side filter is to produce a fast-acting response of the current controller of the GSC with the changes in current during a time of milliseconds and to maintain the stability of the controllers output.

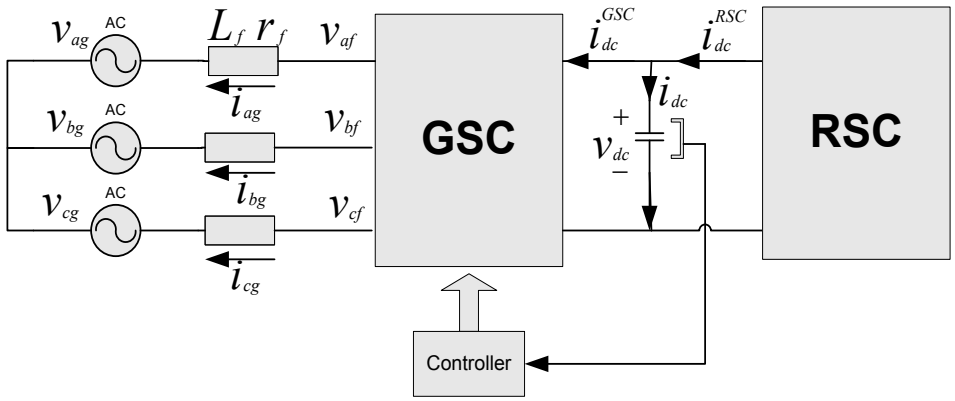

Figure 3.8: The grid-side system.

Modelling of the inductive filter and the grid voltage model in the GSC system is performed using a simple and reliable assumption which adopts an inductive filter and locating an inductance in each phase, as shown in figure 3.9. The grid voltage is modelled as an ideal three-phase balanced voltage. The three-phase system can be modelled as three independent, but equivalent, single-phase systems. Therefore, the balance across the inductor is:

$$\begin{bmatrix} v_{af} \\ v_{bf} \\ v_{cf} \end{bmatrix} - \begin{bmatrix} v_{ag} \\ v_{bg} \\ v_{cg} \end{bmatrix} = r_f \begin{bmatrix} i_{ag} \\ i_{bg} \\ i_{cg} \end{bmatrix} + L_f \frac{d}{dt} \begin{bmatrix} i_{ag} \\ i_{bg} \\ i_{cg} \end{bmatrix} \tag{3.67}$$

Consequently, for modelling purposes, it is necessary to isolate the first derivative of the currents as follows:

$$\frac{d}{dt}\begin{bmatrix} i_{ag} \\ i_{bg} \\ i_{cg} \end{bmatrix} = \frac{1}{L_f}\left(\begin{bmatrix} v_{af} \\ v_{bf} \\ v_{cf} \end{bmatrix} - \begin{bmatrix} v_{ag} \\ v_{bg} \\ v_{cg} \end{bmatrix} - r_f \begin{bmatrix} i_{ag} \\ i_{bg} \\ i_{cg} \end{bmatrix}\right) \tag{3.68}$$

Equation 3.67 can be written in the stationary reference ($\alpha\beta$) frame by transforming the coordination from (abc) to ($\alpha\beta$), which gives:

$$\left.\begin{aligned} v_{\beta f} &= r_f i_{\beta g} + L_f \frac{di_{\beta g}}{dt} + v_{\beta g} \\ v_{\alpha f} &= r_f i_{\alpha g} + L_f \frac{di_{\alpha g}}{dt} + v_{\alpha g} \end{aligned}\right\} \tag{3.69}$$

The cconversion of the coordination of equation 3.69 is performed by multiplying it with the factor $e^{-\theta_e}$, hence:

$$v_{df} = r_f i_{dg} + \frac{di_{dg}}{dt} + v_{dg} - \omega_e L_f i_{qg} \tag{3.70}$$

$$v_{qf} = r_f i_{qg} + \frac{di_{qg}}{dt} + v_{qg} + \omega_e L_f i_{dg} \tag{3.71}$$

The active and reactive power flow between the grid and the grid side converter are expressed as:

$$P_g = \frac{3}{2} Re\{\overline{v_g}.\overline{i_g^*}\} = \frac{3}{2}(v_{dg} i_{dg} + v_{qg} i_{qg}) \tag{3.72}$$

$$Q_g = \frac{3}{2} Im\{\overline{v_g}.\overline{i_g^*}\} = \frac{3}{2}(v_{qg} i_{dg} - v_{dg} i_{qg}) \tag{3.73}$$

For voltage and current coordinate transformations, the angle of the grid voltage is needed. The angular position of the supply voltage is calculated as [22, 127]:

$$\theta_e = \int \omega_e dt = tan^{-1}\left(\frac{v_{\beta g}}{v_{\alpha g}}\right) \tag{3.74}$$

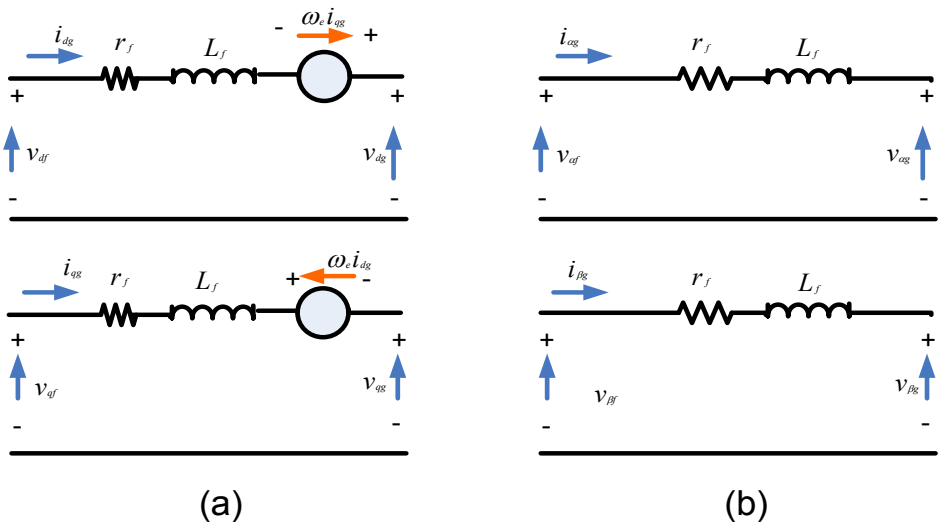

Figure 3.9: Equivalent electric circuit of the GSC system in:
(a) dq coordinates; (b) $\alpha\beta$ coordinates.

In this study, the vector control approach is used in the grid-side converter (GSC) with a reference frame oriented along the grid voltage vector position as shown in figure 3.10 this enables independent control of the active and reactive power flowing between the grid and the GSC. The pulse width modulation (PWM) voltage source converter is a current regulator with d-axis current used to regulate the DC-link voltage and the q-axis current used to control the reactive power.

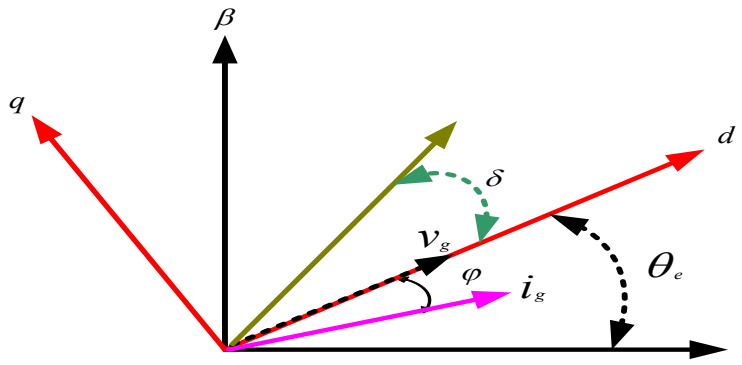

Figure 3.10: Orientation with *d*-axis of the grid voltage space vector in GSC [30].

In the GSC system, the vector control approach is designed with a reference frame oriented along the grid voltage vector ($v_{qg=0}$). Therefore, according the alignment mention above, the system equations will be as follows:

$$v_{df} = r_f i_{dg} + \frac{di_{dg}}{dt} + v_{dg} - \omega_e L_f i_{qg} \tag{3.75}$$

$$v_{qf} = r_f i_{qg} + \frac{di_{qg}}{dt} + \omega_e L_f i_{dg} \tag{3.76}$$

$$P_g = \frac{3(v_{dg} i_{dg})}{2} \tag{3.77}$$

$$Q_g = -\frac{3(v_{dg} i_{qg})}{2} \tag{3.78}$$

By assuming the following terms in equations 3.75 and 3.76:

$$v_{df1} = \left(r_f + L_f \frac{d}{dt}\right) i_{dg} \tag{3.79}$$

$$v_{qf1} = \left(r_f + L_f \frac{d}{dt}\right) i_{qg} \tag{3.80}$$

Equations 3.79 and 3.80 are then converted to the S-plane by taking the Laplace transformation, giving:

$$v_{df1} = (r_f + L_f s) i_{dg} \tag{3.81}$$

$$v_{qf1} = (r_f + L_f s) i_{qg} \tag{3.82}$$

Assume that:

$$i_{dg} = i_{dg0} + \Delta i_{dg} \tag{3.83}$$

$$i_{qg} = i_{qg0} + \Delta i_{qg} \tag{3.84}$$

where i_{dg0} and i_{qg0} are the DC components of i_{dg} and i_{qg} respectively (i.e. i_{dg0}=i_{dg}^{ref}, i_{qg0}=i_{qg}^{ref}). In addition Δi_{dg} and Δi_{qg} are the ripple current components. Then by substituting equations 3.81 and 3.82 in equations 3.83 and 3.84 respectively, and rearranging the equations knowing that $\Delta i_{dg} \ll i_{dg0}$ and $\Delta i_{qg} \ll i_{qg0}$, the transfer function is given from v_{df1} to i_{dg} and v_{qf1} to i_{qg} using the first order transfer function without cross-coupling. Hence the plant model for the current control loops is given by:

$$\frac{i_{dg}}{v_{df1}} = \frac{i_{qg}}{v_{qf1}} = \frac{1}{r_f + L_f s} \tag{3.85}$$

Therefore, it is possible to design a feedback loop and PI controller to generate the reference value of voltage in the current control regulation formula using a PI controller as follows [22, 126]:

$$v_{df1} = \left(k_{p2} + \frac{k_{i2}}{s}\right)\left(i_{dg}^{ref} - i_{dg}\right) \tag{3.86}$$

$$v_{qf1} = \left(k_{p2} + \frac{k_{i2}}{s}\right)\left(i_{qg}^{ref} - i_{qg}\right) \tag{3.87}$$

Substituting equations 3.86 and 3.87 in equations 3.75 and 3.76 respectively gives:

$$v_{df} = \left(k_{p2} + \frac{k_{i2}}{s}\right)\left(i_{dg}^{ref} - i_{dg}\right) + v_{dg} - \omega_e L_f i_{qg} \tag{3.88}$$

$$v_{qf} = \left(k_{p2} + \frac{k_{i2}}{s}\right)\left(i_{qg}^{ref} - i_{qg}\right) + \omega_e L_f i_{dg} \tag{3.89}$$

The transfer function of GSC closed-loop control with the PI controller is given by:

$$\frac{i_{qg}}{i_{qg}^{ref}} = \frac{i_{dg}}{i_{dg}^{ref}} = \frac{\frac{1}{L_f}(s.K_{p3} + K_{i3})}{s^2 + s\frac{(K_{p3} + r_f)}{L_f} + \frac{K_{i3}}{L_f}} \tag{3.90}$$

Therefore, the scheme of the current loop control is shown in figure 3.11. The design of the current controller plant follows directly from equation 3.85, which can be written in the z-domain as:

$$F(z) = \frac{(1-X)r_f}{(z-X)} \tag{3.91}$$

where: $X = e^{-\left(r_f/L_f\right)T_s}$

where (T_s), is the sample time which is equal to 0.5ms. Then equation 3.91 expressed as follows:

$$F(z) = \frac{0.1938}{z-0.737} \tag{3.92}$$

The control of the current in the GSC in the z-domain is shown in figure 3.12 have parameters used in the standard design techniques of the DFIG system may be applied.

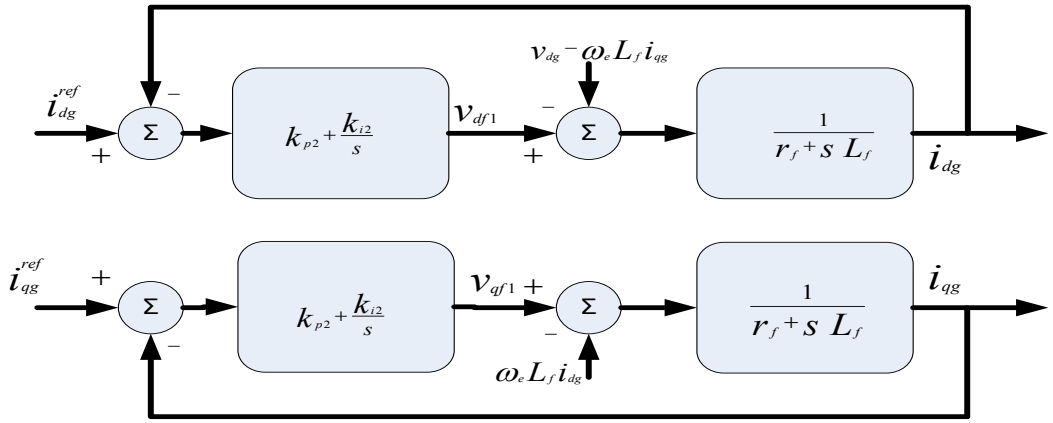

Figure 3.11: Current control loop of the GSC in S-domain [126].

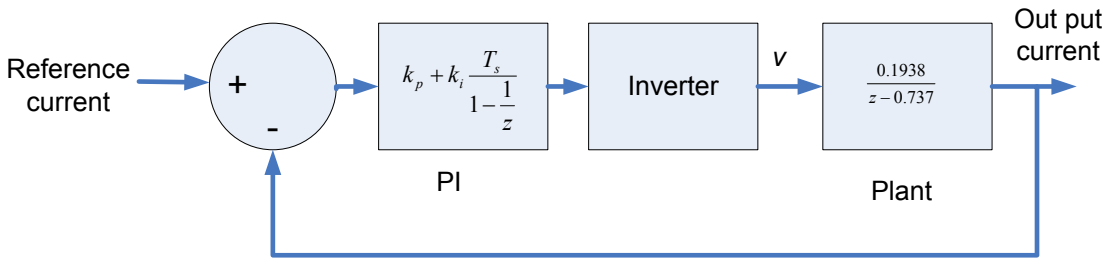

Figure 3.12: The closed loop GSC current-control in z-domain.

The results of the root locus analysis of the inner loop control are shown in figure 3.13 for the *dq*-axis current of the GSC. The poles of the model lies on the-left hand plane (LHP) in the root locus graph thus confirming that the loop control is stable without any oscillation in the frequency response. Hence, there are two closed-loop poles in the

system: the first one has value of pole = -0.283, damping =1 and frequency = 0.823Hz. The second pole has values of = -44.9, damping=1, and frequency = 44.9Hz. In addition, the step response has an overshoot to 1dB at 0.084 sec with, rise time of 0.047sec and settling time of 0.0812sec and with stability margin values of phase margin is 89.6 deg and frequency response of 45.4 rad/sec.

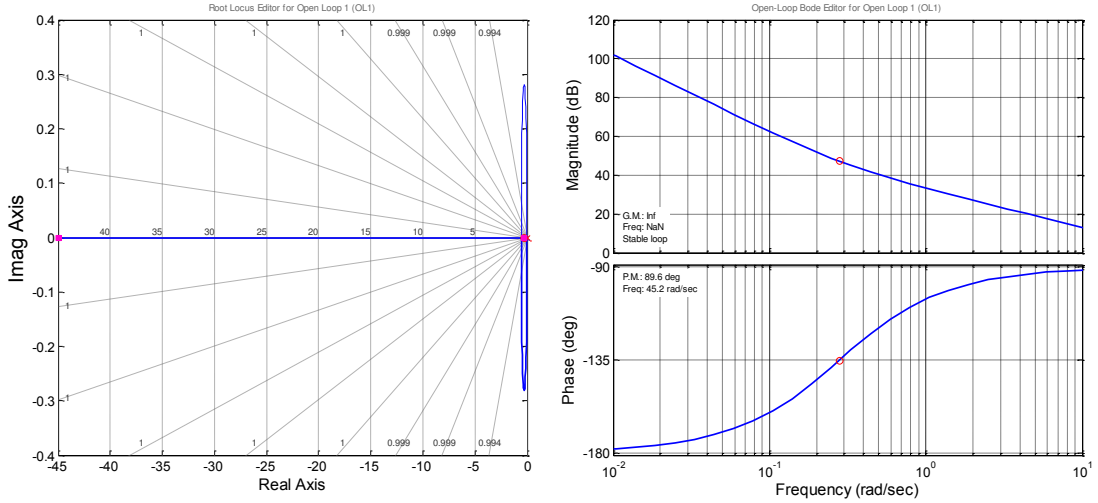

(a)

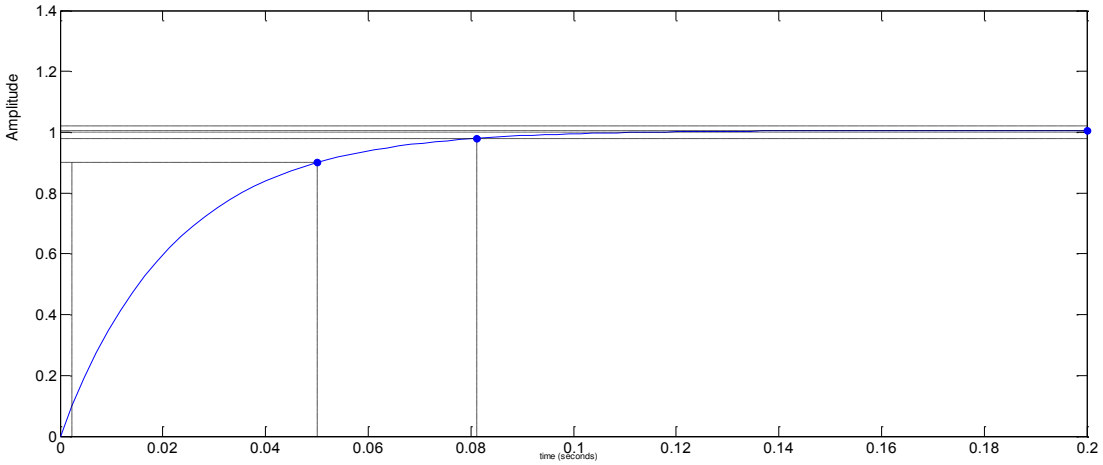

(b)

Figure 3.13: GSC controller tuning the PI parameters: (a) root locus, open loop Bode plot; (b) step response.

3-3-3 Control of the DC-Bus Voltage

The primary objective of the GSC shown in figure 3.14 is to control the value of the DC bus voltage, which the direct current component of the GSC acts on DC-bus voltage. The DC voltage control is adjusted by control of the power exchanged by the converter. An increase or decrease in the DC voltage level is obtained by taking more or less power from the grid with respect to what is required by the DC load, thus varying the value of the reference for the AC inner current control loops. The DC voltage loop is the outer loop and the current control loops are the inner loops in the GSC. These internal loops are implemented so as to achieve short settling times. On the other hand, the main goals of the outer loop are optimum regulation and stability and thus the voltage loop could be designed to be somewhat slower (by 5-20 times). Therefore, the internal and the external loops can be considered to be decoupled [128].

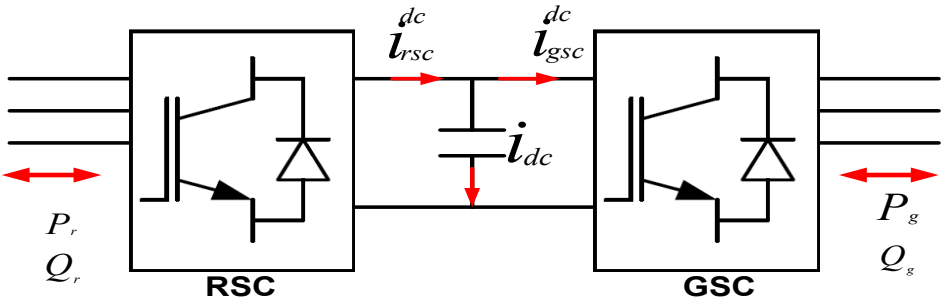

Figure 3.14: Back-to-back power converter [126].

In order to derive the sub-system model of the DC link, the DC bus voltage must be calculated which is dependent on the current flowing through the capacitor as follows:

$$v_{dc} = \frac{1}{C_{dc}} \int i_c \, dt \tag{3.93}$$

The DC voltage control is adjusted by the control of the power exchanged by the converter. The power and current equations of the DC-link are [7, 126, 129]:

$$i_{dc} = C \frac{dv_{dc}}{dt} = i_{dc}^{RSC} - i_{dc}^{GSC} \tag{3.94}$$

$$C.v_{dc}.\frac{dv_{dc}}{dt} = P_{RSC} - P_{GSC} \tag{3.95}$$

Let:

$$v_{dc} = v_{dc0} + \Delta v_{dc} \tag{3.96}$$

where v_{dc0} is the DC component of v_{dc} (i.e. $=v_{dc}^{ref}$), and Δv_{dc} is the ripple component of the DC link voltage. Then by substituting equation 3.95 in equation 3.96 and applying Laplace transformation, the following is given:

$$P_{RSC} - P_{GSC} = C v_{dc0}\, s\, v_{dc} + C\Delta v_{dc}\, s\, v_{dc} \tag{3.97}$$

Since $\Delta v_{dc} \ll v_{dc0}$; therefore, equation 3.97 can be written as follows:

$$\frac{v_{dc(s)}}{P_{GSC}(s)} = \frac{1}{C\, s} \tag{3.98}$$

Because ($P_{GSC} = \frac{3}{2} v_{ds} i_{dg} \approx \frac{3}{2} v_s i_{dg}$) then equation 3.98 then represents the transfer function of the DC bus closed-loop control block diagram shown in figure 3.15:

$$H(s) = \frac{v_{dc(s)}}{i_{dg}(s)} = \frac{\frac{3}{2} v_s}{C\, s} \tag{3.99}$$

Therefore, it is possible to design a feedback loop and PI controller to generate reference value of i_{dg} as follows:

$$i_{dg}^{ref} = C\, s = \left(k_{pdc} + \frac{K_{idc}}{s}\right)\left(v_{dc}^{ref} - v_{dc}\right) \tag{3.100}$$

Then the closed loop transfer function is:

$$\frac{v_{dc}}{v_{dc}^{ref}} = \frac{\frac{1}{C}\left(s.K_{pdc} + K_{idc}\right)}{s^2 + s\frac{K_{pdc}}{C} + \frac{K_{idc}}{C}} \tag{3.101}$$

Similarly, as in the current control plant design, the DC-link plant in the discrete domain characterized by equation 3.99 transformed to the z-domain and substitute sample time equal to 5ms and capacitance value, hence DC-link plant expressed as:

$$H(z) = \frac{0.0136}{z-1} \tag{3.102}$$

The closed-loop block diagram of the DC link is shown in figure 3.16, in which I_{os} is the DC link current of the grid-side converter and m is the modulation index of the PWM. The root locus of the DC-bus control loop is represented in figure 3.17 which shows that the design has a stable loop with following closed loop poles. The first has values of pole= -3.75, damping =1, and frequency=3.75Hz. The second pole is =-42.8, at damping=1, and frequency =42.8 Hz. The step response characteristic are a peak amplitude of 1.05 dB with an overshot of 5.49% at 0.0124 sec, rise time of 0.041 sec, and settling time of 0.148 sec with the value of K in the design equal to 0.61076.

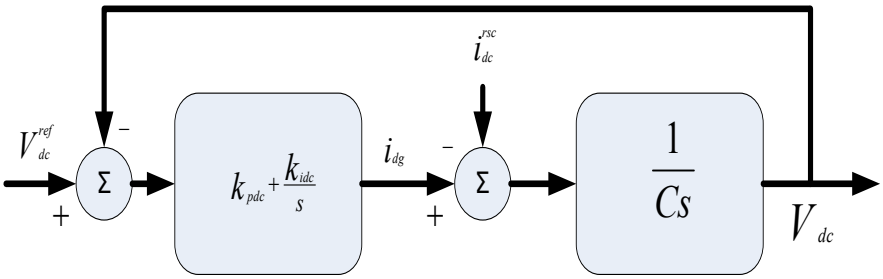

Figure 3.15: DClink loop control of the GSC in S-domain.

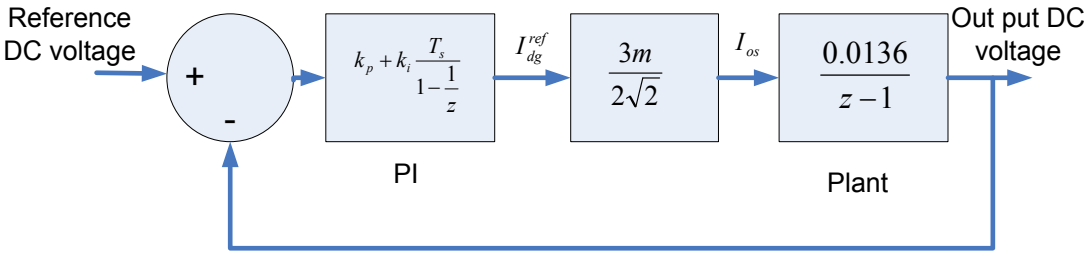

Figure 3.16: The closed loop DC link voltage control in z-domain.

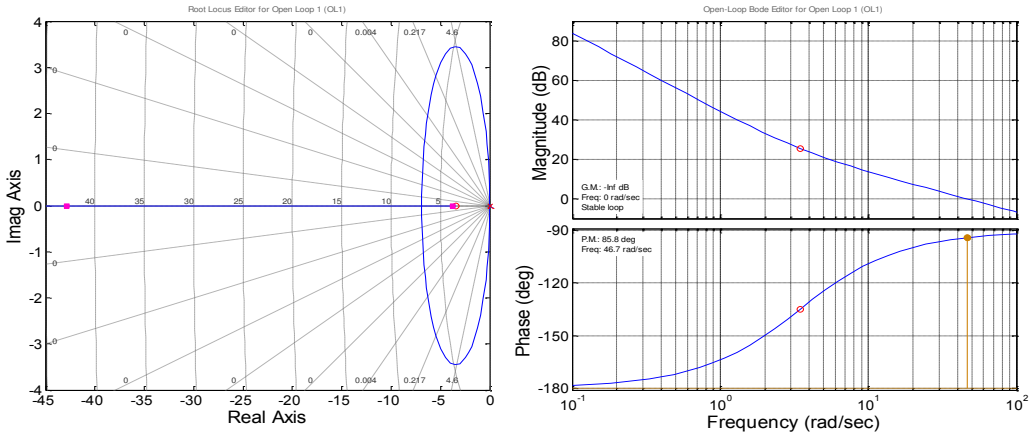

(a)

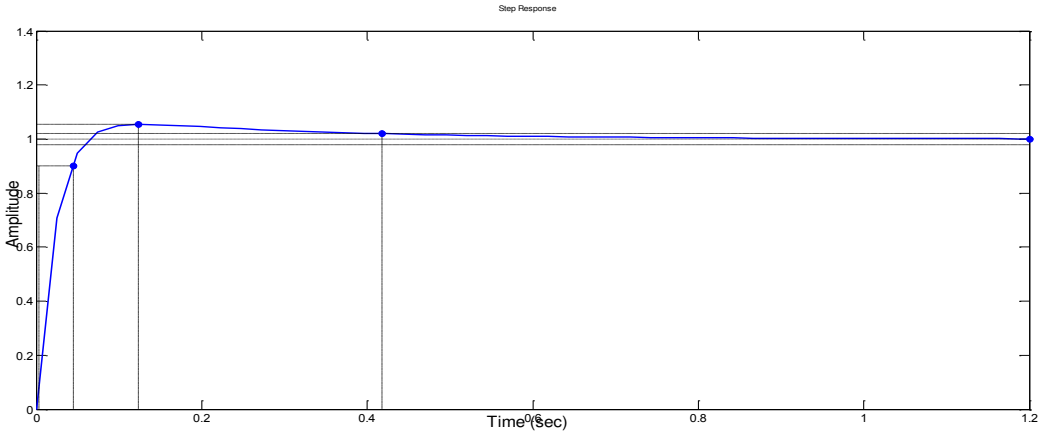

(b)

Figure 3.17: DC-Link controller tuning the PI parameters: (a) root locus, open loop Bode plot; (b) step response

3-4 Drive Train Model

The drive train system could be approximated by a two-mass mechanical spring and damper model connected by a flexible shaft characterized by stiffness and damping coefficients that modeled on the low speed shaft, while the high speed shaft is assumed to be stiff. This gives more accurate responses of the wind turbines during fluctuating wind conditions, as shown in figure 3.18 [130]. This dynamical model is widely accepted as expressing the dynamical behavior of the drive train in this area of research.

The inertia of the low speed shaft comes mainly from the rotating blades and the inertia of the high speed shaft from the generator. The mass of the gearbox itself is insignificant and neglected. Stiffness and damping of the shaft are combined in one equivalent for stiffness and damping placed at the low speed side The aerodynamic torque T_w and the generator reaction torque T_e represent the input quantities for the model while changes in turbine's rotor speed and generator speed are the output. From figure 3.18 the variation in the angular generator speed and angular rotor speed respectively expressed as [38, 126]:

$$T_m - T_e = J_{gen} \frac{d\omega_{gen}}{dt} \tag{3.103}$$

$$T_w - T_{shaft} = J_{rot} \frac{d\omega_{rot}}{dt} \tag{3.104}$$

where:

$$T_m = \frac{T_{shaft}}{K_{gear}}, \quad \text{and} \quad T_{shaft} = K_{shaft}\ \Delta\theta + D_{shaft}\ \Delta\omega \tag{3.105}$$

$$\frac{d\theta_{rot}}{dt} = \omega_{rot} \tag{3.106}$$

$$\frac{d\theta_{gen}}{dt} = \omega_{gen} \tag{3.107}$$

Therefore, after substitution the above equations are simplified to derive the torque equations given by the following:

$$T_w = J_{rot} \frac{d\omega_{rot}}{dt} + K_{shaft}\left(\theta_{rot} - \frac{\theta_{gen}}{K_{gear}}\right) + D_{shaft}\left(\omega_{rot} - \frac{\omega_{gen}}{K_{gear}}\right) \tag{3.108}$$

$$-T_e = J_{gen} \frac{d\omega_{gen}}{dt} - \frac{K_{shaft}}{K_{gear}}\left(\theta_{rot} - \frac{\theta_{gen}}{K_{gear}}\right) - \frac{D_{shaft}}{K_{gear}}\left(\omega_{rot} - \frac{\omega_{gen}}{K_{gear}}\right) \tag{3.109}$$

Equations 3.108 and 3.109 are used to describe the drive train dynamics as follows:

$$\frac{d\omega_{rot}}{dt} = \frac{1}{J_{rot}}\left(T_w - K_{shaft}\left(\theta_{rot} - \frac{\theta_{gen}}{K_{gear}}\right) - D_{shaft}\left(\omega_{rot} - \frac{\omega_{gen}}{K_{gear}}\right)\right) \tag{3.110}$$

$$\frac{d\omega_{gen}}{dt} = \frac{1}{J_{gen}}\left(-T_e + K_{shaft}\left(\theta_{rot} - \frac{\theta_{gen}}{K_{gear}}\right) + D_{shaft}\left(\omega_{rot} - \frac{\omega_{gen}}{K_{gear}}\right)\right) \quad (3.111)$$

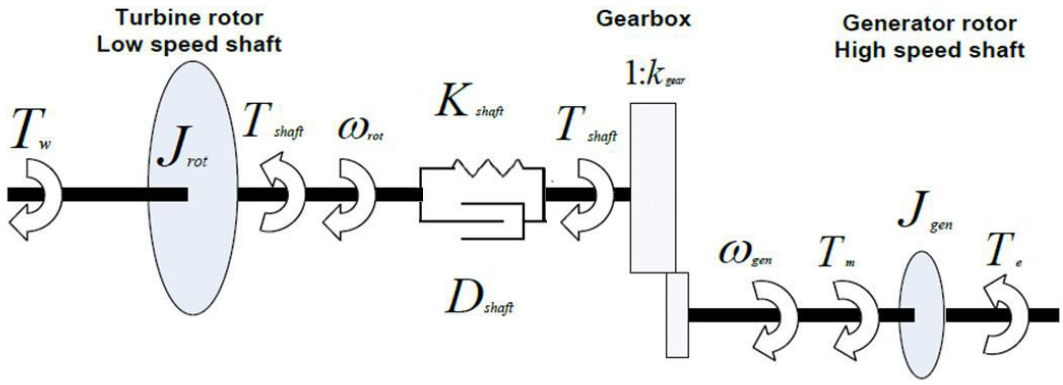

Figure 3.18: Two-mass-model for the drive train [38].

3-5 Wind Turbine Power Characteristics

The wind turbines convert aerodynamic power into electrical energy. In a wind turbine, two conversion processes take place. The first converts the aerodynamic power that is available in the wind into mechanical power. The next process converts the mechanical power into electrical power as in figure 3.19 [130].

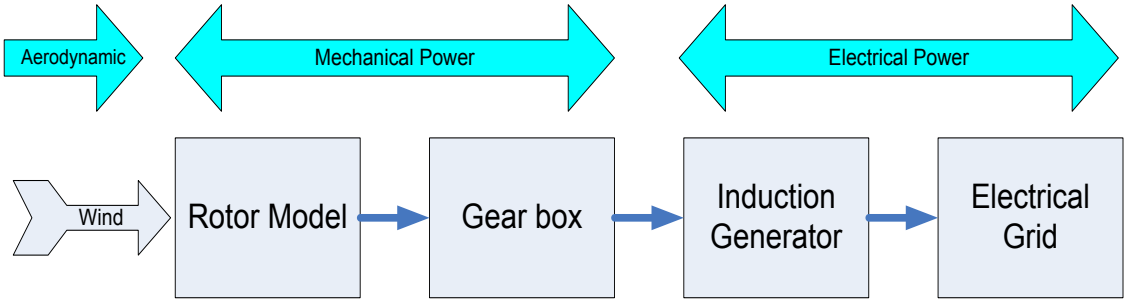

Figure 3.19: Block diagram of wind energy conversion system.

3-5-1 Annual Wind Distribution

Since wind velocities are never the same throughout the year, therefore an important factor that characterizes the output power of a wind turbine is the annual wind speed associated with wind distribution as shown in figure 3.20. The latter can be formed using the statistical concept of the Weibull probability density function [131, 132]:

$$f(v) = (365 * 24)\frac{k}{c}\left(\frac{v}{c}\right)^{k-1} e^{-\left(\frac{v}{c}\right)^{k}} \quad (3.112)$$

where v is the wind speed range where the wind distribution is evaluated, and c and k are parameters of the distribution. These values are taken from the classification given by the International Electro-technical Commission (IEC). The average wind speed can be obtained as follows:

$$v_{avr} = \int_0^{\infty} v.f(v).dv \quad (3.113)$$

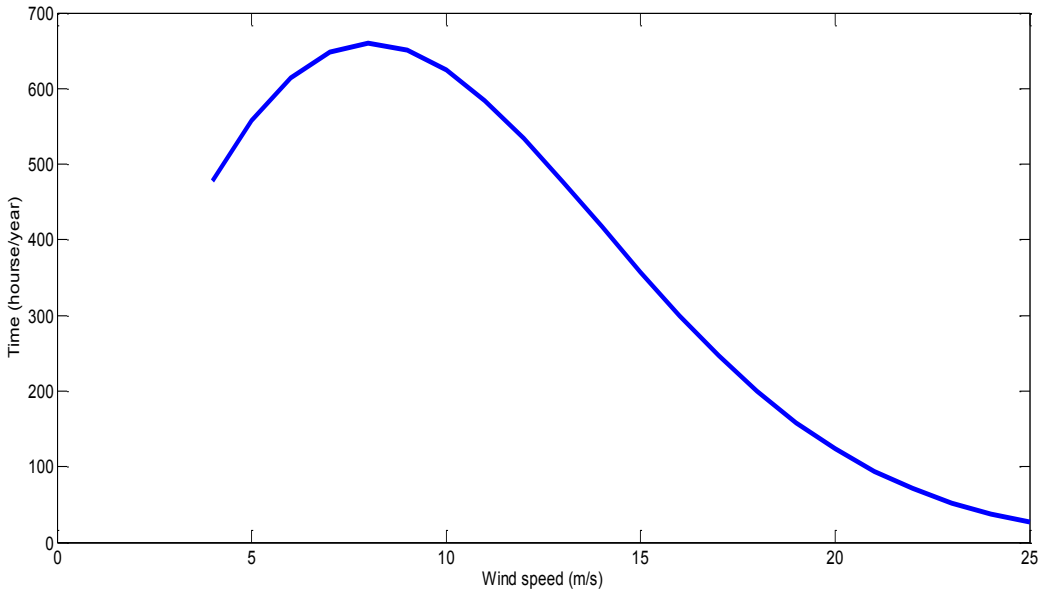

Figure 3.20: Annual wind distribution (c=11.38, k =2) [Appendix E-3].

3-5-2 Aerodynamic Characteristics of the Wind Turbine

Wind turbines convert the kinetic energy present in the wind into mechanical energy by means of producing torque. Since the energy contained by the wind is in the form of kinetic energy, its magnitude depends on the air density and the wind velocity. The wind power developed by the turbine is given by the following equation [130]:

$$P_{air} = \frac{1}{2}\pi\rho R^2 v^3 \quad (3.114)$$

It is not possible to extract all of the kinetic energy of the wind, since this would mean that the air would be standing still directly behind the wind turbine [86]. Therefore, the power captured from the wind turbine is obtained as follows [98, 124]:

$$P_w = \frac{1}{2}C_p(\lambda,\beta)\pi\rho R^2 v^3 \quad (3.115)$$

The power coefficient (C_p) gives the fraction of the kinetic energy that is converted

into mechanical energy by the wind turbine, while the air density (ρ) depends on factors such as plane altitude and air temperature and may vary between 1.07 kg/m^3 in hot and high altitude region to 1.395 kg/m^3 in cold and low-lying regions. The power coefficient is the ratio between the power extracted by turbine relative to the variable wind power and is a function of tip speed ratio (TSR) and the blade pitch angle which is the angle between the chord of the aerofoil section and the plane of rotation and is also called the setting angle. Broadly, different mathematical formulae have been used in previous studies to calculate the power coefficient and one of these is shown below [86, 132, 133]:

$$C_p(\lambda, \beta) = 0.73\left(\frac{151}{\lambda_i} - 0.58\beta - 0.002\beta^{2.14} - 13.2\right)e^{-\frac{18.4}{\lambda_i}} \tag{3.116}$$

where:

$$\lambda_i = \frac{1}{\left(\frac{1}{\lambda - 0.02\beta} - \frac{0.003}{1+\beta^3}\right)} \tag{3.117}$$

Theoretically the maximum achievable power factor coefficient is 59.26% (Betz limit) while in practice it can reach to 45% which is below the theoretical limit due to inefficiencies and losses related to different configurations of airfoil profile, rotor tip end losses, whirlpool losses and rotor blade number losses as shown in the typical characteristic of the power coefficient with respect to the tip speed ratio (TSR λ) and blade pitch control in figure 3.21 [134].

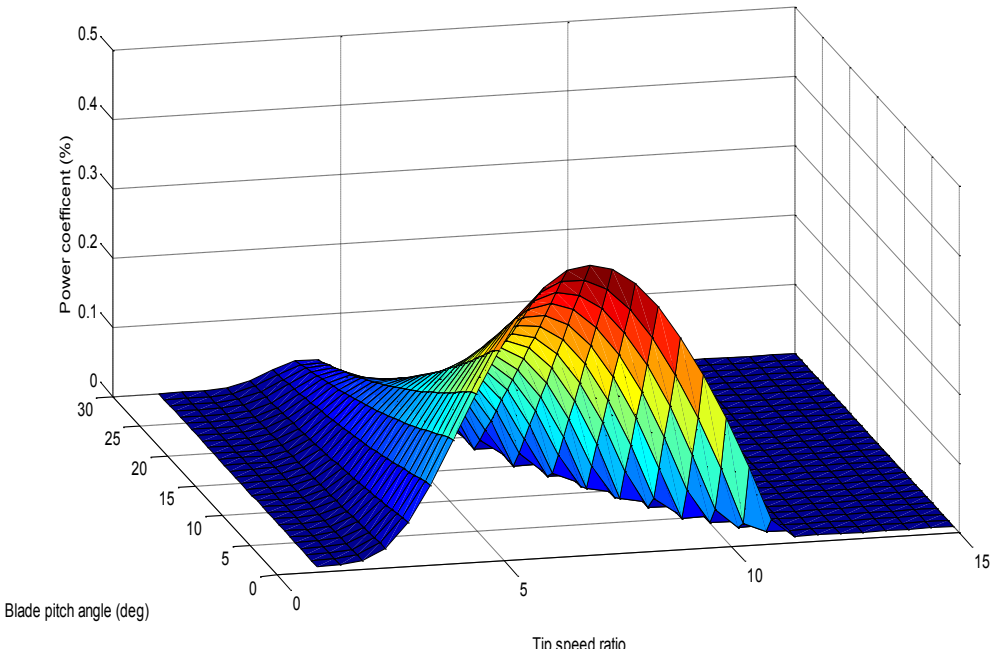

Figure 3.21: Power coefficient curve verses tip speed ratio and pitch blade angle [see Appendix E-2].

3-5-3 Tip Speed Ratio (TSR) of the Wind Turbine

The relationship between the wind speed and the rate of rotation of the rotor is non-dimensional factor named the tip speed ratio (TSR) which is described as follows [132]:

$$\lambda = \frac{R\,\omega_{rot}}{v} \tag{3.118}$$

The number of rotor blades n_b of the wind turbine is proportional to the optimal tip speed ratio, which is approximated empirically determined as follows [134]:

$$\lambda_{opt} \approx \frac{4\pi}{n_b} \tag{3.119}$$

It is clear from equation 3.115 that the maximum available power from the wind occurs with adjusting the power coefficient which is a function of the λ. Hence, from the curves shown in figures 3.22, explain that the maximum efficiency can be achieved at all wind velocities with the optimal tip speed ratio. It is desirable to adapt the rotational angular shaft speed with varying values of wind velocity to keep tip speed ratio satisfy the optimal value associated with the maximum power capture.

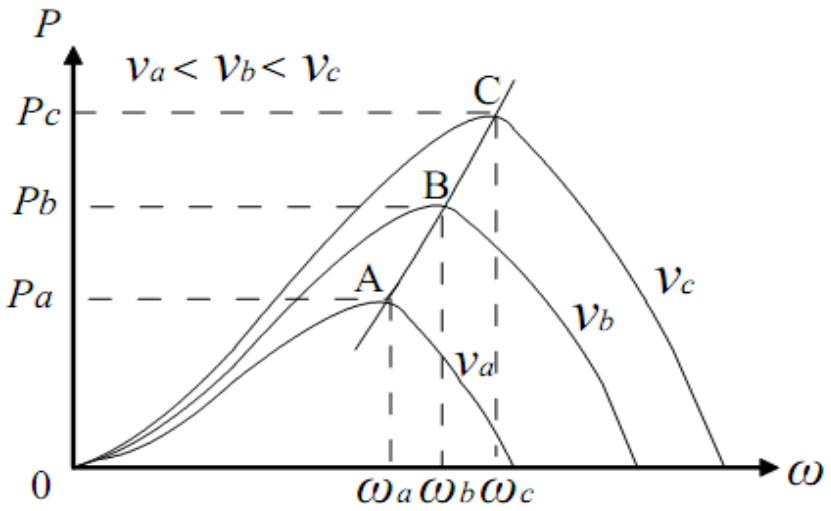

Figure 3.22: Power characteristics of wind turbine verses rotational speed [134].

For each wind turbine, its $(C_p - \lambda - \beta)$ curves depend on the design of the blade as shown in the 3-D curve in figure 3.21. At any specific wind speed, there is a unique rotational speed of the wind turbine that satisfies the maximum power coefficient $(C_{p\,max})$ associated with maximum mechanical power which can be expressed as:

$$P_{w\,max} = \frac{1}{2} C_{p\,max} \pi \rho \frac{R^5}{\lambda_{opt}} {\omega_{rot}}^3 \tag{3.120}$$

Thus the maximum mechanical power that can be extracted from wind is proportional to the cube of the rotor speed, as follows [7]:

$$P_{w\,max} \propto {\omega_{rot}}^3 \tag{3.121}$$

If the wind speed is below the rated value, the pitch angle is deactivated (β is fixed) while the wind turbine operates in variable speed mode with rotational speed adjust by DFIG speed control or active power control. On the other hand when the wind speed is increased above the rated value, at this condition the pitch angle control is activated with an increase in β to reduce the mechanical power extracted from the wind [135].

3-6 Test System

The simulation configuration was set up to execute a variable-step solution using an ode45s (dormand-prince) type solver, with a relative tolerance of 0.001. The solver was chosen to best deal with the combination of discrete and non-discrete variables in conjunction with the moderately stiff problem of grid fault application.

A screen-shoot for the DFIG system in the simulink model is shown in figure 3.23. This includes: the generator, a bidirectional power electronic converter, a digital controller with cascaded feedback control schemes, crowbar, a two-mass drive-shaft model to represent the wind turbine mechanical dynamics, a simplified wind turbine controller and a simplified network model. The wind turbine in this study is on 1.5MW, with a horizontal axis, and three-bladed with blad radius 35.25 m, upwind wind turbine with pitch control. A two-pair pole DFIG using back-to-back PWM voltage source converters in the rotor winding circuit, is adopted in the wind turbine with carrier frequency of 5 KHz and average voltage 398.74 V, and 0.9 is the value of the setting factor which calculated from the equation (setting factor = $\frac{Nominal\ \ voltage\ value \times \sqrt{2}}{Average\ voltage\ vlaue}$).

The parameters used in the DFIG based wind turbine model are close to that of a commercial wind turbine as illustrated in appendix A.

The rotor-circuit crowbar model is connected by the rotor winding of the DFIG. When activated, the DFIG rotor voltage was rendered zero, since its short circuit the rotor winding to isolate the RSC. When disengaged, the crowbar had no effect on the rotor

circuit and the RSC voltage was passed unchanged to the rotor of the DFIG. In the simulation assume an infinitely stiff grid is assumed which entails an ideal voltage source. Specific voltage dips or swells can be applied to the DFIG system with specific period time during system operation. The modelled voltages were applied directly to the stator connection of the DFIG model.

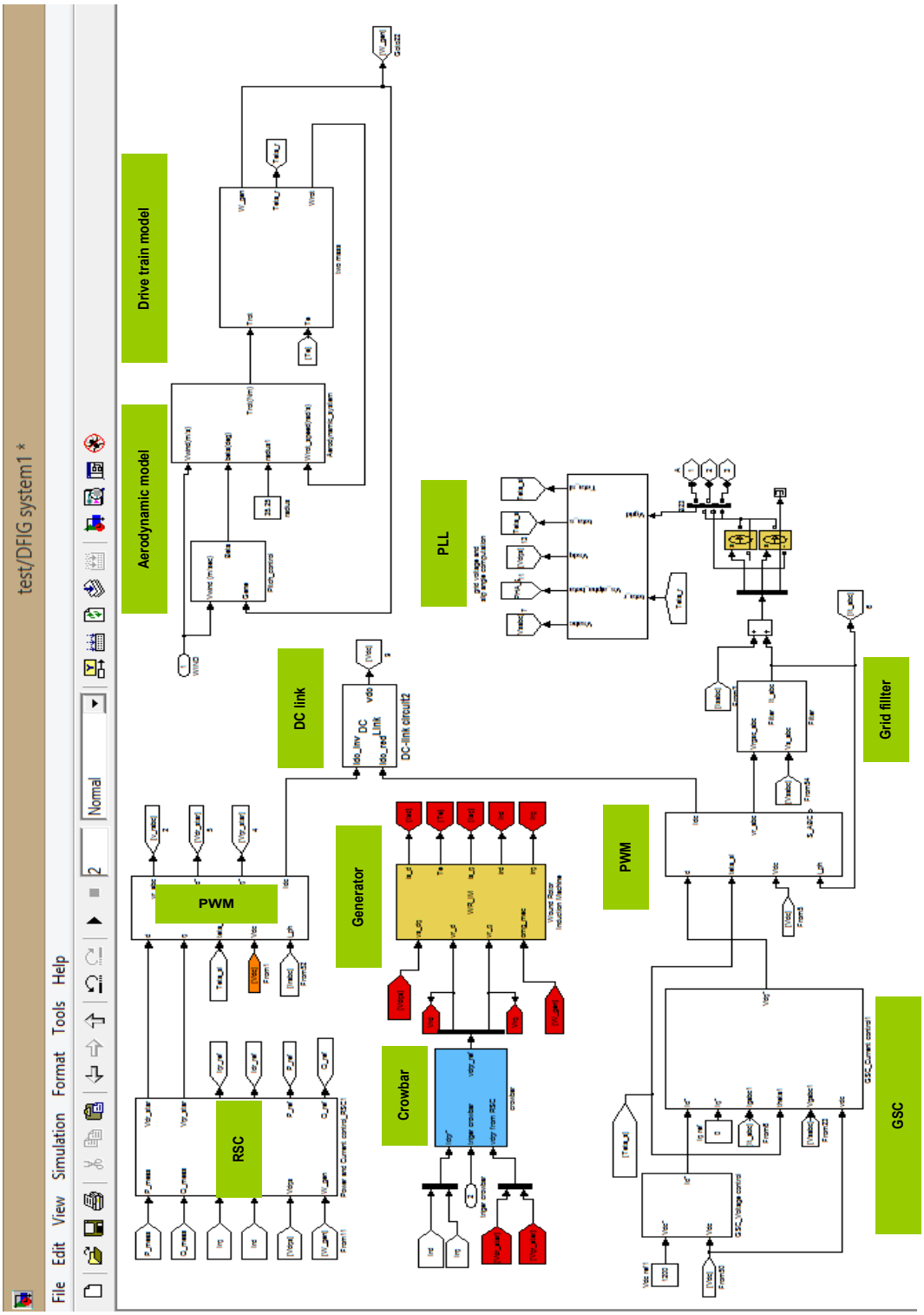

Figure 3.23: Screen-shot of the DFIG system in the MATLAB/SIMULINK® model.

3-7 Phase Locked Loop (PLL) System Performance

Phase locked loop (PLL) performance testing is essential to demonstrate the ability of the PLL in the DFIG-based wind turbine system to track changes in grid frequency in different operation conditions. Figure 3.24 shows the response of the PLL after a 40Hz step frequency reduction during period 0.5-0.6 seconds in the stator voltage signal. In this case, the output angle is shown that the PLL ideally fast control to return tracking the desired angle after the frequency variation end. It is noted that the system behaved as a nearly linear system for solely frequency inputs, and also it can be illustrate the response of the PLL output with higher frequency input produces transients of a similar shape to this changes. As shown in figure 3.25 when the frequency of the grid increase to 40Hz, the measured values of the angle is effected and tracking ability is lost during this scenario.

The PLL responses were also investigated in condition where the input voltage to the DFIG is polluted with harmonics. These harmonics are produced using MATLAB/SIMULINK® programmable voltage source during 100ms. If the input voltages have harmonics, the PLL responses might be influenced in terms of transient performance or steady-state error and the output signal of the PLL may include an undesirably high harmonics level. The PLL system is investigated here with the injection two harmonics components superimposed on the fundamental components during the no fault condition in order to show the system robustness. Figure 3.26 illustrates the PLL responses for voltage depression with an input voltage containing 3^{rd} order harmonic parasitic with the 2^{nd} order. It can be concluded from figure 3.26 that the responses are only slightly influence if input harmonics are present. The PLL has a reasonable error output to track the desired angle which is also observed in the second scenario as shown in figure 3.27 when 3^{rd} order and 7^{th} order harmonic were injected. These results highlighted to less reversible effects with this harmonics which will produce a DC error signal and this will induce a steady-state error in the voltage controller and also in the phase angle controller.

It is desirable that a PLL has the ability to follow phase angle and frequency during periods of voltage sags and harmonics and to exhibit a fast response during the fault recovery stage transient which would demonstrate the PLL's robustness. Figure 3.28 shows the results when PLL was tested with reduced voltage conditions. As the voltage

was reduced to 0.2pu for 100ms between 0.5-0.6 sec and harmonics components 3rd and 7th were injected, the PLL was able to track the desired angle in less than 5ms.

Figure 3.29 shows the responses with a 40% voltage swell for 100ms with 3rd and 2nd harmonic components superimposed with the fundamental voltage signal. Figure 3.30 shows the PLL system test for simultaneous application of the DFIG when a severe single phase fault subjected with inject 3rd and 2nd harmonics components. It is seen that the PLL system is able to follow the reference signal even there is drift error during the fault and it took 20ms after fault clearance to return to tracking the angle correctly. It is concluded that the results for the PLL are acceptable in the DFIG-based wind turbine system application in this study. In addition, it is clear that this PLL is robust and has the ability to track the desired values during different operating conditions of harmonics, voltage sag, and voltage swell.

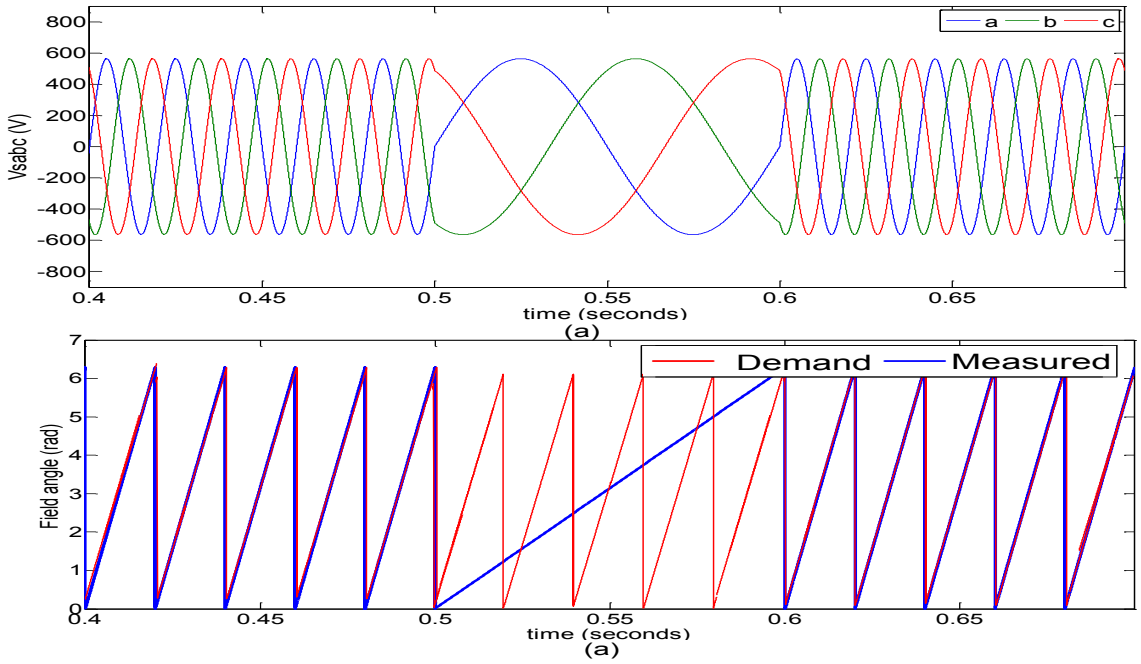

Figure 3.24: Instantaneous measurements of (a) grid voltage and (b) PLL response after 40Hz frequency step change.

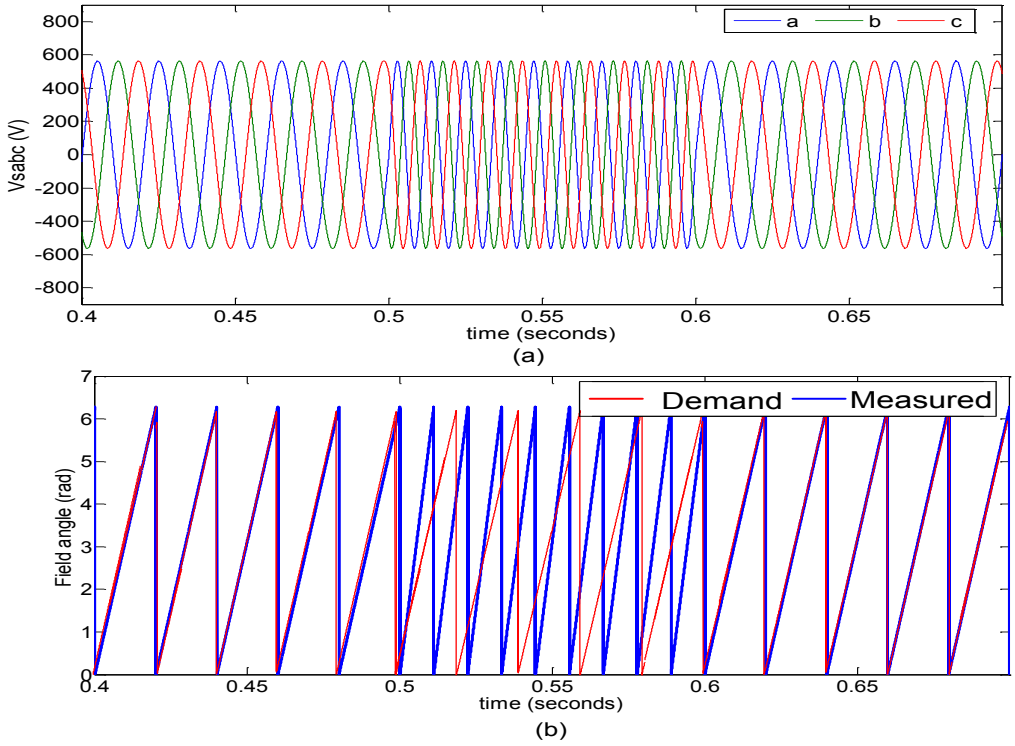

Figure 3.25: Instantaneous measurements of: (a) grid voltage and (b) PLL response after +40 Hz frequency step change.

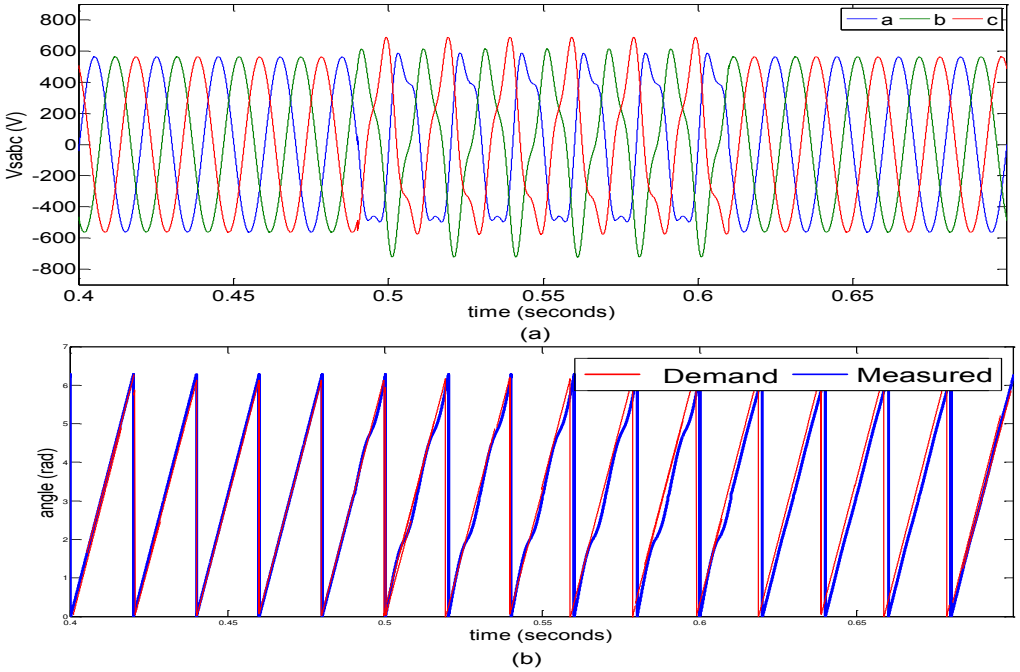

Figure 3.26: Instantaneous measurements of: (a) grid voltage; (b) PLL response during 3rd order harmonic (+*ve* sequence, 20% amplitude, and -25degree phase angle step) parasitic with the 2nd order harmonic (+*ve* sequence, 10% amplitude, and 0 degree phase angle step).

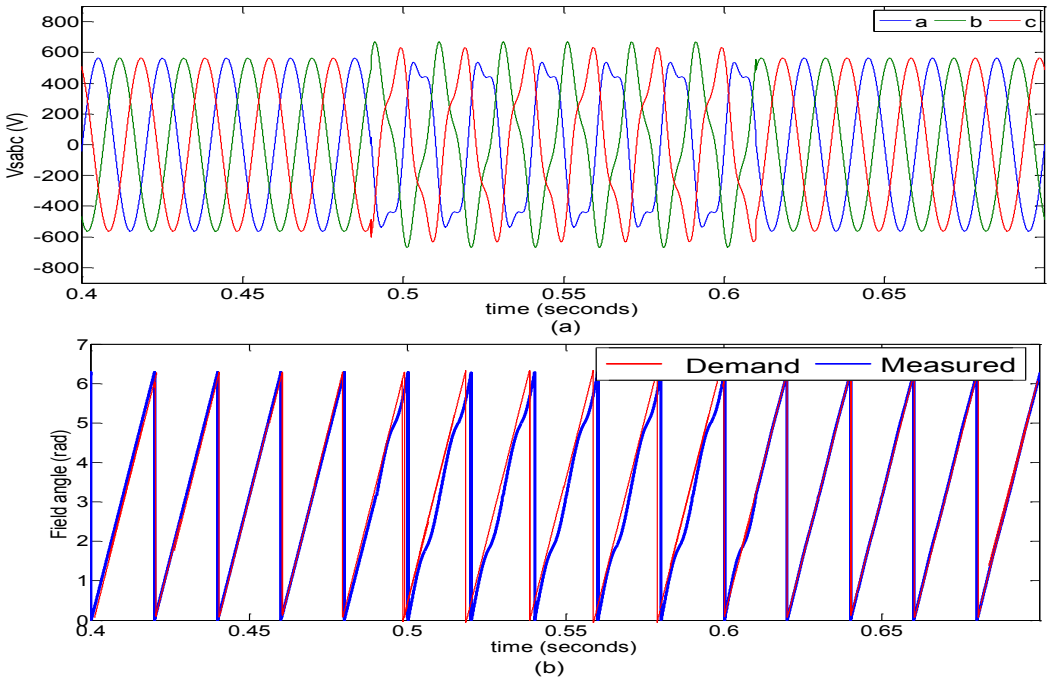

Figure 3.27: Instantaneous measurements of: (a) grid voltage and; (b) PLL response during 3rd order harmonic (+*ve* sequence, 20% amplitude, and -25degree phase angle step) and; 7th order harmonic (+*ve* sequence, 2% amplitude, and 0 degree phase angle step).

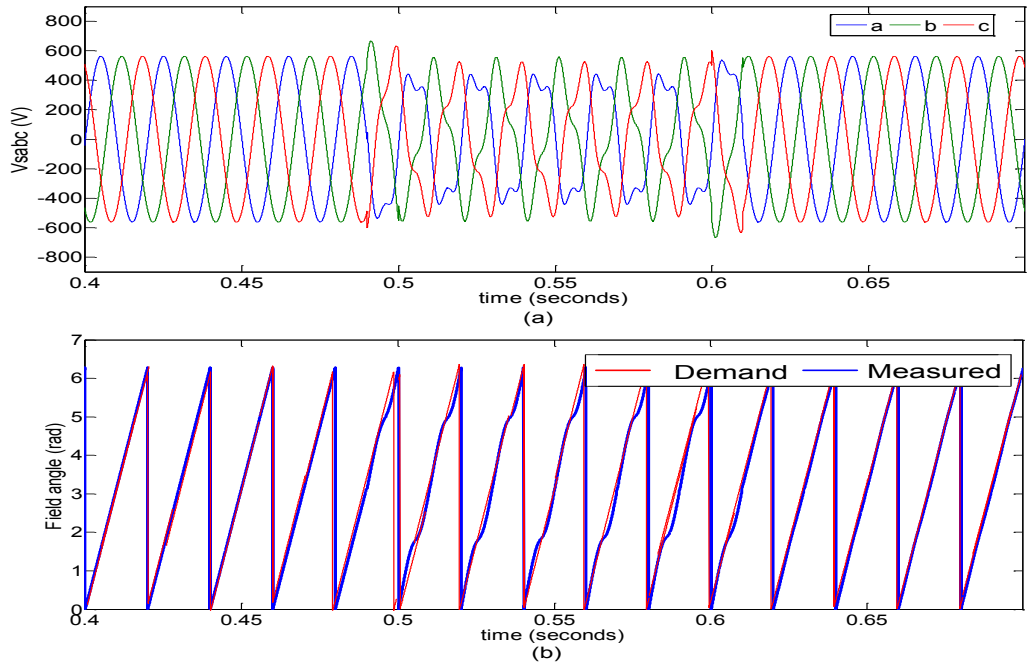

Figure 3.28: Instantaneous measurements of: (a) grid voltage; (b) PLL response during 80% voltage dip, having harmonics (3rd (+ve sequence, 20% amplitude, and -25degree phase angle step) and 7th (+ve sequence, 2% amplitude and 0 degree phase angle step)).

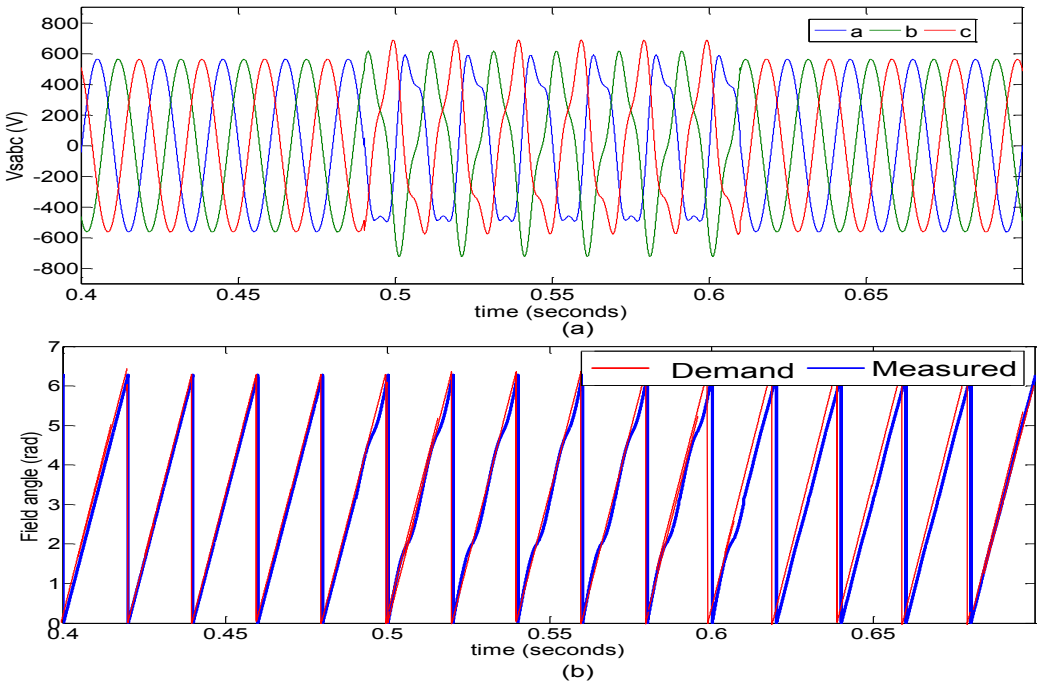

Figure 3.29: Instantaneous measurements of: (a) grid voltage; (b) PLL response during 40% voltage swell, having harmonics (3rd (+ve sequence, 20% amplitude, and 25 degree phase angle step) and 2nd order harmonic (+ve sequence, 10% amplitude, and 0 degree phase angle step)).

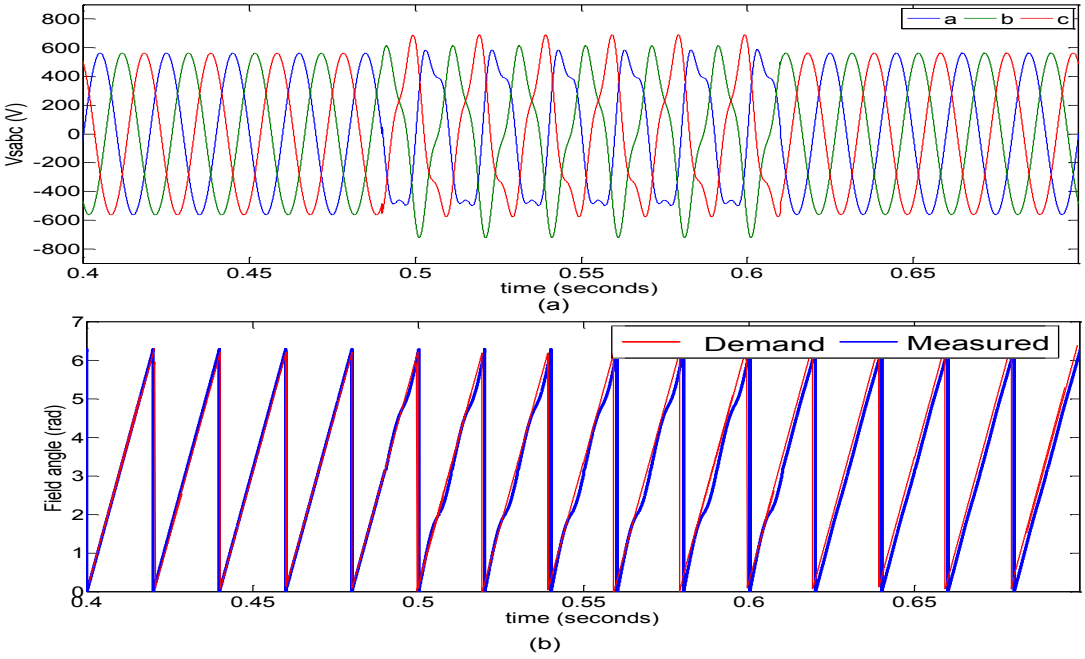

Figure 3.30: Instantaneous measurements of (a) grid voltage and (b) PLL response single phase fault, having harmonics (3rd (+ve sequence, 20% amplitude, and -25 degree phase angle step) and 2nd order harmonic (+ve sequence, 10% amplitude, and 0 degree phase angle step)).

3-8 DFIG System Model Confirmation

The objective of this section is to confirm the model of the doubly fed induction generator (DFIG)-based wind turbine in this study using MATLAB/ SIMULINK®. This process of double checking is conducted by comparing the performance of DFIG against the base model in the PLECS® platform. The DFIG model in PLECS® is built and already exists in standalone simulation platform.

There are several different simulation software products available for electrical system and power production simulations. Some of these simulation tools have similar qualities and were developed and delivered by different companies, but on the other hand, different software packages may have different levels of modeling and simulation precision, and may serve different purposes. PLECS® (Piecewise Linear Electrical Circuit Simulation) is a Simulink toolbox developed by PLEXIM for system-level simulations of electrical circuits [136]. It is especially designed for power electronics but it can be used for any electrical network. The SIMULINK model is ideally suited for the simulation of control system. Therefore, SIMULINK is also a convenient tool for the design of closed loop controlled electrical systems. PLECS® enhances Simulink with the capability to simulate electrical circuits directly. There is also a standalone version of PLECS® that allows the simulation of electrical circuits and control systems directly within the PLECS® package. The complete PLECS® schematic of the DFIG plant that employed in model confirmation is shown in Figure 3.31. The system components are available in platform's library for different physical domains, including electrical, magnetic, mechanical, and control systems. The electrical and mechanical parameters of the DFIG are listed in table 3.2 where the rotor parameters have been converted to the stator-side using the turn's ratio. To evaluate and compare the proposed model of DFIG-based wind turbine theoretically, several measurements have been implemented to the system during normal operating conditions with the MATLAB® and PLECS® simulation platforms. The purpose of double checked between these two SIMULINKs are to assess the provided example/default parameters, parameterized generic model operation/response in behavior comparison and to evaluate in which level of complexity specific wind turbines are necessary to be modelled for certain simulation purposes, e.g. what kind of influence this would have in the overall wind turbine model accuracy under different simulation circumstances.

Table 3.2: Electrical and mechanical parameters of the doubly-fed induction machine used in the PLECS platform [136].

The electrical parameters

Pole pairs n_p	2
Turns ratio n_s/n_r	1/2.6
Stator leakage $L_{s\sigma}$	0.12 mH
Rotor leakage $L'_{r\sigma}$	0.05 mH
Main inductance L_m	2.9 mH
Stator resistance R_s	0.022 Ω
Rotor resistance R'_r	0.0018 Ω

The mechanical parameters

Rotor inertia	75 kgm^2
Gearbox inertia	4.26×10^5 kgm^2
Hub inertia	6.03×10^4 kgm^2
Blade inertia	1.13×10^6 kgm^2
Rotor friction	0.81 Nms/rad
Gearbox friction	1.78×10^4 Nms/rad
Hub friction	8.11×10^3 Nms/rad
Blade friction	1.08×10^3 Nms/rad
Gearbox to rotor stiffness	4.67×10^7 Nms/rad
Hub to gearbox stiffness	1.39×10^1 Nms/rad
Blade to hub rotor stiffness	1.07×10^1 Nms/rad
Gearbox to rotor damping	0.81×10^3 Nms/rad
Hub to gearbox damping	2.84×10^6 Nms/rad
Blade to hub rotor damping	3.24×10^6 Nms/rad

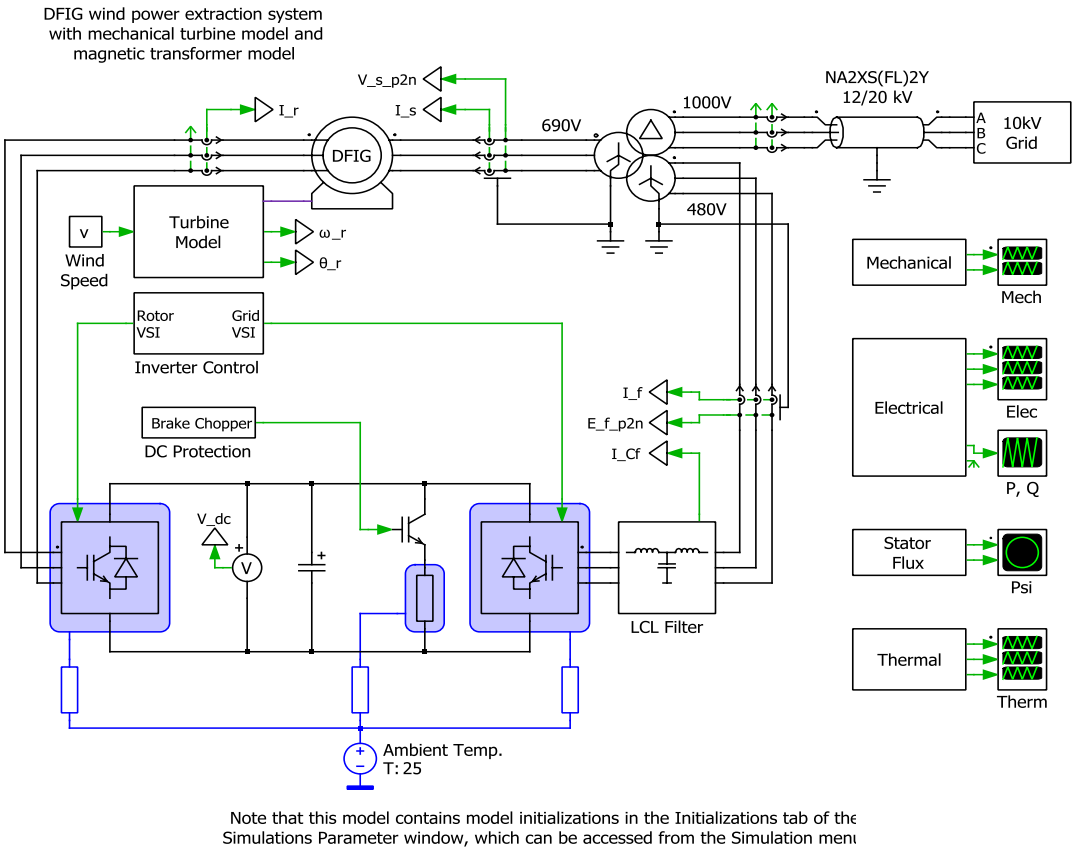

Figure 3.31: The DFIG wind turbine model test system in PLECS®.

By running the two models of the DFIG based wind turbine in MATLAB® and PLECS®) at a constant wind speed of 5 m/sec by fixed the outer loop control of the rotor-side converter in normal grid condition during 2 seconds. It will easy to illustrate that DC-link regulator has good agreement results when compared the PLECS® with

the MATLAB®. The ability to tracking the reference signal is shown in figure 3.32. Figure 3.33 presents the behaviour of the inner loop control of the rotor-side converter of the DFIG system in terms of direct and quadrture component. Figure 3.33a shows that the direct current component have fast and closely regulate around the set value in MATLAB® than PLECS®. On the other hand the q- component of rotor current in PLECS® shows better of tracking the reference value than MATLAB® as shown in figure 3.33-b. The generator's speed in DFIG MATLAB® model has acceptable outcomes which approximately match the measurements in the PLECS® model as shown in figure 3.34a. It can be observed in figure 3.34b that the stator reactive power regulation exhibits more linear behaviour in MATLAB® when compared with the PLECS® system and its tracking around the setting values. It can be concluded from the comparison results that the control concepts implemented for normal operation is as expected in the MATLAB® model. The simulation measurements for the DFIG wind turbine model in MATLAB® and PLECS® show good agreement. In addition, it be noticed that the results for PLECS® have less oscillation because in the demo model the designer used filter for the stator current, rotor current and stator voltage as shown in figure 3.35 to eliminate parasitic harmonic components.

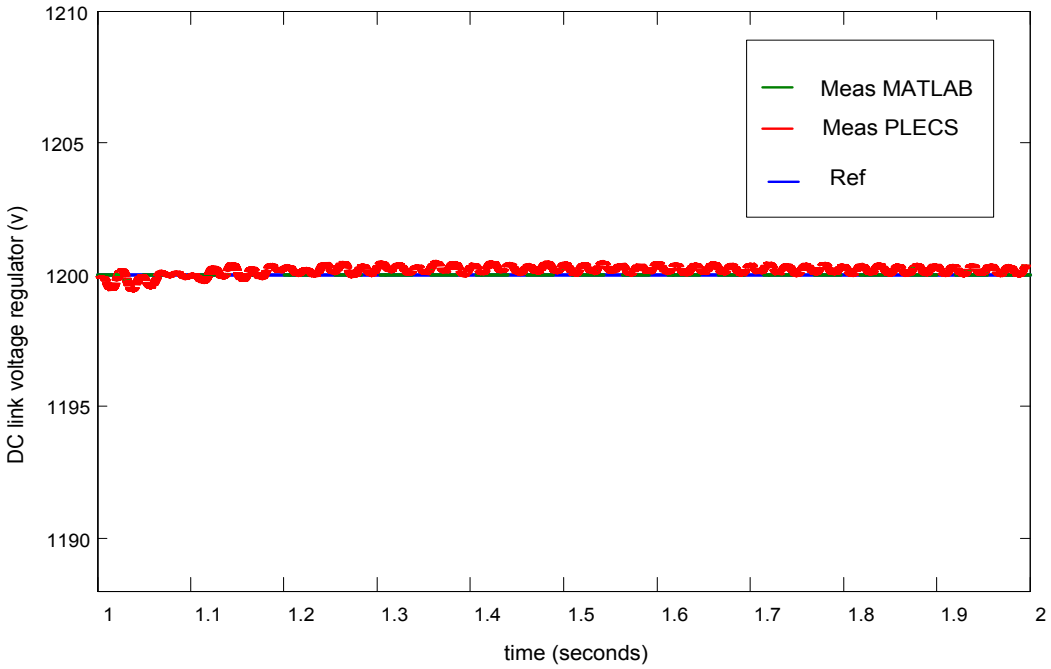

Figure 3.32: Instantaneous comparison measurements of DC link voltage regulator in MATLAB® and PLECS®.

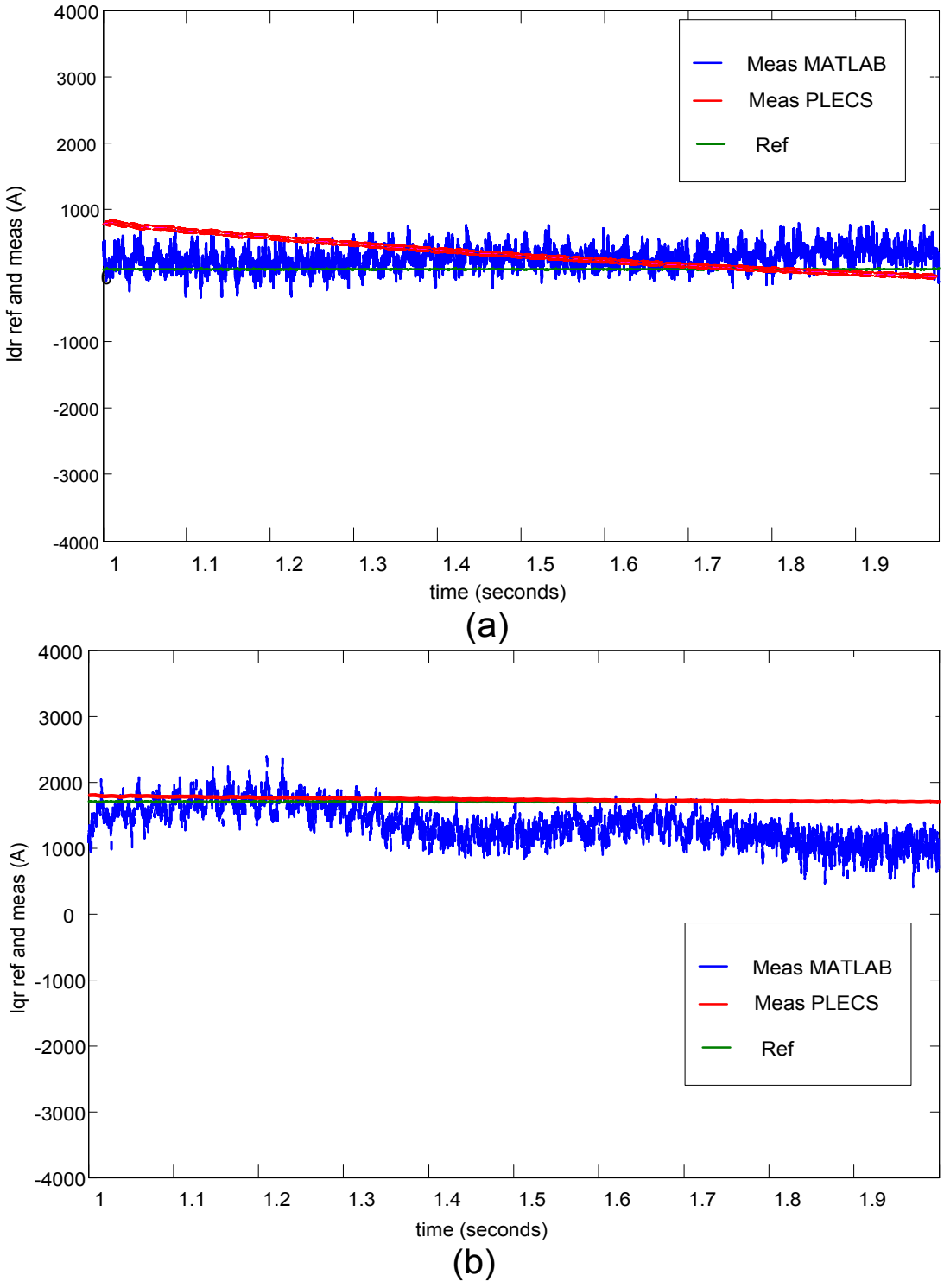

Figure 3.33: Instantaneous measurements of: (a) d-component rotor current in controller MATLAB® and PLECS®; (b) q-component rotor current controller in MATLAB® and PLECS®

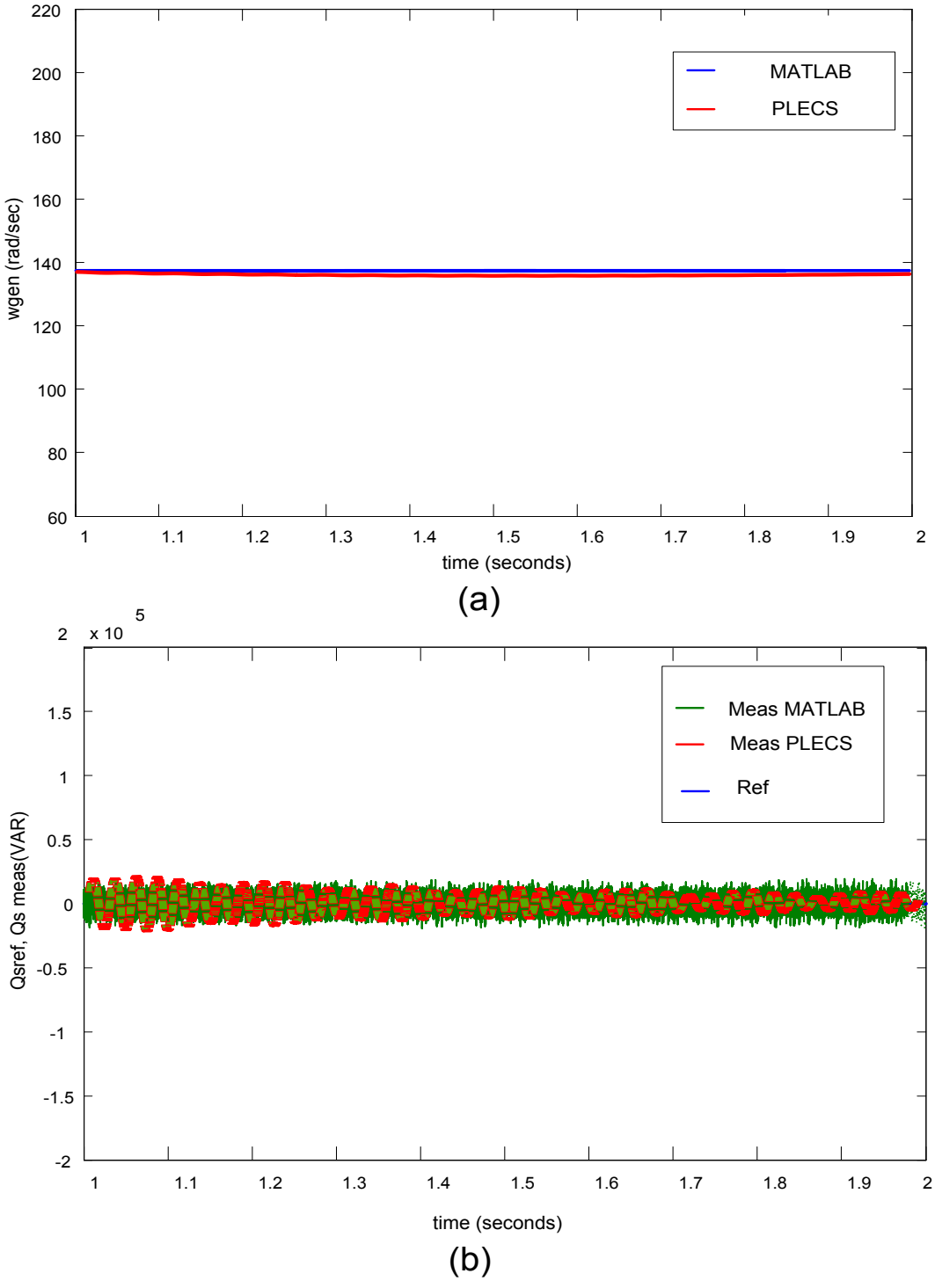

Figure 3.34: Instantaneous measurements of: (a) Generator speed in MATLAB® and PLECS®; (b) Reactive power control in MATLAB® and PLECS®.

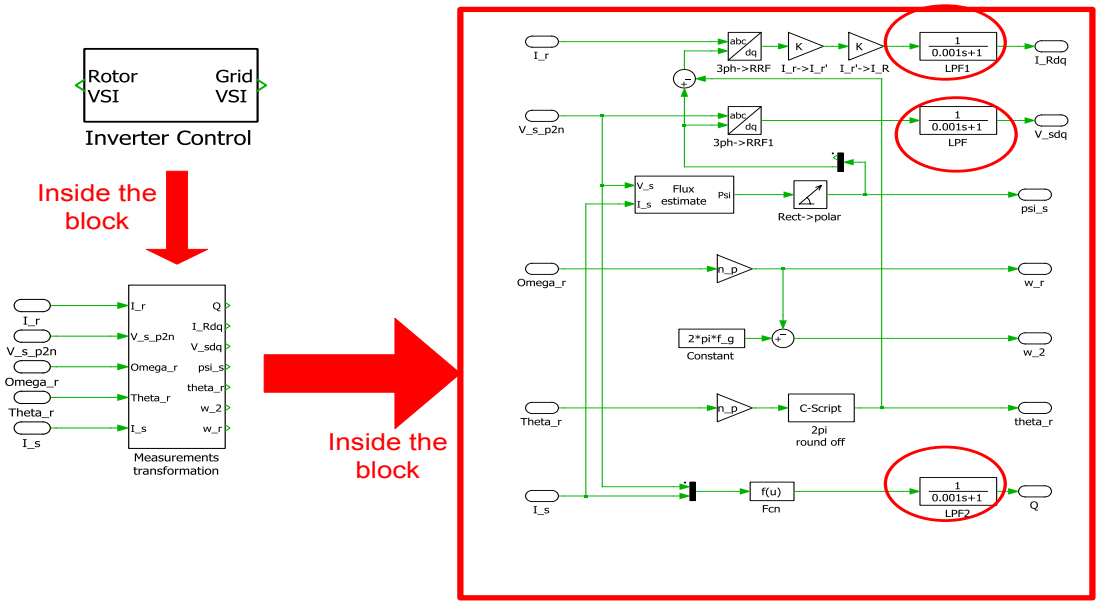

Figure 3.35: Inside the block of RSC and GSC control of PLECS® DFIG model.

3-9 Simulation Results of Modeling the DFIG System

This section includes the results for the simulation model of the DFIG-based wind turbine which has been built in the MATLAB/SIMULINK® platform from the theoretical analysis presented earlier with the grid-connected case. The test is applied to the DFIG system with sensored vector control and subject to constant wind speed. The wind profile signal which has a rated wind speed of 8 m/s is applied to drive the mechanical parts of the DFIG wind turbine system; this wind speed signal is used for a realistic, reliable and accurate simulation analysis.

Step changes occurred in the active component currents in the period between 0.2-1 seconds as shown in figures 3.36-3.39. This corresponds to the stator and rotor three-phase currents in *dq* coordination. This is clear that the step responses of the q axis rotor current component together variation of stator active reference power. This change in current clearly displays the fundamental principle of field orientation, which is a sudden step change from one steady state condition to another.

Figure 3.40 illustrates the grid voltage where the stator of the DFIG as well as the grid-side converter is connected. Under the circumstances of power exchange between the DFIG and the grid, the three-phase grid-side converter current is exchanged with the grid as shown in figure 3.41 with zoom the scope to the period of time between 0.4-0.45 sec. This current is controlled according to the vector control principles of GSC as

presented earlier in this chapter. The direct and quadrture rotor voltage output-fed from the RSC are illustrated in figures 3.42 and 3.43. The dynamic performance of the DFIG is depicted in figures 3.44 and 3.45 were both active and reactive power values accurately track their command signals, which means that the controllers have successfully mitigated the impact of the coupling effect in the tracking of commands signals. This confirms the robustness of the PI stator active power. The output voltage of the sinusoidal pulse width modulation PWM of carrier frequency 5 kHz in the RSC and GSC is shown in figures 3.46 and 3.47. The simulation results in figures 3.48 show the tracking performance of the voltage regulator in the outer loop control of the GSC. The quadrature and direct current control in the inner loop of the GSC is illustrated in figure 3.49. The q-axis current reference of the GSC controller is set to zero, as mention before in the modeling part of the GSC so that the DFIG-based wind turbine reactive power demand is met by the RSC control and its obviously clear that the measured values of q-axis current succeed to track the setting value as shown in figure 3.49a. Figure 3.49b shows the superior performance of the direct-current vector control of the GSC.

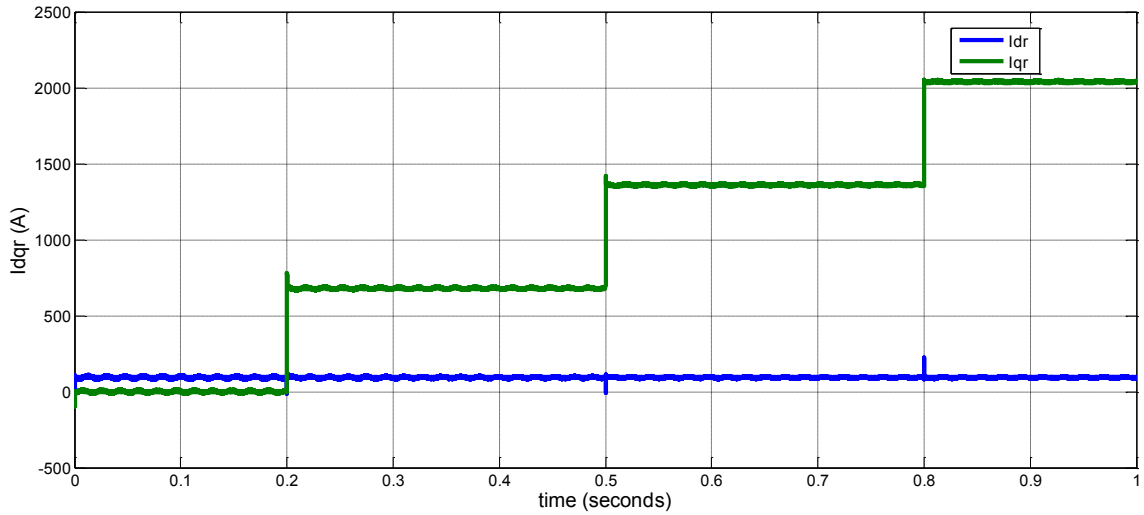

Figure 3.36: Instantaneous measurements of the rotor current in synchronous reference frame i_{dqr}.

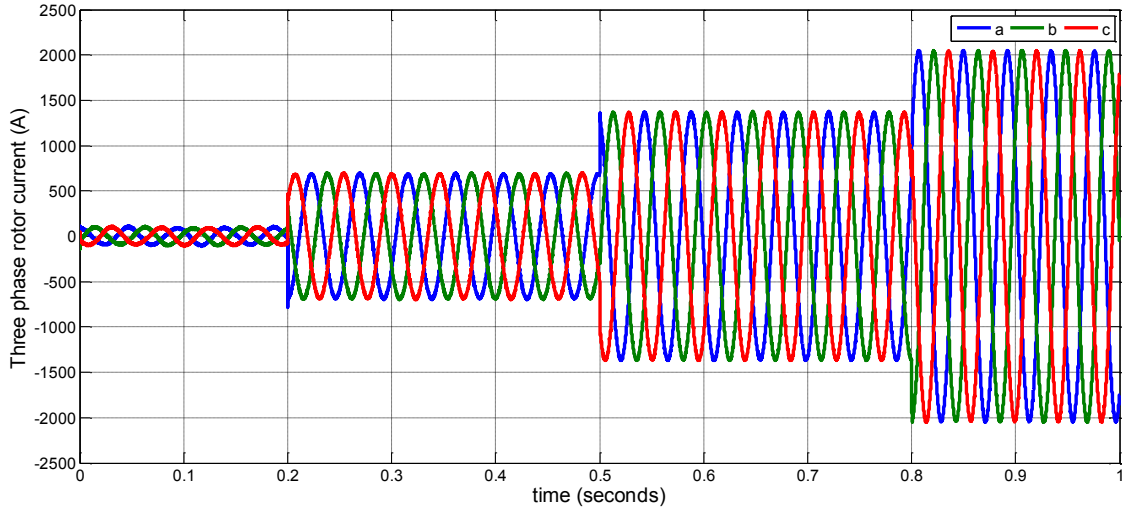

Figure 3.37: Instantaneous measurements of the three phase rotor current.

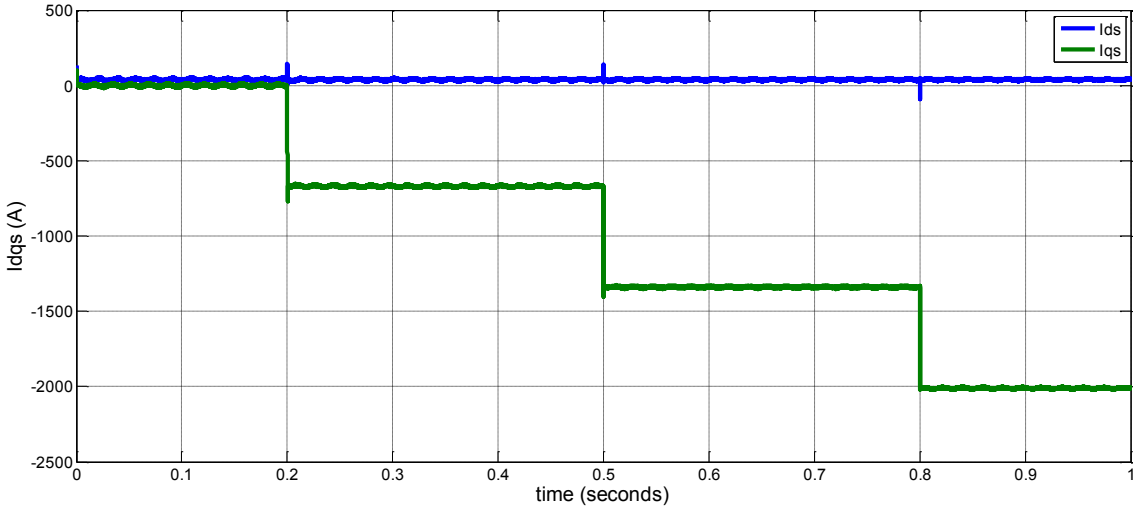

Figure 3.38: Instantaneous measurements of the stator current in synchronous reference frame i_{dqs}.

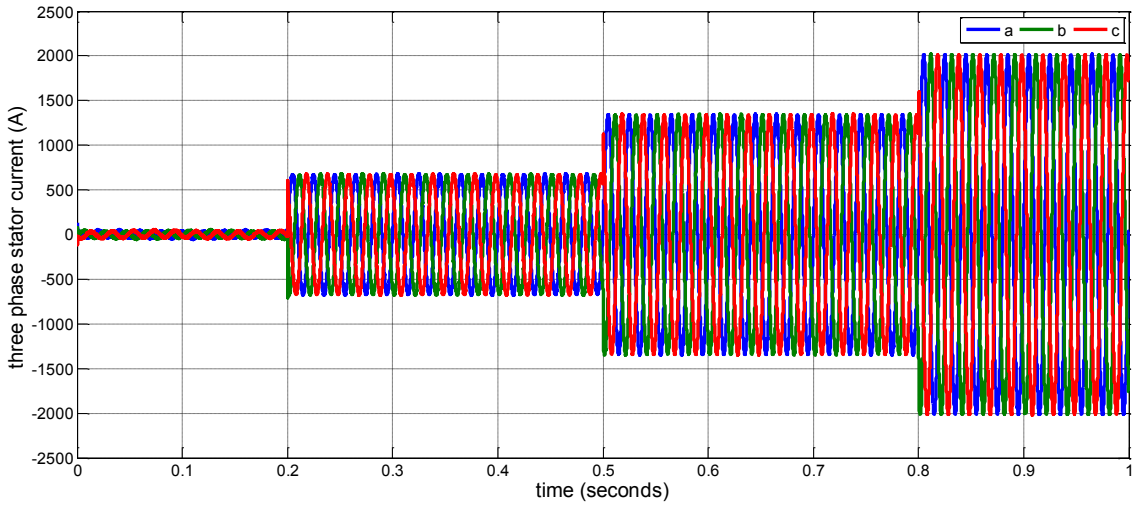

Figure 3.39: Instantaneous measurements of the three-phase stator current.

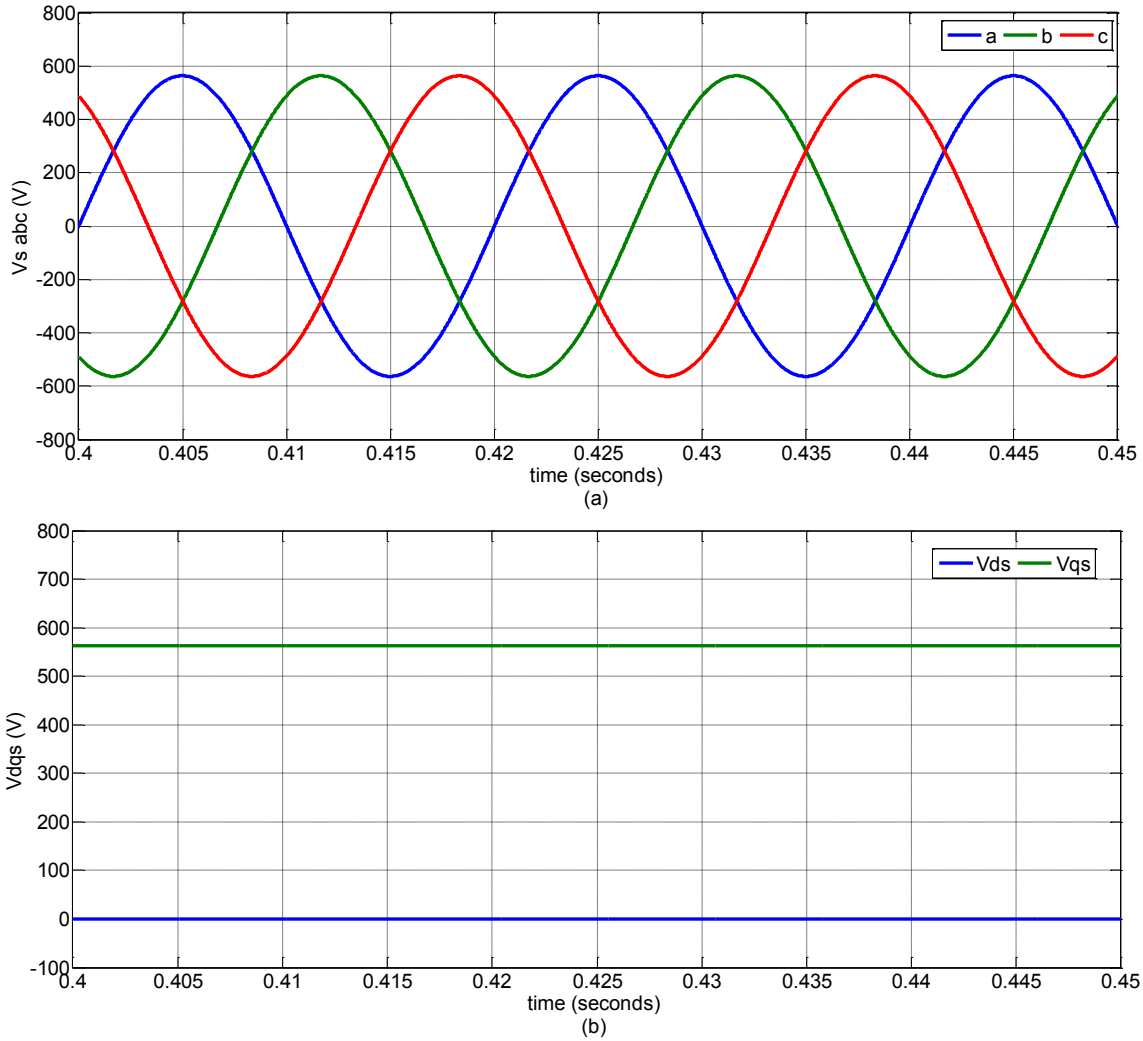

Figure 3.40: Instantaneous measurements of the grid voltage: (a) three phase; (b) in synchronous reference frame coordination.

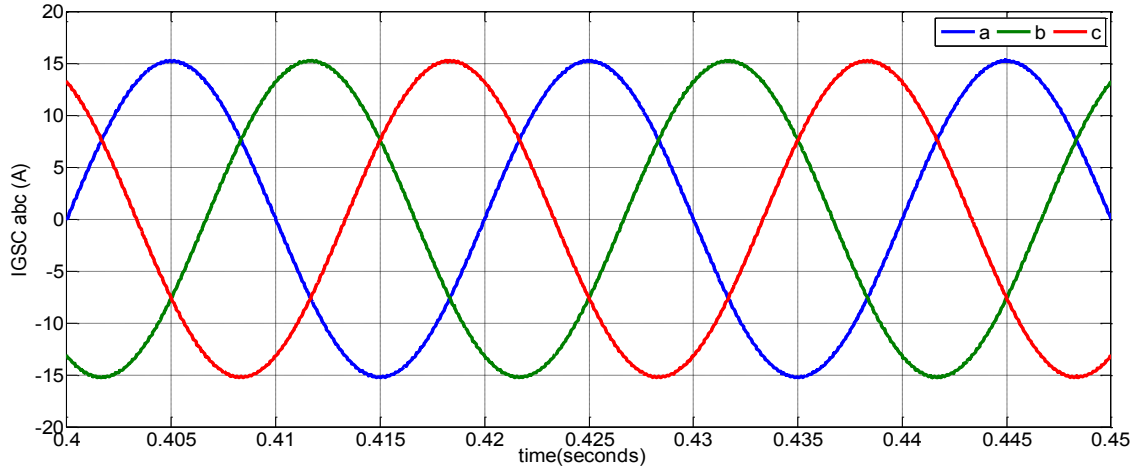

Figure 3.41: Instantaneous measurements of three phase GSC current.

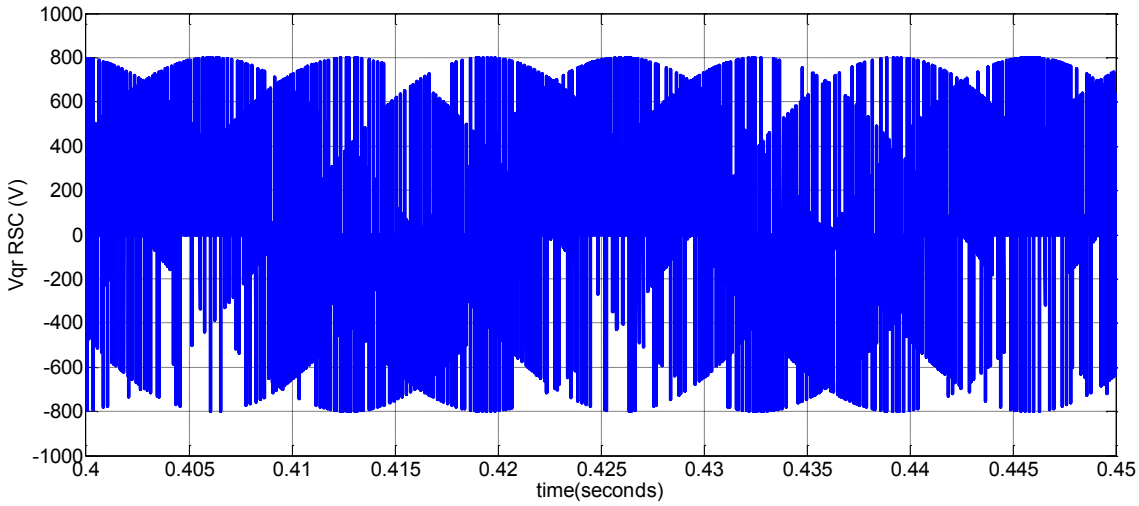

Figure 3.42: Instantaneous measurements of quadrature voltage component of the RSC.

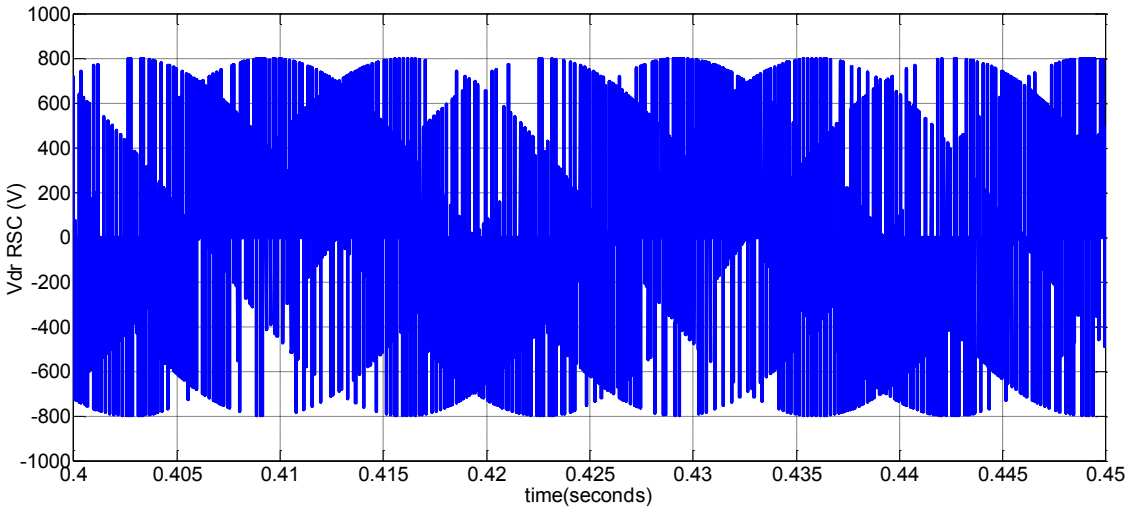

Figure 3.43: Instantaneous measurements of direct voltage component of the RSC.

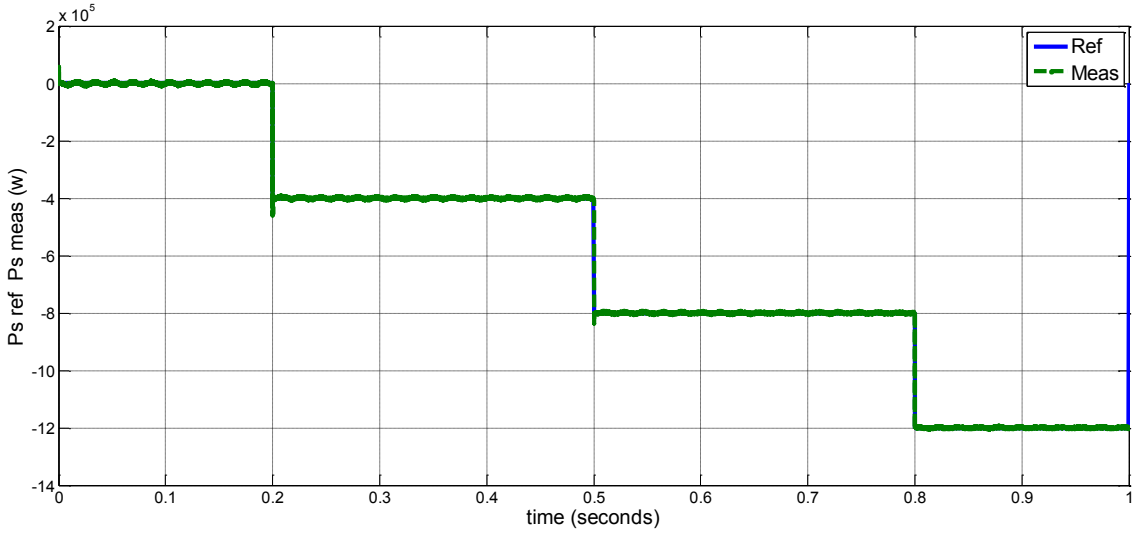

Figure 3.44: Instantaneous measurements comparison reference and measured stator active power.

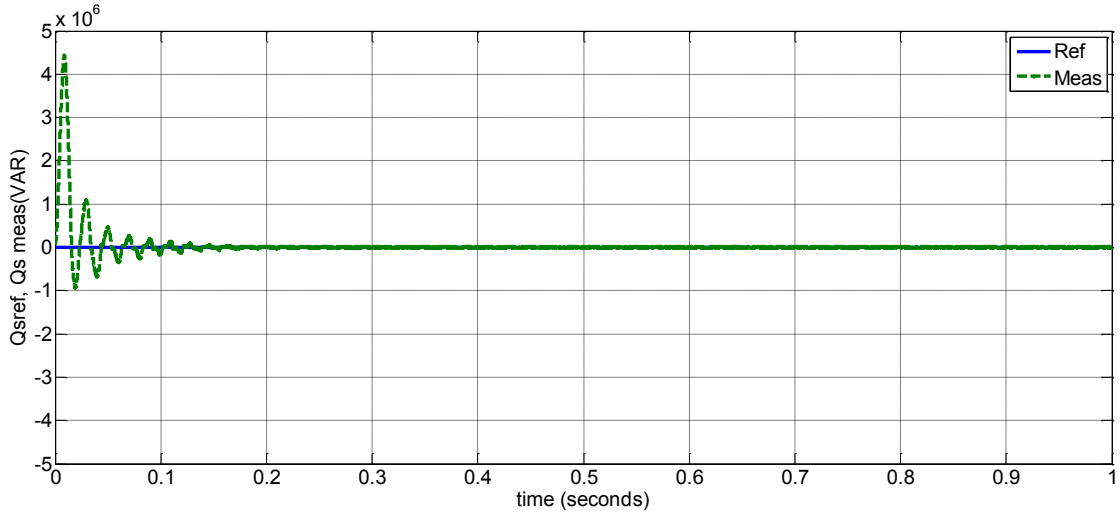

Figure 3.45: Instantaneous comparison reference and measured stator reactive power.

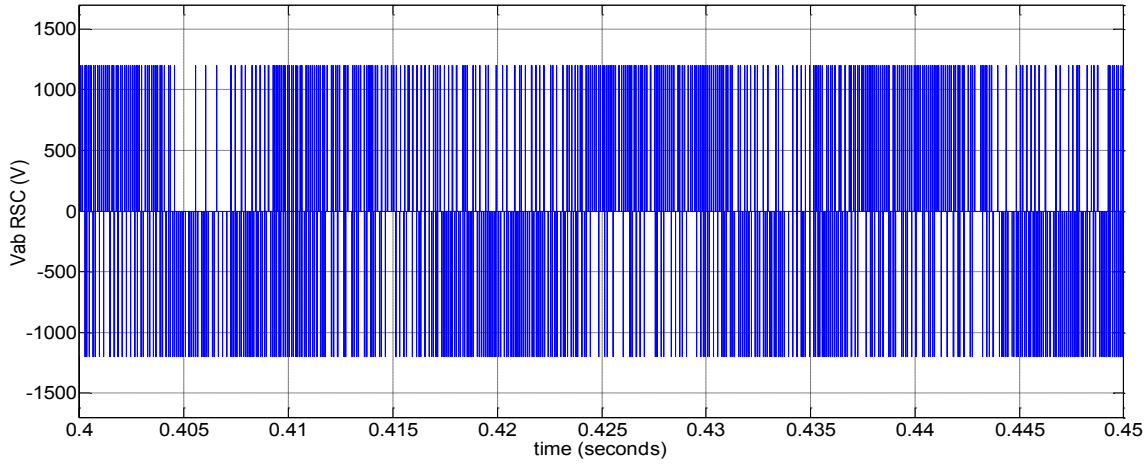

Figure 3.46: Instantaneous measurements phase to phase voltage of rotor voltage.

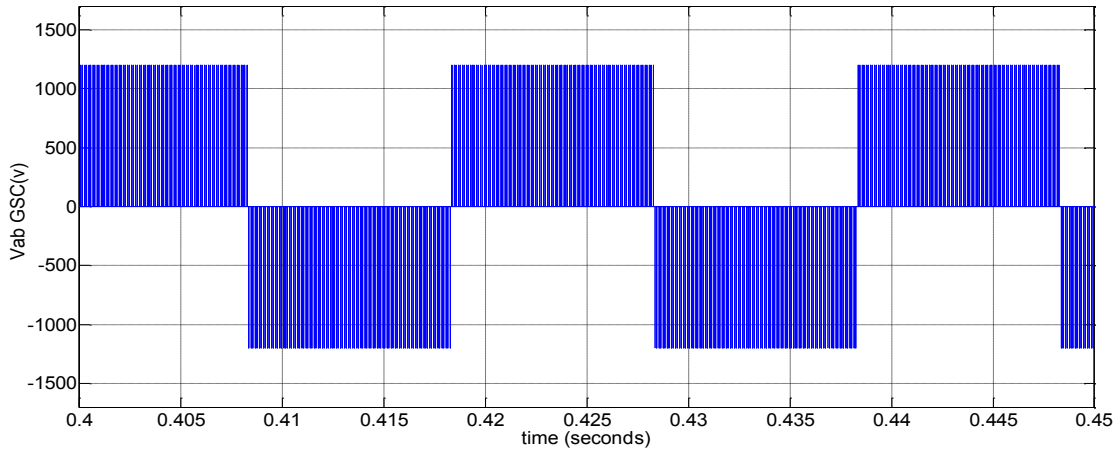

Figure 3.47: Instantaneous measurements phase to phase grid side converter output voltage.

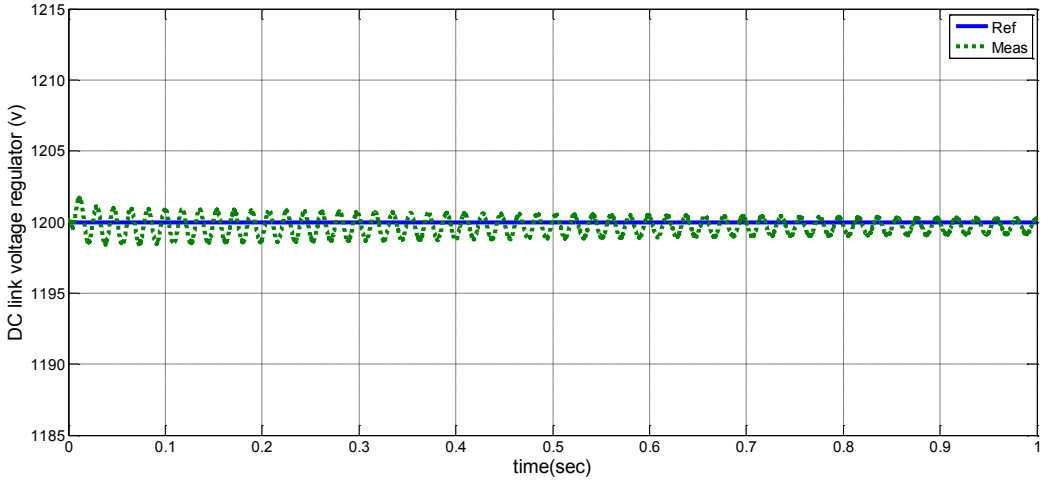

Figure 3.48: Instantaneous measurements DC-link voltage regulator in the GSC.

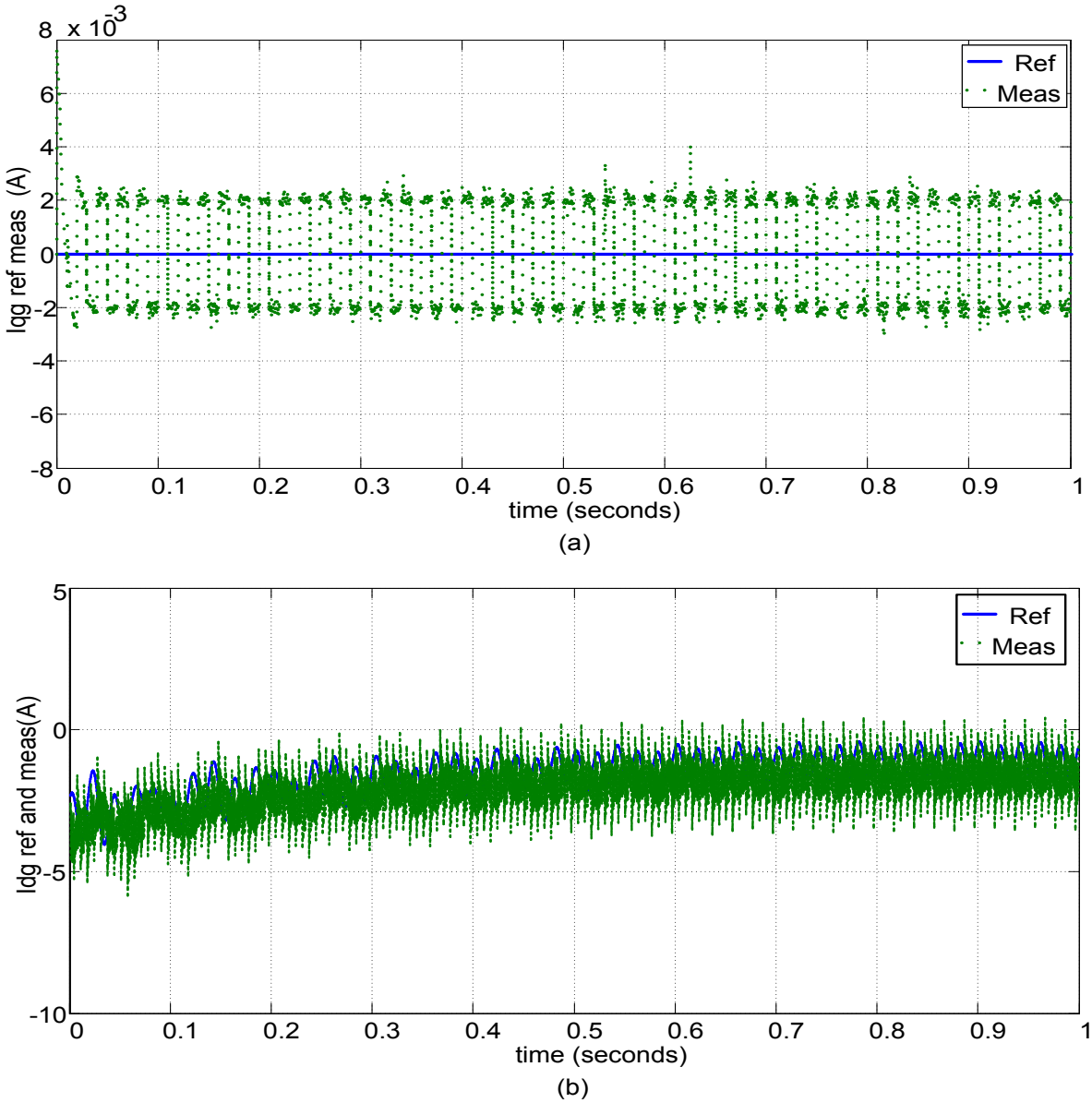

Figure 3.49: Instantaneous comparison reference and measured current regulator in the inner loop GSC control with reference frame oriented along the grid voltage vector (a) i_{qg} (b) i_{dg}.

3-10 Conclusions

The modelling of the DFIG-based wind turbine system is important for the present research work on sensorless vector control, improvement of the fault ride-through capability of the system and its interaction with the grid in normal and fault conditions. This chapter describes a model of wind turbines with the DFIG, developed in the dedicated power system analysis tool Matlab/Simulink, which includes the wind model, the aerodynamic model, the mechanical model, the DFIG model, and the PWM voltage source converter model. The conventional vector control of the DFIG based

wind turbine system is built and tested to illustrate the excellent performance of the system during normal grid condition. The decoupled control of the active and reactive power is easily obtained to improve the dynamic behaviour of the system and the quality of power injected to the grid. Simulation results have proven the precision of the obtained model and the control strategy.

.

CHAPTER FOUR

CHAPTER FOUR

ROTOR POSITION ESTIMATION USING THE MODEL REFERENCE ADAPTIVE SYSTEM (MRAS)

4-1 Introduction

The transformation of voltages and currents from the *a-b-c* reference frame to the *d-q* reference frame is a basic requirement of the vector control. Critical information in the transformations includes the position of the rotor winding axes with respect to the stator winding axes and the stator voltage angle. The rotor position is obtained by an encoder incremental or absolute position. The stator angle is obtained by a hardware or software phase lock loop (PLL). The rotor position signal is essential to give accurate vector control behaviour of DFIG-based variable speed wind turbines. Incorrect rotor position information will not only harm control performance but will also affect system stability. Several computation blocks in the rotor-side converter control utilize the rotor position signal in the vector control scheme to calculate i_d and i_q using the Park transformation, v_d^* and v_q^* using the inverse Park transformation, and rotor speed. The rotor position information needs to be known at every point in time in order to decouple control to be performed. Therefore, one of two solutions can be used to provide accurate information about the rotor's position. Firstly is a mechanical encoder can be used to measure the rotor position, and this signal is continuously sent to the rotor-side converter control loops. Secondly, in the sensorless approach rotor position is calculated from the electric quantities associated with rotor and stator.

The latter rotor position detection method is an attractive technique which contributes to the enhanced reliability of DFIG-based wind turbines. This is use of the mechanical speed/position sensor coupled with the machine rotor shaft has several drawbacks in terms of robustness and reliability since an encoder is sensitive to external perturbations such as electromagnetic interference. Moreover, sensors are often subject to high failure rates in harsh environments such as extreme ambient temperature, super high-speed operation, and other adverse or heavy load conditions. Furthermore, especially in small to medium size machines, the sensor cost is considerable and cabling and maintenance represents extra

costs. On other hand, the computation algorithm for rotor position using sensorless method must be set to be stable at a wide range of operating conditions and should not require initial condition knowledge. In addition, the flux equations are dependent upon the generator parameters, and variations in winding temperature can lead to changes in rotor and stator resistance and inductance.

This chapter presents the modelling of two model reference adaptive system (MRAS) schemes adopted to conduct the rotor angle estimation in the vector controller. These are based on rotor current and rotor reactive power with more complement analysis where the first scheme has been used in many investigations for position detection while the second is utilized in previews study as speed estimator with different orientation analysis.

4-2 Sensorless Control of DFIG system Using MRAS Observer

The model reference adaptive system (MRAS) represents one of the most attractive solutions for the sensorless control of AC drives due to its simplicity and lower computational complexity [137]. MRAS schemes have been employed for position detection [79, 81, 84, 138] or speed estimation [78, 85, 139] which are investigated using a PI or Hysterias controller in DFIG systems which implemented in different stator and rotor reference frames. The MRAS method is utilized to estimate the rotor position signal that implement to the orientation control of the RSC of the DFIG. In an MRAS, as depicted in Figure 2.4, an adaptive (adjustable) model (AM) and a reference model (RM) are connected together in parallel. The output of the adaptive model is expected to converge with the output of the reference model in the presence of a proper adaptation mechanism. The usual MRAS estimates speed or position using the outputs of these two different AM and RM models. The AM is position-dependent while the RM is not related to the estimated position [80]. Based on Popov's hyperstability criterion, the difference between the RM and the AM outputs is used to derive a suitable adaptive mechanism to generate the estimated speed used so as to minimize the error between the reference and estimated values and therefore the stability of the MRAS. The convergence of position estimation can be guaranteed according to this theory [83, 140, 141]. Thus, if the tracking errors between the output states of the AM and RM are close to zero. Then the rotor position can be obtained by using an integrator for the output signal of the PI controller.

4-2-1 Rotor Current-Based MRAS (RCMRAS)

Rotor current-based MRAS represents one of the best types of MRAS models for grid-connected or stand-alone DFIG operation [79, 81, 142]. In this method, the output of the RM is the rotor current measured by transducers in the rotor reference frame, while the estimated rotor current is determined using the stator voltage and stator current in the stationary reference frame to compute the stator flux derived from equations 3.8 and 3.9 equations:

$$\lambda_{\alpha s} = \int (v_{\alpha s} - r_s i_{\alpha s}) dt \tag{4.1}$$

$$\lambda_{\beta s} = \int \left(v_{\beta s} - r_s i_{\beta s}\right) dt \tag{4.2}$$

From the substitution of equations 4.1 and 4.2 in equations 3.16 and 3.17 respectively and rearrangement, the formula for rotor current are estimated in the rotor ($\alpha\beta$) frame:

$$i^r_{r\alpha=} \frac{(\int v^s_{s\alpha} - r_s i^s_{s\alpha}) - L_s i^s_{s\alpha}}{L_m} e^{-j\theta_r} \tag{4.3}$$

$$i^r_{r\beta=} \frac{\left(\int v^s_{s\beta} - r_s i^s_{s\beta}\right) - L_s i^s_{s\beta}}{L_m} e^{-j\theta_r} \tag{4.4}$$

Hence (θ_r) is the rotor's angular position. The cross-product between the output of RM and that of the AM is driven to zero by the adaptation mechanism in order to estimate the rotor speed, which is integrated to get the rotor angle that will be fed back to the AM as shown in figure 4.1. The error between the RM and AM is the cross-product between the measured rotor current and the estimated current from equations 4.3 and 4.4:

$$\varepsilon = \iota'_{\alpha r} . i_{\beta r} - \iota'_{\beta r} . i_{\alpha r} \tag{4.5}$$

The adaptive mechanism is then given by:

$$\acute{\omega}_r = Kp_5 . \varepsilon + \int Ki_5 . \varepsilon . dt \tag{4.6}$$

Minimizing the error between the rotor current output from the AM and RM is conducted by adjusting the rotor position. The rotor's electrical position is determined by the free integral of equation 4.6 as follows:

$$\acute{\theta}_r = \int \acute{\omega}_r . dt \tag{4.7}$$

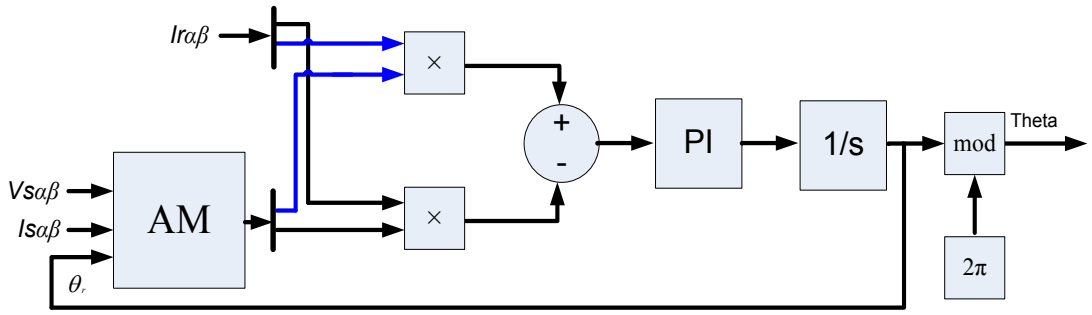

Figure 4.1: Simulink model of rotor current based MRAS (RCMRAS).

4-2-2 Rotor Reactive Power Based MRAS (QRMRAS)

Figure 4.2 depicts the basic structure of the QRMRAS observer. The rotor reactive power error is computed from the difference between the outcomes of the RM and AM used to generate the rotor quantity from the adaptation mechanism, and the output is subjected to an integrator to estimate the rotor position [139].

The expression for instantaneous rotor reactive power is:

$$Q_r = \bar{v}_r \otimes \bar{\imath}_r = v_{\beta r}.i_{\alpha r} - v_{\alpha r}.i_{\beta r} \tag{4.8}$$

It can be assumed that the inverter output voltage ($v_{\alpha r}$ and $v_{\beta r}$) exactly follows the reference signals ($\acute{v}_{\alpha r}$ and $\acute{v}_{\beta r}$), and so equation 4.8 can be expressed as:

$$Q_r^{ref} = \acute{v}_{\beta r}\,.\,i_{\alpha r} - \acute{v}_{\alpha r}.\,i_{\beta r} \tag{4.9}$$

By substituting equations 3.10 and 3.11 in equation 4.8 following results:

$$Q_r^{est} = \left(\left(i_{\alpha r}.\rho\lambda_{\beta r} - i_{\beta r}.\rho\lambda_{\alpha r}\right) - \acute{\omega_r}\,.\left(i_{\alpha r}\lambda_{\alpha r} - i_{\beta r}\lambda_{\beta r}\right)\right) \tag{4.10}$$

It should be noted that the above expressions of Q are free from stator and rotor resistance, which is a notable merit of this MRAS scheme.

The difference between the outputs of the RM and AM will form an error given as:

$$\varepsilon = Q_r^{ref} - Q_r^{adb} \tag{4.11}$$

The error signal is passed through the adaption mechanism (PI controller). The output of the PI controller is the estimated rotor speed, which is then used to tune the adjustable model such that the error converges to zero. The error signal is fed to the adaptation mechanism block, which yields the rotor mechanical speed, as follows:

$$\acute{\omega}_r = Kp_6.\varepsilon + \int Ki_6.\varepsilon.dt \tag{4.12}$$

In the MRAS method, it is possible to reduce the reactive power error by adjusting the rotor position. The rotor electrical position is determined by the free integral of equation 4.12:

$$\acute{\theta}_r = \int \acute{\omega}_r . dt \tag{4.13}$$

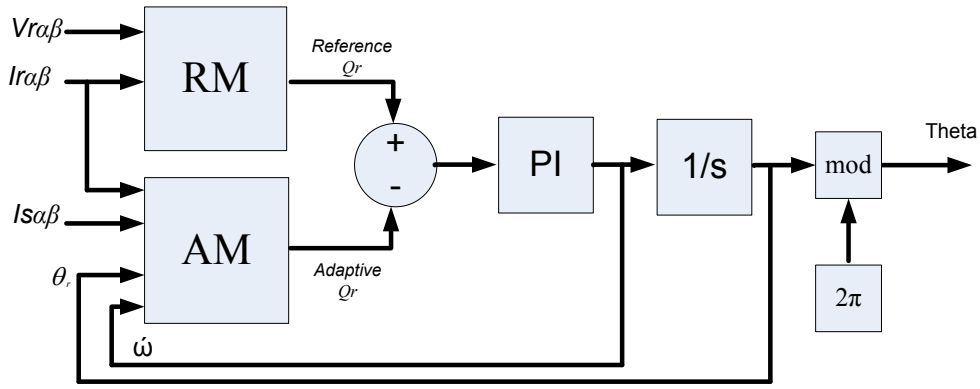

Figure 4.2: Simulink model of rotor reactive power based MRAS (QRMRAS).

4-3 Simulation Results

The performance of the estimation of the rotor position using the MRAS schemes has been investigated in terms of its response against wind speed variations and changes in machine parameters to test which of the two schemes is more robustness and less sensitive to parameter changes during operation of decoupling active and reactive power control. The set of tests conducted with the DFIG system, constant and ramp variations in magnetizing inductance, stator resistance, and rotor resistance of the machine were increased to 30% of the nominal values after 2 seconds of running. The simulation results shown in figure 4.3 indicate the tracking performance in detecting the rotor angle position using the QRMRAS, and RCMRAS as compared with the actual values of steady state with constant value of wind speed of 10 m/sec and constant generator parameters. In this condition, Figure 4.4 shows the comparison between the rotor reactive power that computed in the reference and adaptive model inside the QRMRAS subsystem where the difference between them subjected in the controller of the MRAS to detect the angular position of the rotor. To validate the accuracy of the RCMRAS and the QRMRAS, figure 4.5 shows the difference between the actual and estimated rotor angles in each estimation

scheme. It's clear that the QRMRAS gives less pulsating error as compared with RCMRAS.

The second scenario used to test the robustness of the estimation of the DFIG rotor angle position is implemented by applying step changes to wind speed as shown in figure 4.6. The variation of the wind speed will increase the generator speed from 146 rad/sec to 156 rad/sec after 1.5 sec as illustrate in figure 4.7. The ability of QRMRAS and RCMRAS to track the measured rotor angle during this case is highlighted in figure 4.8.

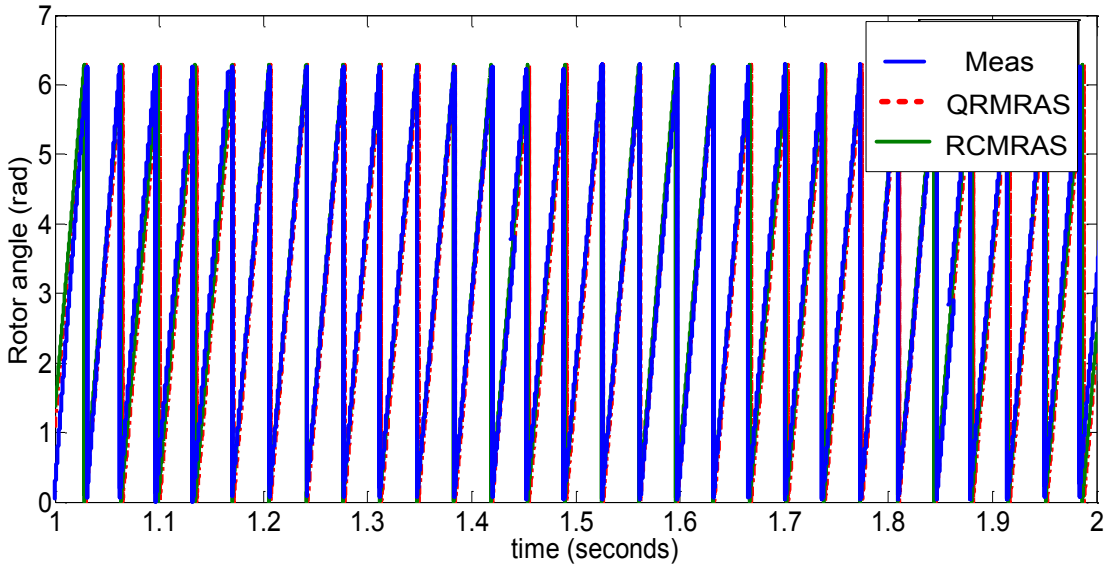

Figure 4.3: Comparison results of the measured and estimated rotor position computed in normal operating conditions.

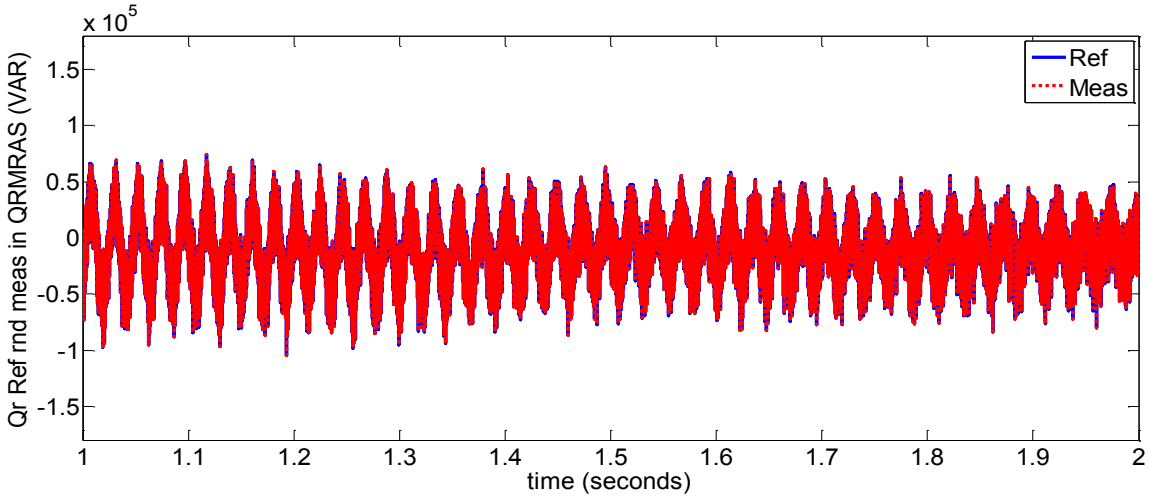

Figure 4.4: Instantaneous comparison of reference and measured values of rotor reactive power in the QRMRAS sub-system computation.

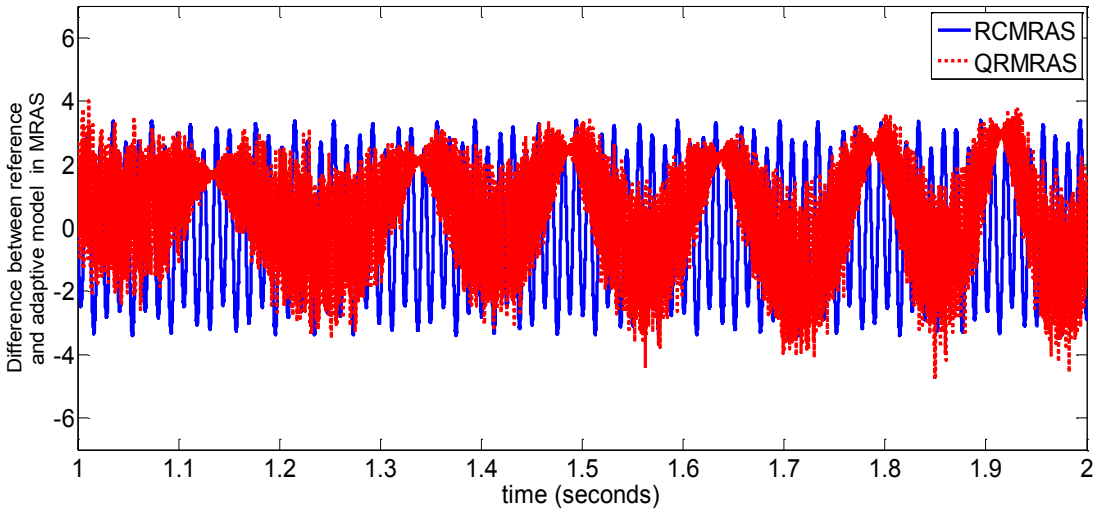

Figure 4.5: Instantaneous error between reference and adaptive model output in rotor RCMRAS and QRMRAS.

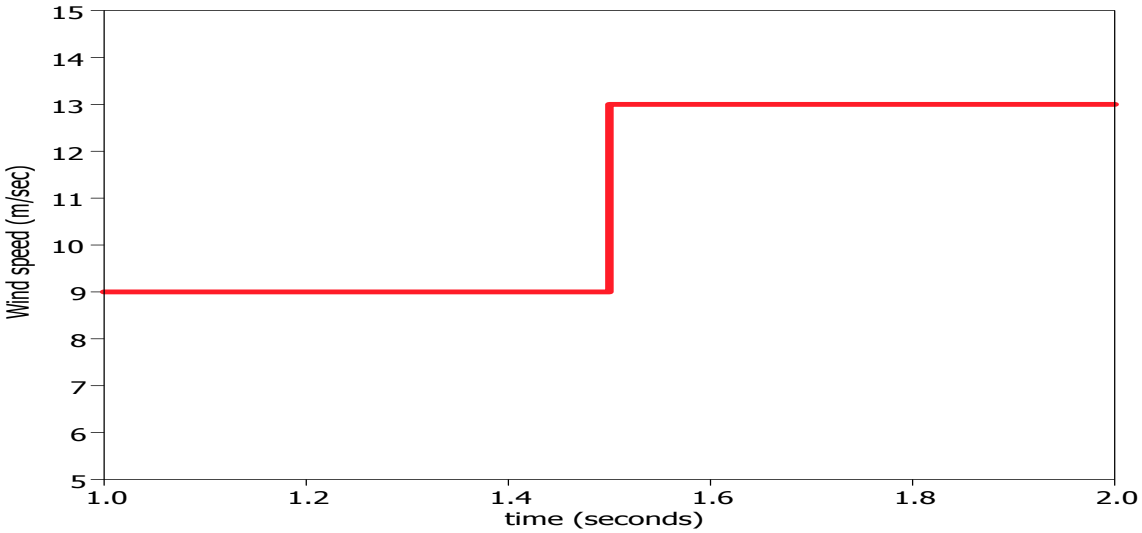

Figure 4.6: Variable wind speed signal.

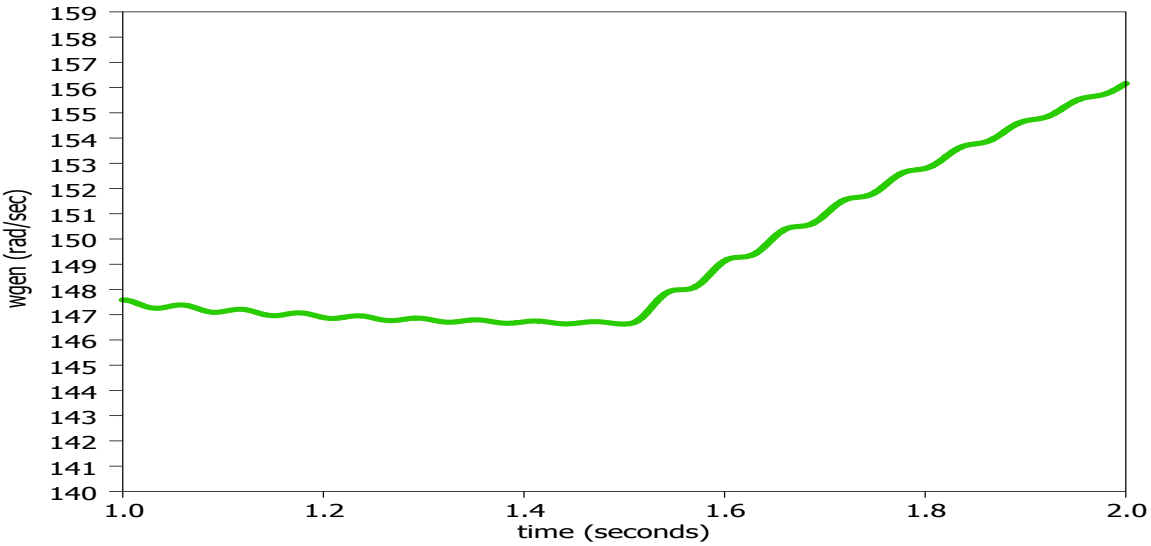

Figure 4.7: Instantaneous results for generator speed (rad/sec).

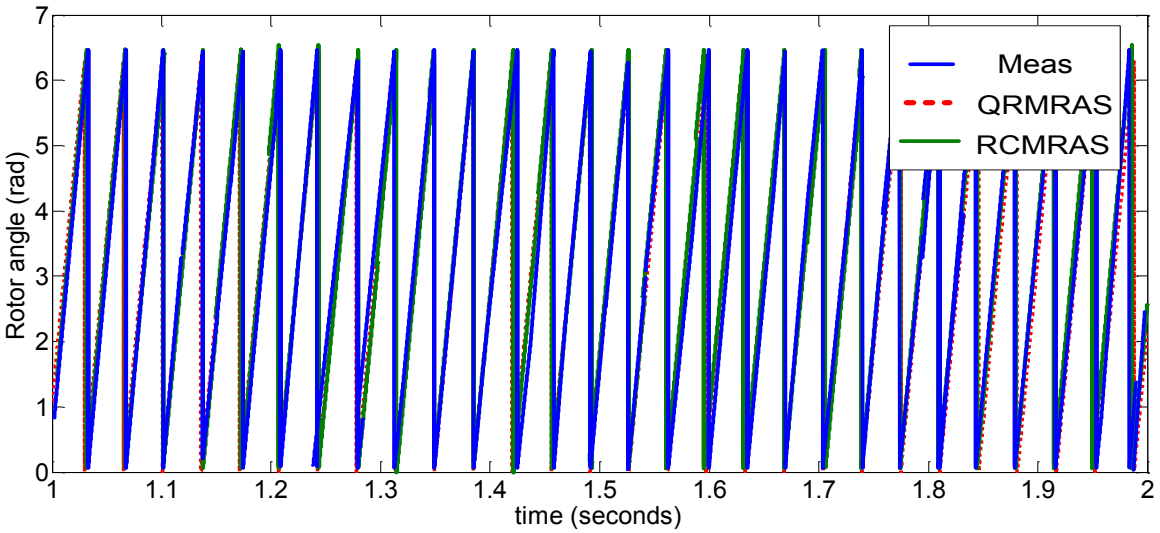

Figure 4.8: Comparison results of the measured and estimated rotor position in step change wind speed operation condition.

The simulation results shown in figure 4.9 indicate the tracking performance in detecting the rotor angle position using the QRMRAS, and RCMRAS as compared with the actual values when the generator is running at 1720 rpm with a step change in the value of L_m of a 30% increase after 1.5 second of operation. The QRMRAS as noted is less sensitive to changes in the generator magnetizing inductance as illustrated in the zoom scope of figure 4.9 where the rotor detection in RCMRAS suffers deviate during this condition. QRMRAS is more accurate in tracking in actual rotor position than the RCMRAS as a results of absent the integration in the formula of computation of the reactive power in AM and RM and it independent on the rotor or stator resistance.

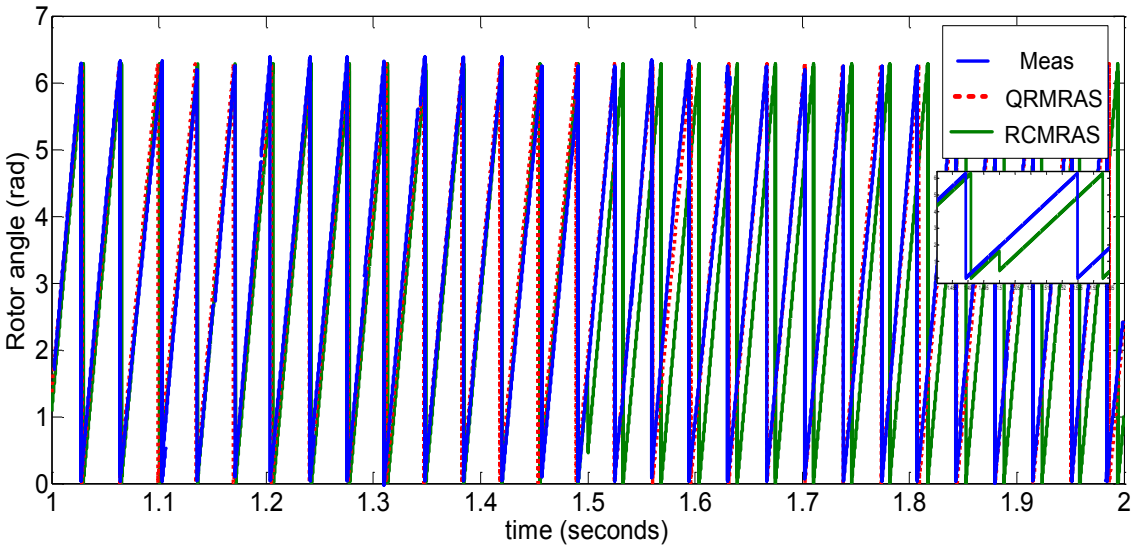

Figure 4.9: Comparison results of the measured and estimated rotor position in condition of 30% increase of. L_m.

Figure 4.10 illustrates the results for a scenario of voltage dip subjected to the DFIG system with sensorless control without employing any protection system to the DFIG. The three-phase voltage drop with high incremental oscillation of the three-phase stator current is shown in figure 4.11. Figures 4.12 and 4.13 depict the instantaneous measurements of the RM and AM outputs in the RCMRAS and QRMRAS sub-systems respectively, and it's clear that the RM output in RCMRAS suffers from phase shift and high oscillation when compare to the RM output meanwhile in QRMRAS the controller succeed to reducing the error between the RM and AM shown in figure 4.14. This condition will lead to a minor cumulative drift in the rotor angle estimation RCMRAS than in QRMRAS in the voltage dip duration as illustrated in figure 4.15.

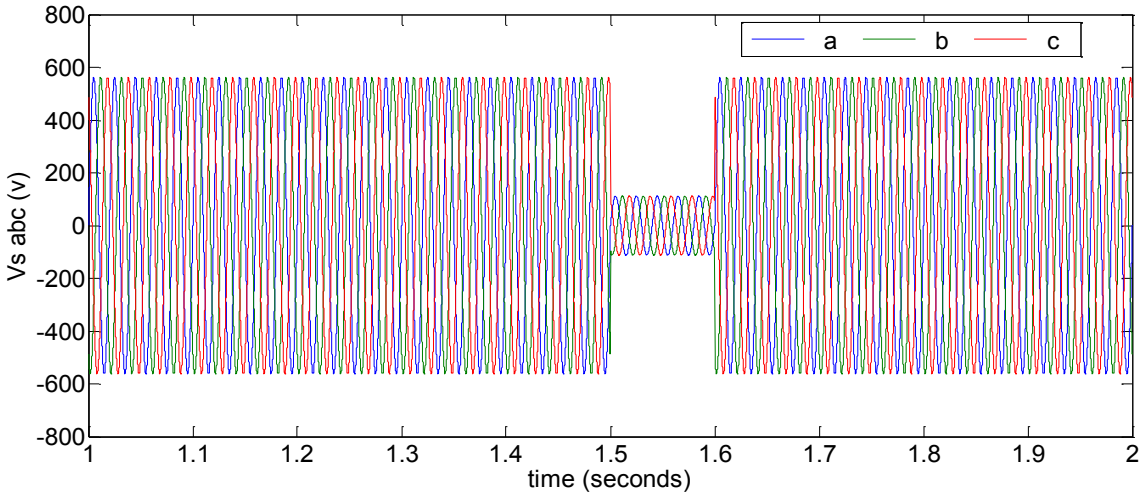

Figure 4.10: Instantaneous measurement of three-phase voltage.

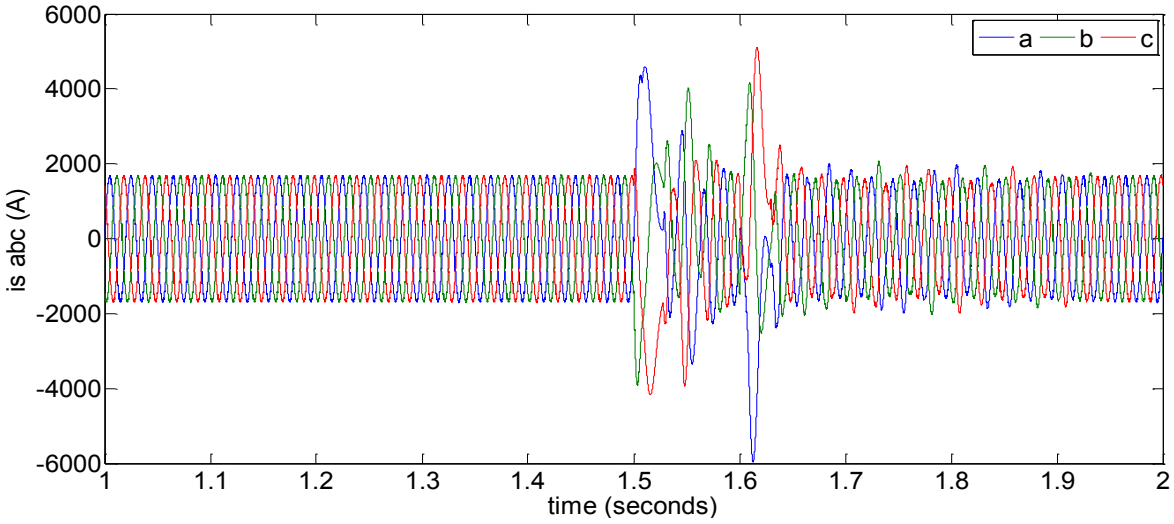

Figure 4.11: Instantaneous measurement of three-phase current during voltage dip condition without protection.

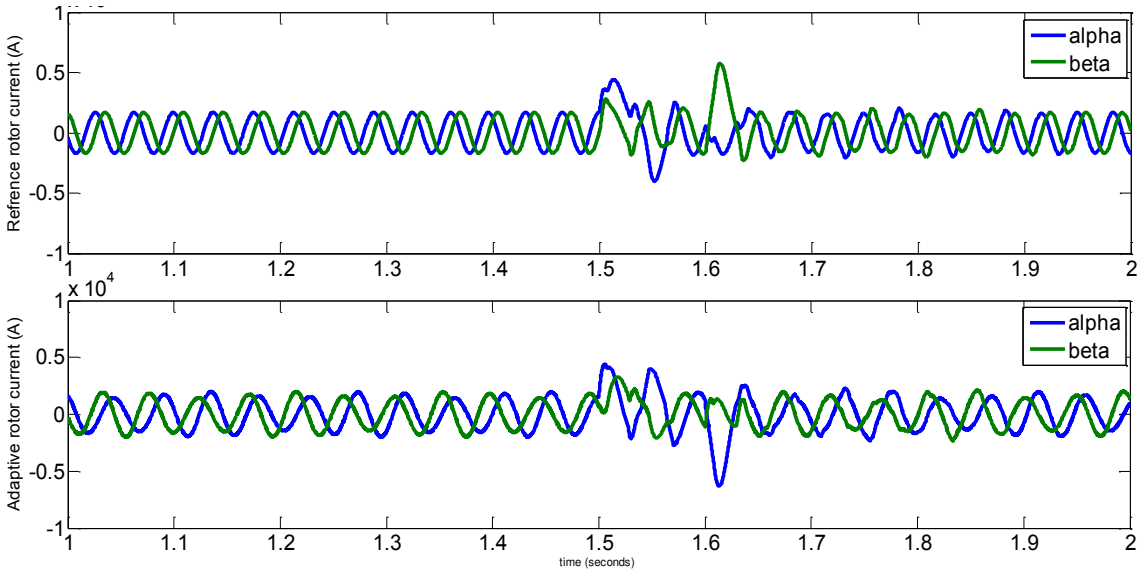

Figure 4.12: Instantaneous comparison between outputs of reference and adaptive models in RCMRAS sub-system computation in fault condition.

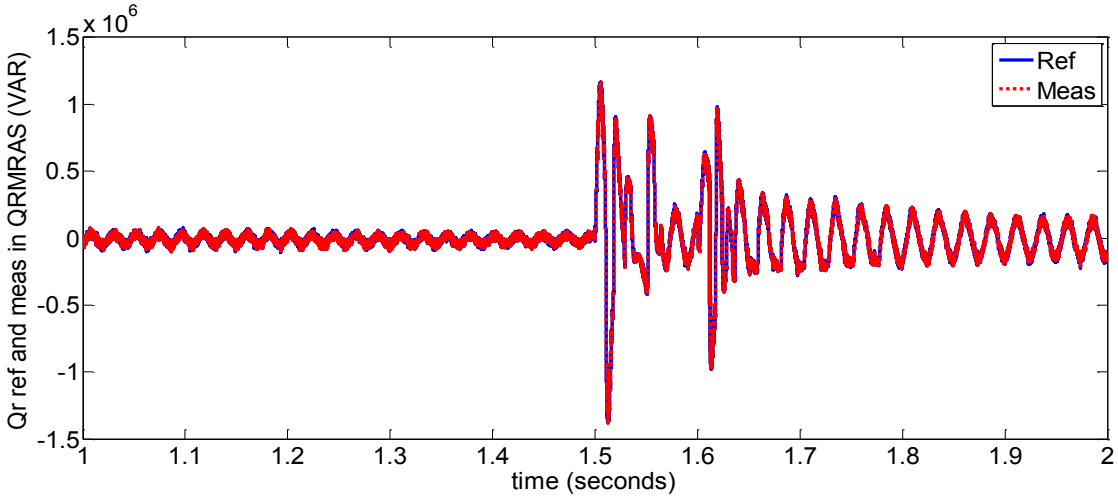

Figure 4.13: Instantaneous comparison of reference and measured values of rotor reactive power in the QRMRAS sub-system computation in fault condition.

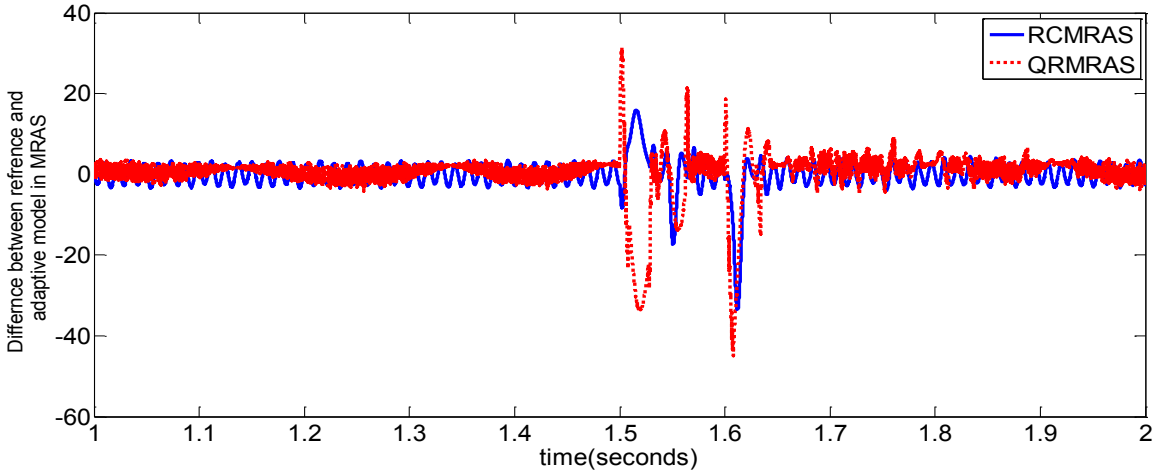

Figure 4.14: Instantaneous error between reference and adaptive model output in RCMRAS and QRMRAS in fault condition.

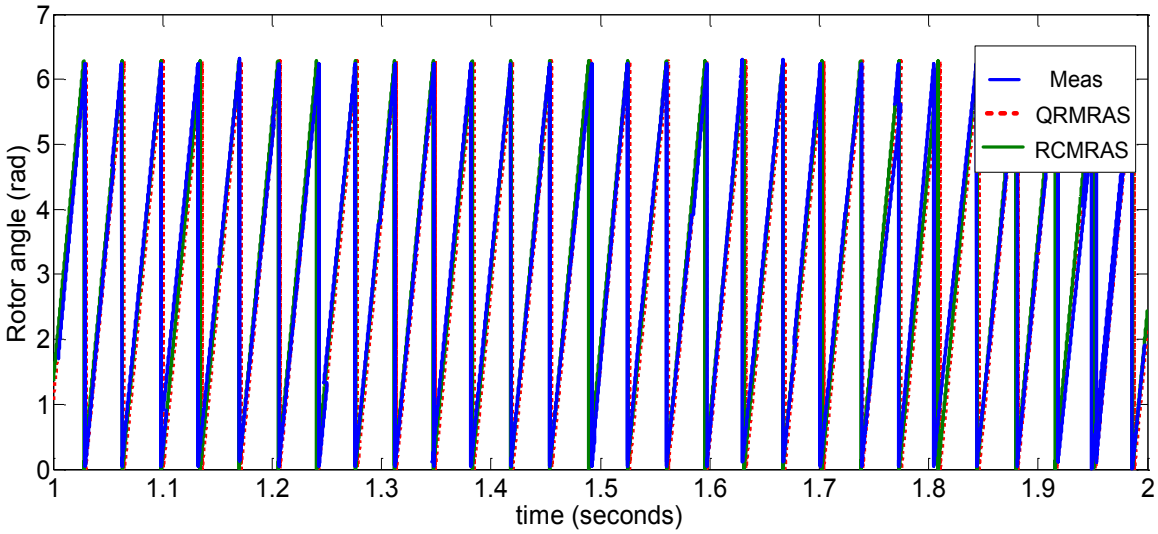

Figure 4.15: Comparison results of the measured and estimated rotor position in voltage dip condition.

The integrated error index which is the integral of time multiplied by absolute error (ITAE=$\int t\ |e(t)|\ dt$) and the integral absolute error (IAE=$\int |e(t)|\ dt$) are used criteria to measure the quality of the system's response in order to assess which of these methods gives response which corresponds to the minimum amount [143]. The ITAE performance index has the advantage of producing smaller overshoots and oscillations than the IAE performance index. In addition, the former is more sensitive since it has the best selectivity [144]. A systematic evaluation of rotor estimation performance has been conducted for different operating conditions by means of the use of ITAE and IAE index as shown in table 4.1 when machine parameters, which indicates that the QRMRAS gives the lower values of ITAE and IAE as compared with RCMRAS which mean that the accuracy of QRMRAS is better.

Table 4.1: Results of performance index of rotor position estimation at t = 1.5 second with ramp variation applied to $r_s\ and\ , r_r$.

	ITAE		IAE	
	QRMRAS	RCMRAS	QRMRAS	RCMRAS
30% $\boldsymbol{r_s}$	6.5459*10^{-3}	0.066	0.0545	0.325
30% $\boldsymbol{r_r}$	6.5459*10^{-3}	0.036	0.0545	0.202
30% $\boldsymbol{r_s\ and\ , r_r}$	6.5459*10^{-3}	0.046	0.0545	0.1259

4-4 Conclusions

In this chapter two different observers utilized to estimate the rotor position using currents and stator voltages were presented. The results of simulations are presented to show the performance of the proposed techniques. The results show that they are well-suited for vector control applications without needing a mechanical sensor in the DFIG. The results demonstrate the feasibility of position tracking performance using the MRAS method. Different operating conditions of constant wind speed, step change wind speed, voltage dips of different severity, and changing in machine parameters to highlight the robustness, fast response and insensitivity of the methods.

The MRAS algorithms which described for rotor position computation will not conduct any integration operation in the equations of adaptive model and reference model when the DFIG operate at region near or equal to synchronous speed. Thus in the mathematical computation, saturation problem of the integrator terms in MRAS scheme cannot take place when the where the slip frequency is low. Therefore, near synchronous speed operation, the reference model and adjustable does not create any error in the said EMF variable calculation due to integrator saturation problem.

CHAPTER FIVE

CHAPTER FIVE

BEHAVIOUR ANALYSIS OF DFIG SYSTEM WITH GRID DISTURBANCES

5-1 Introduction

In this chapter, the fault response of the doubly-fed induction generator (DFIG)-based wind turbine is analyzed and summarized with and without the modified vector control scheme. This shows its influence on the dynamic behaviour of the wind turbine system when faults occur. In addition a comparison is conducted with different operating condition.

5-2 Grid Code Requirements of DFIG system

Grid code requirements vary considerably from region to region and from system to system. The grid codes in a certain country may only cover some specific grid code requirements. The differences in requirements, as well as local traditional practices, are caused by different levels of wind power penetration and different degrees of power network robustness [11, 145]. Grid codes are put in place for all power generation plants transferring power to the grid, in order to increase the efficiency of power transfer and to reduce the damage caused to grid-connected devices [146, 147]. According to recent grid code requirements, one of the conditions for wind turbines that are they must remain connected to the grid during grid disturbances. Moreover, they must also contribute to voltage support during and after grid faults. The major typical grid code requirements for the operation and grid connection of wind turbines are listed as following [148, 149]:

1) Voltage operating range: Wind turbines are required to operate within typical grid voltage variations.

2) Frequency operating range: Wind turbine generation is required to operate within typical grid frequency variations.

3) Active power control: Several grid codes require wind farms to provide active power control in order to ensure a stable frequency in the system and to prevent overloading of lines. Also, wind turbines are required to respond with a ramp rate in the desired range.

4) Frequency control: Several grid codes require wind farms to provide a frequency regulation capability to help maintain the desired network frequency.

5) Voltage control: Grid codes require that individual wind turbines control their own terminal voltage to a constant value by means of an automatic voltage regulator.

6) Reactive power control: Wind farms are required to provide dynamic a reactive power control capability to maintain the reactive power balance and the power factor in the desired range.

7) Low voltage ride-through (LVRT): In the event of voltage sags, wind turbines are required to remain connected for a specific period of time before being allowed to disconnect. In addition, some utilities require that wind turbines help to support grid voltage during faults.

8) High voltage ride-through (HVRT): In the event that the value of voltage goes above its upper limit, wind turbines should be capable of staying on line for a given length of time.

9) Power quality: Wind farms are required to provide electrical power of a desired quality; for example, maintaining constant voltage or voltage fluctuations in the desired range and maintaining voltage/current harmonics in the desired range.

10) Wind farm modelling and verification: Some grid codes require wind farm owners or developers to provide models and system data so as to enable the system operator to investigate by simulation the interaction between the wind farm and the power system. They also require installation of monitoring equipment to verify the actual behaviour of the wind farm during faults and to check the model.

11) Communications and external control: Wind farm operators are required to provide signals corresponding to a number of parameters important for system operator to

enable proper operation of the power system. Moreover, it must be possible to connect and disconnect the wind turbines remotely.

5-3 Fault Ride-Through (FRT) of DFIG System

Generally; faults are classified into as an open circuit and short circuit which occurring on the grid side terminal. Short circuit in the power system is referring to the term fault in this study which categorize to a temporary and permanent faults. Temporary type results in momentarily interruption such as an insulator flashover which is cleared by the immediate tripping of one or more circuit breakers to isolate the fault. Whereas the permanent faults are caused by sustained disruption such as falling debris on the line such as a tree, or snowfall causing short circuit among the phases and this type essentially need protection devices in order to disconnect the grid from system entirely. There are mainly two types of faults in the electrical power system. Those are symmetrical and asymmetrical faults. But when fault occurs, it causes excessively high currents to flow which causes the damage to equipments and devices. Fault detection and analysis is necessary to select or design suitable switchgear equipments, electromechanical relays, circuit breakers and other protection devices [150, 151].

Symmetrical fault refer to power system faults where all three phases are influenced equally. These can occur when insulation fails due to system over-voltage resulting from lighting, or switching surges, insulation contamination, or due to other physical reasons and as well a result of adverse weather including falling trees on transmission lines. On other hand Asymmetrical faults are unbalanced faults between one or two of the three-phases usually caused by mechanical contact as a result of weathering on the transmission line. These faults occur more often than the symmetrical type [152].

Basically; the configuration of the DFIG has the stator circuit directly connected to the grid, while the rotor winding is connected to the grid via the back-to-back converter, and this is the reason for all efforts made to develop the FRT capability. In the case of a power grid system face the condition of a voltage drop at the PCC, the stator voltage of the DFIG will immediately change and if it not suddenly varies the rotor voltage will be compensate the dropping in stator voltage and this will drive to oscillate the stator and rotor currents with high incremental in its values [106]. This disturbance in the stator and rotor currents will cause damage to the rotor converter and increase the mechanical

stress on the wind turbine as a result of the transient in the electromagnetic torque of the generator. A wind energy conversion system (WECS) can only be disconnected from the grid during a fault condition which causes the voltage drop to exceed permitted limit, figure 5.1 depicted the ratio as a percentage of the actual voltage and normal voltage of the grid against time, during LVRT the systems requires reactive power from the WECS this reduces the instabilities to the to the grid voltage. Therefore wind farms are required to remain on line during voltage disturbances for up to specified time periods and associated voltage levels.

A key issue of concern regarding DFIG performance is that of fault ride-through. Network faults produce rapid voltage dips in any of the three phases connecting to a generating unit. The standard DFIG system is sensitive to such severe dips, inducing large transient currents in the stator and rotor circuits and risking over-current damage to the power electronic devices in the converters. Traditionally, to protect these devices, the rotor circuit is typically shorted or 'crowbarred', resulting in a considerable demand for reactive power from the grid, exacerbating the voltage problem [153]. The crowbar protection system is one type of the equipment used to avoid the disconnection of doubly-fed induction wind generators from the network during faults. The crowbar is inserted in the rotor circuits for a short period of time to isolate the RSC. As a general rule, the activation and deactivation of the crowbar system is based only on the DC-link voltage level of the back-to-back converters [146, 147]. However, wind power plants based on the DFIG are very sensitive to grid disturbances, especially voltage dips. When faults occur and cause voltage dips, the current flowing through the power converter may subsequently represent a very high over-current. During this situation, it is common to block the converter to avoid any risk of damage, and then to disconnect the generator from the grid [148, 149]. The disadvantage of utilizing the crowbar is that the RSC has to be disabled when the crowbar is activated and this means that the generator starts to consume reactive power leading to further deterioration of the grid voltage. Some studies employ an active crowbar control scheme to enhance the FRT capability, but this modification dose not avoids the consumption of reactive power [154, 155].

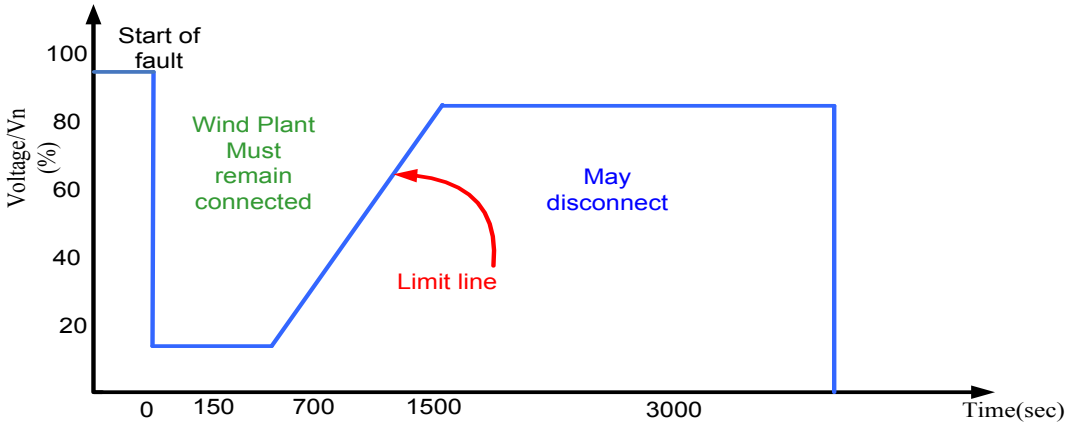

Figure 5.1: Typical voltage dip limit for LVRT [6, 145].

In the normal mode of operation, the RSC decouple controls the injection of active and reactive power. The optimum electric power reference is then calculated taking into account the optimal rotor speed for the incoming wind by the maximum value of the *Cp* curves. An encoder can pass the generator's rotor position (θ_r) to the *abc-dq0* and to the *dq0-abc* transformations. The direct axis component is used to maintain the generator power factor of 1 p.u., and thus the absorbed reactive power reference (Q^{ref}) is equal to zero. The quadrature axis component is controlled in a similar way the direct axis; however, it regulates the electrical power to the optimal value. The (v_d^*) and (v_q^*) reference signals are sent to the *dq0-to-abc* transformation and, then to the signal generator based on the PWM methodology. Finally v_{abcr}^* represents the three phase-voltages desired at the RSC output. In fault mode operation, the crowbar system is activated, where the three-phase series resistance (crowbar system) is connected to the rotor windings, and therefore the RSC is blocked.

The GSC control regulates the voltage of the DC link between the RSC and GSC. The controller employs a PLL to provide the angle (θ_s) to the *abc-to-dq0* and *dq0-to-abc* transformations. This angle gives the reference for the synchronization of the three-phase voltages of the converter output with the terminal voltage. The direct axis component is used to regulate the DC link voltage (v_{dc}^{ref}). The quadrature axis component of the reference current is set to zero $(i_q^{ref} = 0)$, since power factor control has already been accomplished by the GSC. (v_d^*) and the (v_q^*) reference signals are sent to the *dq0-to-abc* transformation, and then to the PWM signal generator. Finally, $(v_{abcgrid}^*)$ is the three-phase voltage desired at the grid-side converter output. In fault mode operation, the DC chopper is activated to dissipate the unbalanced active power

between the RSC and GSC. Meanwhile the GSC still maintains control of the DC link voltage. The reference quadreture current is switched from zero to the loop that generates this current in comparison voltage reference and terminal voltage to inject reactive power into the network. Tables 5.1 summarize the behavior of the RSC and GSC in normal and fault modes of operation.

Although the main task of GSC is to keep the DC-link voltage constant, it may also be used to compensate for the reactive power and magnetizing the DFIG or in some cases to remove the reactive power pulsation during unbalanced conditions. The RSC would provide the required magnetization current waveforms in rotor windings to generate the required active and reactive power at stator terminals. Voltage can be controlled by either RSC or GSC independently. If both, RSC and GSC are used for voltage control but operated in an uncoordinated mode there is a capability that one of them may dominate the response and take over the control that ultimately could lead to the absorption of reactive power by the other. In large disturbances, the excitation of rotor circuit through RSC may be limited or may even be completely isolated. using the reactive power generation limit of the GSC in a coordinated manner with the stator reactive power output contributes to terminal voltage support and reduces the requirements imposed on the RSC [164].

Table 5.1: Summery of the conventional modes of DFIG based WT operation in normal and fault conditions.

Normal Mode Operation	V <nominal	RSC	Tracking the Max Power
		GSC	Regulate the v_{dc}
		β*(pitch blade angle)*	Set $\beta = 0$
	V >nominal	RSC	Limiting the Power.
		GSC	Regulate the v_{dc}
		β(pitch blade angle)	Activated to limit power
Fault Mode Operation	Crowbar	Activated by inserted in series with the rotor windings	
	RSC	blocked	
	GSC	control reactive power	
	β	set to diminish the energy capture from the wind	
	crowbar	Removed after 100 *ms*	
	RSC	restarted	

5-4 Performance Analysis of the DFIG System with Voltage Dips

Over-voltages and over-current conditions are generated in the rotor winding of the DFIG-based wind turbine when voltage dip conditions occur on the PCC. These can be understood using the following analysis based on the voltage and flux equations in the stationary reference frame [7]:

$$v_s^s = r_s i_s^s + \frac{d}{dt}\lambda_s^s \tag{5.1}$$

$$v_r^s = r_r i_r^s + \frac{d}{dt}\lambda_r^s - j\,\omega_r\,\lambda_r^s \tag{5.2}$$

$$\lambda_s^s = L_s i_s^s + L_m i_r^s \tag{5.3}$$

$$\lambda_r^s = L_m i_s^s + L_r i_r^s \tag{5.4}$$

From equation 5.3; the stator current is:

$$i_s^s = \frac{1}{L_s}(\lambda_s^s - L_m i_r^s) \tag{5.5}$$

Then equation 5.5 is substituted in equation 5.4 to eliminate the stator current from the rotor flux as follows:

$$\lambda_r^s = \frac{L_m}{L_s}\lambda_s^s + L_r \sigma i_r^s \tag{5.6}$$

where ($\sigma = 1 - L_m^2/L_s L_r$), and the rotor voltage in equation 5.2 will have the following expression:

$$v_r^s = \frac{L_m}{L_s}\left(\frac{d}{dt} - j\omega_r\right)\lambda_s^s + (r_r + L_r\sigma\left(\frac{d}{dt} - j\omega_r\right))i_r^s \tag{5.7}$$

where the term ($\frac{L_m}{L_s}\left(\frac{d}{dt} - j\omega_r\right)\lambda_s^s = v_{ro}^s$) is the rotor voltage at open circuit and it due to the stator flux of magnetic coupling. The final term in equation 5.7 is the voltage resulting from rotor-side circuit (RSC) and crowbar. In normal conditions, the space vector of the stator voltage is:

$$v_s^s = v_s e^{j\omega_s t} \tag{5.8}$$

where v_s is the constant amplitude. Now equation 5.8 is substituted in equation 5.1, and therefore:

$$v_s e^{j\omega_s t} = r_s i_s^s + \frac{d}{dt}\lambda_s^s \tag{5.9}$$

If the stator resistance is neglected and integration conducted on both sides of equation 5.9, then:

$$\frac{v_s}{j\omega_s} e^{j\omega_s t} = \lambda_s^s \tag{5.10}$$

Substituting equation 5.10 in the term for the rotor open circuit:

$$v_{ro}^s = \frac{S.L_m}{L_s} v_s e^{j\omega_s t} \tag{5.11}$$

The term (s) in equation 5.11 is the slip. Therefore, the maximum value of the rotor open circuit is:

$$v_{ro}^s = \frac{S.L_m}{L_s} v_s \tag{5.12}$$

Then the total value of rotor voltage will be:

$$v_r^s = \frac{s.L_m}{L_s} v_s + (r_r + L_r\sigma\left(\frac{d}{dt} - j\omega_r\right))i_r^s \tag{5.13}$$

In equation 5.13, the first term is related to stator voltage and the second term is related to rotor current. If the rotor is open-circuit, the rotor voltage, which is (v_{r0}^s), is proportional to the slip frequency and stator voltage. Even if the rotor is connected and rotor current is present, since (r_r) and $(L_r\sigma)$ are usually very small, the total rotor voltage v_r^s is still dominated by (v_{r0}^s). Therefore, considering $|s| \leq 0.3$ in the normal operation of a typical DFIG, the amplitude of rotor voltage usually does not exceed 30% of the nominal stator voltage.

In conditions where three-phase voltage dips occur due to a symmetrical voltage disturbance on the stator's DFIG system terminal, DFIG performance can be investigated by characterize the limits and values of the voltage varying in the range $(v_0 > v_1)$. Since $v_0 = v_s$ and $v_1 = (1-p)v_s$ where (p) is the voltage dip ratio [11], thus, if it is assumed that the DFIG is to operate in the normal condition when at a specific time (t_0) a voltage dip of depth (p) occurs, the stator voltage is given by:

$$v_s^s = \begin{cases} v_0 e^{j\omega_s t} & for\ t < t_0 \\ v_1 e^{j\omega_s t} & for\ t \geq t_0 \end{cases} \tag{5.14}$$

By substituting equation 5.5 in equation 5.1 with the assume that the condition for the open rotor circuit (i_r^s =0) is met the following is given:

$$v_s^s = \frac{r_s}{L_s}\lambda_s^s + \frac{d}{dt}\lambda_s^s \tag{5.15}$$

Solving the differential equation, the stator flux in conditions of voltage dip is then:

$$\lambda_s^s = \frac{v_1}{j\omega_s}e^{j\omega_s t} + \frac{v_0 - v_1}{j\omega_s}e^{-jt/\tau_s} \tag{5.16}$$

where:

- $\frac{v_1}{j\omega_s}e^{j\omega_s t}$ (forced flux) is the rotation flux space vector corresponding to the grid during voltage dip.
- $\frac{v_0 - v_1}{j\omega_s}e^{-jt/\tau_s} = \frac{(1-p)v_s}{j\omega_s}e^{-jt/\tau_s}$ (natural flux) is the fixed flux of the stator which decreases exponentially to zero by the stator time constant ($\tau_s = \frac{L_s}{r_s}$).

Substituting the stator flux in equation 5.16 in the rotor open voltage equation gives:

$$v_{ro}^s = \frac{L_m}{L_s}(s.v_1 e^{j\omega_s t} - (\frac{1}{\tau_s} + \omega_r)\frac{v_0 - v_1}{\omega_s}e^{-jt/\tau_s}) \tag{5.17}$$

Canceling ($\frac{1}{\tau_s}$), since it is very small, gives:

$$v_{ro}^s \approx \frac{L_m}{L_s}(s.v_1 e^{j\omega_s t} - (1-s)(v_0 - v_1)e^{-jt/\tau_s}) \tag{5.18}$$

Equation 5.18 can be expressed in the rotor reference frame by multiplying it by($e^{-j\omega_r t}$) to give:

$$v_{ro}^r \approx \frac{v_s L_m}{L_s}(s.(1-p)e^{js\omega_s t} - (1-s)pe^{-j\omega_r t}e^{-t/\tau_s}) \tag{5.19}$$

And then the maximum rotor voltage is:

$$v_{ro}^s = \frac{L_m}{L_s}(|s|v_1 + (1-s)(v_0 - v_1)) \tag{5.20}$$

5-5 DFIG Analysis During Voltage Swell

Of the different grid faults, voltage swells are less common than voltage sags, but are also usually associated with system fault conditions. A swell can occur due to a single line-to-ground fault in the system, which can result in a temporary voltage rise in the not fault-free phases. Swells can also be generated by sudden drops in load. The abrupt interruption of the current can generate a large voltage. Switching on large capacitor

banks may also cause a swell [32]. High voltage ride-through means that the DFIG-based wind turbine needs to stay connected to the grid when over-voltage occurs with continuous and stable performance. It is necessary to reverse the power flow across the GSC, and thus the current will flow from the grid-side into the DC-link. The DFIG's performance under symmetrical voltage swell conditions can be investigated by characterizing the limits and values of the voltage variation in the range ($v_1 > v_0$), knowing that $v_0 = v_s$ and $v_1 = (1+p)v_s$where(p) is the voltage incremental ratio [156].

$$v_s^s = \begin{cases} v_0 e^{j\omega_s t} = v_s e^{j\omega_s t} \ \ for\ t < t_0 \\ v_1 e^{j\omega_s t} = (1+p)v_s e^{j\omega_s t} \ \ for\ t \geq t_0 \end{cases} \tag{5.21}$$

By solving equation 5.15 with the condition of equation 5.21, hence the stator flux will be formulated as:

$$\lambda_s^s = \frac{(1+p)v_s}{j\omega_s} e^{j\omega_s t} - \frac{pv_s}{j\omega_s} e^{-(t-t_0)/\tau_s} \tag{5.22}$$

where:

- $\frac{(1+p)v_s}{j\omega_s} e^{j\omega_s t}$ represents the forced flux which is proportional to grid voltage $(1+p)v_s$ and which rotates at synchronous speed.
- $\frac{pv_s}{j\omega_s} e^{-(t-t_0)/\tau_s}$ represents the natural flux which is a transient flux that guarantees no discontinuities appear in the machine. Its amplitude decreases exponentially to zero and it does not rotate.

By substituting equation 5.22 in first term of equation 5.7, the rotor voltage:

$$v_{ro}^s = \frac{L_m}{L_s}(s.v_s(1+p)e^{j\omega_s t} + (1-s)v_s p e^{j\omega_s t_o} e^{-\frac{t-t_0}{\tau_s}} + \frac{v_s p}{j\omega_s \tau_s} e^{j\omega_s t_o} e^{-\frac{t-t_0}{\tau_s}}) \tag{5.23}$$

Neglect term $(\frac{1}{\tau_s})$ in the open circuit rotor voltage induced by stator flux:

$$v_{ro}^s \approx \frac{L_m}{L_s}(s.v_s(1+p)e^{j\omega_s t} + (1-s)v_s p e^{j\omega_s t_o} e^{-\frac{t-t_0}{\tau_s}}) \tag{5.24}$$

5-6 Reactive Current Constraint of the GSC During Grid Voltage Dips and Swells

The stability of the DC bus voltage is the premise of uninterrupted operation of DFIG systems when grid faults occur. The steady-state voltage equation of the GSC in the synchronously rotating coordinate can be derived from equations 3.70 and 3.71, hence:

$$v_{df} = r_f i_{dg} + v_{dg} - \omega_e L_f i_{qg} \tag{5.25}$$

$$v_{qf} = r_f i_{qg} + \omega_e L_f i_{dg} + v_{qg} \tag{5.26}$$

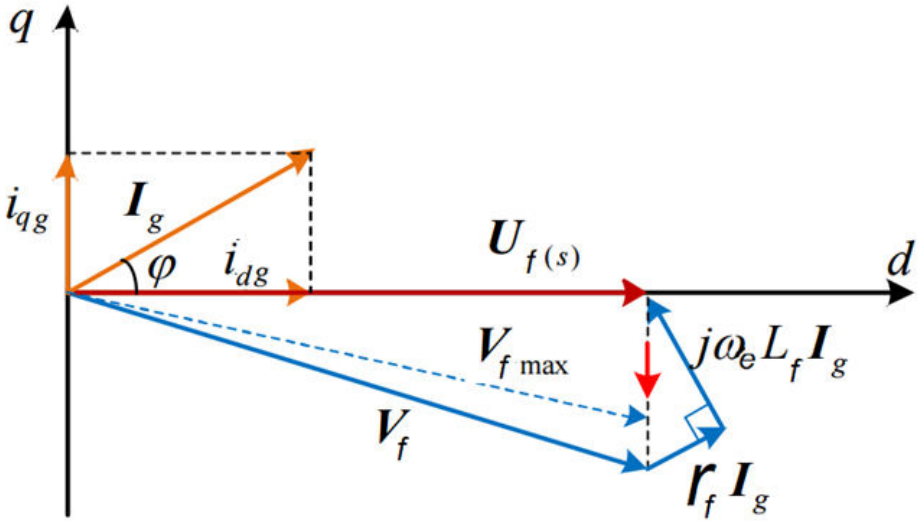

Figure 5.2: Spatial relationship of GSC steady-state voltage vectors [157].

DC link voltage should obey the power balance relationship shown in equation 3.95. The steady-state voltage space vector diagram of the GSC can be depicted as in figure 5.2 with (φ) being the power factor angle. From figure 5.2, it can be concluded that the terminal of the output voltage vector should always fall on the hypotenuse of the impedance triangle, with its magnitude restricted by the rated operational voltage across the DC-bus capacitor. This is actually based on voltage modulation theory, which states that without over-modulation the modulation ratio m needs to satisfy the following equation [157]:

$$m = \sqrt{v_{dg}^2 + v_{qg}^2} / \left({}^{v_{dc}}/_{2}\right) \leq 2/\sqrt{3} \tag{5.27}$$

If grid voltage orientation is adopted, v_{df} is the magnitude of the grid phase voltage vector. Meanwhile, if small voltage drops across r_f are ignored, equations 5.25 and 5.26 can be further simplified as:

$$v_{dg} = v_{df} + \omega_e L_f i_{qg} \tag{5.28}$$

$$v_{qg} = -\omega_e L_f i_{dg} \tag{5.29}$$

Substituting equations 5.28 and 5.29 into equation 5.27, it is found that [158]:

$$v_{dc} \geq \sqrt{3}\sqrt{\left(v_{df} + \omega_e L_f i_{qg}\right)^2 + \left(-\omega_e L_f i_{dg}\right)^2} \tag{5.30}$$

Equation 5.30 gives the operational constrains of the GSC with the DC link voltage, grid voltage, and inductor and load currents being the main parameters. It can be determined that the minimum value of the DC link voltage should be no less than the grid line voltage (i.e. $v_{dc} \geq \sqrt{3}v_{df}$) when the GSC operates in unity power factor mode, i.e., $i_{qg=0}$. Actually, this is caused by the natural attributes of the GSC boost circuit. Based on the above discussion, the GSC reactive current limit can then be analyzed and acquired for voltage sags and swells. In voltage sag conditions the maximum reactive current i_{qg} of the GSC depends on the overall active power of the system and the slip ratio while in the voltage swell conditions the minimum reactive current depends on both the grid voltage and the active current i_{dg} [157, 158]. The stable control of DC-bus voltage value is the mark for deciding whether the wind power generators can detect voltage swell. In order to ensure the stable control of the normal operation of GSC and DC voltage during the voltage swell of the power grid, DC-bus voltage needs to meet the limits in equation 5.30. The right side of formula 5.30 is expressed as minimum value of DC voltage. When GSC absorbs certain inductive reactive current, therefore the minimum DC voltage limit is reduced. Then, when the voltage swell of the power grid causes the voltage rise of the wind power generator port, the normal operation of GSC can be realized through the control of quadrture current component. If the voltage continuously rises, then the output range of GSC will be exceeded. Therefore, GSC is based on the reactive power outputted which is cannot meet the high voltage ride-through demand for the DFIG system. The GSC reactive current usually possesses an inductive behaviour, which is useful for reducing the required DC-bus voltage. Due to the fact that the current capacity of the RSC is

usually designed a approximately larger than that of the GSC, the output active power of the RSC during the voltage swell cases should be set so that it is not more than that of the GSC [157].

5-7 Improved FRT Control Scheme for the DFIG Wind Turbine

Different methods have been investigated to monitor the improvement of the DFIG-based wind turbine's ride-through ability during severe voltage dip conditions. These techniques of control have several advantages, since they fully utilize existing electrical resources in DFIG wind turbine system without the need for additional hardware components. In addition these strategies will keep the back-to-back converter connected to the DFIG even when the grid suffers from voltage drops, and also the DFIG can be equipped with a crowbar to protect against severe grid faults but to reduce the activation of the crowbar during the brief periods of voltage dips. It is necessary to formulate the stator and rotor currents in terms of stator voltage in order to approximately describe the influence of voltage on these currents. The stator flux equations 3.20 and 3.21 are used along with the stator voltage in the synchronous reference frame as formulated in equations 3.12 and 3.13 and by apply the Laplace transformation to equations 3.12 and 3.13, and after substitute into equations 3.20 and 3.21 in the stator voltage equations, the stator currents can be characterized in terms of stator voltages and rotor currents as follows [120, 121]:

$$i_{ds} = \frac{(L_s S + r_s)\, v_{ds} + L_s\, \omega_s\, v_{qs}}{L_s^2 S^2 + 2L_s r_s S + r_s^2 + L_s^2 \omega_s^2} - \frac{(L_s\, S^2 + r_s S + L_s\, \omega_s^2) L_m i_{dr} - \omega_s\, L_m r_s i_{qr}}{L_s^2 S^2 + 2L_s r_s S + r_s^2 + L_s^2 \omega_s^2} \tag{5.31}$$

$$i_{qs} = \frac{(L_s s + r_s)\, v_{qs} - L_s\, \omega_s\, v_{ds}}{L_s^2 s^2 + 2L_s r_s s + r_s^2 + L_s^2 \omega_s^2} - \frac{(L_s\, s^2 + r_s s + L_s\, \omega_s^2) L_m i_{qr} + \omega_s\, L_m r_s i_{dr}}{L_s^2 s^2 + 2L_s r_s s + r_s^2 + L_s^2 \omega_s^2} \tag{5.32}$$

By simplifying equations 5.31 and 5.32 by assuming that ($\lambda_{ds} = \lambda_s$), ($\lambda_{qs} = 0$), ($v_{ds} = 0$), ($v_{qs} = v_s$), and ($L_m \ll L_s, L_r$), then [155]:

$$i_{ds} = \frac{\omega_s\, v_{qs}}{L_s\, (s^2 + \frac{2r_s s}{L_s} + \omega_s^2)} - \frac{L_m i_{dr}}{L_s} \tag{5.33}$$

$$i_{qs} = \frac{(s + \frac{r_s}{L_s}) v_{qs}}{L_s\, (s^2 + \frac{2r_s s}{L_s} + \omega_s^2)} - \frac{L_m i_{qr}}{L_s} \tag{5.34}$$

As can be noticed from equations 5.33 and 5.34, the rotor current and the stator voltage appear as input variables, as the former is fixed by the RSC while v_{qs} depends on the grid behaviour. Any variation in stator voltage introduces oscillations in the *dq* components of the stator currents in the synchronous reference frame. The frequency of such oscillations is equal to the grid frequency and its damping is very poor, due to the low value of the stator resistance (r_s).

The configuration set the reference values set for active and reactive power in the outer RSC loop control, as soon as the voltage dips detect by the fault relies that activate the values until the fault clear to limit the fluctuating of stator and rotor currents. This scheme is already existing strategy for reducing the current peaks during voltage sag. The condition of this case considering that the control of the power delivery is based on the field-oriented control (FOC) philosophy where the active and reactive power magnitudes can be calculated from equations 5.35 and 5.36 [120]:

$$P_s^{ref} = \frac{3}{2}\, v_{qs}\ \ i_{qs} \tag{5.35}$$

$$Q_s^{ref} = -\frac{3}{2}\, v_{qs}\ \ i_{ds} \tag{5.36}$$

The second term of equations 5.35 and 5.36 represents the stator currents, and these can be substituted with the expressions found in equations 5.33 and 5.34 and condition of null active and reactive power:

$$P_s^{ref} = \frac{3}{2}\, v_{qs} \left(\frac{\left(s+\frac{r_s}{L_s}\right) v_{qs}}{L_s\left(s^2+\frac{2r_s s}{L_s}+\omega_s^2\right)} - \frac{L_m i_{qr}}{L_s} \right) = 0 \tag{5.37}$$

$$Q_s^{ref} = -\frac{3}{2}\, v_{qs} \left(\frac{\omega_s\ v_{qs}}{L_s\left(s^2+\frac{2r_s s}{L_s}+\omega_s^2\right)} - \frac{L_m i_{dr}}{L_s} \right) = 0 \tag{5.38}$$

Now the rotor currents equations can be deduced from equations 5.37 and 5.38. Given that the magnitude of the stator voltage can be different from zero, the only way to guarantee a null delivery of active and reactive power is to set the rotor current reference equal to zero. This yield the rotor current components shown in equations 5.39 and 5.40 which will regulate in the inner control loop will take in consideration the drop of in stator voltage.

$$i_{dr} = \frac{\omega_s \, v_{qs}}{L_m(S^2+\frac{2r_s S}{L_s}+\omega_s^2)} \tag{5.39}$$

$$i_{qr} = \frac{(S+\frac{r_s}{L_s})v_{qs}}{L_m(S^2+\frac{2r_s S}{L_s}+\omega_s^2)} \tag{5.40}$$

From equations 5.39 and 5.40, it can be concluded that the feedback of the rotor currents produce an oscillation with an attenuation factor equal to $(1/L_m)$ and the rotor currents will never be equal to zero since there is always a small residual voltage at the PCC. Thus, there is a small magnetizing current. The proposed control strategy will permit to reduction the over-currents in the generator's windings during the fault. The soft damping of the oscillations in the currents is due to the relationship between the stator resistance and the magnetizing inductance which yields a low damping factor. Figure 5.3 depicts the RSC outer loop control modification to improve the FRT ability of the DFIG system using the PQ null method.

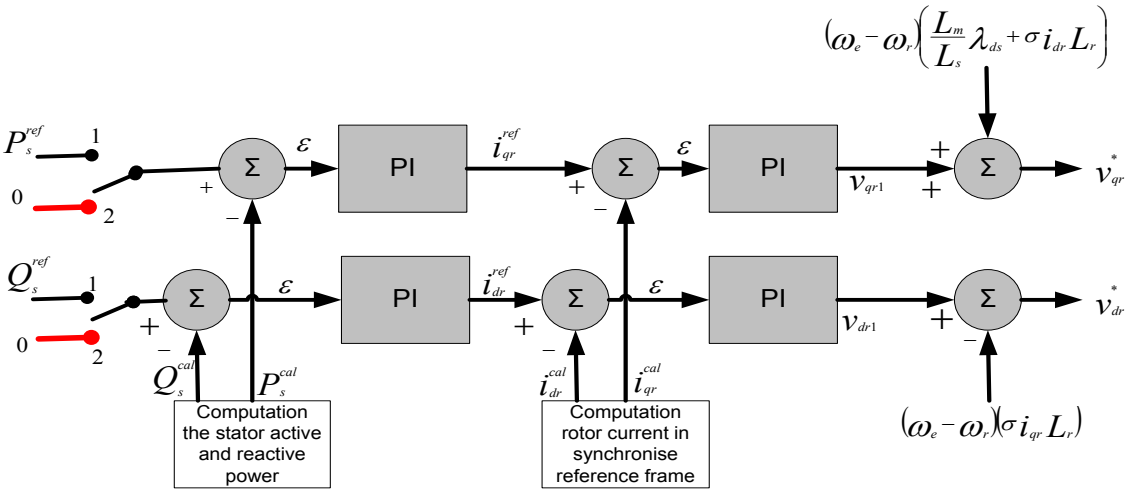

Figure 5.3: Diagram of null the active and reactive power method.

5-8 Detection of Disturbances in the DFIG System

The over-current relay has an inverse time-current characteristic where the tripping time becomes longer as the fault current decreases, and the tripping time is at a maximum for a fault current equal to the pick-up current $\boldsymbol{I_{pick}}$ of the relay. The

following equation represents the relationship between the fault current and the tripping time [159]:

$$\boldsymbol{t_p = \frac{T_1}{\left(I/I_{pick}\right)^{\propto}} + T_2} \tag{5.41}$$

where t_p is the time for pick-up, T_1 is a time constant depending on the trip relay design parameters, T_2 is a time constant that accounts for saturation in the magnetic circuit, $\propto$ changes according to the type of relay (inverse, extremely inverse ..and so on), and finally I_{pick} is the relay set pick-up current [159]. Equation 5.41 implies that the relay responds to the true rms value of the input current. Figure 5.4 shows the relay's current-time characteristics which were employed to the delay time of the over-current protection system in this study. This is 0.03 second and because at the instant of an 80% voltage dip test the maximum over-current in the system reached 3500A as shown in figure 5.5 where the relay characteristics are superimposed on the over-current seen by the relay.

As shown in figure 5.6a, an over-current trip model is used in the grid-connected DFIG-based wind turbine system. In the model, amplitude phase currents are compared with a defined current in p.u, which represents the protection activation trip. The three-phase current is split into its three phase counterparts which are inputted to the amplitude operator. If the current of any phase exceeds the set tolerances then the system will be assume that the over-currents are a direct result of a fault occurrence. If the input current has amplitude greater than the stipulated limits, the output will then become logic "1". In other words if any of the phase currents exceed the threshold, the protection is activated.

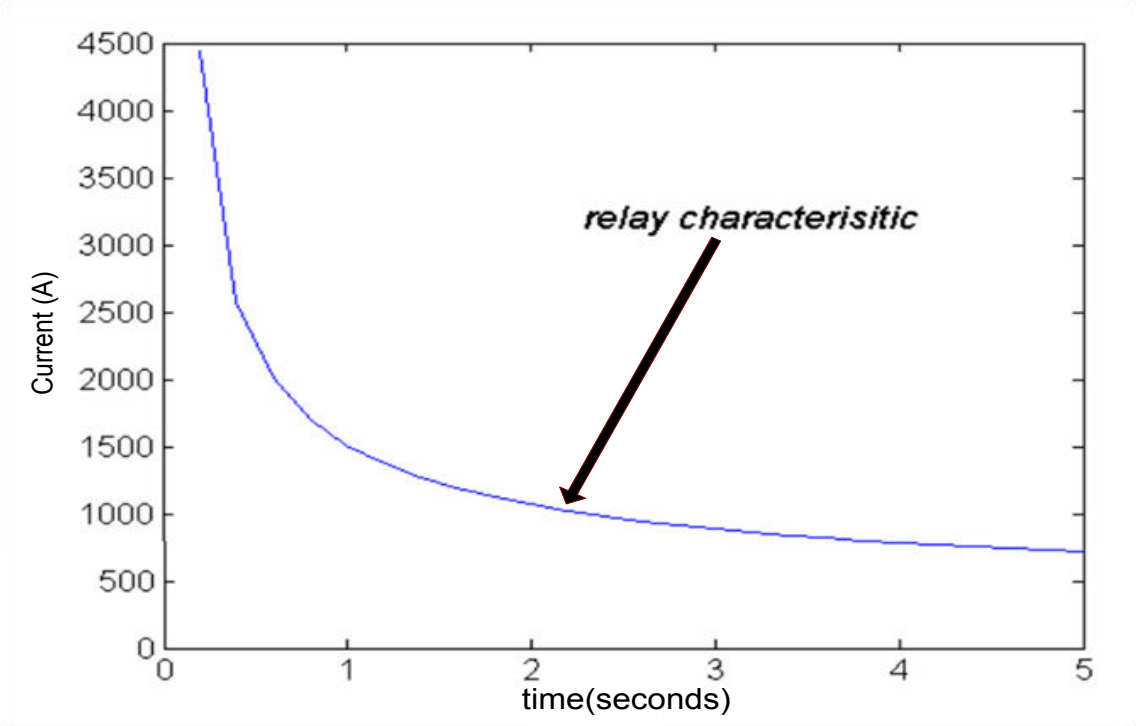

Figure 5.4: Inverse time relay characteristics [159].

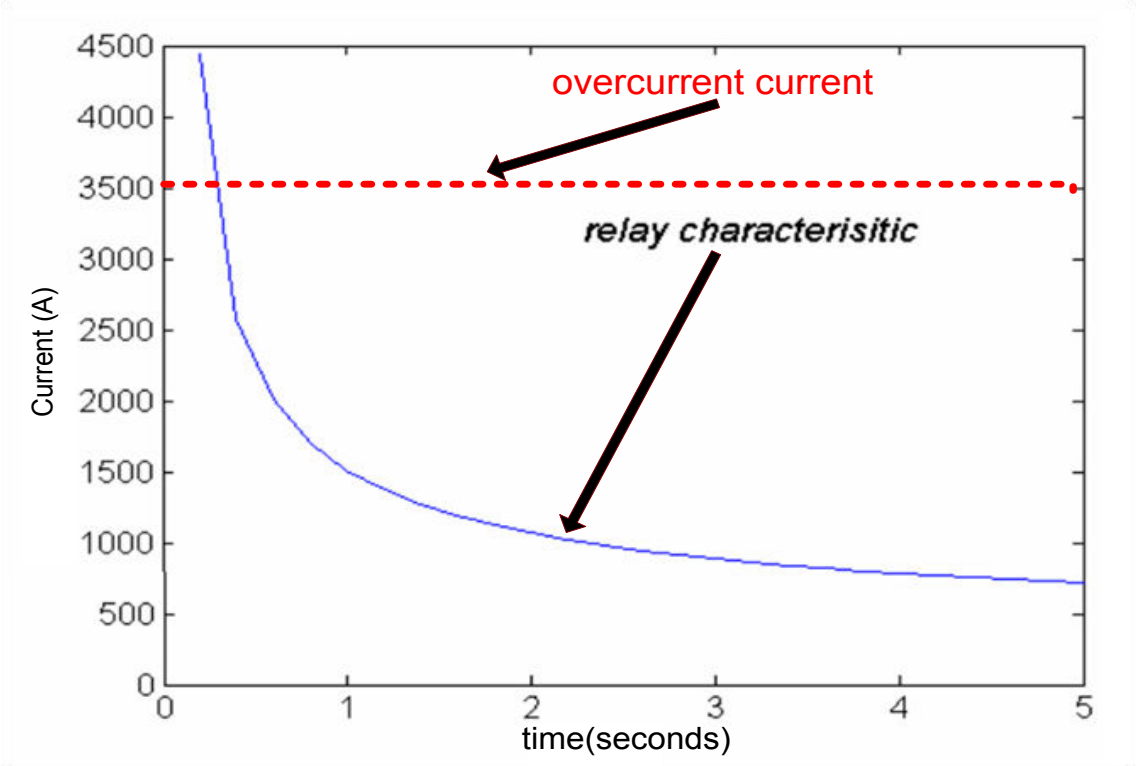

Figure 5.5: Relay characteristic and over-current.

The model for wind turbine voltage trip protection used in this study is the same as that in 1.5 MW DFIG Demo/ MATLAB® in which the positive sequence voltage is given as an input, and for its corresponding value trip data is used to see whether it should be

tripped or not. The different reasons for tripping may be AC over-voltage, under-voltage. Figure (5.6b) illustrates the under/over voltage trip model that compares of the positive sequence voltage component magnitude calculated from the input three-phase voltage with the upper and lower limits of the normal operation voltage as well as detecting any disturbance in the voltage profile and sending the logic signal to the crowbar system in the DFIG to active if with an appropriate delay. The under-voltage setting shall be less than or equal to the lowest operation voltage of the grid.

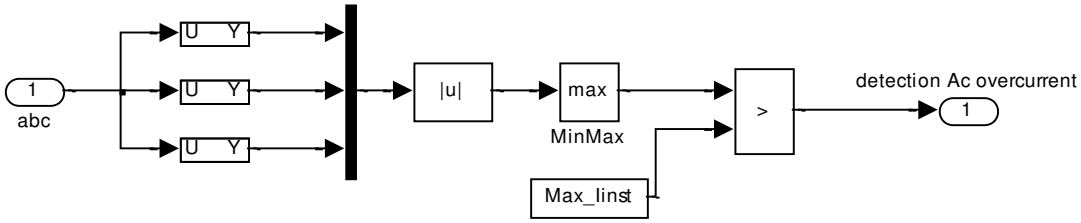

(a)

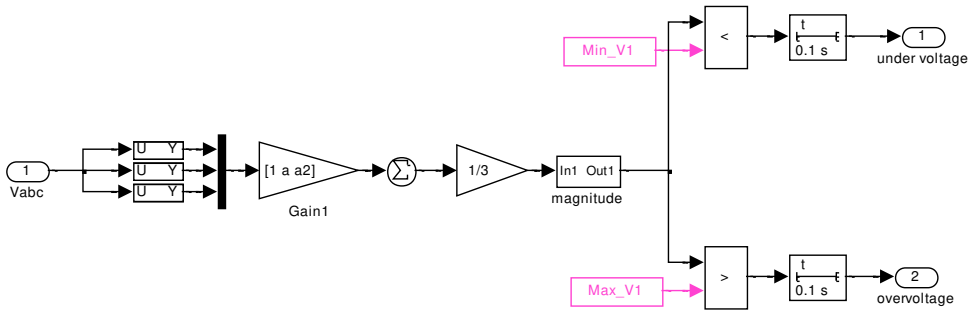

(b)

Figure 5.6: MATLAB/SIMULINK® subsystem: (a) over-current trip model; (b) over/under voltage trip model

5-9 Performance of Grid Connected DFIG System Without Protection

5-9-1 The Case of (80%) Voltage Dips

The transfer function of the DFIG machine have two poorly damped poles which oscillated frequency approach to the line frequency and these poles will leads to a fluctuation in the flux if a grid disturbance occur on the PCC of the DFIG. Therefore,

after the system is subjected to grid disturbance, it will be important to increase the rotor voltage to control the rotor currents if this needs the voltage of exceed the limits of the power converter, thus it will be incapable of control the current as required. This reveals that the voltage dip will cause highly induced voltage and currents if there is no longer a protection strategy adapted to the system. In this investigation the DFIG is subjected to a severe voltage dip with drop value of 80% depth for a period of 0.5-0.6 second. The RSC and GSC have both been controlled using the vector control with assume the DFIG system produce zero reactive power and the nominal rated active power is injected to the grid during a constant wind speed of 4 m/sec during this simulation. When reductions in stator flux result from the voltage dip, the direct and quadrature flux components will fluctuate during the voltage dip and after the clearance of the fault. In addition, the *q*-axis stator flux cannot be maintained at zero due to the voltage dip.

As shown in figures 5.7 and 5.8 the voltage dip of 80% at the terminal of the DFIG system leads to transient over-currents in both the stator and rotor windings as illustrated in figures 5.9-5.12 with increments of about 2 p.u. Then it decays exponentially subject to the RSC which causes a large stress upon it. In addition, the step increment is clearly depicted in the total *rms* grid current in figure 5.13 as a result of the sag condition. On the other hand the DC-link voltage fluctuated during the voltage dip until it reaches limit and then returns to regulate it around the set value after fault removal as depicted in figure 5.14.

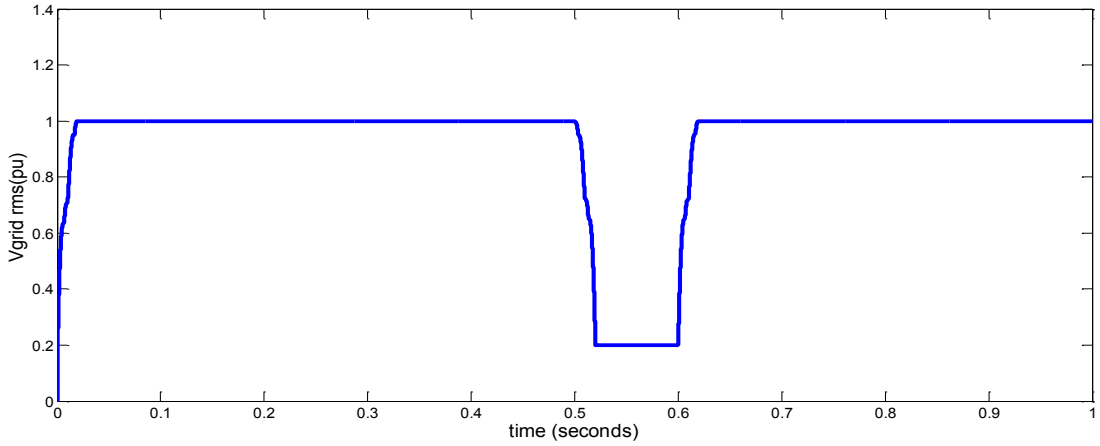

Figure 5.7: Instantaneous *rms* grid voltage.

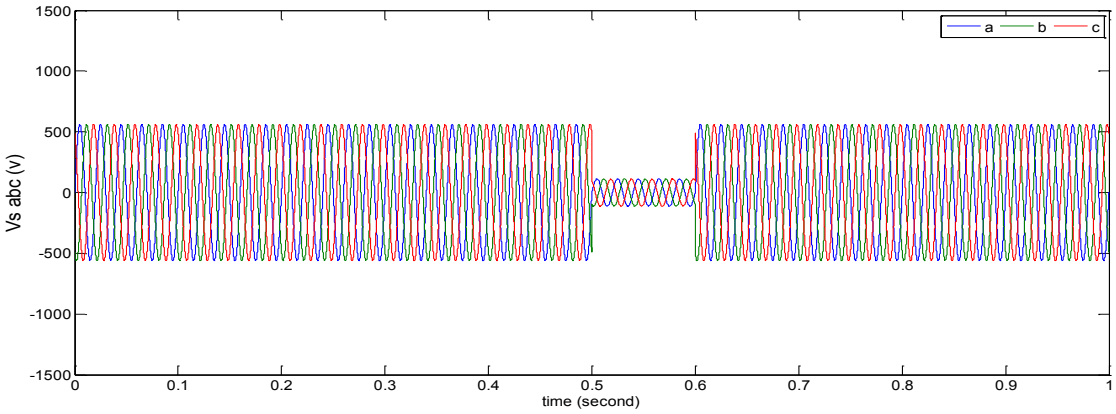

Figure 5.8: Instantaneous three-phase stator voltage.

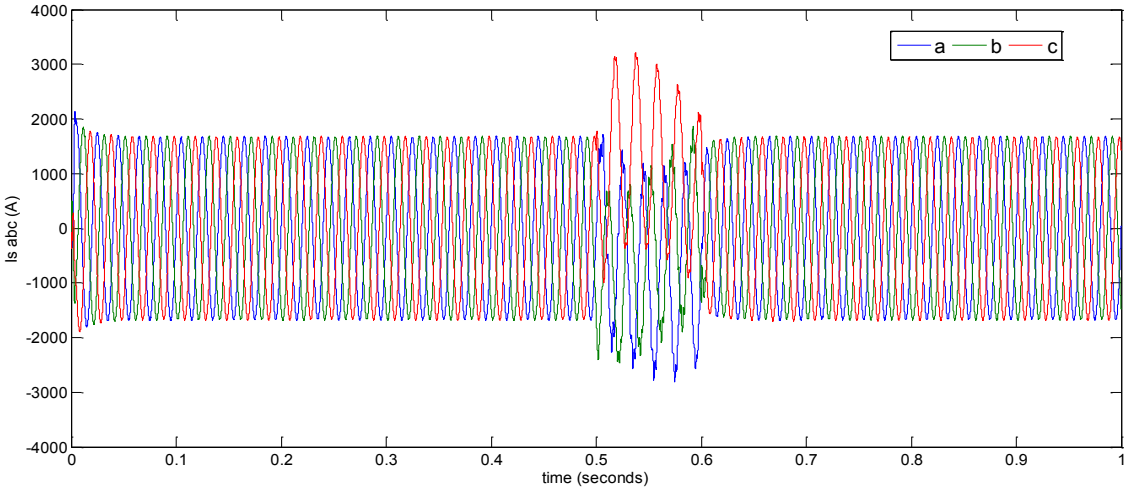

Figure 5.9: Instantaneous three-phase stator current.

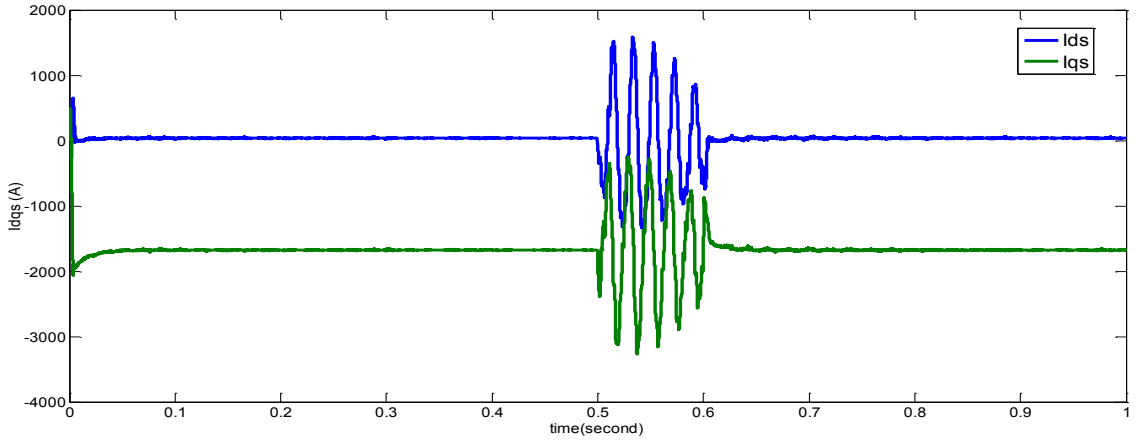

Figure 5.10: Instantaneous *dq* stator current.

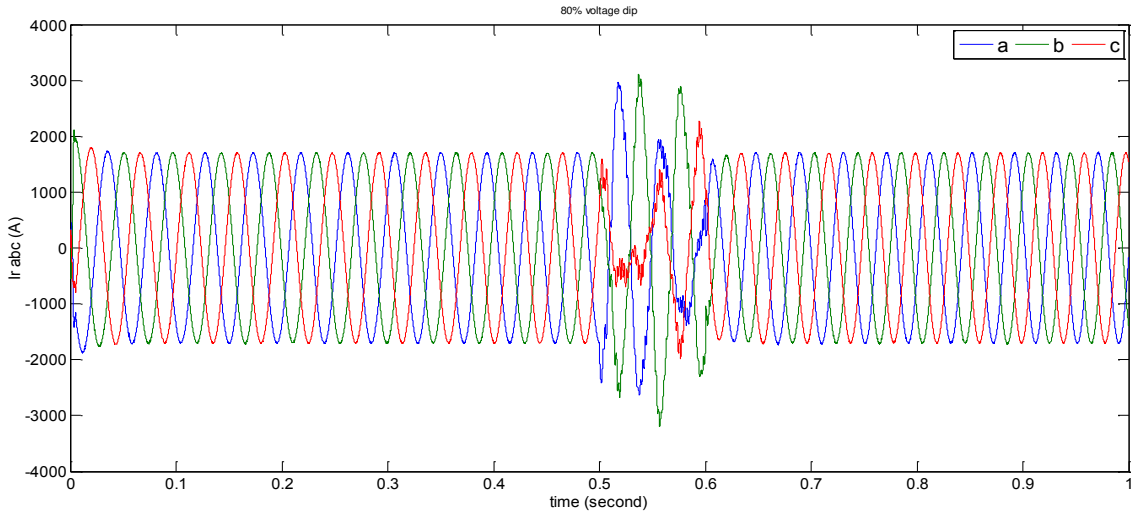

Figure 5.11: Instantaneous three-phase rotor current.

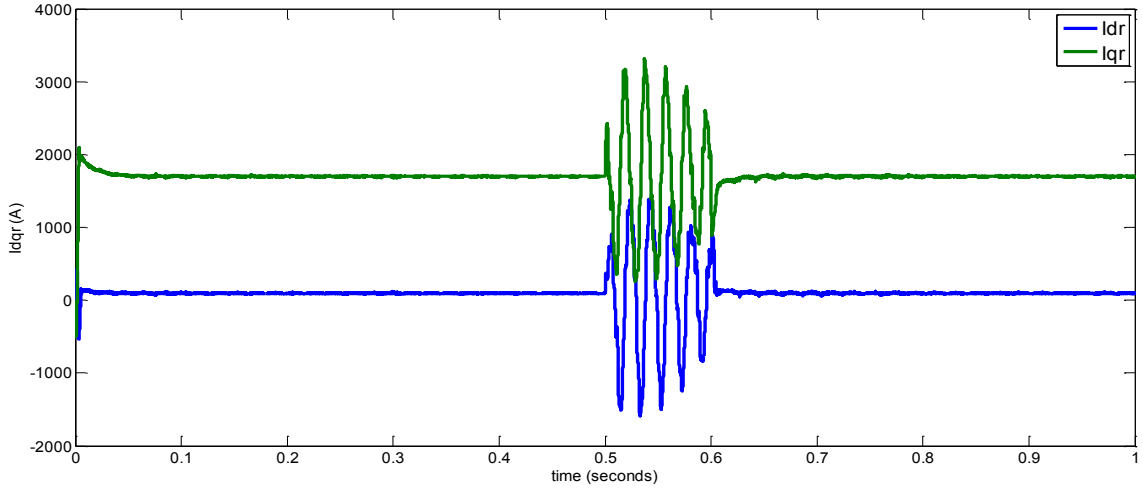

Figure 5.12: Instantaneous *dq* rotor current.

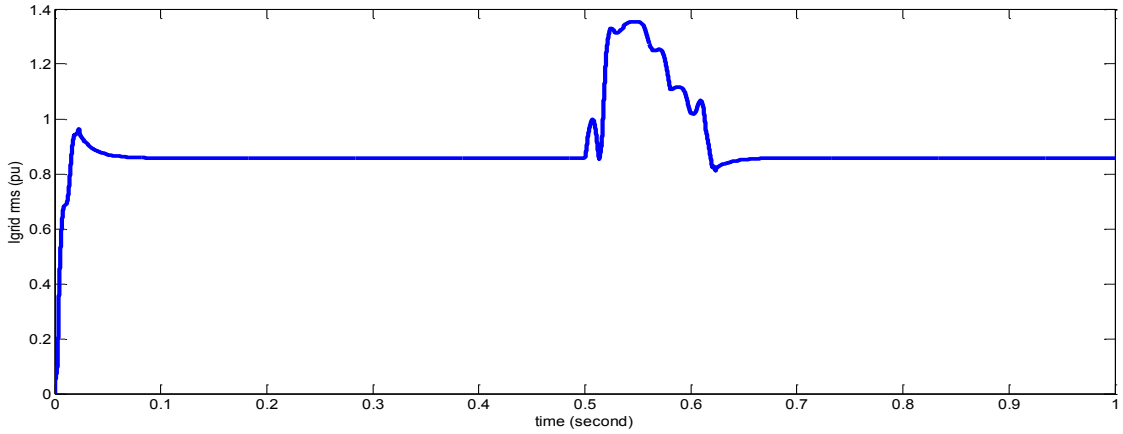

Figure 5.13: Instantaneous measurements of *rms* grid current.

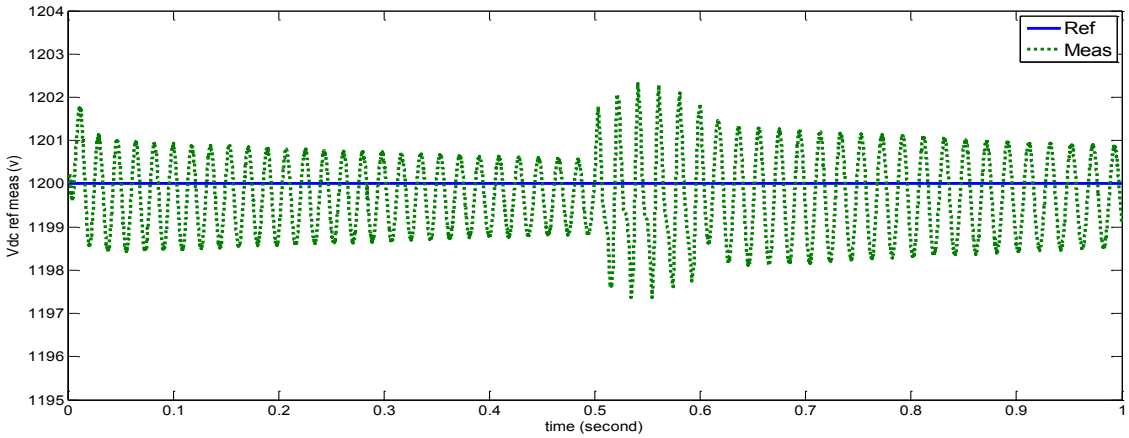

Figure 5.14: DC-link voltage regulator in the GSC.

The stator active and reactive power tracking of the reference set points is shown in figure 5.15 and figure 5.16, the results indicate severity of the system simulation during the voltage dip period where both the active and reactive power vary and lose controllability. The active power decreases nearly to zero while the reactive power is absorbed by the machine. At voltage dip initiation, the vector control of the rotor-side converter is provisionally lost. The brief surge in power output is associated with the rapid demagnetization of the DFIG associated with large, oscillatory active and reactive power as illustrated in figures 5.15 and 5.16. After fault clearance, the power controller requires 20ms to settle the highly oscillatory output, and its ability for recovery depends on the magnitude of the recovery voltage and the stabilize the generator speed. The reactive power rises quickly after fault initiation to the same peak level as the active power, of 0.1 MVAR, before oscillatory decay. After fault

clearance, the DFIG start to re-magnetize. However, this effect lasts for less than one system cycle.

The generator speed shown in figure 5.17 represent as increase of 0.19% associated with the brief increase in power output following the fault. The DFIG rotor speed confirmed the relatively small impact after a voltage dip duration. Although the speed rises by over 6% during the voltage dip, this was partially offset by a 2% decrease in speed associated with the demagnetization energy dissipated from the machine. The currents of the grid-side converter (GSC) shown in figure 5.18 appear thicker with high frequency noise due to the relatively low-impedance low-pass filter fitted to the converter. Note that the pre-fault currents are far smaller than the rotor current because only active power is delivered to the grid. In normal conditions, the rotor converter also provides a magnetisation current to the generator. The GSC inject only enough current to balance the rotor exchang power input. The grid fault caused an immediate increase in converter current. After a small spike in current, the active current was brought downto -40 A by the controller in an attempt to reduce the DC-link voltage.

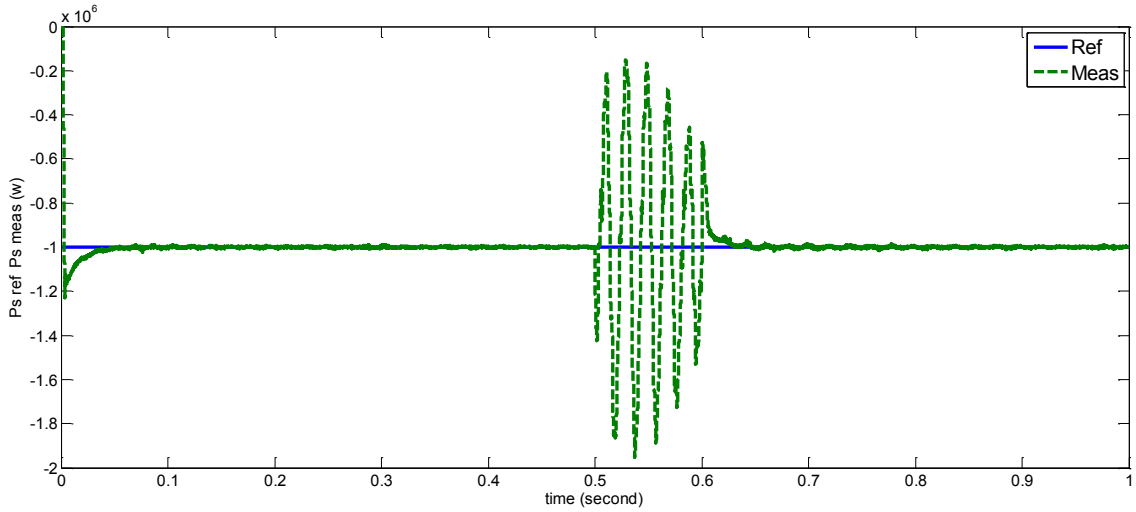

Figure 5.15: Instantaneous regulation of the stator active power in the RSC.

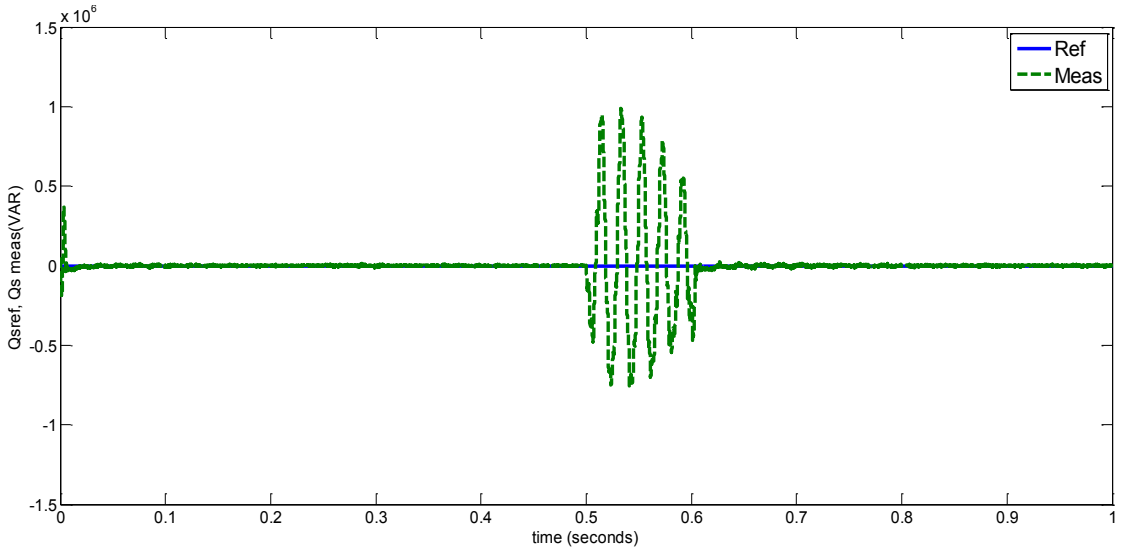

Figure 5.16: Instantaneous regulation of the stator reactive power in the RSC

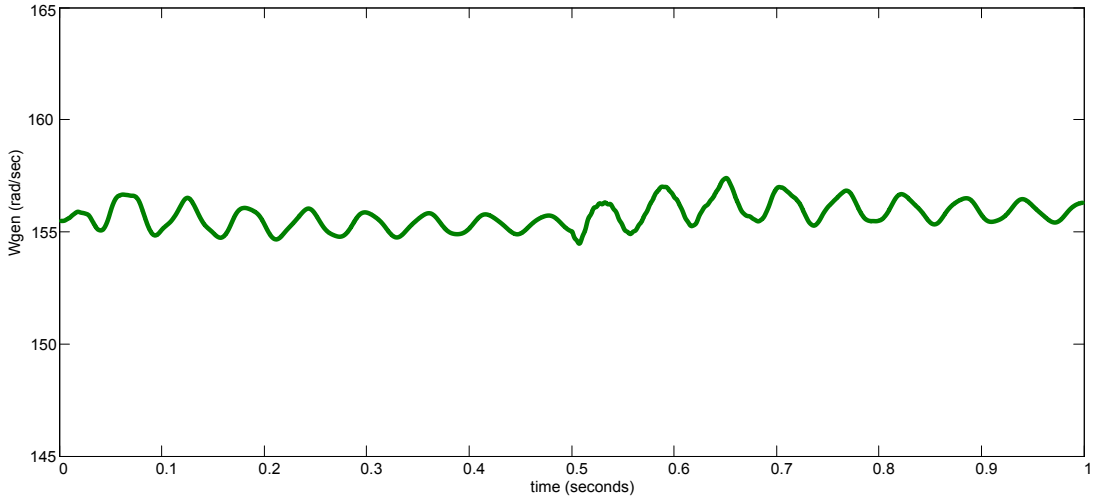

Figure 5.17: Instantaneous measurement of generator speed.

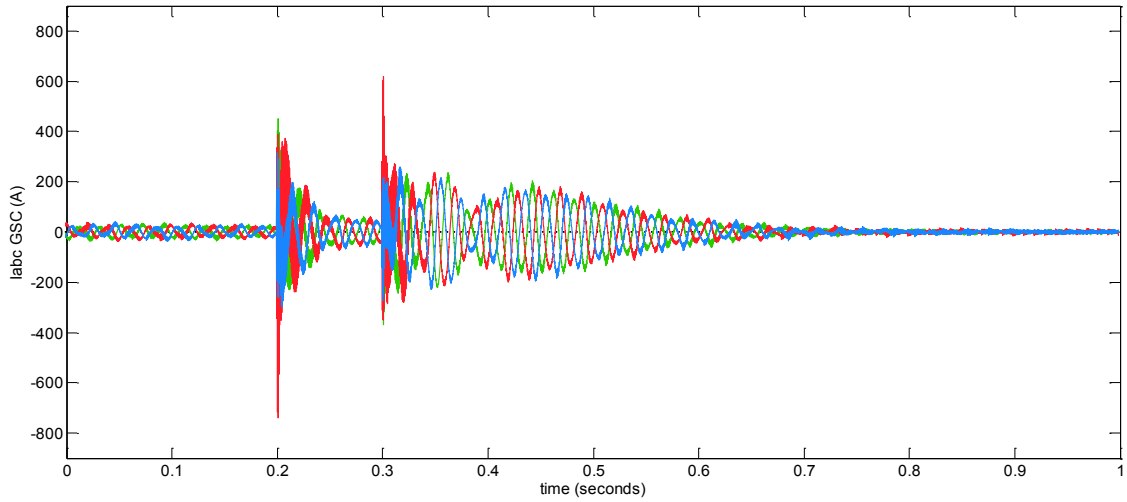

Figure 5.18: Instantaneous measurement of three-phase current of the GSC.

To demonstrate the performance of the mechanical drive train 2-mass model during voltage dips, The electromagnetic and aerodynamic torque behaviour and rotational speed generator and rotor are illustrated in figures 5.19 and 5.20 respectively. Here the speed and torque values of the low-side shift have been converted to the high-speed side of the gearbox which is the induction machine shaft side to allow a simpler evaluation of the system during voltage dip conditions.

Aerodynamic and electromagnetic torque represent the input quantities for the model, while changes in the turbine‘s rotor speed and generator speed are the output. During a worst case grid-side voltage dip condition, where the grid voltage falls to 20% at 0.5 sec, the stator flux decreases to an extremely small value, and the induction machine is no longer able to generate electrical torque. When this happens, the power absorbed by the blades from the wind will be completely stored in the rotating mechanical components in the form of kinetic energy, and the generator will accelerate. After the voltage starts to recover due to the clearing of the fault after 0.6 sec, the stator flux gradually recovers such that electrical torque can be produced again to counteract the driving torque from the wind. As a result, the electromagnetic torque will be restored back to the reference value after approximately 200 msec, as shown in figure 5.19.

It should be noted that, during the voltage sag, the active power delivered to the grid is not balanced (voltage dip increases active and reactive powers continue to swing as rotor speed varies) with the mechanical power obtained from the wind turbine. This causes an acceleration of the generator that in any case will be dangerous due to the exceptional moment of inertia of the drive train itself to compensate for the power drop due to the voltage drop. In figure 5.20 it can be seen that the expected acceleration is only 17 rad/sec during the dip’s duration 0.5-0.6 sec which is less than a 2% increase. The 17 rad/sec increase in the machine rotor speed represents a 0.4 rad/sec increase in the turbine’s rotating speed and this can be considered to be negligible as shown in figure 5.20.

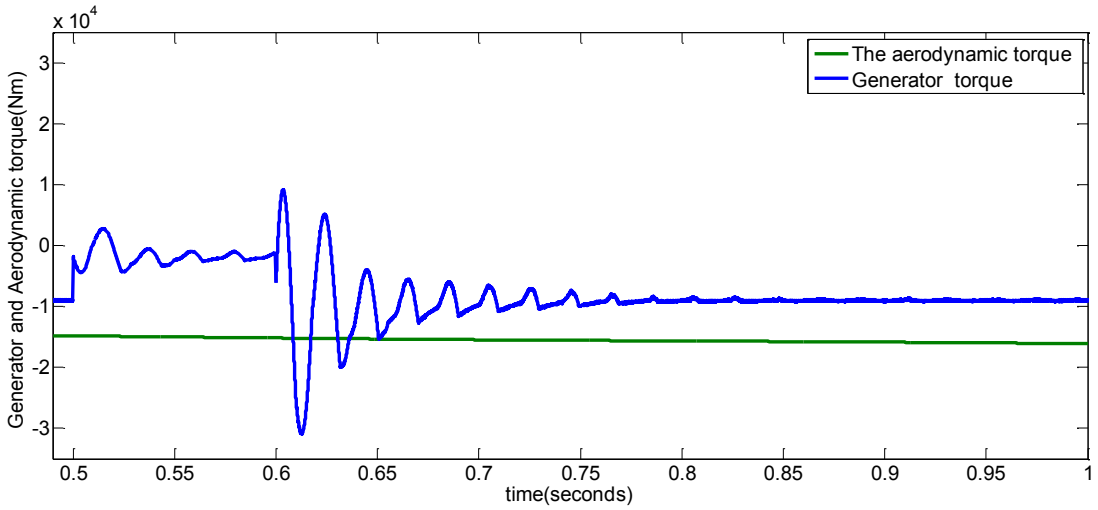

Figure 5.19: Electromagnetic and aerodynamic torque during voltage dip.

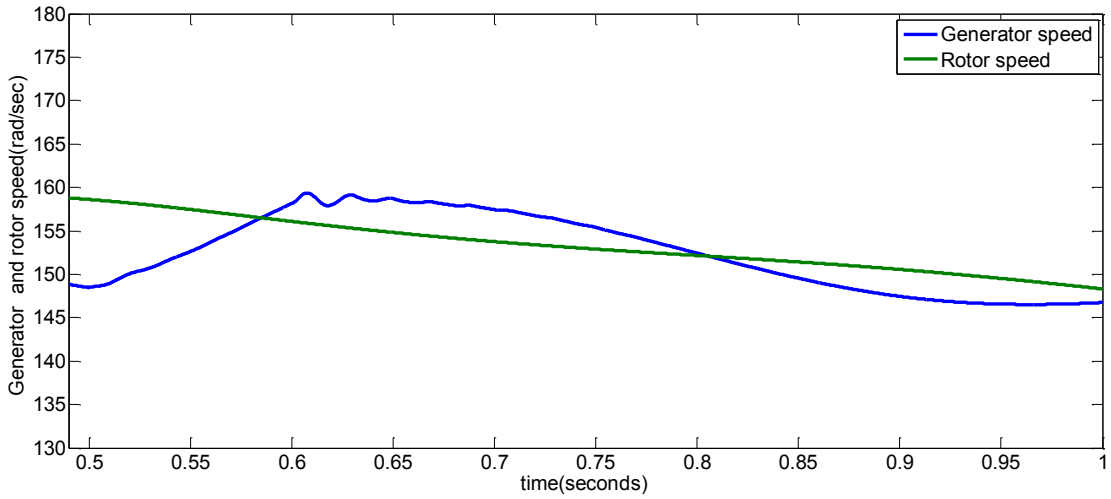

Figure 5.20: Generator speed and rotor speed during the voltage dip.

5-9-2 Case of Voltage Swell of 1.3 p.u.

A voltage swell can result from either switching off a large load or switching on a large capacitor bank across the PCC. The behaviour of the DFIG during voltage swell is investigated by increasing the PCC voltage level at the grid-side terminal to 1.3 p.u. which tested in operating period 0.5-0.6 sec. In this case an increment in the power generated will noted by the DFIG system in parallel to voltage swell occurrence, and this will then be reduced after clearance the fault. Under normal conditions, active and reactive power decoupling control is adopted for the rotor side-converter (RSC) and grid-side converter (GSC) to adjust the active and reactive powers output by the DFIG stator by controlling the exciting current output by the RSC, wherein GSC control aims at stabilizing the DC-link voltage. When DC link voltage is higher than the maximum

continuous operating voltage, any conventional protection circuit used in a DFIG, such as the DC chopper in parallel connection to the DC-bus, can be triggered for break-over to restrain the possible bus voltage pumping-up at the moment of sudden voltage change, so as to ensure the safety the DC-link.

From the simulation results shown in figures 5.23-5.30, it is clear that when the voltage swell occurs, the DFIG-based wind turbine changes from being in an excited condition to over-excited mode for LVRT voltage support. After voltage recovery and to reduce of the adverse influence on grid voltage upon the DFIG, the system will dynamically operate in excited mode again. The reactive power support is shared between the stator winding and GSC so as to reduce the GSC output voltage in order to avoid the over modulation of the PWM via the control of DC voltage, as shown in figure 5.22. Therefore, during grid voltage swell conditions, from the wind turbine needs to inject reactive current into the power system with specific proper control design of the GSC (which is not included in this study), but of inductive property to ensure the safe operation of the capacitor so that the GSC will contribute in support reactive power. In addition, the incremental of total *rms* grid current over-shoot to 1.2 p.u. As shown in figure 5.21, the PCC voltage rise to 1.3 p.u. and therefore the direct and quadrature axis rotor currents in the synchronous reference frame have rise as shown in figure 5.26 at the start of voltage swell. Then after fault clearance while the stator current in figure 5.24 increased by step and recovered at the end of the swell condition. In figure 5.26 *d* axis rotor current and *q* axis rotor current fluctuated bigger under voltage recovery condition as compared to voltage swell since stator oscillation of voltage recovery will based on natural flux decay which is not zero.

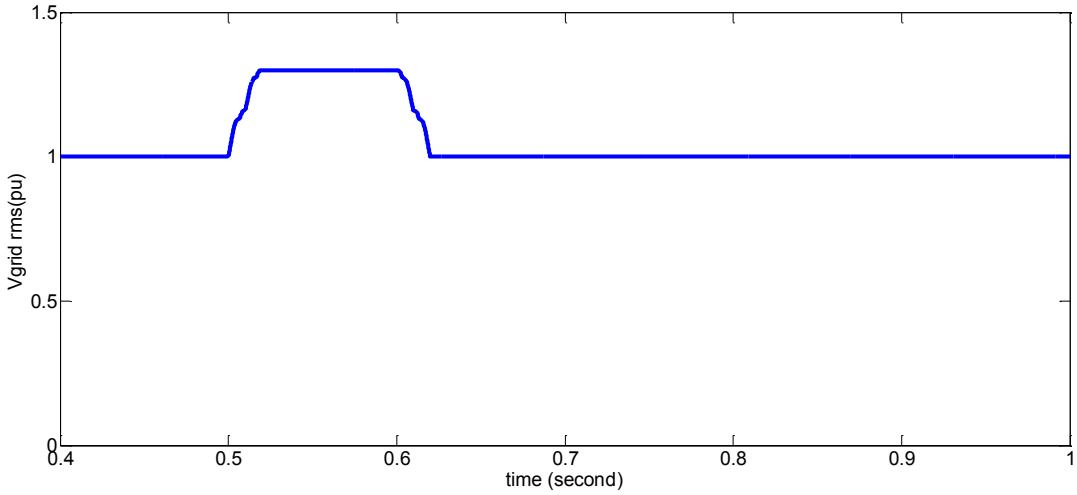

Figure 5.21: Instantaneous *rms* stator voltage.

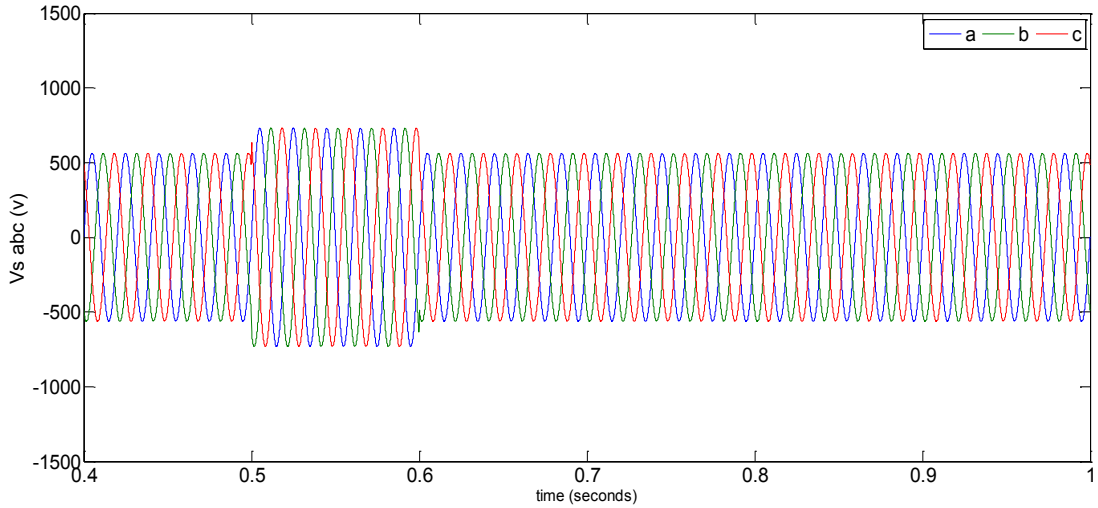

Figure 5.22: Instantaneous measurement of the three-phase stator voltage.

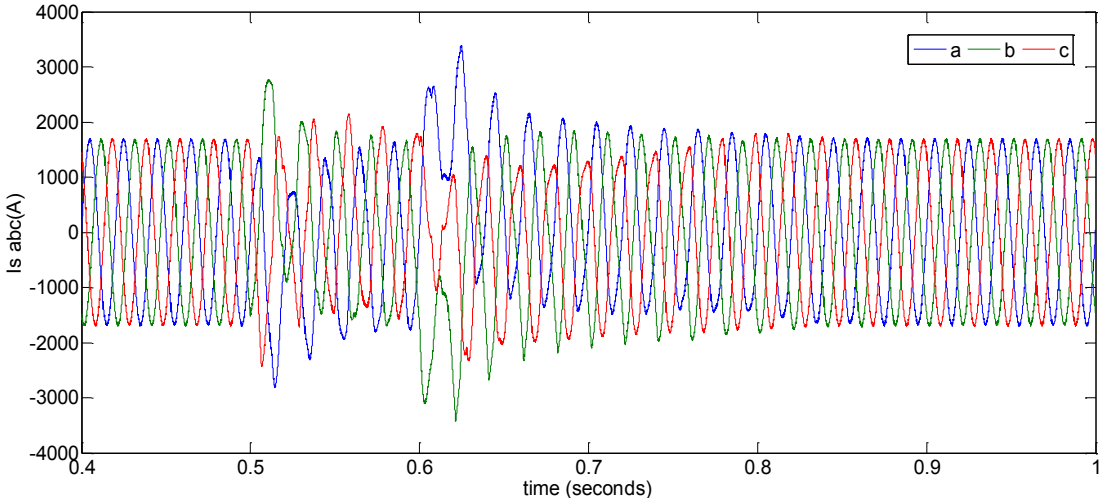

Figure 5.23: Instantaneous three-phase stator current.

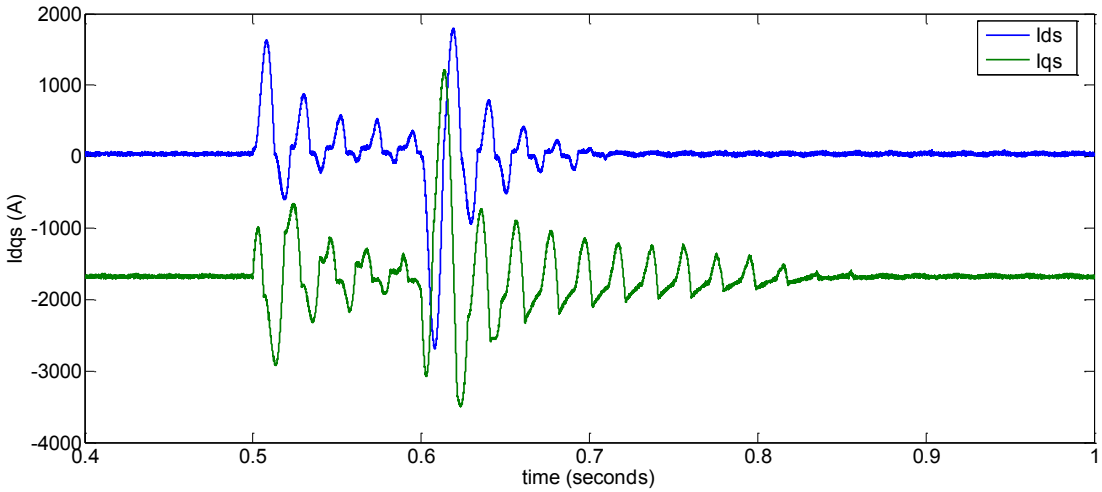

Figure 5.24: Instantaneous *dq* stator current.

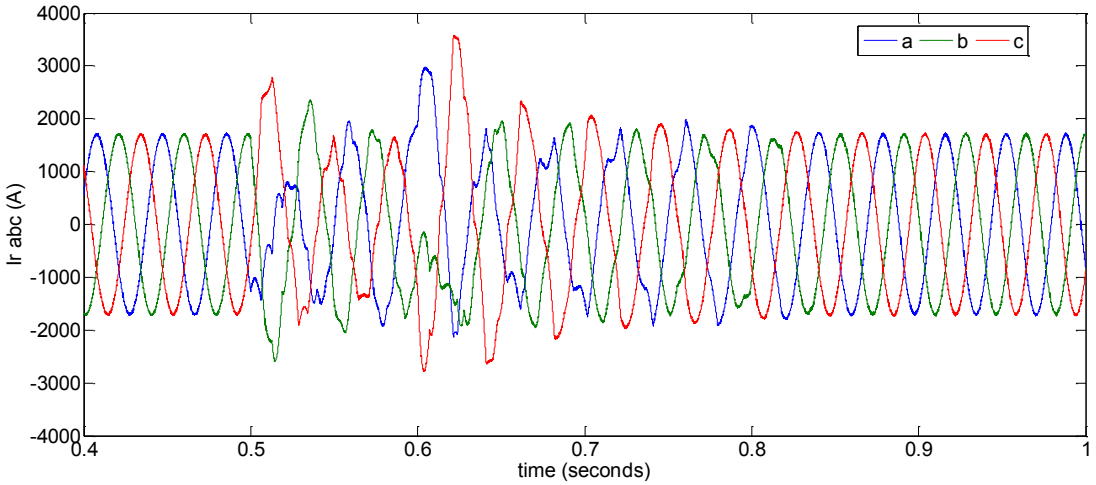

Figure 5.25: Instantaneous three-phase rotor current.

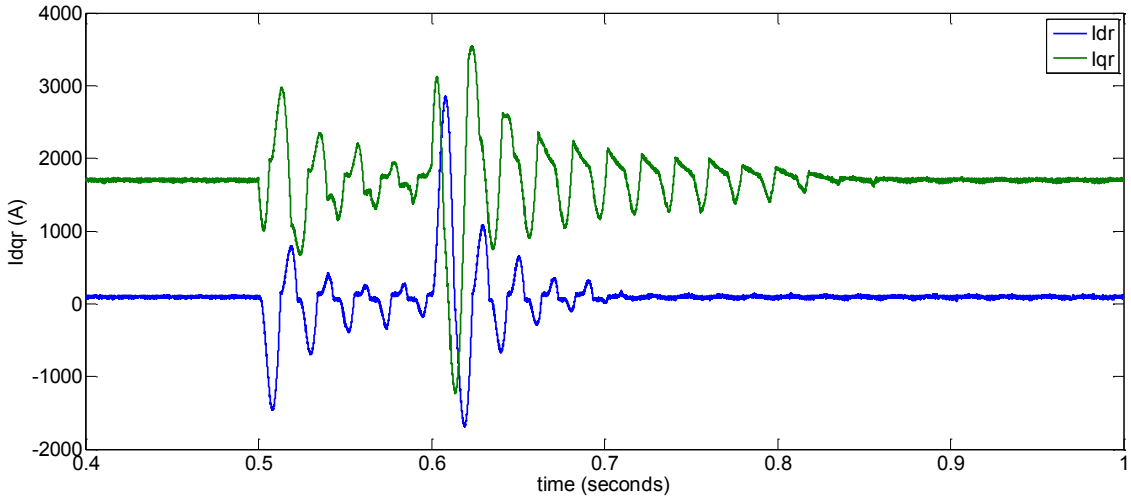

Figure 5.26: Instantaneous *dq* rotor current.

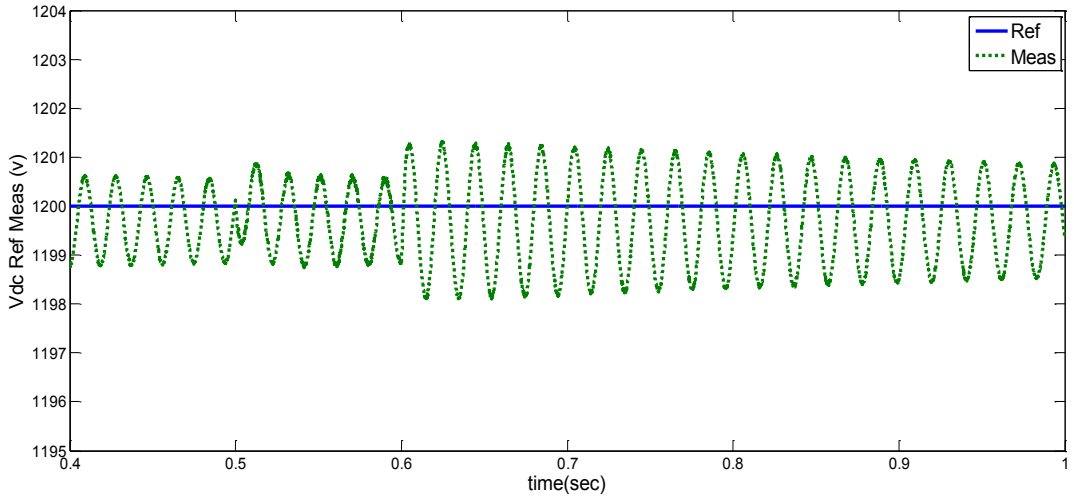

Figure 5.27: DC-link voltage regulator.

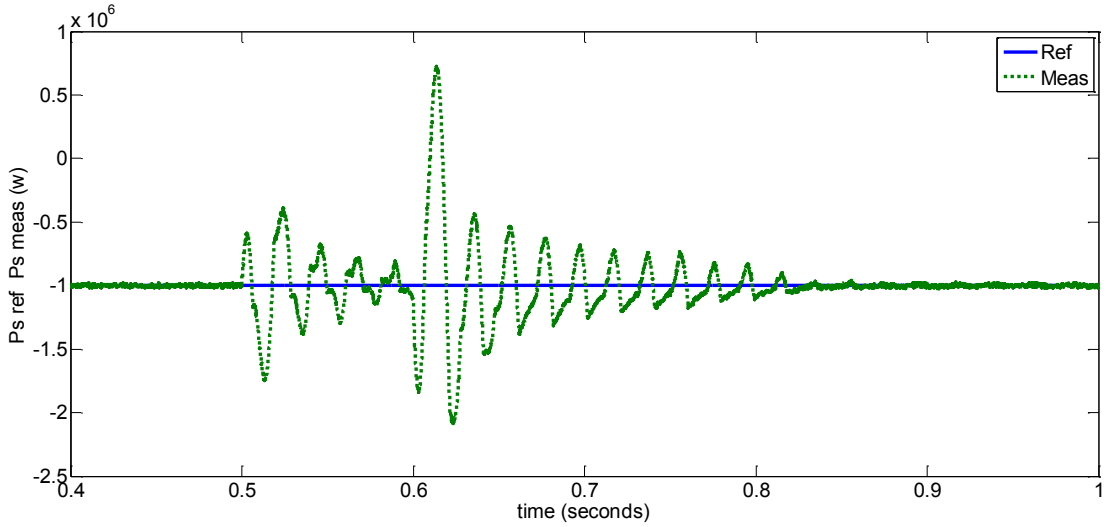

Figure 5.28: Instantaneous regulation of the stator active power in the RSC.

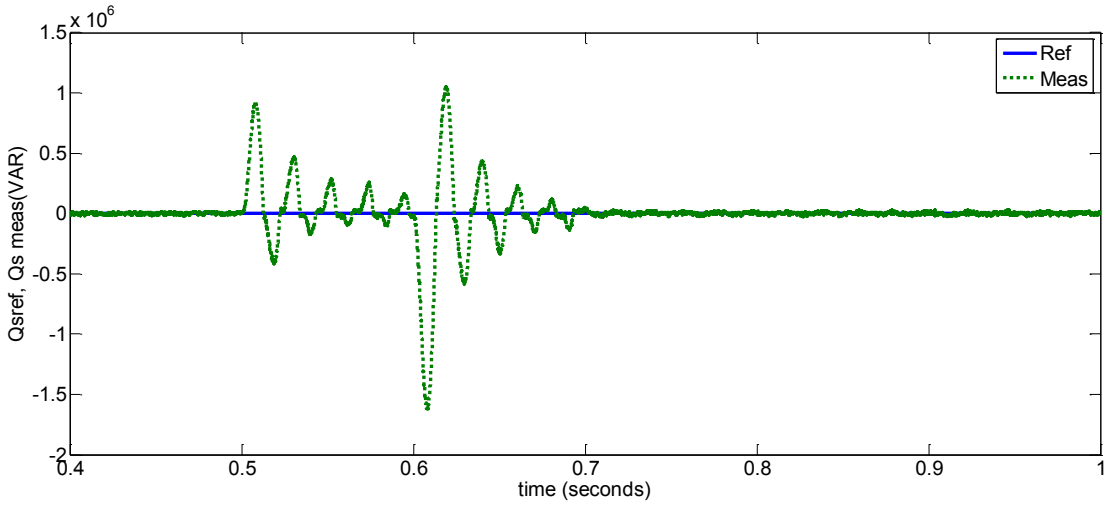

Figure 5.29: Instantaneous regulation of the stator reactive power in the RSC.

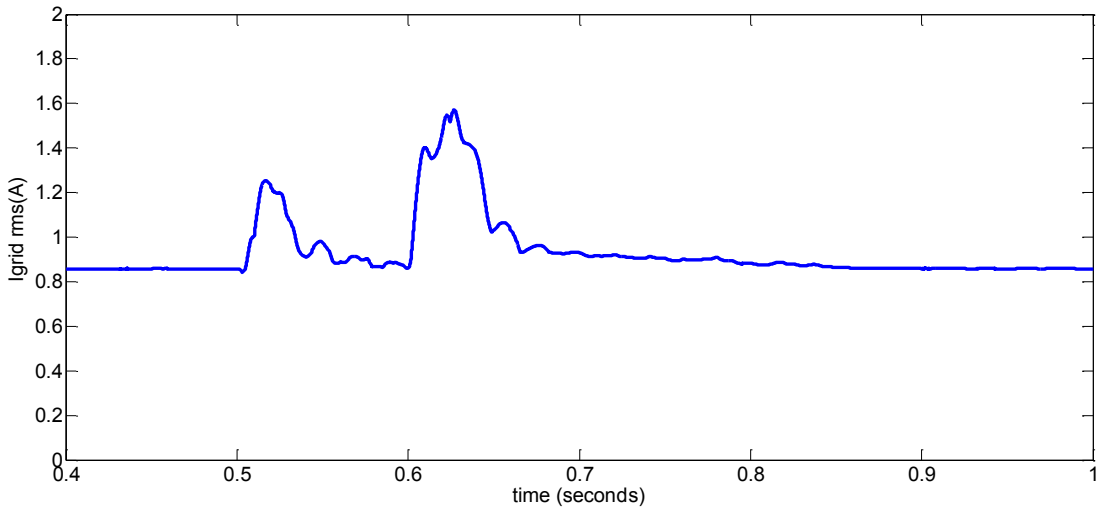

Figure 5.30: Instantaneous *rms* grid current.

5-10 Performance of Sensored and Sensorless Vector Control in DFIG System with PQ Null Modification during Disturbances

The aim of this set of tests is to illustrate some of the most representative MATLAB/SIMULINK® dynamic behaviour results so as to evaluate and compare the performance of sensored and sensorless vector control of the DFIG system during fault conditions in the grid connection. In order to study the validity of enhanced FRT using the PQ null control strategy against voltage dips, a three-phase fault is considered which causes a voltage dip of about 80% in depth and of duration in the range 0.5-0.6 seconds at the stator terminal of the DFIG. Both RCMRAS and QRMRAS have been employed in this investigation with a constant wind speed of 4 m/sec in the grid fault calculation to conduct the vector control associated with the PQ null method in the RSC. As shown in figures 5.33 –5.42, three major sets of simulink models were conducted, including: in the first a model of the PQ null method used with a sensored drive DFIG. In the second, RSMRAS model used to verify the PQ null with sensorless drive. In the third, QRMRAS model was utilized to validate the PQ null with sensorless drive based DFIG operation. Immediately after the fault occurs at 0.5 second, the voltage at the wind turbine terminal drops, as shown in figures 5.31 and 5.32. The DFIG reacts to the three-phase voltage dip with dramatic increments of the stator currents and thus high rotor currents are induced in the rotor winding. At the moment when the stator voltage becomes lower than the sett values in the fault detectors, this will directly activate the PQ null method by switching off the

conventional power loop control and using the zero values as a reference to reduce over-current of the rotor/stator in parallel with regulation the DC-bus voltage with an acceptable fluctuation level, as shown in figures 5.33, 5.36 and 5.41. here the PQ null method proves its success in employing the available resources instead of using conventional protection devices. In addition, this method has been tested with RCMRAS and QRMRAS, as depicted in figures 5.33-5.42, and it succeeds in tracking the performance of sensored vector control with results based on estimation of the rotor position. In this condition these schemes have proved their ability to eliminate the need for conventional position detectors with less sensitivity to some types of regular grid disturbances such as voltage dips. As shown in figure 5.33 and 5.36, the wind turbine system is protected by the PQ null solution which is activated before the crowbar because the voltage dip is very short-lived. The stator and rotor currents are reduced, and the stator currents decay slowly having a DC component. The RSC can stay running and connected to the DFIG rotor windings. When the PQ null control is activated, the outer power control loops are disabled and thus active and reactive power controls are not achieved. The power control can be implemented to fulfill grid code requirements when the transients have decayed. After fault clearance, the wind turbine system can continue with normal operation.

Figures 5.33 - 5.42 illustrate the comparison of the responses of this system in sensored and sensorless vector control of an 80% voltage dip using RCMRAS and QRMRAS to estimate the rotor position and employ this information in the closed loop decouple control. Rotor and stator currents begin to drop with the activation of the PQ null loop at the RSC without any crowbar engagement at around 4m/sec. Rotor and stator currents in each approach show acceptable fluctuation levels around their pre-fault values. Voltage recovery allows sufficient control of the GSC currents to return the DC link voltage to the reference value. However, from the performance evaluation of DFIG system based on the results, it is clear that the QRMAS succeeds to estimating the rotor angle under these operating conditions.

The dynamic behaviour of the *dq* stator and rotor currents when both RCMRAS and QRMRAS are implemented during a 80% voltage dip can be compared with the sensored outcomes from the simulation plots depicted in figures 5.34, 5.35, 5.37 and 5.38. Figure 5.35 shows the response of the quadrature stator currents during the

voltage sag, and they oscillate around zero during the sage duration, while the direct component exponentially fluctuate and then returns to zero after the end of the sag. The reduction of the *rms* value of grid current during the fault, shown in figure 5.42 with no protection condition. In figure 5.42, it is clear that the method with either sensored or sensorless vector control succeed in reducing the currents in the generator's windings during the fault.

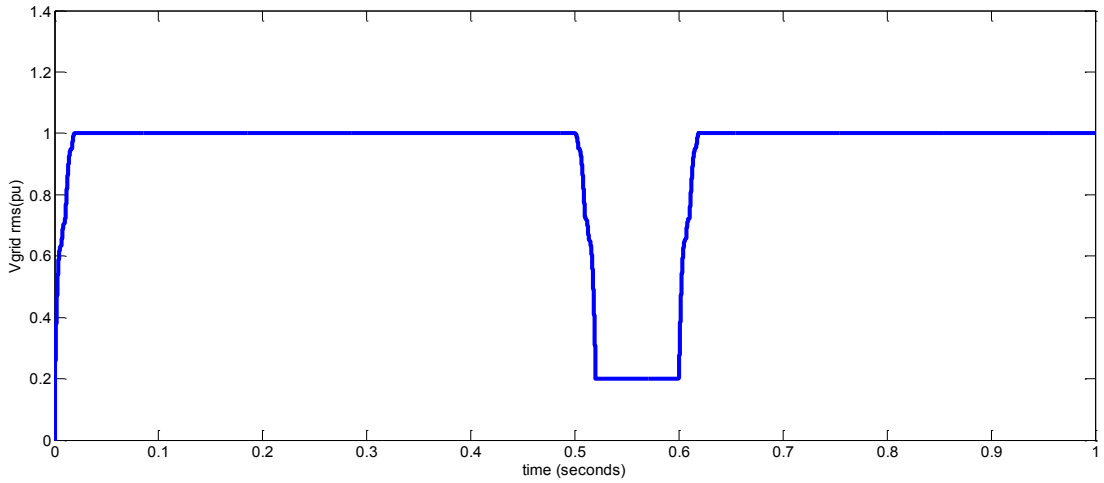

Figure 5.31: Instantaneous *rms* grid voltage.

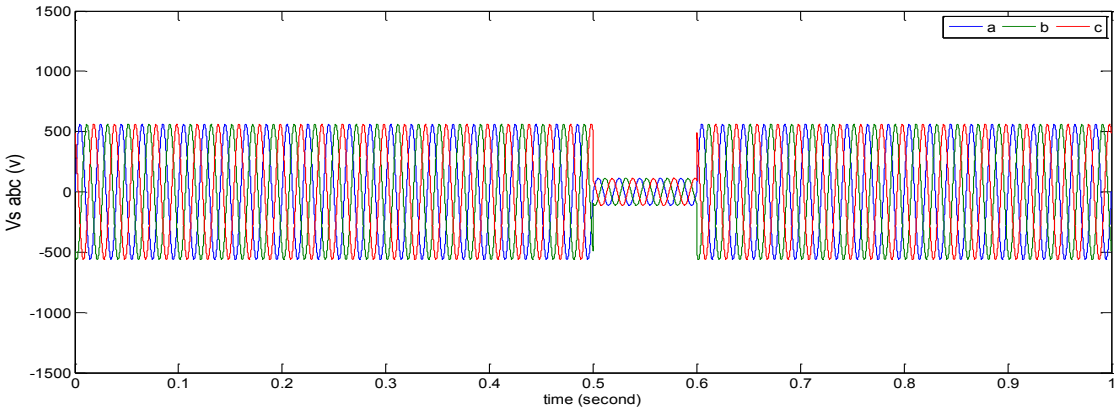

Figure 5.32: Instantaneous three-phase stator voltage.

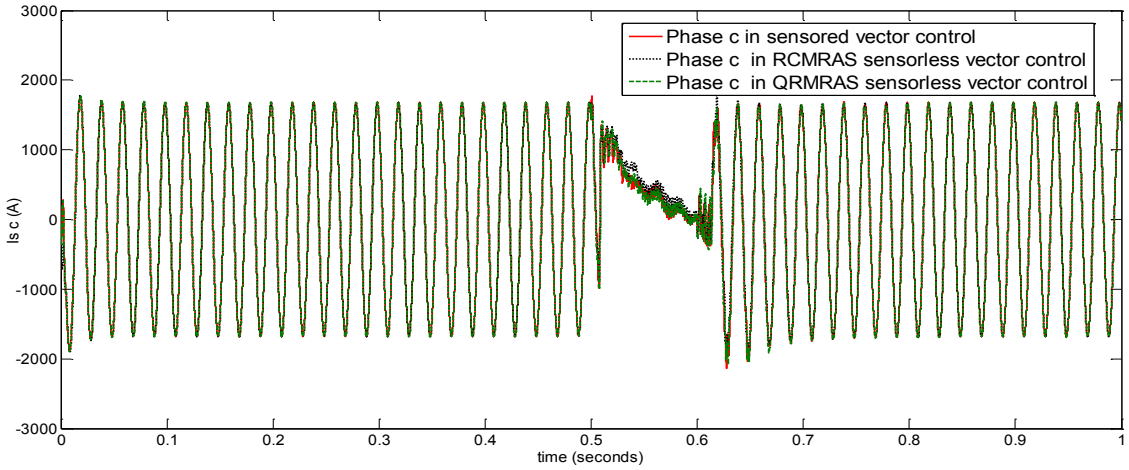

Figure 5.33: Instantaneous measurements of phase c stator current.

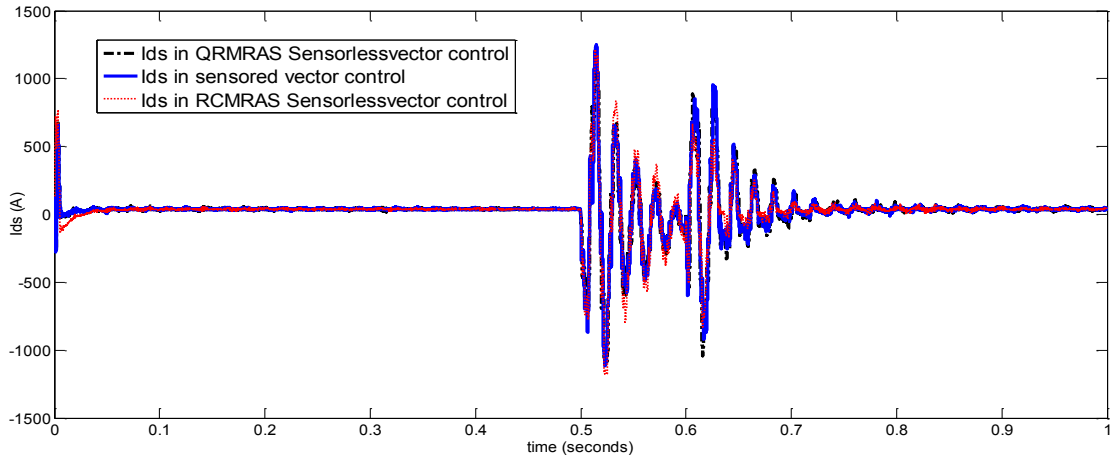

Figure 5.34: Instantaneous value of the *d* components stator current.

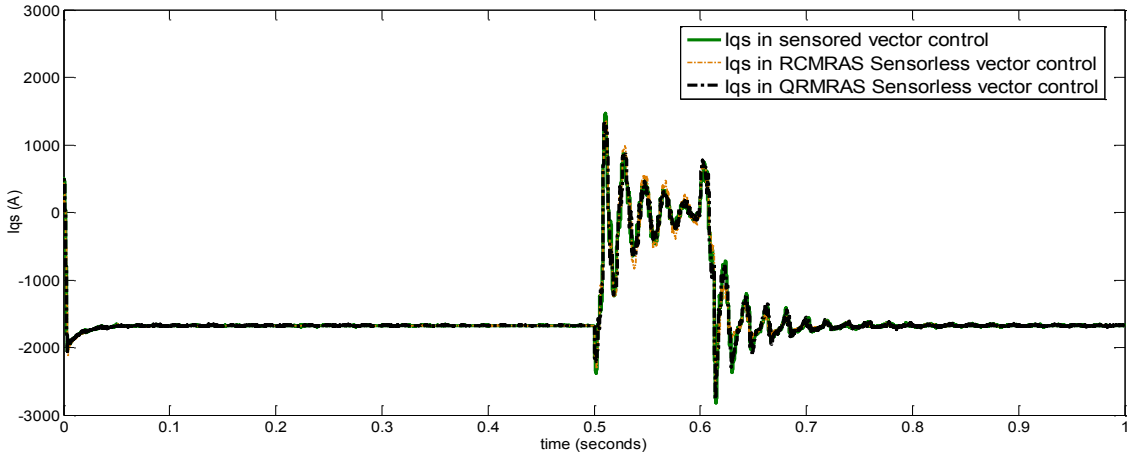

Figure 5.35: Instantaneous value of the *q* components stator current.

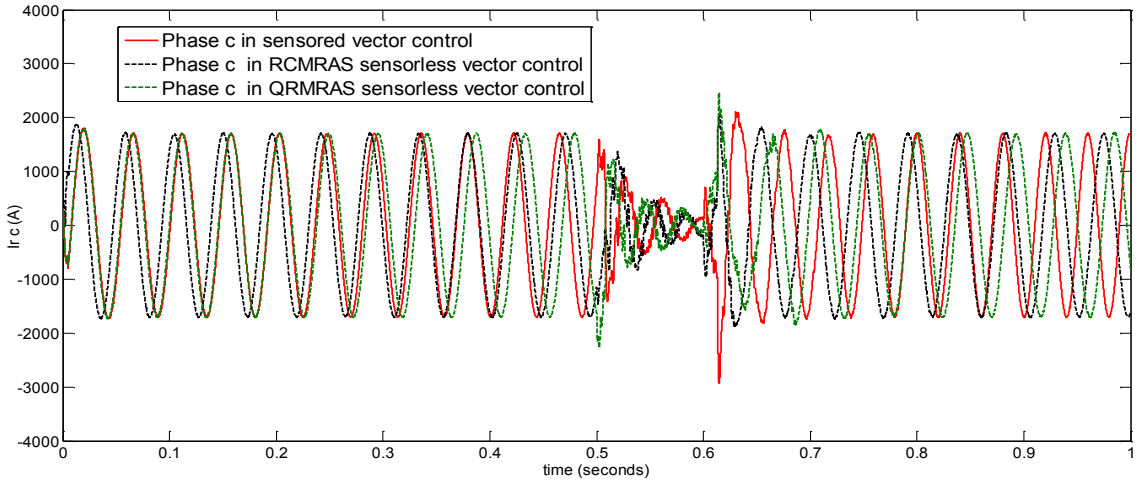

Figure 5.36: Instantaneous measurements of phase *c* rotor current.

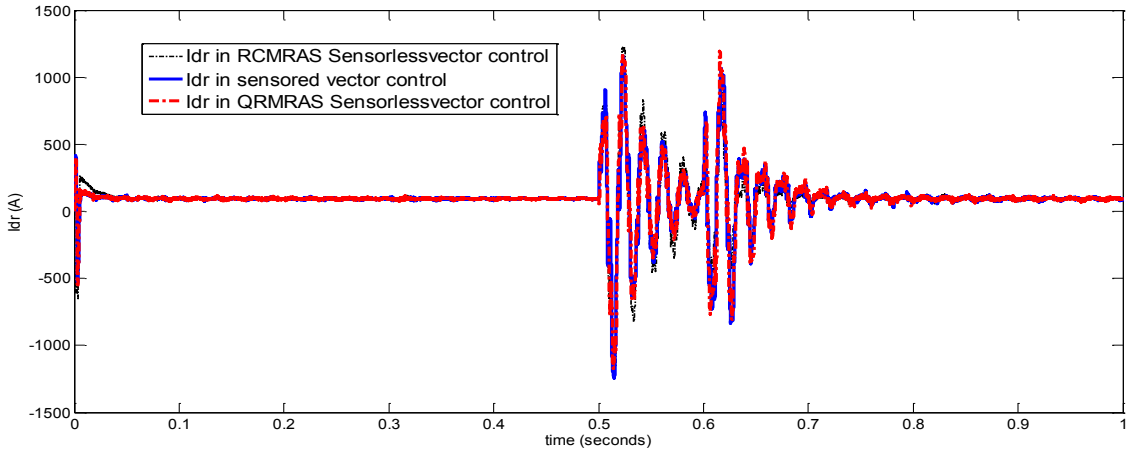

Figure 5.37: Instantaneous *d*-component rotor current.

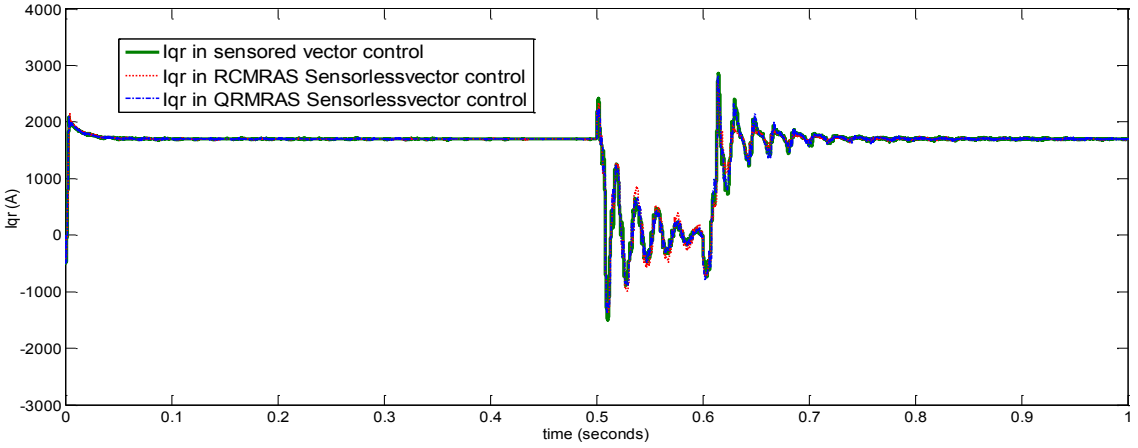

Figure 5.38: Instantaneous *q*-component rotor current.

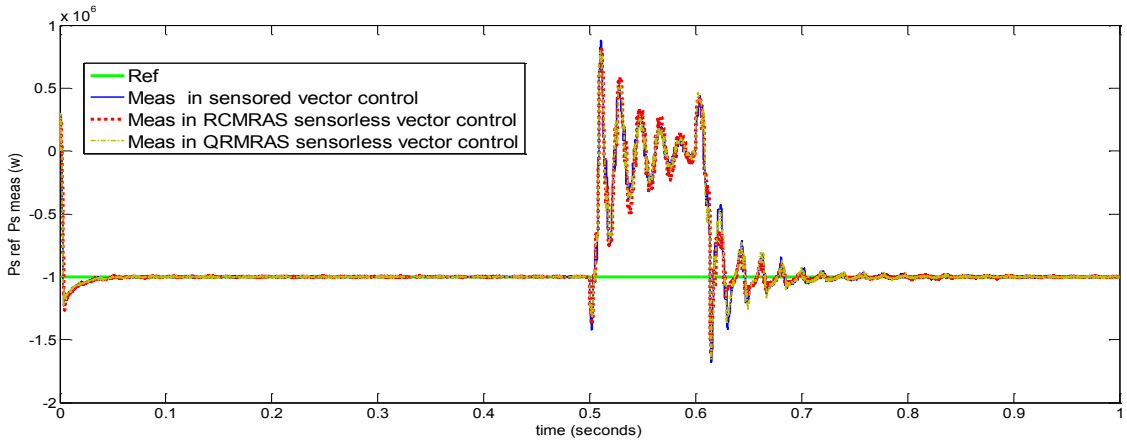

Figure 5.39: Instantaneous regulation of the stator active power in the RSC.

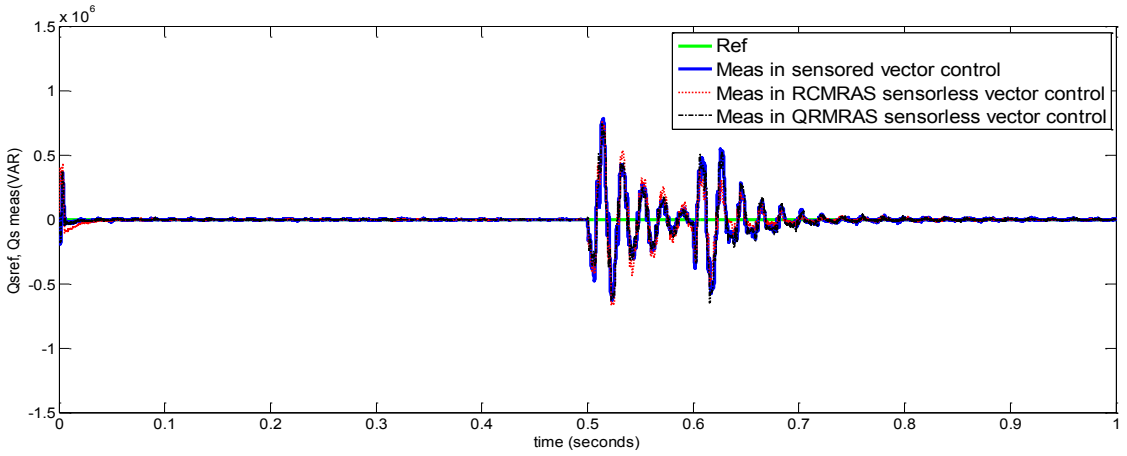

Figure 5.40: Instantaneous regulation of the stator reactive power in the RSC.

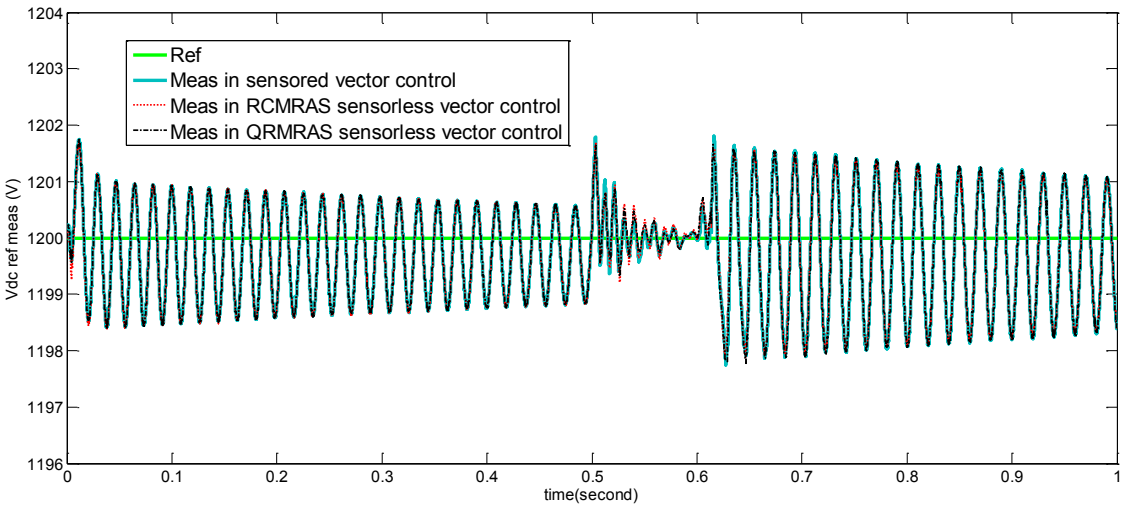

Figure 5.41: DC-link voltage regulator.

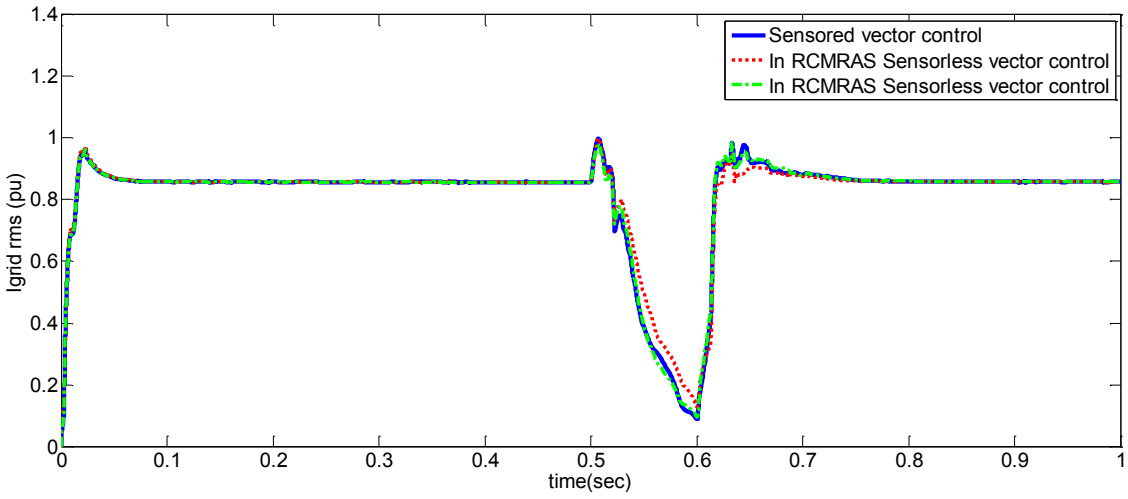

Figure 5.42: Instantaneous-three phase grid current.

5-11 Conclusions

Given the new grid code requirements, it is of great importance that variable-speed wind turbines to remain connected to the grid network during severe grid voltage dips and they must contribute to voltage recovery in these conditions. The necessities of fault ride-through (FRT) have been explained in this chapter and the requirements made of grid operators have been explained. The fault ride-through ability of the DFIG-based turbine is highly dependent on the speed and the converter's ability to withstand heavy rotor current transients with or without crowbar protection. The FRT behaviour could thus be improved by designing the electrical drive so that it can handle large currents, but this is limited by commercial viability. This technology has full employing the available resource also it can be used as a back up to the crowbar.

CHAPTER SIX

CHAPTER SIX

CONCLUSIONS AND FURTHER WORK

6-1 Conclusions

- This investigation include the principles of the modelling and design the DFIG-based wind turbine system along with its vector control strategy of the back-to-back converter includes the aerodynamic, mechanical and electrical components and controllers. The system's performance during normal operation was conducted.
- This study includes complement analysis of the vector control DFIG-based wind turbine in two operating conditions of sensored and sensorless vector control. The QRMRAS algorithm has been employed with a PI controller to detect the rotor position and its performance compared with that of the RCMRAS. Effects of parameter variations on the dynamic rotor detection of QRMRAS and RCMRAS have been investigated
- By employing the integrated error index; integral of time multiplied by absolute error and integral absolute error were used as criteria to measure the quality of system response. A systematic evaluation of rotor angle detection has been accomplished for different operating condition, and the results show QRMRAS gives lower value of ITAE and IAE as compared with the RCMRAS.
- Given the new grid code requirements, it is of great importance that variable-speed wind turbines remain connected to the grid network during severe grid voltage dips and that they contribute to voltage recovery. When subjected to severe grid voltage dips, this will be responsible for the deterioration of the back-to-back converter. The whole DFIG system previously needed to be disconnected from the grid during severe voltage sags. This is inconsistent with the standards set in the new grid requirements, which demand the DFIG system have FRT capability or already-used protection schemes should be

activated to enable the system stay connected to the network and behave as a typical power generator.

- The results show that the system can more easily ride-through a voltage swell of 0.3pu compared to a voltage dip of 0.8pu.

6-2 Contributions

The main contributions of this thesis are summarized as follows:-

- A complete dynamic comparative performance assessment for grid-connected variable-speed wind turbines based on the DFIG has been built mathematically in MATLAB/SIMULINK® platform and confirmed the system with PLECS® model.
- The rotor reactive power-based MRAS (QRMRAS) is used to estimate the rotor position with normal and voltage dip condition where the results has been tested with the conventional rotor current based MRAS (RCMRAS) observer. The QRMRAS shows it has insensitive response to the parameter variation of the DFIG as compared with the RCMRAS.
- This study put the use of QRMRAS as a back-up to the conventional mechanical encoder to increase the DFIG system reliability in the remote areas and harsh environment of operation.

6-3 Further Work

There are many possibilities for future development, improvement, verification and analysis of the present project to overcome the present research limitations. The following recommendations can be made.

- If possible, experimental sets of tests should be conducted to verify the simulation results documented in this study. With the verification work, the proposed measures, sensorless control strategies and enhanced fault ride-through (FRT) capability could be improved. Furthermore, the field validation of the proposed system is needed. A small-scale kit DFIG system could be used which has behaviour similar to a full-scale machine, and also a proper grid-simulator should be used to emulate a realistic voltage drop.

- Voltage recovery investigation should be carried out with interaction among wind turbines in wind-farms after grid disturbances.
- The accuracy and sensitivity of several sensorless methods should be investigated, includes the use QRMRAS in the DFIG-based stand-alone system with different operating conditions.
- Converter protection strategies for asymmetrical faults still need to be developed for the DFIG system in terms of the behaviour and FRT strategies because such faults induce permanent negative sequence components whose influence persist throughout the duration of voltage dip.
- Further studies should focus on improving the power converter controller of the DFIG to contribute to the FRT capability for faults of longer duration.
- Complete speed and frequency deviation protection schemes should be improved with more attention to providing a robust DFIG system.

REFERENCES

REFERENCES

[1] S. Rahman, "Going Green: The Growth of Renewable Energy", *IEEE Power and Energy Magazine*, Vol. 99, No. 6, pp. 16-17, Nov. /Dec. 2003.

[2] B. Fox, D. Flynn, L. Bryans, N. Jenkins, D. Milborrow, M. O. Malley, R. Waston and Olimpo Anaya-lara, "Wind Power Integration Connection and System Operational Aspects", *IET Power and Energy series 50*, 2007.

[3] P. A. Lynn, "Onshore and Offshore Wind Energy", 2012 *John Wiley & Sons Ltd*.

[4] http://www.gwec.net/global-figures/graphs/

[5] A. Z. Amin, "Renewable Power Generation Costs in 2012: An Overview", International Renewable Energy Agency, 2013.

[6] B. Wu, Y. Lang, N. Zargari, S. Kouro, and Institute of Electrical and Electronics Engineers, *Power Conversion and Control of Wind Energy Systems*. Oxford: Wiley Blackwell, 2011.

[7] G. Abad, J. Lopez, A. R. Miguel, M. Luis and G. Iwanski, *Doubly Fed Induction Machine: Modeling and Control For Wind Energy Generation*, 1st edition. John Wiley & Sons, INC., Publication, 2011.

[8] J. F. Manwell, J. G. McGowan, and A. L. Rogers, *Wind Energy Explained Theory, Design, and Application*, 2nd edition, 2009, John Wiley & Sons Ltd.

[9] F. Blaabjerg and Z. Chen, *Power Electronics for Modern Wind Turbines*, San Rafael, Calif.: Morgan & Claypool, 2006.

[10] C. Zhe, J. M. Guerrero, and F. Blaabjerg, "A Review of the State of the Art of Power Electronics for Wind Turbines", *IEEE Transactions on Power Electronics,* Vol. 24, No. 8, pp. 1859-1875, Aug. 2009.

[11] F. Blaabjerg, and Z. Chen, *Power Electronics for Modern Wind Turbines*, Morgan & Claypool Publishers, 1st edition, 2006.

[12] G. O. Suvire, Wind *Farm Technical Regulations, Potential Estimation and Siting Assessment*, InTech, June, 2011.

[13] http://www.energy.gov/eere/wind/how-does-wind-turbine-work.

[14] L. Wang, Y.-F. Yang, and S.-C. Kuo, "Analysis of Grid-connected Induction Generators Under Three-phase Balanced Conditions", *IEEE*, *Power Engineering*

Society Winter Meeting, Vol. 1, pp. 413 – 417, 2002.

[15] C. S. Demoulias and P. S. Dokopoulos, "Transient behavior and self excitation of wind-driven induction generator after its disconnection from the power grid", *IEEE Transactions on Energy Conversion*, Vol. 5, No. 2, pp. 272-278, June, 1990.

[16] M. A. Ouhrouche, D. D. Xuan, M. L. Quang, and C. Robert, "EMTP Based Simulation of a Self-Excited Induction Generator After its Disconnection From the Grid", *IEEE Transactions on Energy Conversion*, Vol. 13, No. 1, March 1998.

[17] H. L. Hess, N. A. Abdul Melek, and E. Muljadi, "Power Converter for Wind Turbine Application", *IEEE Power Engineering Society Summer Meeting*, Vol. 2, pp. 1275 -1276, 2000.

[18] S. M. Muyeen, T. Junji, and M. Toshiaki, "Stability Augmentation of a Grid-connected Wind Farm", *Springer*, 2009, page 61-62.

[19] B. Singh, R. B Saxena, S. S. Murthy, and B. P Singh, "A Single-Phase Self-Excited Induction Generator for Lighting Loads in Remote Areas", *International Journal on Electricity Engineering Education*, Vol. 25, pp. 269-275, 1988.

[20] D. Rane, "Voltage and Frequency Control of Wind generator System", M.sc. thesis, University of Delhi, 2008.

[21] I. Cadirei, and M. Ermis, "Performance Evaluation of Wind Driven DOIG using a Hybrid Model", *IEEE Transactions on Energy Conversion*, Vol. 13, No. 2, June 1998.

[22] R. Pena, J. C. Clare and G. M. Asher, "Doubly Fed Induction Generator Using Back-To-Back PWM Converters and Its Application to Variable-Speed Wind-Energy Generation*", IEE Proceedings Electric Power Applications*, Vol. 143, No. 3, pp. 231-241, May 1996.

[23] L. Refoufi, B. A. T. Al Zahawi, and A. G. Jack, "Analysis and Modeling of the Steady State Behavior of the Static Kramer Induction Generator", *IEEE Transactions on Energy Conversion*, Vol. 14, No. 3, pp. 333-339, Sept. 1999.

[24] J. W. Kolar, T. Friedli, J. Rodriguez, and P. W. Wheeler, "Review of Three-Phase PWM AC-AC Converter Topologies", *IEEE Transactions on Industrial Electronics*, Vol. 58, No. 11, pp. 4988-5006, Nov.2011.

[25] E. D. Basset and F. M. Potter, "Capacitive Excitation for Induction Generators",

Transactions of the American Institute of Electrical Engineers, Vol. 54, No. 5, pp. 540-545, May 1935.

[26] P. K. Shadhu Khan and J. K. Chatterjee, Three-Phase Induction Generators: A Discussion on Performance, Taylor & Francis on Electric Machines and Power Systems, Vol. 27, No. 8, pp. 813-832, 1999.

[27] J. M. Elder, J. T. Boys and J. L. Woodward, "Self-Excited Induction Machine as a Small Low-cost Generator", *IEE Proceedings*, Vol. 131, Pt. C, No. 2, 1984.

[28] K. K. Raj, E. Swati, Ch. Ravindra, "Voltage Stability of Isolated Self Excited Induction Generator (SEIG) for Variable Speed Applications using Matlab/Simulink", *International Journal of Engineering and Advanced Technology (IJEAT)*, Vol. 1, Issue-3, pp.2249 – 8958,February 2012.

[29] B. Hopfensperger and D. Atkinson, "Doubly-Fed A.C. Machines: Classification and Comparsion", *European Conference on Power Electronics and Applications (EPE), topic 06f, Graz*, 2001.

[30] B. Hopfensperger, D. Atkinson, and R. A. Lakin, "Stator Flux Oriented Control of a Cascaded Doubly-Fed Induction Machine", *IEE Proceedings: Electric Power Applications*, Vol. 146, No. 6, pp. 597–605, Nov. 1999.

[31] A. Petersson, "Analysis, Modeling and Control of Doubly-Fed Induction Generators for Wind Turbines", Ph.D. dissertation, Chalmers University of Technology, Sweden, 2005.

[32] A. K. Wallace, R. Spee, and G. C. Alexander, "The Brushless Doubly-Fed Machine: Its Advantages, Applications and Design Methods", *In 6th IEE International Conference on Electrical Machines and Drives,* 8–10 Sept. 1993, *No.376,* pp. 511–517.

[33] A. J. S. Filho, and E. R. Filho, "Model-Based Predictive Control Applied to the Doubly-Fed Induction Generator Direct Power Control", *IEEE Transactions on Sustainable Energy*, Vol. 3, No. 3, pp. 398-406, July 2012.

[34] W. Leonhard, *Control of Electrical Drives*, Berlin, Heidelberg, New York, and Tokyo: Springer-Verlag, 1985.

[35] X. Yu, Z. Jiang, and Y. Zhan, "Control of Doubly-Fed Induction Generators for Distributed Wind Power Generation", *IEEE Power and Energy Society General Meeting Conversion and Delivery of Electrical Energy in the 21st Century,* 20-24 July 2008, pp. 1-6.

[36] L. Yang, Z. Xu, J. Østergaard, Z. Y. Dong, and K. P. Wong, "Advanced Control Strategy of DFIG Wind Turbines for Power System Fault Ride Through", *IEEE Transactions on Power Systems*, Vol. 27, No. 2, pp. 713-722, May 2012.

[37] V.T. Phan and H. H. Lee, "Stationary Frame Control Scheme for A Stand-Alone Doubly Fed Induction Generator System with Effective Harmonic Voltages Rejection", *IET Electric Power Applications*, Vol. 5, No. 9, pp. 697–707, 2011.

[38] M. G. Gracia, M. P. Comech, J. Sallán, and A. Llombart, "Modelling Wind Farms for Grid Disturbance Studies", *Renewable Energy*, Vol. 33, No. 9, pp. 2109–2121, 2008.

[39] A. Abbaszadeh, S. Lesan, V. Mortezapour, "Transient Response of Doubly Fed Induction Generator under Voltage Sag Using an Accurate Model", Sustainable Alternative Energy (SAE), *2009 IEEE PES/IAS Conference*, pp. 1 – 6, 28-30 Sep. 2009.

[40] K. Elkington and M. Ghandhari, "Comparison of Reduced Order Doubly Fed Induction Generator Models for Nonlinear Analysis", *IEEE Electrical Power & Energy Conference*, pp.1-6, Oct. 2009.

[41] P. Sørensen, A. D. Hansen, T. Lund and H. Bindner, "Reduced Models of Doubly Fed Induction Generator System for Wind Turbine Simulations", *Wind Energy*, Vol. 9, No. 4, pp. 299-311, Aug. 2006.

[42] A. S. Neto, S. L. A. Ferreira, J. P. Arruda, F. A. S. Neves, P. A. C. Rosas and M. C. Cavalcanti, "Reduced Order Model for Grid Connected Wind Turbines with Doubly Fed Induction Generators", *IEEE International Symposium on Industrial Electronics*, pp. 2655-2660, June 2007.

[43] P. Ledesma and J. Usaola, "Effect of Neglecting Stator Transients in Doubly Fed Induction Generators Models", *IEEE Transactions on Energy Conversion*, Vol. 19, No. 2, pp. 459-461, June 2004.

[44] I. Erlich and F. Shewarega, "Modeling of Wind Turbines Equipped with Doubly-Fed Induction Machines for Power System Stability Studies", *2006 IEEE Power Systems Conference and Exposition*, pp. 978-985, November 2006.

[45] W. Qiao, W. Zhou, J. M. Aller, and R. G. Harley, "Wind Speed Estimation Based Sensorless Output Maximization Control for a Wind Turbine Driving a DFIG", *IEEE Transactions on Power Electronics*, Vol. 23, No. 3, pp. 1156-1169, May 2008.

[46] A. Tapia, G. Tapia, J. X. Ostolaza and J. R. Sáenz, "Modeling and Control of a Wind Turbine Driven Doubly Fed Induction Generator", *IEEE Transactions on Energy Conversion*, Vol. 18, No. 2, pp. 194-204, June 2003.

[47] S. Muller, M. Deicke, R. De Doncker, "Doubly Fed Induction Generator Systems for Wind Turbines", *IEEE Industry Applications Magazine*, Vol. 8, No. 3, pp. 26-33, May/Jun 2002.

[48] S. Chondrogiannis and M. Barnes, "Stability of Doubly-Fed Induction Generator Under Stator Voltage Orientated Vector Control", *IET Renewable Power Generation*, Vol. 2, No. 3, pp. 170-180, Sep. 2008.

[49] C. Batlle, A. D. Cerezo and R. Ortega, "A Stator Voltage Oriented PI Controller for the Doubly-Fed Induction Machine", *Proceedings of the 2007 American Control Conference, New York City, USA*, pp. 5438-5443, July 2007.

[50] A. Petersson, L. Harnefors, and T. Thiringer, "Comparison Between Stator-Flux and Grid-Flux-Oriented Rotor Current Control of Doubly-Fed Induction Generators", *2004 35th Annual IEEE Power Electronics Specialisfs Conference*, 1: pp.482-486.

[51] H. Akagi, and H. Sato, "Control and Performance of a Doubly-Fed Induction Machine Intended for a flywheel Energy Storage System", *IEEE Transactions Power Electronics*, Vol. 17, No. 1, pp. 109–116, Jan. 2002.

[52] M. Yamanmoto, and O. Motoyoshi, "Active and Reactive Power Control of Doubly-Fed Wound Rotor Induction Generator", *IEEE Transactions on Power Electronics*, Vol. 6, No. 4, pp.624-629, Oct. 1991.

[53] T. M. Masaud and P.K. Sen, "Modeling and Control of Doubly Fed Induction Generator for Wind Power", *IEEE Conference on North American Symposium (NAPS)*, pp. 1-8, 4-6 Aug. 2011.

[54] F. Wu, X. P. Zhang, K. Godfrey, and P. Ju, "Modeling and Control of Wind Turbine with Doubly Fed Induction Generator", *IEEE PES Conference on Power Systems Conference and Exposition*, pp. 1404-1409, 2006.

[55] Y. Zhang, J. Jia, W. Li, D. Wang, and J. Liu, "Steady State Characteristic Analysis and Stability Assessment of Doubly Fed Induction Generator Based Wind Power Generation System", *IEEE International Conference on Power System Technology*, pp. 1-5, 24-28 Oct. 2010.

[56] A. Ostadi, , A. Yazdani, and R. k. Varma, "Modeling and Stability Analysis of a

DFIG-Based Wind-Power Generator Interfaced With a Series-Compensated Line", *IEEE Transactions on Power Delivery*, Vol. 24, No. 3, pp. 1504-1514, July 2009.

[57] Y. Zhang, Z. Li, J. Hu, W. Xu and J. Zhu, "A Cascaded Brushless Doubly Fed Induction Generator for Wind Energy Applications Based on Direct Power Control", *2011 International Conference on Electrical Machines and Systems* , pp.1-6, Aug. 2011.

[58] K. Protsenko and D. Xu, "Modeling and Control of Brushless Doubly-Fed Induction Generators in Wind Energy Applications", *IEEE Transactions on Power Electronics*, Vol. 23, No. 3, pp.1191- 1197, May 2008.

[59] S. Arnalte, J. C. Burgos and J. L. Rodríguez-Amenedo, "Direct Torque Control of a Doubly-Fed Induction Generator for Variable Speed Wind Turbines", *Electric Power Components and Systems*, Vol. 30, No. 2, pp. 199-216, Nov. 2002.

[60] K. C. Wong, S. L. Ho and K. W. E. Cheng, "Direct Torque Control of a Doubly-fed Induction Generator with Space Vector Modulation", *Electric Power Components and Systems*, Vol. 36, No. 12, pp. 1337-1350, Nov. 2008.

[61] F. Bonnet, P. E. Vidal and M. Pietrzak-David, "Direct Torque Control of Doubly Fed Induction Machine", *Bulletin of the Polish Academy of Sciences Technical Sciences,* Vol. 54, No. 3, pp. 307-314, 2006.

[62] J. Arbi, M. J. B. Ghorbal, I. S. Belkhodja and L. Charaabi, "Direct Virtual Torque Control for Doubly Fed Induction Generator Grid Connection", *IEEE Transactions on Industrial Electronics*, Vol. 56, No. 10, pp. 4163-4173, Oct. 2009.

[63] M. Tazil, V. Kumar, R. C. Bansal, S. Kong, Z. Y. Dong, W. Freitas and H. D. Mathur, "Three-Phase Doubly Fed Induction Generators: an Overview", *IET Electric Power Applications*, Vol. 4, No. 2, pp. 75-89, Feb. 2010.

[64] T. Noguchi, H. Tomiki, S. Kondo and I. Takahashi, "Direct Power Control of PWM Converter Without Power-Source Voltage Sensors", *IEEE Transaction on Industry Application*, Vol. 34, No. 3, pp. 473-479, May/June 1998.

[65] R. Datta and V. T. Ranganathan, "Direct Power Control of Grid-Connected Wound Rotor Induction Machine Without Rotor Position Sensors", *IEEE Transactions on Power Electronics*, Vol. 16, No. 3, pp. 390-399, May 2001.

[66] D. S. Martin, J. L. Amenedo and S. Arnalte, "Direct Power Control Applied to Doubly Fed Induction Generator Under Unbalanced Grid Voltage Conditions", *IEEE Transactions on Power Electronics*, Vol. 23, No. 5, pp. 2328-2336, September 2008.

[67] G. Abad, M. Rodrıguez, G. Iwanskiand and J. Poza, "Direct Power Control of Doubly-Fed-Induction-Generator-Based Wind Turbines Under Unbalanced Grid Voltage", *IEEE Transactions on Power Electronics*, Vol. 25, No. 2, pp. 442-452, Feb. 2010.

[68] L. Xu and P. Cartwright, "Direct Active and Reactive Power Control of DFIG for Wind Energy Generation", *IEEE Transactions on Energy Conversion*, Vol. 21, No. 3, pp. 750-758, Sep. 2006.

[69] E. Tremblay, S. Atayde, and A. Chandra, "Comparative Study of Control Strategies for the Doubly Fed Induction Generator in Wind Energy Conversion Systems: A DSP-Based Implementation Approach", *IEEE Transactions on Sustainable Energy*, Vol. 2, No. 3, pp. 288-299, July 2011.

[70] F. Iov, A. D. Hansen, P. Sørensen, and F. Blaabjerg, "Wind Turbine Blockset in Matlab/ Simulink, General Overview and Description of the Models", Aalborg University , March, 2004.

[71] K. Rajashekara, A. Kawamura, and K. Matsuse, *Sensorless Control of AC Motors*, Piscataway, NJ: IEEE Press, 1996.

[72] J. Holtz, "Sensorless Control of Induction Motor Drives", *Proceedings IEEE*, Vol. 90, No. 8, pp. 1359-1394, Aug. 2002.

[73] J. Holtz, "Sensorless Control of Induction Machines With or Without Signal Injection", *IEEE Transactions on Industrial Electronics*, Vol. 53, No. 1, pp. 7-30, Feb. 2006.

[74] L. Xu and W. Cheng, "Torque and Reactive Power Control of a Doubly-Fed Induction Machine by Position Sensorless Scheme", *IEEE Transactions Industrial Applications*, Vol. 31, No. 3, pp. 636- 641, May 1995.

[75] L. Morel, H. Godfroid, A. Mirzaian, and J. M. Kauffmann, "Doubly-Fed Induction Machine: Converter Optimization and Field Oriented Control without Position Sensor", *IEE Proceedings Electric Power Applications*, Vol. 145, No. 4, pp. 360-368, Jul. 1998.

[76] B. Hopfensperger, D. J. Atkinson, and R. A. Lakin, "Stator Flux Oriented Control

of A Doubly-Fed Induction Machine with and without Position Encoder *IEE Proceedings Electric Power Applications*, Vol. 147, No. 4, pp. 241-250, Jul. 2000.

[77] R. Datta and V. T. Ranganathan, "A Simple Position Sensorless Algorithm For Rotor Side Field Oriented Control of Would Rotor Induction Machine", *IEEE Transactions on Industrial Electronic,* Vol. 48, No. 4, pp. 786-793, Aug. 2001.

[78] X. Hao, W. Change and X. Zahay, "A Comparision of Sensorless Control Strategies of DFIG", *2009 International Conference on Energy and Environment Technology*, Oct. 2009, pp. 3-6.

[79] G. D. Marques and D. M. Sousa, "Air-gap Power Vector Based Sensorless Method for DFIG Control without Flux Estimator", *IEEE Transactions on Industrial Electronics*, Vol. 58, No. 10, Oct. 2011.

[80] J. W. Finch and D. Giaouris, "Controlled AC Electrical Drives", *IEEE Transactions on Industrial Electronics*, Vol. 55, No. 2, pp. 481-491, Feb. 2008.

[81] R. Cárdenas, R. Peña, J. Clare, G. Asher, and J. Proboste, "MRAS Observers for Sensorless Control of Doubly-Fed Induction Generators", *IEEE Transactions on Power Electronics*, Vol. 23, No. 3, pp. 1075-1084, May 2008.

[82] A. A. Naassani and A. Ghazal, A. Joukhadar and A. El Shafei, "Speed Sensorless Control of DFIG Based MRAS Observer", *Proceedings of the 14th International Middle East Power Systems Conference (MEPCON'10),* December, 2010, pp. 476-481.

[83] S. M. Gadoue, D. Giaouris, and J. W. Finch, "Sensorless Control of Induction Motor Drives at Very Low and Zero Speeds Using Neural Network Flux Observers", *IEEE Transaction on Industrial Electronics*, Vol. 56, No. 8, Aug. 2009, pp.3029-3039.

[84] G. D. Marques, V. F. Pires, S. Sousa and D. M. Sousa, "A DFIG Sensorless Rotor-Position Detector Based on a Hysteresis Controller", *IEEE Transactions on Energy Conversion*, Vol. 26, No. 1, March. 2011, pp. 9-17.

[85] L. Gao, B. Guan, Y. Zhou, and Longya Xu, "Model Reference Adaptive System Observer Based Sensorless Control of Doubly-Fed Induction Machine", *International Conference on Electrical Machines and Systems (ICEMS),* Oct .2010, pp. 931 – 936.

[86] T. Ackermann, *Wind Power in Power Systems*, John Wiley & Sons, 2006.

[87] R. Cárdenas, R. Peña, J. Proboste, G. Asher, and J. Clare, "MRAS Observer for Sensorless Control of Stand-Alone Doubly-Fed Induction Generators", *IEEE Transaction Energy Conversion*, Vol. 20, No. 4, Dec. 2005, pp. 710-718.

[88] B. Boukhezzar and H. Siguerdidjane, "Nonlinear Control of a Variable-Speed Wind Turbine Using a Two-Mass Model", *IEEE Transactions on Energy Conversion*, Vol. 26, No. 1, March 2011, pp.149-162.

[89] M. Soliman, O. P. Malik, and D. T. Westwick, "Multiple Model Predictive Control for Wind Turbines With Doubly Fed Induction Generators", *IEEE Transactions on Sustainable Energy*, Vol. 2, No. 3, July 2011, pp. 215- 225.

[90] D. Zhi, L. Xu and B. W. Williams, "Model-Based Predictive Direct Power Control of Doubly Fed Induction Generators", *IEEE Transactions on Power Electronics*, Vol. 25, No. 2, Feb. 2010, pp. 341-351.

[91] L. Xu, D. Zhi and B. W. Williams, "Predictive Current Control of Doubly Fed Induction Generators", *IEEE Transactions on Industrial Electronics*, Vol. 56, No. 10, pp. 4143-4153, Oct. 2009.

[92] F. E. V. Taveiros, L.S. Barros, and F.B. Costa, "Back-to-Back Converter State - Feedback Control of DFIG (doubly-fed induction generator)-Based Wind Turbines", Energy, Vol. 89, issue C, pp. 896-906, 2015.

[93] S. M. Muyeen, *Wind Power*, INTECH, June 2010.

[94] A. B. Xavier and S. Betty, "Energetic Macroscopic Representation and Inversion Based Control Illustrated on a Wind-Energy-Conversion System Using Hardware-in the Loop Simulation", *IEEE Transactions on Industrial Electronics*, Vol. 56, No. 12, pp. 4826-4835, Dec. 2009.

[95] S. Drid, A. Makouf and M. Naït-Saïd, "Variable Speed DFIG Power Control with Wind Turbine Maximum Power Point Tracking", *JHMER*, Vol. 2, No. 1, pp. 13-18, 2011.

[96] G. Simões, and F. Farret, "Alternative Energy Systems: Design and Analysis with Induction Generators", *Power Electronics and Applications Series CRC Press*, (2008).

[97] T. Pan, Z. Ji, and Z. Jiang, "Maximum Power Point Tracking of Wind Energy Conversion System Based on Sliding Code Extremum Seeking Control", *IEEE Energy 2030 Conference*, 17-18 Nov. 2008.

[98] B. Shen, B. Mwinyiwiwa, Y. Zhang, and B. T. Ooi, "Sensorless Maximum Power Point Tracking of Wind by DFIG using Rotor Position Phase Lock Loop(PLL)", *IEEE Transactions on Power Electronics*, Vol. 24, No. 4, pp. 942-951, April 2009.

[99] K. Han and G. Chen, "A Novel Control Strategy of Wind Turbine MPPT Implementation for Direct-Drive PMSG Wind Generation Imitation Platform", *Power Electronics and Motion Control Conference, 2009. IPEMC '09. IEEE 6th Internation*al, pp. 2255 - 2259, 17-20 May 2009.

[100] G. Ahmed and A. Kalil, "Maximum Power Point Tracking Based on Sensorless Wind Speed Using SVR", *Proceedings of the 14th International Middle East Power Systems Conference (MEPCON'10), Cairo University, Egypt, December 19-21, 2010, Paper ID 264, pp. 678-682.*

[101] S. Bhowmik, R. Spee, and J. H. R. Enslin, "Performance Optimization For Double Fed Wind Power Generation System", *IEEE Transactions on Industry Applications*, Vol. 35, No. 4, pp. 949-958, July/Aug. 1999.

[102] K. Tan and S. Islam, "Optimal Control Strategies in Energy Conversion of PMSG Wind Turbine System without Mechanical Sensors", *IEEE Transactions on Energy Conversion*, Vol. 19, No. 2, pp. 392-399, June 2004.

[103] L. Fan, Z. Miao, X. Wang, "Sensorless Maximum Power Point Tracking in Multi-Type Wind Energy Conversion Systems", *Proceedings of the 48th IEEE Conference on Decision and Control, 2009 held jointly with the 2009 28th Chinese Control Conference. CDC/CCC 2009*, pp. 6823- 6828, 15-18 Dec. 2009.

[104] S. Nouali and A. Ouali, "Sensorless Control Strategy for Wind Energy Conversion System Based on Cascaded Doubly Fed Induction Generator Using Artificial Neuronal Network"*, International Journal of Electrical and Power Engineering*, Vol. 5, No. 1, pp. 42-48, 2011.

[105] C. Feltes, H. Wrede, and F. Koch, "Fault Ride-Through of DFIG-based Wind Farms connected to the Grid through VSC-based HVDC Link", *16th PSCC, Glasgow, Scotland*, July 14-18, 2008.

[106] F. Iov, A. D. Hansen, P. Sørensen, N. A. Cutululis, "Mapping of Grid Faults and Grid Codes", *Riso-R-1617(EN), January 2007*.

[107] V. Ignatova, P. Granjon, S. Bacha and F. Dumas, "Classification and Characterization of Three Phase Voltage Dips by Space Vector Methodology",

Future Power Systems, 2005 International Conference, pp. 1-6, 18 Nov. 2005.

[108] S. Choudhury, K. B. Mohanty, B. C. Babu, "Performance Analysis of Doubly fed Induction Generator for Wind Energy Conversion System", *The 5th PSU-UNS International Conference on Engineering and Technology (ICET-2011), Phuket*, pp. 532-536, 2-3 May 2011.

[109] M. B. C. Salles, K. Hameyer, J. R. Cardoso, A. P. Grilo and C. Rahmann, "Crowbar System in Doubly Fed Induction Wind Generators", *Energies*, Vol. 3, No. 4, pp.738-753, Feb. 2010.

[110] C. Abbey, and G. Joos, "Supercapacitor Energy Storage for Wind Energy Applications", *IEEE Transactions On Industry Applications*, Vol. 43, No. 3, pp. 769-776, May/June 2007.

[111] A. Petersson, S. Lundberg, T. Thiringer, "A DFIG Wind Turbine Ride-Through System. Influence on The Energy Production", *Wind Energy*, Vol. 8, No. 3, pp. 251–263, July/Sep. 2005.

[112] P. S. Flannery, and G. Venkataramanan, "A Fault Tolerant Doubly Fed Induction Generator Wind Turbine Using a Parallel Grid Side Rectifier and Series Grid Side Converter", *IEEE Transactions on Power Electronics*, Vol. 23, No. 3, pp. 1126-1135, May 2008.

[113] A. H. Kasem, E. F. EI-Saadany, H. H. EI-Tamaly, and M. A. A. Wahab, "An Improved Fault Ride-Through Strategy for Doubly Fed Induction Generator-Based Wind Turbines", *IET Renewable Power Generation*, Vol. 2, No. 4, pp.201–214, Dec. 2008.

[114] S. Foster, L. Xu, and B. Fox, "Coordinated Reactive Power Control for Facilitating Fault Ride Through of Doubly Fed Induction Generator- and Fixed Speed Induction Generator-Based Wind Farms", *IET Renewable Power Generation*, Vol. 4, No. 2, pp. 128–138, Mar. 2008.

[115] L. Peng, B. Francois, and Y. Li, "Improved Crowbar Control Strategy of DFIG Based Wind Turbines for Grid Fault Ride-Through", Applied Power Electronics Conference and Exposition, 2009. *APEC 2009. Twenty-Fourth Annual IEEE*, pp. 1932–1938, *15-19 Feb. 2009*.

[116] M. B. C. Salles, J. R. Cardoso, A. P. Grilo, C. Rahmann, and K. Hameyer, "Control Strategies of Doubly Fed Induction Generators to Support Grid Voltage", *IEEE International Electric Machines and Drives Conference, 2009.*

IEMDC '09, pp. 1551–1556, May 2009.

[117] J. López, E. Gubía, E. Olea, J. Ruiz, and L. Marroyo, "Ride Through of Wind Turbines With Doubly Fed Induction Generator Under Symmetrical Voltage Dips", *IEEE Transactions On Industrial Electronics*, Vol. 56, No. 10, pp. 4246–4254, Oct. 2009.

[118] L. G. Meegahapola, T. Littler, and D. Flynn, "Decoupled-DFIG Fault Ride-Through Strategy for Enhanced Stability Performance During Grid Faults", *IEEE Transactions on Sustainable Energy*, Vol. 1, No. 3, pp. 152–162, Oct. 2010.

[119] K. E. Okedu, S. M. Muyeen, R. Takahashi, and J. Tamura, "Wind Farms Fault Ride Through Using DFIG with New Protection Scheme", *IEEE Transactions on Sustainable Energy*, Vol. 3, No. 2, pp. 242-254, April 2012.

[120] C. Wessels, and F. W. Fuchs, "Fault Ride Through of DFIG Wind Turbines During Symmetrical Voltage Dip with Crowbar or Stator Current Feedback Solution", *Energy Conversion Congress and Exposition (ECCE), 2010 IEEE*, pp. 2771- 2777, 12-16 Sept. 2010.

[121] K. Lima, A. Luna, P. Rodriguez, E. Watanabe, R. Teodorescu, and F. Blaabjerg, "Doubly-Fed Induction Generator Control Under Voltage Sags", *IEEE Energy 2030 Conference, 2008. ENERGY 2008*, pp.1- 6, 17-18 Nov. 2008.

[122] A. Petersson, T. Thiringer, L. Harnefors, and T. Petru, "Modeling and Experimental Verification of Grid Interaction of a DFIG Wind Turbine", *IEEE Transactions on Energy Conversion*, Vol. 20, No. 4, pp. 878-886, Dec. 2005.

[123] F. K. A. Lima, A. Luna, P. Rodríguez, E. H. Watanabe, and M. Aredes, "Study of a Simplified Model for DFIG-Based Wind Turbines", *IEEE Transactions on Energy Conversion Congress and Exposition*, pp. 345-349, 20-24 Sept. 2009.

[124] H. Polinder, F. F. A. Pijl, G. Vilder, and P. J. Tavner, "Comparison of Direct-Drive and Geared Generator Concepts for Wind Turbines", *IEEE Transactions on Energy Conversion*, Vol. 21, No. 3, pp. 725-733, Sep. 2006.

[125] Y. Lei, A. Mullane, G. Lightbody, and R. Yacamini, "Modeling of The Wind Turbine with a Doubly Fed Induction Generator for Grid Integration Studies", *IEEE Transactions on Energy Conversion,* Vol. 21, No. 1, pp. 257-264, March, 2006.

[126] M. Ali Dami, K. Jemli, M. Jemli, and M. Gossa, "Doubly Fed Induction Generator, With Crow-Bar System, under Micro-Interruptions Fault",

International Journal on Electrical Engineering and Informatics, Vol. 2, No.3, p.p 216 – 231, 2010.

[127] A. D. Hansen, P. Sørensen, F. Blaabjerg, and J. Bech, "Dynamic Modelling of Wind Farm Grid Interaction", *Wind Engineering*, Vol. 26, No. 4, pp. 191-208, 2002.

[128] M. Liserre, A. Aquila, and F. Blaabjerg, "Design and Control of a Three-Phase Active Rectifier Under Non-Ideal Operating Conditions", *37th IAS Annual Meeting Conference Record of The Industry Applications Conference*, Vol.2, pp. 1181–1188, 2002.

[129] E. Carrasco, A. Gómez, R. Amenedo, and J. L. EPS, "Sensorless Control of Doubly-fed Asynchronous Machines for WECS *Applications", Universidad Carlos III de Madrid, España*, http://www.aedie.org/9CHLIE-paper-send/279-garcia.pdf.

[130] A. D. Hansen, C. Jauch, P. Sørensen, F. Iov, and F. Blaabjerg, "Dynamic Wind Turbine Models in Power System Simulation Tool Digsilent", *Risoe Report R1400(EN), Risø National Laboratory, Denmark, 2003.*

[131] G. L. Johnson, *Wind Energy Systems*, Prentice-Hall, 1985.

[132] J. V. Barreras, F. V. Sánchez, "A Fast Method To Evaluate Annual Energy Production of Different Off-Shore Wind Farm Configurations Connected to a VSC-HVDC Line Transmission Including Evaluation of a New Variable Speed Wind Turbine Concept Based on RCC-WRIG", *Aalborg University, Institute of Energy Techonology, Msc. Thesis, 2009.*

[133] A. M. Eltamaly, A. I. Alolah, and M. H. Rahman, "Modified DFIG Control Strategy for Wind Energy Applications", *SPEEDAM 2010, International Symposium on Power Electronics, Electrical Drives, Automation and Motion, pp. 653-658, 14-16 June 2010.*

[134] N. S. Çetin, M. A. Yurdusev, R. Ata, and A. Özdemir, "Assessment of Optimum Tip Speed Ratio of Wind Turbine", *Mathematical and Computational Applications*, Vol. 10, No. 1, pp. 147-154, 2005.

[135] W. Qiao, "Dynamic Modelling and Control of Doubly Fed Induction Generators Driven by Wind Turbines", *Power Systems Conference and Exposition, 2009. PSCE '09. IEEE/PES*, pp. 1-8, 15-18 March 2009.

[136] J. H. Allmeling and W. P. Hammer, "PLECS - Piece-wise Linear Electrical

Circuit Simulation for Simulink". *IEEE 1999 International Conference on Power Electronics and Drive Systems, PEDS'99, July 1999, Hong Kong.*

[137] M. Rashed and A. F. Stronach, "A Stable Back-EMF MRAS-Based Sensorless Low Speed Induction Motor Drive Insensitive to Stator Resistance Variation", *IEE Proceedings Electric Power Application*s, Vol.151, pp. 685-693, 2004.

[138] G. D. Marques and D. M. Sousa, "New Sensorless Rotor Position Estimator of a DFIG Based on Torque Calculations—Stability Study", *IEEE Transactions on Energy Conversion*, Vol. 27, No. 1, March 2012, pp. 196-203.

[139] A. A. Naassani, A. Ghazal, A. Joukhadar and A. El Shafei, "Speed Sensorless Control of DFIG Based MRAS Observer", *International Middle East Power Systems Conference (MEPCON'10), Cairo University, Egypt*, Paper ID 210, pp. 476-481, Dec, 2010.

[140] F. Peng, and T. Fukao, "Robust Speed Identification for Speed Sensorless Vector Control Of Induction Motors", *IEEE Transactions on Industry Applications*, Vol. 30, No. 5, pp. 1234–1240, Sep/Oct. 1994.

[141] F. C. Dezza, G. Foglia, M. F. Iacchetti, and R. Perini, "An MRAS Observer for Sensorless DFIM Drives with Direct Estimation of the Torque and Flux Rotor Current Components", *IEEE Transactions on Power Electronics*, Vol. 27, No. 5, pp. 2576-2584, May 2012.

[142] R. Peña, R. Cárdenas, J. Proboste, G. Asher and J. Clare, "Sensorless Control of Doubly-Fed Induction Generators Using a Rotor-Current-Based MRAS Observer", *IEEE Transactions on Industrial Electronics*, Vol. 55, No. 1, Jan. 2008.

[143] S. M. Shinners, *Modern Control System Theory and Design*, John Wiley & Sons, Inc., 2nd edition, 1998.

[144] W. C. Schultz and V. C. Rideout, "Control System Performance Measures: Past, Present and Future", *IRE Trans. on Automatic Control, AC-6: 22-35, 1961.*

[145] W. Qiao' and R. G. Harley, "Grid Connection Requirements and Solutions for DFIG Wind Turbines", *IEEE Energy 2030 Conference*, pp.1-8, 17-18 Nov. 2008.

[146] X. Zheng, and D. Guo, "A Noval Ride-Through Control Strategy of DFIG Wind Generation Under Grid Voltage Dip", *Journal of Information & Computational Science*, Vol. 8, No. 3, pp. 579-591, 2011.

[147] M. Rahimi, and M. Parniani, "Grid Fault Ride Through Analysis and Control of

Wind Turbines with Doubly Fed Induction Generators", Science direct, Electrical Power System Research, Vol. 80, No. 2, pp. 184-195, Feb. 2010.

[148] M. Rahimi, and M. Parniani, "Efficient Control of Wind Turbines with Doubly Fed Induction Generators for Low-Voltage Ride-Through Capability Enhancement", *IET Renewable Power Generation*, Vol. 4, No. 3 , pp. 242-252, May 2010.

[149] A. D. Hansen, and G. Michalke, "Fault Ride-Through Capability of DFIG Wind Turbines", *Renewable Energy*, Vol. 32, No. 9, pp. 1594–1610, July 2007.

[150] G. C. Lampley, "Permanent and Temporary Faults", *IEEE Industry Applications Magazine*, Vol. 15, No. 5, pp. 25 – 31, Sept/Oct. 2009.

[151] H. L. Zhou, G. Yang, and D.Y. Li, "Short Circuit Current Analysis of DFIG Wind Turbines with Crowbar Protection", Electrical Machines and Systems, 2009. ICEMS 2009. International Conference, pp. 1 – 6, 15-18 Nov. 2009.

[152] J. D. Glover, M. S. Sarma, and T. J. Overbye, "*Power System Analysis and Design*", *Wadsworth Publishing co. Inc,* 4th edition, 2007.

[153] G. Pannell, D. Atkinson, R. Kemsley, L. Holdsworth, P. Taylor, and O. Moja, "DFIG Control Performance Under Fault Conditions For Offshore Wind Applications", 18th International Conference and Exhibition on Electricity Distribution, 2005, Cired 2005, pp. 1 – 5, 6-9 June 2005.

[154] J. Morren, and S. W. H. Haan, "Ridethrough of Wind Turbines with Doubly-Fed Induction Generator During a Voltage Dip", *IEEE Transactions On Energy Conversion,* Vol. 20, No. 2, pp. 435-44, June 2005.

[155] I. Erlich, J. Kretschmann, J. Fortmann, S. Engelhardt, and H. Wrede, "Modeling of Wind Turbines Based on Doubly-Fed Induction Generators for Power System Stability Studies", *IEEE Transactions On Power Systems*, Vol. 22, No. 3, pp. 909-919, Aug. 2007.

[156] X. Zhang, T. Qu, Z. Xie, and R. Cao, "Dynamic analysis of doubly fed induction generator during symmetrical voltage swells", *IEEE, 2011 Second International Conference on Mechanic Automation and Control Engineering, pp.* 1245–1248, 15-17 July 2011.

[157] H. Xu, X. Ma, and D. Sun, "Reactive Current Assignment and Control for DFIG Based Wind Turbines during Grid Voltage Sag and Swell Conditions", *Power Electronics*, Vol. 15, No. 1, pp. 235-245, January 2015.

[158] H. Zehua, "Safety Voltage Control Strategy for High Voltage Ride-Through of Doubly Fed Induction Generator (DFIG) ", *International Power, Electronics and Materials Engineering Conference (IPEMEC 2015),* pp. 562-566.

[159] P. M. Anderson, *Power System Protection*, John Wiley & Sons, INC., Publication, 1999.

[160] D. Aouzellag, K. Ghedamsi, and E. M. Berkouk, "Network Power Flux Control of a Wind Generator"*, Renewable Energy*, Vol. 34, No. 3, pp. 615–622, March 2009.

[161] J. Sundvall, M. C. P. Værens, T. Ofeigsson, and M. Swierczynski, "Dynamic Control of an Electrical Truck Motor", *Institute of Energy Technology,* 8. Semester Report, spring 2007.

[162] R. Carriveau, *Advances in Wind Power*, InTech, November, 2012

[163] J. A. Baroudi, V. Dinavahi, and A. M. Knight, " A Review of Power Converter Topologies for Wind Generators", *Renewable Energy*, Vol. 32, No. 14, pp. 2369-2385, Nov 2007

[164] M. Edrah, K. L. Lo, and O. Lara, " Impact of High Penetration of DFIG Wind Turbines on Rotor Angle Stability of Power Systems", *IEEE Transactions on Sustainable Energy*, Vol. 6, No. 3, pp. 759-766, July, 2015.

APPENDICES

APPENDIX [A]

MODEL PARAMETERS

A-1- DFIG [160]

Rated power = 1.5 MW;

Rated R.M.S. line-to-line voltage (stator) = 690 V;

Rated R.M.S. line-to-line voltage (rotor) = 389 V;

Nominal current: In=1900 A;

Frequency = 50Hz;

Rated rotational speed=1450 rev/min;

Number of pole pairs = 2;

Stator resistance = 0.012 Ω.;

Stator leakage inductance (Ls) =0.0137 H.;

Rotor resistance = 0.021Ω.;

Rotor leakage inductance (Lr) =0.0136 H;

Magnetizing inductance (Lm) =0.0135 H;

A-2 Grid Side Filter

The objective of this filter in the design is to enable fast-acting response of the current controller of the GSC to any variation in current in a time scale of milliseconds. In addition it is responsible for maintaining a stable controller output.

Filter series inductance (L_f) = 0.0006 H;

Filter parallel resistance (r_f) = 0.37 Ω;

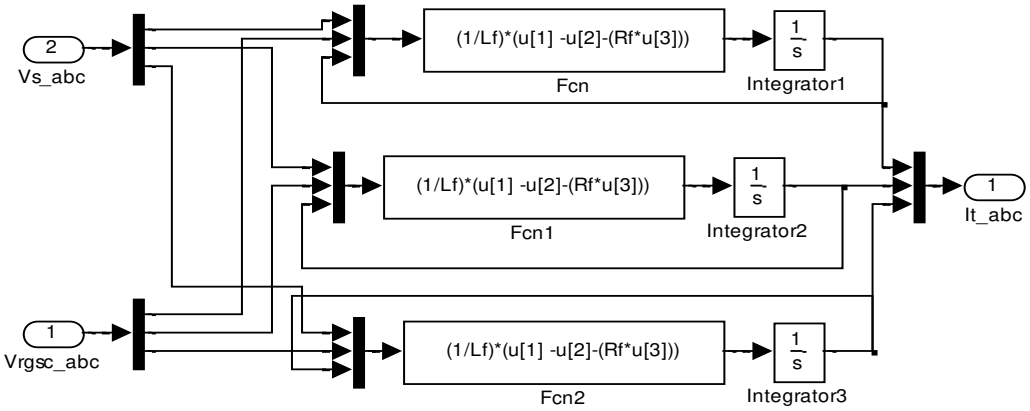

Figure A.1: Simulink model of grid side filter.

A-3 DC- Link

The DC-link capacitor is usually not big enough to smooth the DC-link voltage variation caused by the alternating rotor current [155].

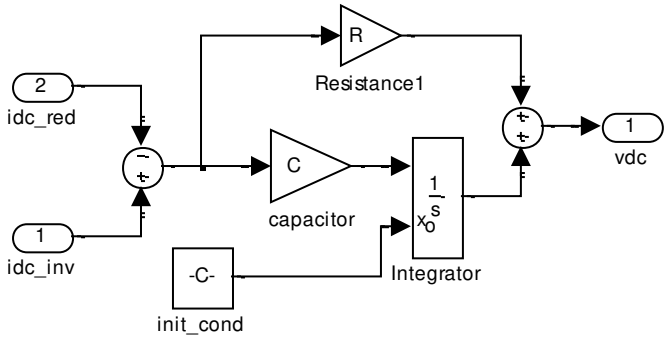

Figure A.2: Simulink model of the DC-link

Nominal DC Link voltage = 1200 V;

DC Link capacitor = 0.038 F;

Resistor= 0.004 Ω

A-4 Wind Turbine

Blade radius R= 35.25 m;

Gear-box ratio= 90;

Air density (ρ) = 1.255 Kg/m^3

Electric machine - Moment of inertia = 90 [kg m^2]

Wind turbine rotor - Moment of inertia: 49.5 ×10^5 [kg m^2]

Shaft stiffness: 114×10^6 [Nm/rad]

Damping coefficient of shaft: 755.658×10^3 [Nm sec/rad]

Friction = 0.0024 Nm/s.

Cut-in wind speed 3 m/s

Optimum tip-speed ratio 6.3

Maximum power coefficient 0.44

A-5 Simulation Controller Parameters

RSC PWM Switching frequency = 5 kHz;

GSC PWM Switching frequency = 5 kHz;

Table A.1: PI controller parameters.

Controller		K_p	K_i
RSC	Current control	2	0.016
	Power control	50	5354.55
GSC	Current control	33	50
	DC-link voltage control	5	350
PLL		180.03	127.2265
QRMRAS		4	70
RCMRAS		2/70	15
Pitch angle controller		200	60

APPENDIX [B]

TRANSFORMATION PROCESS OF THE CURRENTS

After the state space vector model parameters of the induction machine have been calculated, the stator and rotor currents are to be transformed from the two-phase DC current *dq –axis* frame back to the three-phase AC quantities. The transformation process required is the inverse of the two-step voltage transformation used for supply quantities.

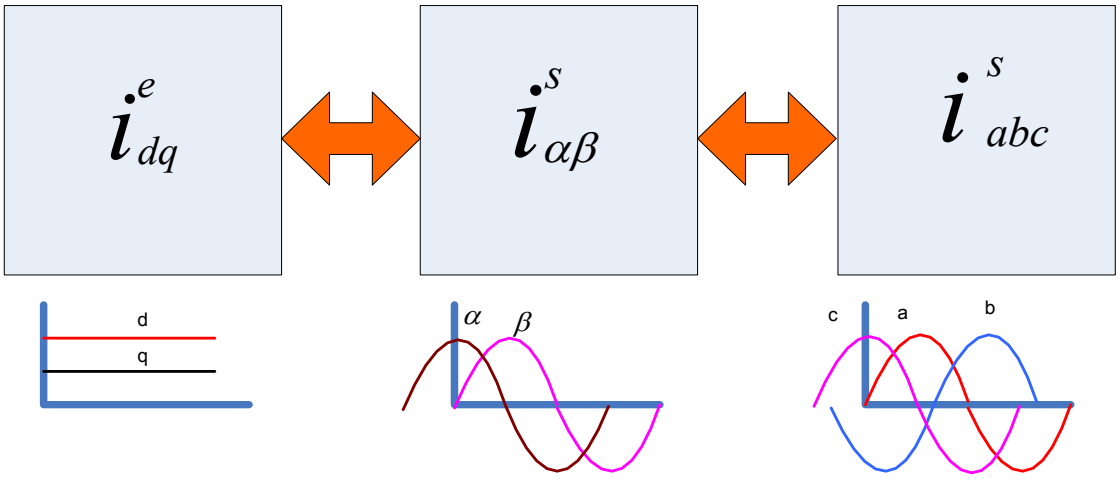

Figure B.1: Current Transformation Process [7].

$$Step\ \{1\} \quad \begin{bmatrix} i^s_{s\alpha} \\ i^s_{s\beta} \end{bmatrix} = \begin{bmatrix} \cos(\theta_s) & -\sin(\theta_s) \\ \sin(\theta_s) & \cos(\theta_s) \end{bmatrix} \begin{bmatrix} i^e_{sd} \\ i^e_{sq} \end{bmatrix} \tag{B.1}$$

$$Step\ \{1'\} \quad \begin{bmatrix} i^s_{r\alpha} \\ i^s_{r\beta} \end{bmatrix} = \begin{bmatrix} \cos(\theta_{sl}) & -\sin(\theta_{sl}) \\ \sin(\theta_{sl}) & \cos(\theta_{sl}) \end{bmatrix} \begin{bmatrix} i^e_{sd} \\ i^e_{sq} \end{bmatrix} \tag{B.2}$$

Step one is to transform the 2-phase DC currents to their 2-phase AC currents. By applying the appropriate angular position of the stator and rotor, this will give their true magnitude and sine wave position [6].

$$Step\ \{2\} \quad \begin{bmatrix} i^s_{sa} \\ i^s_{sb} \\ i^s_{sc} \end{bmatrix} = \begin{bmatrix} 1 & 0 \\ -\frac{1}{2} & \frac{\sqrt{3}}{2} \\ -\frac{1}{2} & -\frac{\sqrt{3}}{2} \end{bmatrix} \begin{bmatrix} i^s_{s\alpha} \\ i^s_{s\beta} \end{bmatrix} \tag{B.3}$$

$$Step\ \{2'\} \quad \begin{bmatrix} i_{ra}^{s} \\ i_{rb}^{s} \\ i_{rc}^{s} \end{bmatrix} = \begin{bmatrix} 1 & 0 \\ -\frac{1}{2} & \frac{\sqrt{3}}{2} \\ -\frac{1}{2} & -\frac{\sqrt{3}}{2} \end{bmatrix} \begin{bmatrix} i_{r\alpha}^{s} \\ i_{r\beta}^{s} \end{bmatrix} \tag{B.4}$$

Step 2 transforms the current quantities from their 2-phase alpha beta magnitudes and positions to their 3-phase magnitude and positions. The ratio applied keeps the 2-phase to 3-phase magnitudes and positions in equal quantities; therefore, the output for the 3-phase system is balanced providing the input is also balanced [6].

APPENDIX [C]

PULSE GENERATION OF THE CONTROLLED SWITCHED MODULATION

The design of the modulation technique should allow for the conversion of the bi-directional power flow. The switching design has to be capable of the inversion and rectification of the bi-directional power flow.

The switching illustrated in figure C.1 represents the rectification of the 3-phase AC voltages to DC voltages through SPWM.
The switching algorithm is:

$$m_a = \frac{\widehat{V_m}}{\widehat{V_{cr}}} \tag{C.1}$$

$$m_f = \frac{f_{cr}}{f_m} \tag{C.2}$$

Definition of switching states

$$\left.\begin{array}{ll} V_{ma} > V_{cr}\ S_1\ ON\ \therefore S_4\ OFF & V_{aN} = V_{dc} \\ V_{ma} < V_{cr}\ S_1\ OFF \therefore S_4\ ON & V_{aN} = 0 \\ V_{mb} > V_{cr}\ S_3\ ON \therefore S_6\ OFF & V_{bN} = V_{dc} \\ V_{mb} < V_{cr}\ S_3\ OFF \therefore S_6\ ON & V_{bN} = 0 \\ V_{mc} > V_{cr}\ S_5\ ON \therefore S_2\ OFF & V_{cN} = V_{dc} \\ V_{mc} < V_{cr}\ S_5\ OFF \therefore S_2\ ON & V_{cN} = 0 \end{array}\right\} \tag{C.3}$$

$$f_{sw} = f_{cr} = f_m * m_f$$

The triangular wave form overlapping the 3 sinusoidal waveforms are the pulses from the switching on/off of the IGBT power devices, through a successfully designed switching algorithm, the back to back inversion and rectification for voltage transformation can be used for the RSC and GSC of a DFIG system.

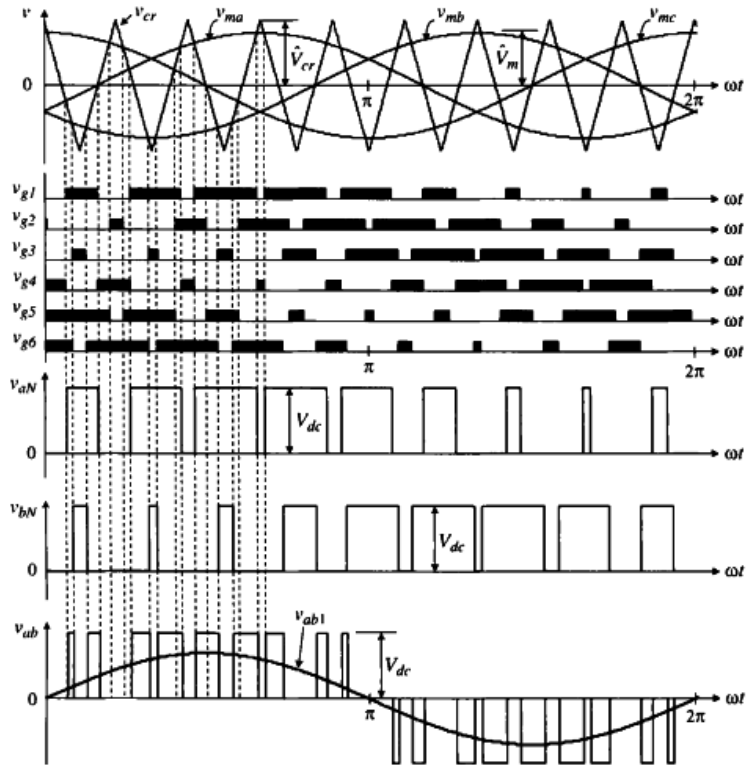

Figure C.1: Output voltages of two level converters with sinusoidal SPWM [6, 7].

APPENDIX [D]

SIMULINK MODEL

D-1 Complete DFIG system

The DFIG wind turbine model mainly comprises the turbine block, DFIG, transformer, PWM voltage source converters, the DC-link block and the grid- and rotor-side PWM converter control blocks. The output voltages of the PWM voltage source converters are applied in the electrical circuit as controllable voltage sources. In the following sections, the functions of the turbine block, DFIG, PWM voltage source converter and the grid and rotor-side PWM converter control blocks are described in detail.

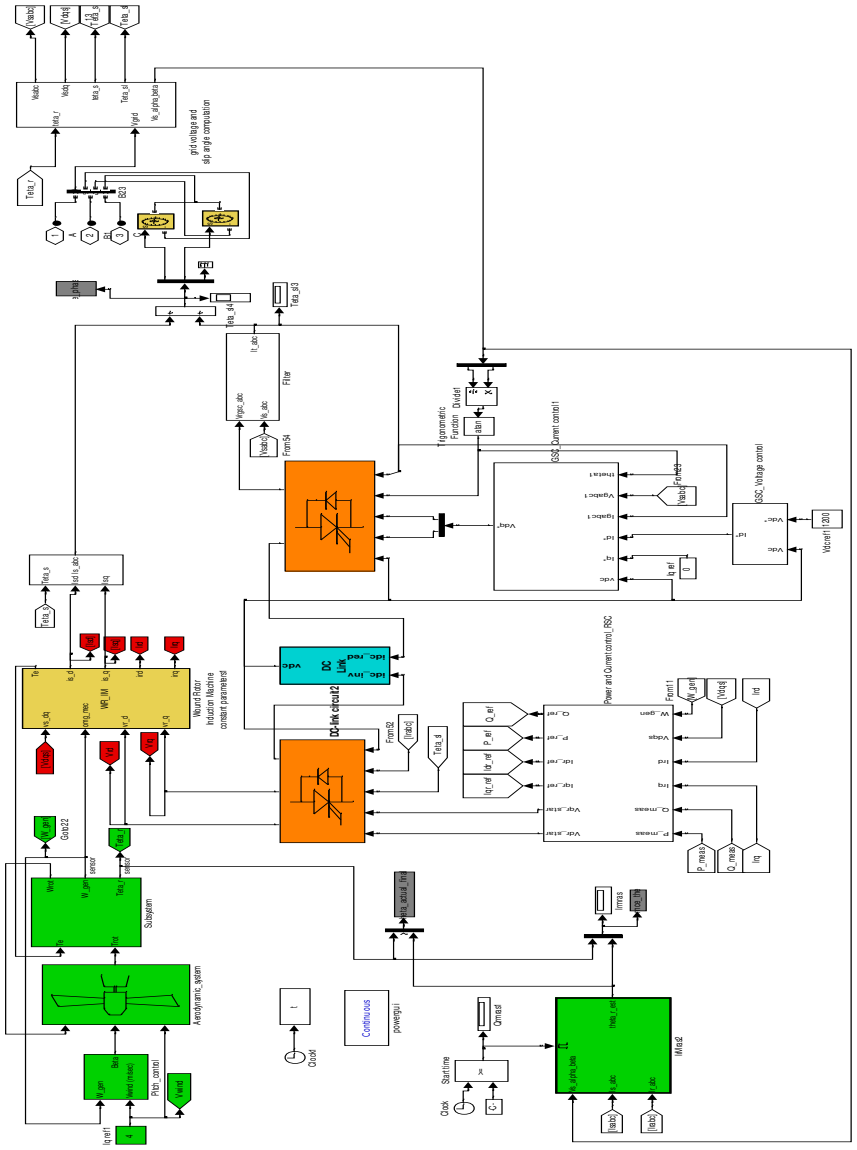

Figure D.1: Block diagram of the DFIG wind turbine model.

D-2 Aerodynamic Model

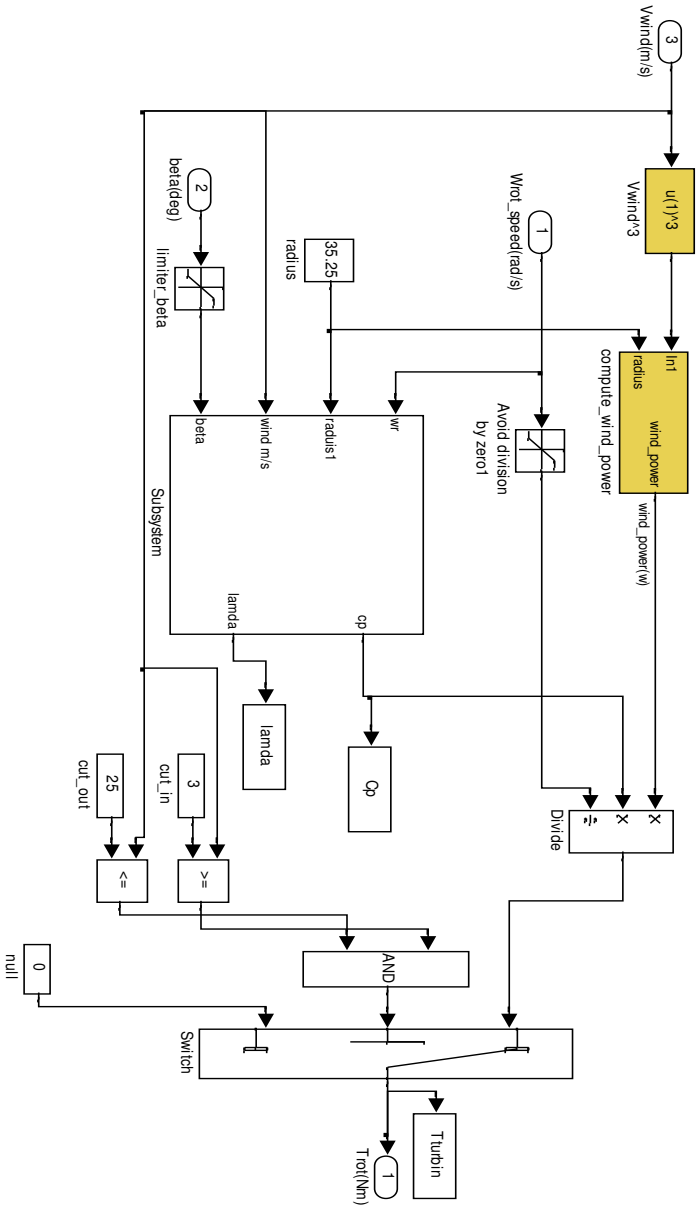

Figure D.2: Diagram of the aerodynamic block in the DFIG wind turbine model.

D-3 Pitch Angle Controller Model

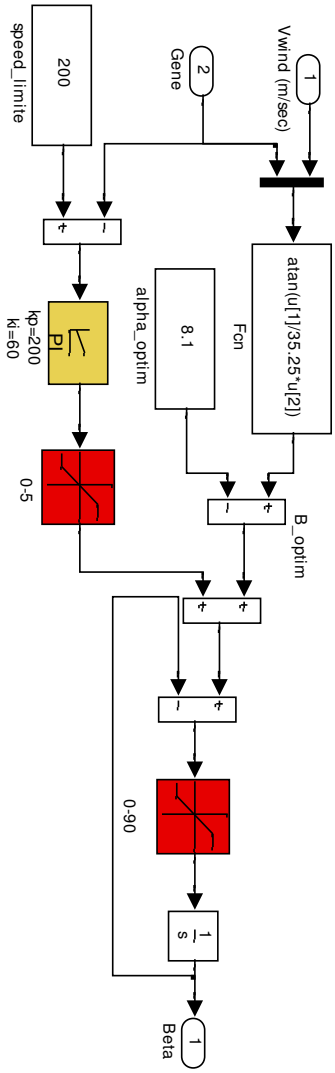

Figure D.3: Diagram of the pitch angle control block in the DFIG wind turbine model.

D-4 Generator Model

The model is shown in Figure D.4. The wound rotor induction generator is modelled in the state variable form using generalized machine theory. The stator and the rotor windings are transformed into their 2-phase equivalents using the *dq0*- transformation.

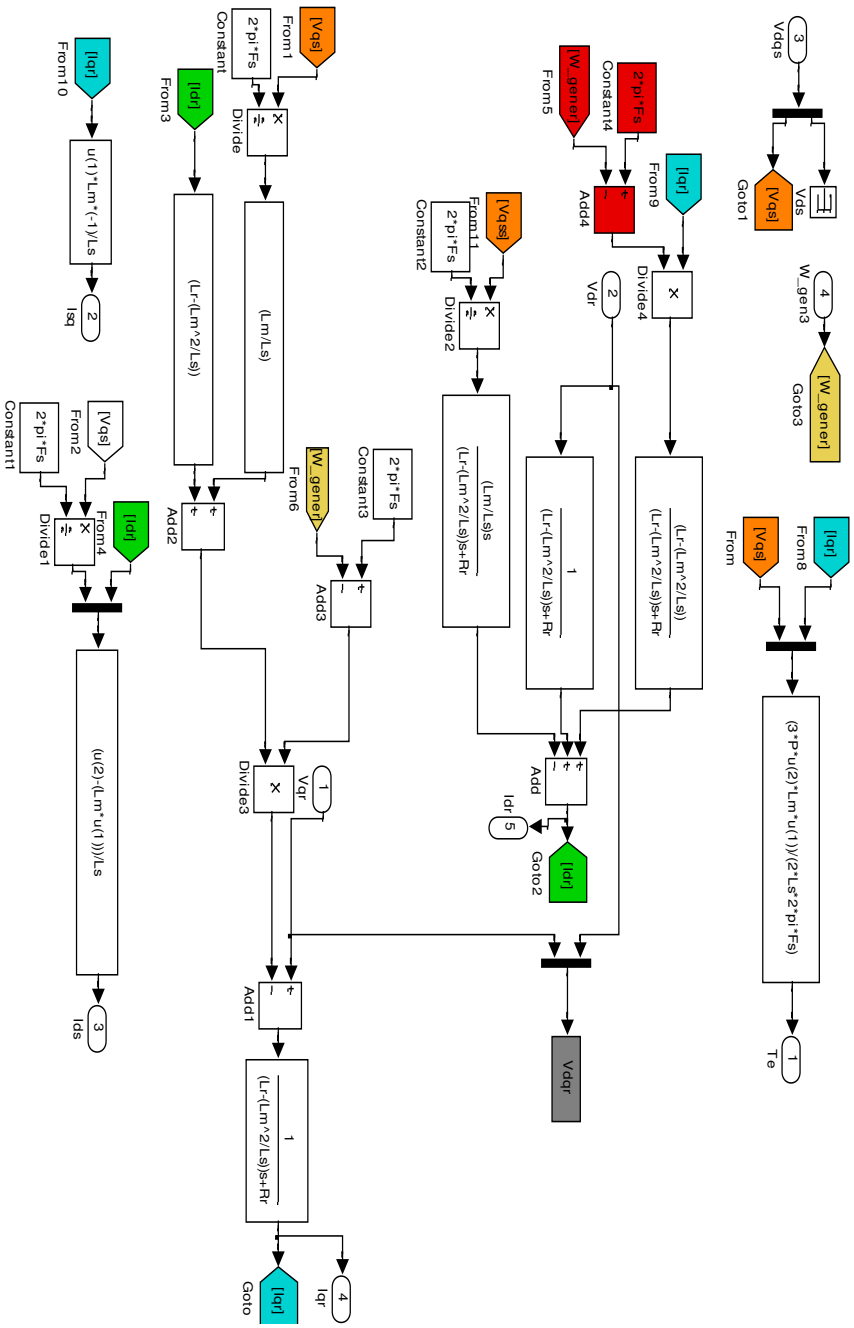

Figure D.4: Diagram of the mathematical model of DFIG.

D-5 PWM Voltage Source Converter Model

The PWM converter block, built with custom components, is shown in Figure D.5.

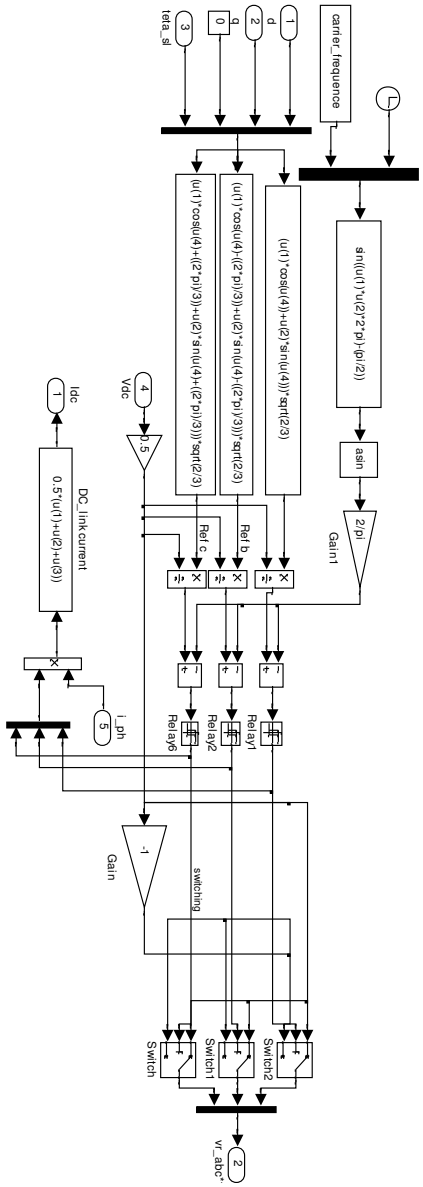

Figure D.5: Block diagram of the PWM.

D-6 GSC and RSC Model

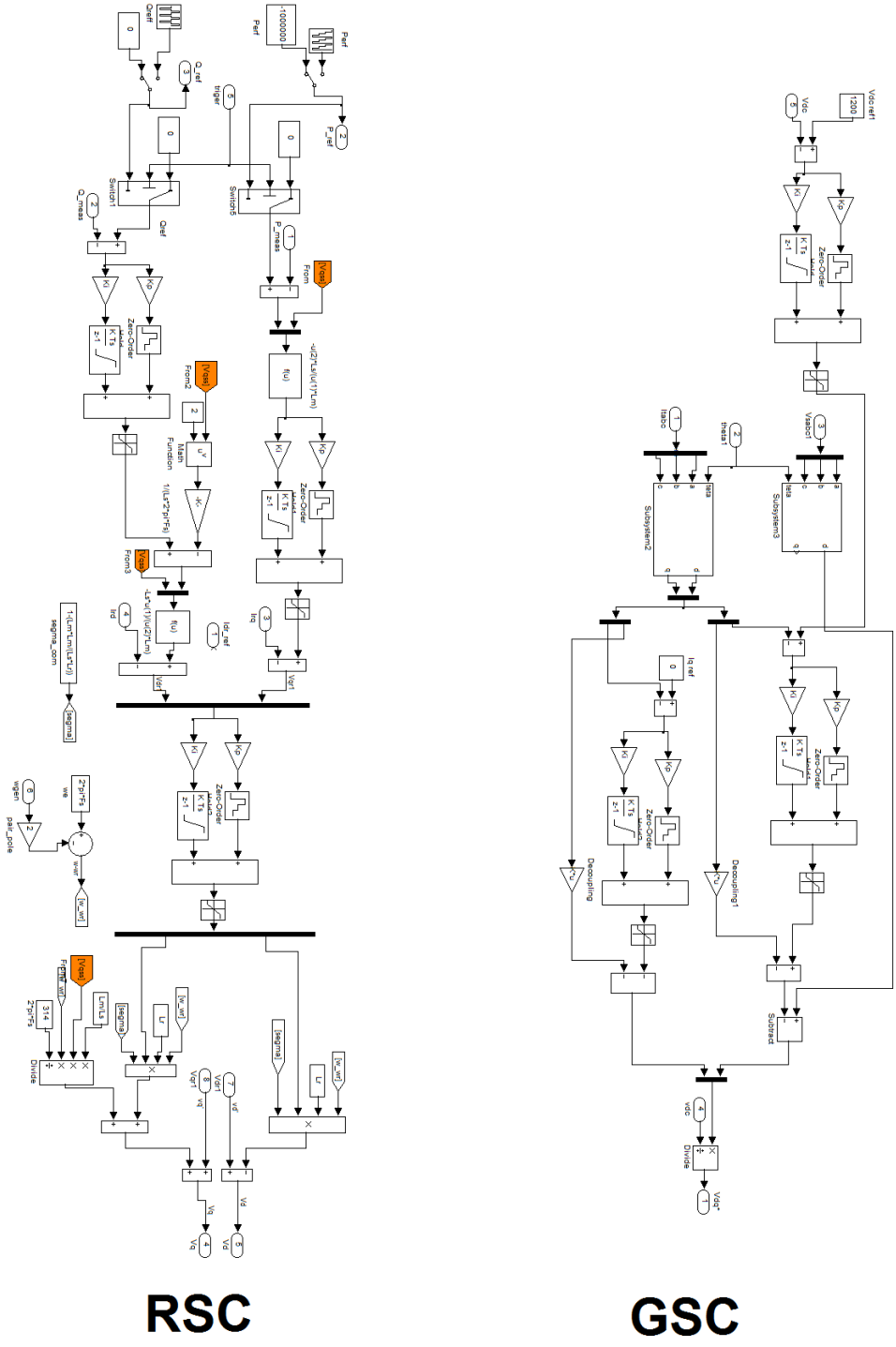

Figure D.6: Diagram of inner and outer loops control blocks in the RSC and GSC.

D-7 Stator Angle Estimator Model

The stator voltage angle is determined by a PLL and a VCO as shown in Figure D.7.

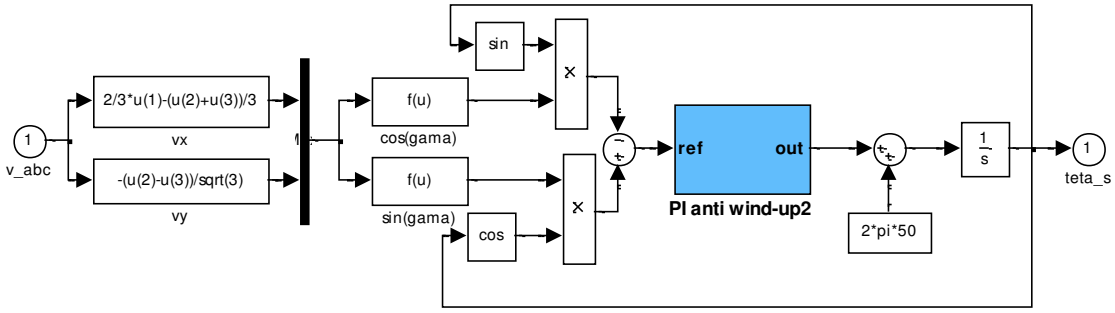

Figure D.7: Diagram of PLL used to compute the stator voltage angle.

D-8 Rotor Reactive Power MRAS (QRMRAS) Model

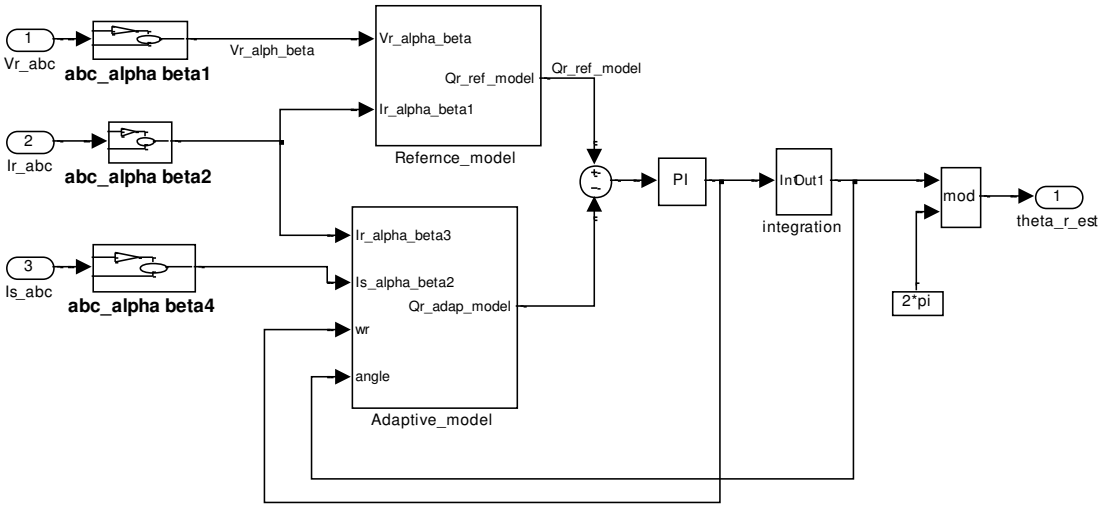

Figure D.8: Diagram of rotor reactive power-based MRAS (QRMRAS).

D-9 Rotor Current MRAS (RCMRAS) Model

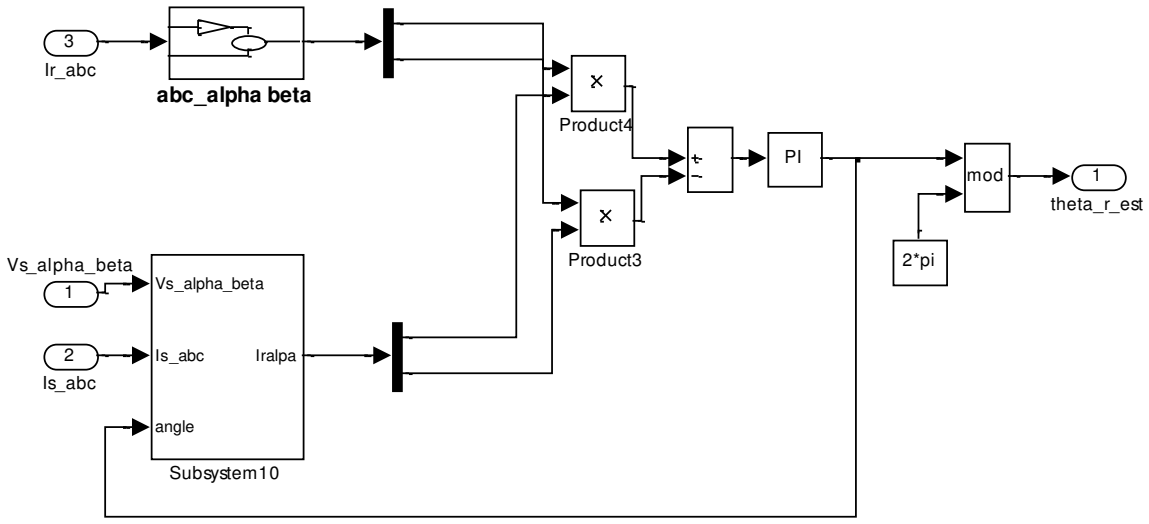

Figure D.9: Diagram of rotor current MRAS (RCMRAS) subsystem.

D-10 Crowbar Model

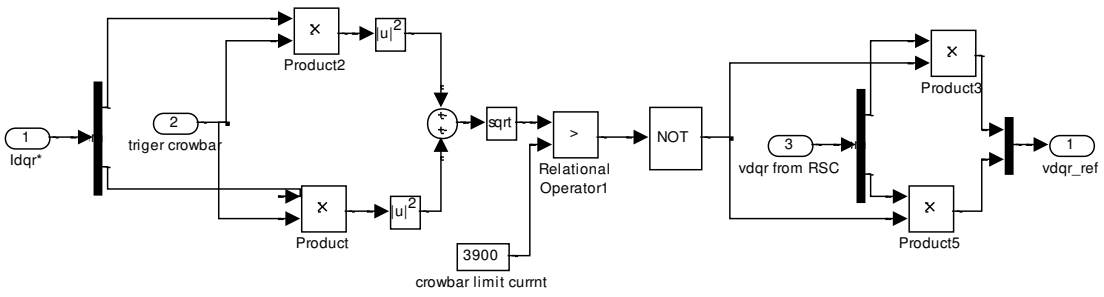

Figure D.10: Diagram of Crowbar subsystem.

APPENDIX [E]

MATLAB INITIALISATION CODE

E-1 Appendix Model Parameter

```
%Generated power=1.5 MW
%Rated voltage (stator):398/690 V.
Vs=398;
%rated voltage (rotor):225/389 V
Vr=225;
% nominal current: In=1900 A.
%Rated rotational speed :1450 rev/min
% slip: g
p=2;
Rr=0.021;
Rs=0.012;
Ls=0.0137;
Lr=0.0136;
Lm=0.0135;
g=0.03;
f=50;
ws=2*pi*f;
G=90;
R=35.25;
Tr=Lr/Rr;
Ts=Ls/Rs;
sig=1-((Lm^2)/(Ls*Lr));
k=Lm/(sig*Ls*Lr);
Y=1/(sig*Tr);
T_ond=0.01;
```

E-2 Plotting Tip Speed Ratio Variation with Power Coefficient and Pitch Blade Angle

```
%plotting curve of lambda with power coefficient and
%pitch blade angle
clc
clear all
%Cp parameters from Thomas Ackermann, ?Wind Power in Power Systems?
c1=0.73;
c2=151;
c3=0.58;
c4=0.002;
c5=2.14;
c6=13.2;
c7=18.4;
c8=-0.02;
c9=-0.003;
[lambda,Beta]=meshgrid(1:0.5:15,1:1:30);
vwind=(3:1:25); %wind-speed [m/s];
```

```
R=35.25; %radius of the rotor or the blade length [m];
%in next steps the calculation of the cp curve for different
lambda_i=1./(lambda+c8.*Beta)-c9./(Beta.^3+1);
cp = c1 * (c2*lambda_i - c3*Beta - c4.*Beta.^c5 -c6).* exp( -
c7*lambda_i);
cp=1/2*(cp+abs(cp)); %only positive values of Pref
mesh(lambda,Beta,cp)
surf(lambda,Beta,cp)
```

E-3 Calculation of the Annual Weibull Distribution of the Wind [132]

```
%Calculation of the annual WEIBULL distribution of the Wind
clc
clear all
V=(4:1:25); %Wind speed [m/s]
% constant of Weibull parameters from IEC classification
c=2;
a=11.38;
%Calculation of the distribution
P=365*24*(c./a.^c).*Vwind.^(c-1).*exp(-(Vwind./a).^c);
plot (Vwind,P)
title('annual wind distribution curve based on weibull distribution
function')
xlabel('wind speed (m/s)')
ylabel('time (hourse/year)')
```

APPENDIX [F]

PI CONTROLLER DESIGN IN Z DOMAIN

The general equation for PI control in the time domain as follows [161]:

$$u(t) = k_p\, e(t) + k_i \int_{t_0}^{t} e(t)d(t) \tag{F.1}$$

where $u(t)$ is the output signal, $e(t)$is the error signal, 'k_p' is the proportionality constant and 'k_i' is the integration constant. PI control in z-domain for a backward transform previous equation is expressed as:

$$\frac{U(z)}{E(z)} = k_p + k_i \frac{T_s}{1-\frac{1}{z}} \tag{F.2}$$

where T_s is the sampling time. In Figure (F.1) is presented the diagram of the PI in z domain.

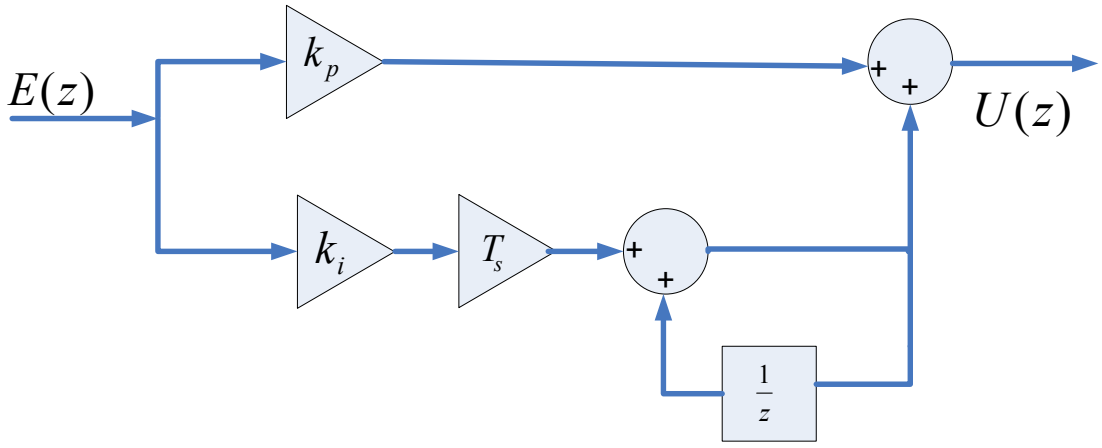

Figure F.1: PI control in the z-domain using backward transform.